UNIVERSITÀ DEGLI STUDI DI PADOVA

UNIVERSITÀ DEGLI STUDI DI PADOVA

DIPARTIMENTO DI BIOLOGIA

SCUOLA DI DOTTORATO DI RICERCA IN:

BIOSCIENZE E BIOTECNOLOGIE

INDIRIZZO: BIOLOGIA CELLULARE

CICLO: XXVIII

Sympathetic innervation controls cardiac trophism and physiology

Direttore della Scuola: Ch.mo Prof. Paolo Bernardi

Coordinatore d'indirizzo: Ch.mo Prof. Paolo Bernardi

Supervisore: Ch.mo Prof. Marco Mongillo

Dottorando: Nicola Pianca

Index

Abbreviations **5**

Summary **9**

Riassunto **15**

Introduction **21**

The heart: structure and function *21*
The electrocardiography *31*
Innervation of the heart *33*
The cardiac sympathetic nervous system plays a key role in the regulation of the myocardial mass *39*
Optogenetics *45*

Results **49**

Sympathetic innervation locally modulates cardiomyocyte proteolysis inside the working myocardium *51*
Optogenetic determination of the myocardial requirements for extrasystoles by cell type-specific targeting of ChannelRhodopsin-2 *75*
Optogenetic interrogation of cardiac sympathetic neurons shed light on the "neuro-cardiac junction". *103*
Cardiac optogenetics as an alternative to electrical pacemaking and cardioversion: insights from an in vivo animal model *121*

Conclusions **129**

Future perspectives **130**

References **133**

Appendix **147**

Acknowledgments **173**

Abbreviations

6-OH-DA	6-Hydroxy-DopAmine
α-MyHC	alpha-MYosin Heavy Chain
ANS	Autonomic Nervous System
AP	Action Potential
APD	Action Potential Duration
ATP	Adenosine-1,4,5,-TriPhosphate
AV	AtrioVentricular
AVN	AtrioVentricular Node
β-AR	beta-Adrenergic Receptor
BBB	Bundle Branch Block
BSA	Bovine Serum Albumin
cAMP	Cyclic-Adenosine MonoPhosphate
ChR2	ChannelRhodopsin-2
CICR	Calcium-Induced Calcium Release
CM	CardioMyocyte
CTRL	Control
Cy3	Cyanine-3
Cx	ConneXin
DAPI	4,6-DiAmidino-2-Phenyl-Indole
DNA	DeoxyriboNucleid Acid
DTT	DiThioTreitol
ECC	Excitation Contraction Coupling
ECG	ElectroCardioGram
ENDO	subEndocardium
EPI	subepicardium
ERP	Effective Refractory Period
FOXO3	Forkhead Box O3
FRET	Föster Resonance Energy Transfer
GAPDH	GlycerAldehyde 3-Phosphate DeHydrogenase
GFP	Green Fluorescent Protein

HR	Heart Rate
HRP	HorseRadish Peroxidase
ICD	Implantable Cardioverter Defibrillator
IF	ImmunoFluorescence
ISH	*In Situ* Hybridization
IVS	InterVentricular Septum
KO	Knock-Out
K_v 4.2	Voltage-gated K^+ channel 4.2
LA	Left Atrium
LAD	Left Anterior Descending coronary artery
LBB	Left Bundle Branch
LBBB	Left Bundle Branch Block
LED	Light Emitting Diode
LV	Left Ventricle
MI	Myocardial Infarction
MOPS	4-MorpholinePropane Sulfonic acid
MuRF1	Muscle RingFinger protein 1
NCX	Na^+/Ca^{2+} eXchanger
NE	NorEpinephrine
NGF	Nerve Growth Factor
NT-3	NeuroTrophin-3
OCT	Optimal Cutting Temperature embedding matrix
OPT	Optical Projection Tomography
PBS	Phosphate Buffered Saline
PCR	Polymerase Chain Reaction
PF	Purkinje Fiber
PFA	Para-Formaldehyde
PKA	Protein Kinase A
PLB	PhopshoLamBan
PVDF	PolyVyniliDene Fluoride
PVC	Premature Ventricular Complex
RBB	Right Bundle Branch
RBBB	Right Bundle Branch Block
RFP	Red Fluorescent Protein

RNA	RiboNucleic Acid
RT	Room Temperature
RT-qPCR	Real Time Quantitative Polymerase Chain Reaction
RV	Right Ventricle
RVOT	Right Ventricular Outflow Tract
RyR2	Ryanodine Receptor 2
SAN	SinoAtrial Node
SCD	Sudden Cardiac Death
SDS	Sodium Dodecyl Sulfate
SEM	Standard Error Mean
SER	SarcoEndoplasmic Reticulum
SERCA	Sarco-Endoplasmic Reticulum Calcium ATPase
SN	Sympathetic Neuron
SNS	Sympathetic Nervous System
SR	Sarcoplasmic Reticulum
TBS	Tris Buffered Saline
TnC	Troponin-C
TnI	Troponin-I
TnT	Troponin-T
TOH	TyrOsine Hydroxylase
TTBS	Tween20-Tris Buffered Saline
UPS	Ubiquitin Proteasome System
VERP	Ventricular Effective Refractory Period
VF	Ventricular Fibrillation
VT	Ventricular Tachycardia
WB	Western Blot
WGA	Wheat Germ Agglutinin
WT	Wild Type

Summary

Rationale

Cardiac sympathetic neurons (SNs) are the main physiologic regulators of heart activity during stress conditions, operating in the so called "*fight or flight"* response, which is mainly composed by an increase in heart rate (*chronotropy*) and an increase in contraction force (*inotropy*). The former is exerted by SNs innervating heart physiological pacemaker (*sinoatrial node*) and the latter by SNs innervating the working myocardium. At the level of the working myocardium, we have recently uncovered an additional novel role for SNs in modulating cardiomyocyte (CM) trophism. Indeed, we have demonstrated that SNs modulates CM proteolysis rate through the activation of β2-adrenoceptors and the downstream AKT/FOXO pathway, resulting in the repression of the two main muscle specific ubiquitin ligases: MuRF1 and Atrogin1[1]. We described that SNs distribute inside the ventricular myocardium with a well-defined pattern. Moreover, data obtained in our laboratory from electron microscopy and immunofluorescence analysis provided structural suggestions of a direct contact between SNs and CMs: such as thickening of the CM membrane juxtaposed to the neuronal terminal, polarization of the neurotransmitter-containing vesicles into SN terminal and a close distance between the membrane of SN terminal and the one of contacted CM, all features that resemble a sort of neuro-cardiac junction, similar to what is described in literature for the neuromuscular junction. This concept has been already proposed in literature, in descriptive studies although it has never been directly proved so far.

Aims and scopes

In this thesis I will investigate the characteristics of SN-CM interaction, to elucidate if the control of CM activity by SNs occur through a direct cell to cell interaction. I will study SN-CM interaction at the level of the working myocardium, to assess if SN innervation is able to modulate locally CM structural properties. Moreover, using an *in vitro* model of SNs and CMs coculture I will test the hypothesis of the direct interaction between SN and CM and I will evaluate the functional effects of this interaction, *in vivo*, at the level of the sinoatrial node, exploting the advantages of a novel optogenetic approach. To reach this aim,

I will implement cardiac optogenetics on CM, Purkinje fibers and SNs. Finally, I will inquire possible translational applications of cardiac optogenetics for clinically relevant situations. The understanding of the mechanism of SN-CM interaction is of great clinical relevance since cardiac innervation impairment has been associated to a growing amount of pathological situations, such as myocardial infarction, diabetes and different types of cardiomyopathies.

Results

Based on our recently published evidence that cardiac SNs provide trophic signal to CMs by constitutive repression of proteolysis (see **Appendix**), we aimed to define whether the distribution of SN throughout the myocardium could determine the appearance of local differences in CM size. We quantified the SN density inside the ventricular wall, and we observed that SNs are mainly concentrated in the outer part of the ventricular wall, which is called subepicardium (hereafter EPI), as compared to the inner part, which is called subendocardium (hereafter ENDO) in the mouse heart, while they had an inverse distribution in the heart of other mammals, such as rat, rabbit and also in the human heart. By morphometric analysis we observed a correlation between CM size and SN density, which showed that regions that are more innervated, present CMs with bigger size. We decided to analyze in better detail this correlation focusing on the mouse heart, given the well known advantages of this animal model in terms of genetic, pharmacology and handling, moreover, mouse heart seems to show the highest heterogeneity among the species analyzed. Cardiac sympathetic innervation occurs during the first three postnal weeks, and consistently our results showed that differences in EPI vs ENDO CM size establishes progressively along with the process of myocardium innervation, reaching the definitive pattern in the adult. On the contrary, mice denervated since birth never show heterogeneity in CM size from the neonatal life till the adulthood. We then demonstrated that SN modulation of CM size is not only established in the neonatal life but also maintained in the adulthood, since hearts mice denervated in the adulthood loss the CM heterogeneity. Moreover, the systemic continuous delivery of either an agonist (i.e. clenbuterol) or an antagonist (i.e. ICI 118,551) of the β2-AR, resulted in the abolishment of CM heterogeneity. In these hearts SN patterning was unaltered, but consistently with our hypothesis, its regional control over CM size was by-passed by the diffuse action of the drug. To assess if SN modulates one of the two major proteolitic systems i.e. the ubiquitin proteasome system (UPS) in CMs differentially throughout the myocardium, we evaluated the mRNA expression level of MuRF1 using in

situ hybridization (ISH) in control and denervated adult mouse hearts. In normal condition mRNA levels of MuRF1 are comparable between EPI and ENDO, but when we perturbed this equilibrium by the ablation of SNs we found that upregulation of MuRF1 is significantly more pronounced in the EPI region compared to the ENDO.

Altogether, our results indicate that cardiac SNs, by exerting a regional modulation of CM proteolytic machinery, determine the physiological patterning of CM size into the myocardium. Moreover, these results points in the direction of a direct contact between SNs and CMs. The elucidation of the physiological mechanism implicated in the "SN-to-CM" signalling is of great relevance since impairment of this signalling has been implicated in several cardiovascular disorders and β-blockers represent the pharmacological tool widely used in such disease conditions.

To test the functional implication of this direct contact in the intact heart, we implemented the technique of optogenetics to the heart cells. Optogenetics exploits the targeting of photoactivatable ion channels in specific cell types to achieve non-invasive control of membrane potential in excitable cells. Channelrhodopsin-2 (ChR2) is a microbial derived cation channel that undergoes a conformational change upon illumination resulting in the immediate increase in ionic permeability, with high conductance to Na^+. We have generated transgenic lines of mice expressing ChR2 selectively in different excitable cells of the heart such as: CMs, conduction system cells and sympathetic neurons. First we set up the technique using the models in which ChR2 is expressed in the working and conducting CMs and we succeeded in inducing ectopies with high spatial and temporal resolution, arising from working or conducting CMs selectively. Exploiting the high versatility of optogenetics, that allowed us to finely shape the volume of illuminated tissue, and by developing a mathematical modelling of light penetration into the myocardium, we have been able to measure the minimal number of depolarized working CMs (≈1800) and PFs(≈160) needed to evoke an extrasystole. By using the same epicardial photostimulation assay, we successfully obtained ectopic beats arising from the AV bundle, the septal branches and the distal part of the PFs and measured, *in vivo,* the PF effective refractory period, an electrophysiological parameter that so far has only been estimated in *ex vivo* preparations. Cardiac optogenetics allowed us to identify a site, at the origin of right ventricular outflow tract, that is highly prone to develop arrhythmias during acute ischemia, probably because of the presence of an underlying complex arrangement of PFs that we described through a 3D reconstruction. In conclusion, we quantified the minimal number of cells needed to evoke an ectopic beat from working and conducting CMs in the intact heart;

we achieved the first characterization of PFs electrophysiology *in vivo* and defined their role in arrhythmogenesis during acute ischemia. All these results have been published in PNAS.

After having set up cardiac optogenetic experiment in mice models expressing ChR2 in working and conducting CMs, we then moved to the model in which ChR2 is expressed in cardiac SNs. To investigate in detail the functional implications of the direct interaction between SNs and CMs, we first used optogenetics in an *in vitro* model of SN-CM co-culture and performed real-time live imaging by the application of FRET-based biosensors to explore the effects of the SN-CM interaction at the subcellular level. We demonstrated that even a minimal activation of SNs (*i.e.* one action potential) is sufficient to stimulate cAMP pathway exclusively in the contacted CMs, while it exerts no effects on non-innervated CMs, providing evidence of a direct cell to cell interaction. Then we moved to the *in vivo* situation where we exploit optogenetics to stimulate SN processes directly at the level of sinoatrial node, in order to dissect the effect of SN activation on heart rate. Sinoatrial node is highly innervated by SNs, which are closely associated to pacemaker cells. Indeed, *in vivo* photostimulation experiments showed a short delay between light pulse and the onset of the next *p* wave (44±3 ms), which results in a fast increase in heart rate upon the start of photostimulation and a fast decrease after stopping the stimulation. Moreover, we found that stimulations can be repeated several times without apparent changes in the kinetics of the heart rate increase and that just 2 light pulses are sufficient to provoke a shorter sinus beat. In conclusion the photostimulation of SN projections, probed the kinetics of sympathetic heart rate control, which are characterized by a fast, repeatable and efficient mechanism and add a strong evidence in favor of the existence of a *quasi-synaptic* interaction between SNs and CMs.

Finally, having demonstrated that optogenetics could be successfully applied to obtain cell type-specific control of the different cells composing the myocardium. We wanted to provide a proof-of-principle of the possibility to translate cardiac optogenetics from a scientific investigation tool to a potential therapeutic approach in the treatment of heart rhythm diseases. Indeed, the use of electronic devices for the treatment of arrhythmia had improved life expectancy and reduced mortality in different types of acquired and inherited cardiac diseases. Nevertheless, electric stimulation of heart tissue still has some disadvantages, especially in the longer period, deriving from the lack of specificity of this approach, the inherent damages produced by the electrical currents imposed to the myocardium and the physical contact between the electrodes and the tissue. The specific features of selectivity, non invasiveness and harmlessness of cardiac optogenetics, could

overcome the limits of the current technologies used for the control of heart rhythm. In detail, we demonstrated, in an *in vivo* mouse model, the feasibility of cardiac optogenetics in obtaining: prolonged cardiac pacing without functional nor structural damage, cardioversion from ventricular arrhythmias and recovery from atrioventricular block.

Conclusions

In conclusion during my PhD training I obtained the following results: I) Uncovered a novel role for sympathetic innervation of the heart in modulating the proteostasis of CMs; II) Demonstrated that SNs locally modulate CMs properties; III) Implemented cardiac optogenetics on CMs and PFs; IV) Proposed the first *in vivo* determination of the critical mass of working and conducting CMs needed to obtain an extrasystole; V) Characterized PF physiology *in vivo* with unprecedented detail and specificity; VI) Performed the first example of *in vivo* optogenetic stimulation of sympathetic efferents to the heart; VII) Demonstrated that fast, efficient and repeatable control of heart rate is achieved through a *quasi-synaptic* interaction between SNs and CMs; VIII) Provided a proof-of-principle study for the application of cardiac optogenetics in clinical relevant conditions, as an alternative to current therapies based on electrical stimulation of the heart

Published papers during the PhD (see Results section and Appendix)

1. T. Zaglia*, N. Pianca*, G. Borile, F. Da Broi, C. Richter, M. Campione, S. E. Lehnart, S. Luther, D. Corrado, L. Miquerol, M. Mongillo, Optogenetic determination of the myocardial requirements for extrasystoles by cell-type specific targeting of Channelrhodopsin-2, *PNAS* (2015) Aug 11;112(32):E4495-504.

2. T. Zaglia, G. Milan, A. Ruhs, M. Franzoso, E. Bertaggia, N. Pianca, A. Carpi, P. Carullo, P. Pesce, D. Sacerdoti, C. Sarais, D. Catalucci, M. Krüger, M. Mongillo, M. Sandri, Atrogin-1 deficiency promotes cardiomyopathy and premature death via impaired autophagy, *J Clin Invest.* (2014);124(6):2410-24.

3. T. Zaglia, G. Milan, M. Franzoso, E. Bertaggia, N. Pianca, E. Piasentini, V. A. Voltarelli, P. C. Brum, D. J. Glass, S. Schiaffino, M. Sandri, M. Mongillo, Cardiac sympathetic neurons provide trophic signal to the heart via β2-adrenoreceptor dependent regulation of proteolysis, *Cardiovasc. Res.* (2013) ;97(2):240-50.

Riassunto

Razionale

I neuroni simpatici cardiaci (NS) sono i principali regolatori fisiologici dell'attività cardiaca in condizioni di stress, attuando la cosiddetta risposta "*combatti o fuggi"*, che è composta principalmente da un aumento della frequenza cardiaca (effetto cronotropo) e un aumento della forza di contrazione (effetto inotropo). Il primo effetto viene esercitato dai NS che innervano il *pacemaker* fisiologico del cuore (il *nodo seno-atriale*), e il secondo dai NS che innervano il miocardio di lavoro. A livello del miocardio di lavoro, il nostro gruppo ha scoperto di recente un ruolo aggiuntivo per i NS nella modulazione del trofismo dei cardiomiociti (CM). Abbiamo dimostrato che i NS modulano la proteolisi nei CM attraverso l'attivazione dei recettori beta2-adrenergici e la via di segnalazione AKT/FOXO, con conseguente repressione delle due principali ubiquitina ligasi muscolo specifiche: MuRF1 e atrogin-1. Inoltre, abbiamo osservato che i NS si distribuiscono all'interno del miocardio ventricolare con un profilo ben definito. Inoltre, dati ottenuti nel nostro laboratorio, provenienti da analisi di microscopia elettronica e immunofluorescenza, forniscono evidenze strutturali di un contatto diretto tra NS e CM quali: ispessimento della membrana del CM giustapposto al terminale neuronale, polarizzazione delle vescicole di neurotrasmettitore nel terminale del NS e la stretta distanza tra la membrana del terminale neuronale e quella del CM contattato, caratteristiche che suggeriscono una sorta di giunzione neuro-cardiaca, simile a quanto avviene nella giunzione neuromuscolare. Questo concetto è stato proposto in letteratura, in studi principalmente descrittivi, anche se mai dimostrato direttamente finora.

Obiettivi e scopi della tesi

In questa tesi intendo indagare l'interazione tra NS e CM, per chiarire se il controllo dell'attività dei CM operato dai NS avvenga attraverso un *signalling* locale. Studierò questa interazione a livello del miocardio di lavoro, per valutare se l'innervazione simpatica generi delle differenze regionali in termini di dimensioni dei CM. Inoltre, utilizzando un modello *in vitro* di co-coltura NS-CM testerò l'ipotesi di una interazione diretta tra NS e CM e valuterò l'effetto funzionale di questa interazione, *in vivo*, al livello del nodo senoatriale, sfruttando i vantaggi di un nuovo approccio optogenetico. Per raggiungere questo obiettivo, intendo implementare l'optogenetica cardiaca su CM, fibre di Purkinje e NS e fornire delle prove di principio per possibili applicazioni traslazionali di questa tecnica.

La comprensione del meccanismo di interazione NS-CM è di grande rilevanza clinica poiché uno squilibrio nell'innervazione cardiaca è stato associato ad una quantità crescente di situazioni patologiche, come l'infarto miocardico, il diabete e diversi tipi di cardiomiopatie.

Risultati

Sulla base della nostra recente pubblicazione in cui abbiamo dimostrato che i NS cardiaci forniscono un segnale trofico ai CM che va a reprimere la proteolisi (vedi **Appendix**), abbiamo voluto verificare se la distribuzione dei NS nel miocardio possa determinare delle differenze nella dimensione dei CM. Abbiamo scoperto che i NS sono principalmente concentrati nella parte esterna della parete ventricolare, definita subepicardio (di seguito EPI), rispetto alla parte interna, definita subendocardio (di seguito ENDO), nel cuore del topo, mentre hanno una distribuzione inversa nel cuore di altri mammiferi, come il ratto, il coniglio e nel cuore umano. Abbiamo osservato una correlazione tra le dimensioni dei CM e la densità dei NS. In particolare la regione più innervata (EPI per il topo ed ENDO per gli altri mammiferi analizzati), presenta CM con dimensioni maggiori, ed è interessante notare come questo sia vero anche per il cuore umano. Abbiamo deciso di analizzare più in dettaglio questa correlazione concentrandosi sul cuore del topo, dati i ben noti vantaggi di questo modello animale, in termini di genetica, farmacologia e manipolazione, inoltre, il cuore del topo sembra mostrare la massima eterogeneità tra le specie analizzate. L'innervazione simpatica cardiaca si verifica durante le prime tre settimane di vita postnatale, in accordo con questo, i nostri risultati hanno dimostrato che le differenze nelle dimensioni dei CM tra EPI ed ENDO si stabiliscono progressivamente con l'avanzare del processo di innervazione del miocardio, raggiungendo il compimento definitivo nell'adulto. Abbiamo in seguito dimostrato che la modulazione della dimensione dei CM da parte dei NS non solo si stabilisce nella vita neonatale, ma viene anche mantenuta nell'età adulta, dal momento che i cuori di topi adulti denervati con 6-OH-DA perdono l'eterogeneità dimensionale dei CM. Ad ulteriore sostegno di questi dati, il rilascio sistemico continuo sia di un agonista (clenbuterolo), che di un antagonista (ICI 118.551) del β2-AR, ha portato alla perdita della eterogeneità dimensionale dei CM. In questi cuori la distribuzione dei NS era inalterata, ma in coerenza con la nostra ipotesi, il controllo regionale sulla dimensione dei CM è stato by-passato dall'azione diffusa del farmaco. Per valutare se i NS modulassero uno dei due principali sistemi proteolitici vale a dire il sistema ubiquitina proteasoma (UPS) nei CM in modo diverso all'interno del miocardio, abbiamo valutato il livello di espressione di MuRF1 usando ibridazione in situ (ISH) in cuori di topi adulti di controllo e denervati. In condizioni

normali i livelli di mRNA di MuRF1 sono comparabili tra EPI e ENDO, ma quando abbiamo turbato questo equilibrio tramite l'ablazione dei NS abbiamo scoperto che l'espressione di MuRF1 è significativamente aumentata nella regione EPI rispetto a quella ENDO.

Nel complesso, i nostri risultati indicano che i NS cardiaci, esercitando una modulazione regionale della proteolisi dei CM, determinano il pattern fisiologico di dimensione dei CM nel miocardio. Inoltre, questi risultati puntano nella direzione di un contatto diretto tra NS e CM. Chiarire il meccanismo fisiologico implicato nell'interazione NS-CM è di grande rilevanza in quanto difetti nel funzionamento del sistema nervoso simpatico cardiaco sono associati a numerosi disturbi cardiovascolari e i farmaci betabloccanti rappresentano lo strumento farmacologico ampiamente usato in tali condizioni di malattia.

Per testare l'implicazione funzionale di questo contatto diretto nel cuore intatto, abbiamo sviluppato la tecnica dell'optogenetica applicata alle diverse cellule che compongono il miocardio. L'optogenetica sfrutta l'espressione di canali ionici fotoattivabili in tipi cellulari specifici per ottenere il controllo non invasivo del potenziale di membrana. Channelrhodopsin-2 (ChR2) è un canale cationico derivato da un microrganismo, che subisce un cambiamento conformazionale in seguito a illuminazione, con conseguente immediato aumento della permeabilità ionica con un'alta conduttanza per Na^+. Abbiamo generato delle linee transgeniche di topi che esprimono ChR2 selettivamente nelle diverse cellule eccitabili del cuore quali: CM, cellule del sistema di conduzione, e neuroni simpatici. In primo luogo abbiamo settato la tecnica utilizzando i modelli in cui ChR2 si esprime nei CM di lavoro e del tessuto di conduzione e siamo riusciti a indurre extrasistoli con elevata risoluzione spaziale e temporale, derivanti da CM di lavoro e da CM di conduzione in modo selettivo. Sfruttando l'elevata versatilità dell'optogenetica, che ci ha permesso di modellare con precisione il volume del tessuto illuminato, e attraverso lo sviluppo di un modello matematico di penetrazione della luce nel miocardio, siamo stati in grado di misurare il numero minimo di cardiomiociti di lavoro depolarizzati (≈1800) e fibre di Purkinje (FP) (≈160) necessari per evocare un'extrasistole. Utilizzando lo stesso sistema di fotostimolazione epicardico, abbiamo ottenuto con successo battiti ectopici derivanti dal fascio AV, i rami settali e la parte distale delle FP e misurato, *in vivo*, il periodo refrattario effettivo delle FP, un parametro elettrofisiologico che finora era stato solo stimato in preparati *ex vivo*. L'optogenetica cardiaca ci ha permesso di identificare un sito, all'origine del tratto di efflusso del ventricolo di destra, molto incline a sviluppare aritmie durante ischemia acuta, a causa della presenza di un complesso reticolo sottostante di FP che

abbiamo descritto attraverso una ricostruzione 3D. In conclusione, abbiamo quantificato il numero minimo di CM di lavoro e conduttivi necessari per evocare un battito ectopico nel cuore intatto; abbiamo ottenuto la prima caratterizzazione dell'elettrofisiologia delle FP *in vivo* e definito il loro ruolo nella aritmogenesi durante l'ischemia acuta. Tutti questi risultati sono stati pubblicati in PNAS.

Dopo aver settato l'esperimento di optogenetica cardiaca in modelli di topi che esprimono ChR2 nei CM di lavoro e di conduzione, ci siamo spostati al modello nel quale ChR2 è espresso nei NS cardiaci. Per indagare l'implicazione funzionale del contatto diretto tra NS e CM, abbiamo dapprima utilizzato l'optogenetica in un modello *in vitro* di co-colture NS-CM e eseguito esperimenti di *live imaging* utilizzando biosensori FRET per esplorare gli effetti dell'interazione NS-CM al livello subcellulare. Abbiamo dimostrato come anche una minima attivazione dei NS (e.g. un solo potenziale d'azione) sia sufficiente ad attivare la via di cAMP esclusivamente nei CM innervati, mentre non abbia alcun effetto su quelli non innervati, suggerendo l'esistenza di un contatto diretto tra NS e CM. Successivamente ci siamo spostati nel modello *in vivo*, nel quale abbiamo sfruttato l'optogenetica per stimolare le efferenze dei NS direttamente a livello del nodo senoatriale, per isolare l'effetto dell'attivazione dei NS sulla frequenza cardiaca. Il nodo senoatriale è altamente innervato dai NS, che sono strettamente associati alle cellule pacemaker. Infatti, esperimenti di fotostimolazione *in vivo* mostrato un breve ritardo tra impulso di luce e l'inizio della successiva onda P (44 ± 3 ms), che si traduce in un rapido aumento della frequenza cardiaca all'avvio delle fotostimolazione e una diminuzione rapida dopo l'arresto della stimolazione. Inoltre, abbiamo trovato che stimolazioni possono essere ripetute più volte senza cambiamenti apparenti nella cinetica di aumento della frequenza cardiaca e che solo 2 impulsi di luce sono sufficienti a provocare un ritmo sinusale più veloce. In conclusione, la fotostimolazione dei processi dei NS, ha dimostrato che la cinetica del controllo della frequenza cardiaca attuata dal sistema nervoso simpatico, è caratterizzata da un meccanismo rapido, ripetibile ed efficiente e fornisce una forte evidenza a favore dell'esistenza di un'interazione quasi-sinaptica tra NS e CM.

Abbiamo dimostrato che l'optogenetica può essere applicata con successo per ottenere il controllo del potenziale di membrana delle diverse cellule che compongono il miocardio. Con il presente studio vogliamo fornire una prova di principio della possibilità di traslare l'optogenetica cardiaca da uno strumento di indagine scientifica ad un potenziale trattamento terapeutico per le patologie del ritmo cardiaco. Infatti, l'uso di dispositivi elettronici per il trattamento delle aritmie ha migliorato la speranza di vita e ridotto la

mortalità in diversi tipi di malattie cardiache acquisite e ereditarie. Tuttavia, la stimolazione elettrica del tessuto cardiaco ha ancora alcuni inconvenienti, soprattutto nel lungo periodo, derivanti dalla mancanza di specificità di questo approccio, dai danni prodotti dalle correnti elettriche imposte al miocardio e dal contatto fisico tra gli elettrodi ed il tessuto. Le caratteristiche specifiche di selettività, non invasività e innocuità dell'optogenetica cardiaca, potrebbero superare i limiti delle attuali tecnologie utilizzate per il controllo del ritmo cardiaco. In particolare, abbiamo dimostrato, in un modello di topo *in vivo*, la fattibilità dell'uso dell'optogenetica cardiaca per ottenere: una prolungata stimolazione cardiaca senza danni funzionali e strutturali, la cardioversione da aritmie ventricolari e il recupero dal blocco atrioventricolare.

Conclusioni

In conclusione, durante il mio dottorato ho ottenuto i seguenti risultati: I) Scoperto un nuovo ruolo dell'innervazione simpatica del cuore nel modulare la proteostasi dei CM; II) Dimostrato che i NS modulano localmente le proprietà dei CM; III) Implementato l'optogenetica cardiaca in CM e FP; IV) Proposto la prima determinazione *in vivo* della massa critica di CM di lavoro e di conduzione necessaria per ottenere un'extrasistole; V) Caratterizzato la fisiologia delle FP *in vivo* con un dettaglio ed una specificità senza precedenti; VI) Eseguito il primo esempio di stimolazione optogenetica *in vivo* di efferenze simpatiche del cuore; VII) Dimostrato che un controllo rapido, efficiente e ripetibile della frequenza cardiaca è ottenuto attraverso una interazione quasi-sinaptica tra i NS e i CM; VIII) Fornito una prova di principio per l'applicazione dell'optogenetica cardiaca in condizioni cliniche, come alternativa alle attuali terapie basate su stimolazione elettrica del cuore.

Articoli scientifici pubblicati durante il dottorato (vedi le sezioni Results e Appendix)

1. T. Zaglia*, N. Pianca*, G. Borile, F. Da Broi, C. Richter, M. Campione, S. E. Lehnart, S. Luther, D. Corrado, L. Miquerol, M. Mongillo, Optogenetic determination of the myocardial requirements for extrasystoles by cell-type specific targeting of Channelrhodopsin-2, PNAS (2015) Aug 11;112(32):E4495-504.
2. T. Zaglia, G. Milan, A. Ruhs, M. Franzoso, E. Bertaggia, N. Pianca, A. Carpi, P. Carullo, P. Pesce, D. Sacerdoti, C. Sarais, D. Catalucci, M. Krüger, M. Mongillo, M. Sandri, Atrogin-1 deficiency promotes cardiomyopathy and premature death via impaired autophagy, J Clin Invest. (2014);124(6):2410-24.
3. T. Zaglia, G. Milan, M. Franzoso, E. Bertaggia, N. Pianca, E. Piasentini, V. A. Voltarelli, P. C. Brum, D. J. Glass, S. Schiaffino, M. Sandri, M. Mongillo, Cardiac sympathetic neurons provide trophic signal to the heart via β2-adrenoreceptor dependent regulation of proteolysis, Cardiovasc. Res. (2013) ;97(2):240-50.

Introduction

The heart: structure and function

Organ architecture

The heart is the organ responsible for the flowing of blood in the organism, by pumping the blood from the lungs to the systemic circulatory system and from that back to the lungs. Thus delivering oxygen and nutrients to all the cells of the body. The mammalian heart can be viewed as two pumps working in series: the *right* (RA) and the *left atria* (LA), which collect the blood coming respectively from systemic circulation and pulmonary circulation, that pump blood into the ventricular cavities, and the *right* (RV) and *left ventricles* (LV) that pump blood into the pulmonary and systemic circulation, respectively. At the interface between the atria and ventricles there are the *atrioventricular* (AV) *valves*, which guarantee the unidirectional flow of blood from atria to the ventricles, named *tricuspid valve* for the right section and *mitral valve* for the left section. Moreover, with the same scope the *semilunar valves* are located at the interface between ventricles and their great artery.

(**Figure I**)

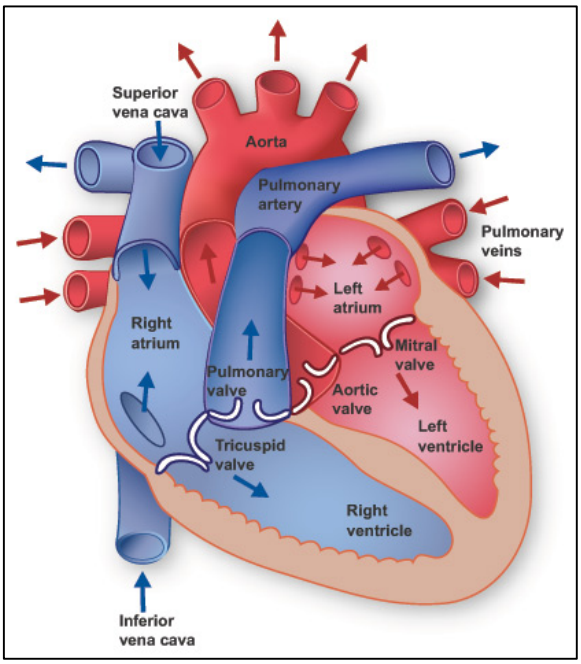

Figure I: *Anatomy of the heart.*

All these four valves lie in a plane within a scaffold of connective tissue, which electrically insulates the atria from the ventricles. The *AV bundle* (also called *His bundle*), a strand of specialized ventricular myocardium, penetrates this barrier and provide the only electrically conducting pathway between the atria and the ventricles, forming the *AV node* in the atrial region[2]. The larger cusps of the mitral and tricuspid valves are bound to a fibrous structures called *chordae tendinae* that link the leaflet of the valves to particular regions of the myocardium, called *papillary muscles*, that projects from the right and left ventricular cavities[3]. The four chambers of the heart are different in shape and morphology: the atria have an almost rounded shape and similar morphology, while left and right ventricle are different in size and morphology and possess a thicker wall compared to the atria. In detail, the LV is considerably thicker than the RV, and it has a cavity, which resembles a cone with inflow from the mitral valve and outflow from the semilunar valve placed side-to-side in the wider end. RV instead has a crescent shape with blood entering through the tricuspid valve at one end and exiting through the semilunar valve at the other[2]. The portion of myocardium that lies between RV and LV is called *interventricular septum* (IVS). A fibrous sac called *pericardium,* encapsulates externally the heart and its inner surface is in contact with the *epicardium,* a layer of endothelial cells that lies just above the myocardium. A similar layer of connective cells called *endocardium*, instead, lines the cavity of atria and ventricles[4].

Blood supply to the heart is provided by large epicardial coronary arteries, the most important being: left main coronary artery, right coronary artery, left anterior descending (LAD), circumflex and posterior descending coronary artery; these large vessels then branch into smaller ones and penetrate into the myocardium to ensure a homogenous perfusion.

Histology and cytoarchitecture of the myocardium

The myocardium is composed by different cell populations including: *cardiomyocytes* (CMs), *fibroblasts*, *endothelial cells*, *smooth muscle cells* and *neurons* (see below). CMs are the cells responsible for heart contraction and although are only the 30% of the total number of heart cells, they represent most of the myocardial mass. CMs can be divided into two main populations: *working CMs*, responsible for the contractile activity and *conducting CMs*, specialized cells that lost their contractile apparatus and conduce the electrical impulse that initiate heart contraction.

Working CMs can be subdivided into atrial, smaller in size, and ventricular CMs. Moreover, inside the ventricular walls three subtypes of ventricular CMs can be found, that

are distinguished for their different electrophysiological properties[5-7]. These cells are organized in the transmural direction into three juxtaposed layers, that differ for fiber orientation, that are called, going from the outer part to inner part: *subepicardium* (EPI), *midmyocardium* (MID) and *subendocardium* (ENDO). Recent studies in the murine heart, using the technique of "diffusion tensor cardiovascular magnetic resonance" (DTI), that exploits the anisotropy of water diffusion exerted by the molecular environment[8,9], allowed to precisely define the CMs orientation in the different regions of the ventricles and showed that CMs in EPI and ENDO have their long axis aligned parallel to the base-apex direction, while CMs in MID have an orientation that progressively changes moving from the border zone with EPI to the one with ENDO[10-14] (**Fig. II**).

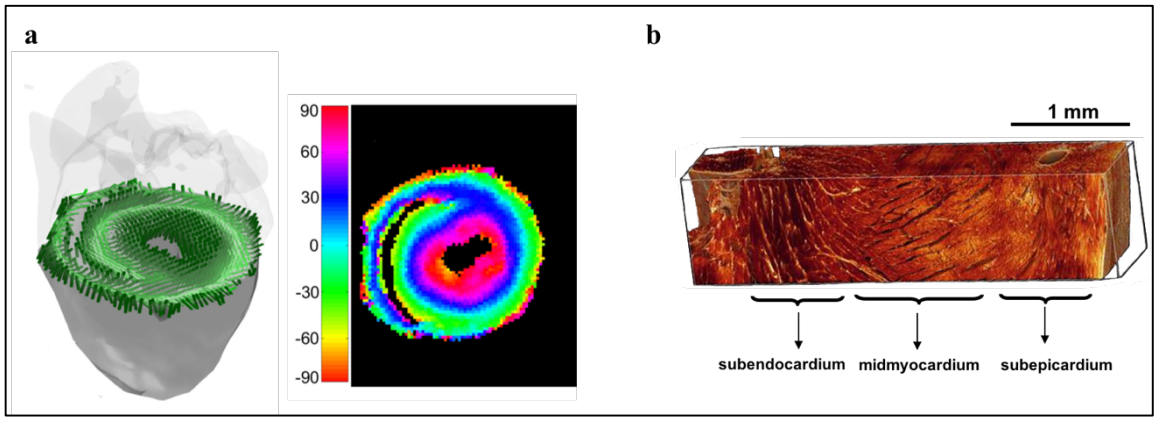

Figure II: (a) *3D reconstruction of the myocardial fiber orientation in the ventricles of mouse heart, obtained with DTI* ***(left panel)****. False color map indicating the angle formed by the intersection of the long axis of CMs and the transversal plane* ***(right panel)****.* ***(b)****3D reconstruction of a ventricular myocardial section showing the complex cytoarchitecture of the tissue with highlighted the three regions composing the ventricular wall (Healy 2011, Sands 2008).*

Conducting CMs are distributed as a network into the heart in order to achieve the coordinated activation of CMs that allow the sequential contraction of atria and ventricles. Conducting CMs can be divided into two subtypes of cells: *Nodal cells*, found in the *sinoatrial node* (SAN) and *AV node,* which are characterized by a small size and a slow electrical conduction and *Purkinje fibers* (PF), found in the AV bundle, *right* (RBB) and *left bundle branch* (LBB) and interspersed throughout the subendocardium, which in turn are bigger and show a rapid electrical conduction.

Ultrastructure of cardiomyocytes

Working CMs have most of their cytoplasmic volume occupied by contractile proteins (≈50%), organized in myofibrils, the remaining volume is mainly occupied by mitochondria (≈35%) and by the other subcellular compartments. Contractile proteins are organized into fundamental units called *sarcomeres.* The sarcomere is composed of overlapping thick and thin filaments. The thick filaments are made of *myosin* polymers that interact with the thin filaments, made of double-stranded *actin* polymers, through the globular part of myosin thus generating the so-called "cross bridges". In addition to actin, the thin filaments are composed of other interacting proteins, namely *tropomyosin* and *troponins*. There are three different troponins: troponin I (TnI), troponin C (TnC) and troponin T (TnT), that form a complex attached to tropomyosin. Sarcomere shortening takes place by the interaction between actin and myosin. When Ca^{2+} binds to TnC, it induces a conformational change in the troponin complex proteins allowing the direct interaction between actin and myosin. TnI exposes a site on the actin molecule that binds the myosin ATPase located on the myosin head. Such event results in ATP hydrolysis that supplies energy for a conformational change to occur in the actomyosin complex: the actin and myosin filaments slide along each other, thereby shortening the sarcomere length and thus inducing cell contraction. The length of thick and thin filaments remains constant during the phases of contraction and relaxation, the shortening of the cell is solely due to the extent of overlap between the filaments[15].

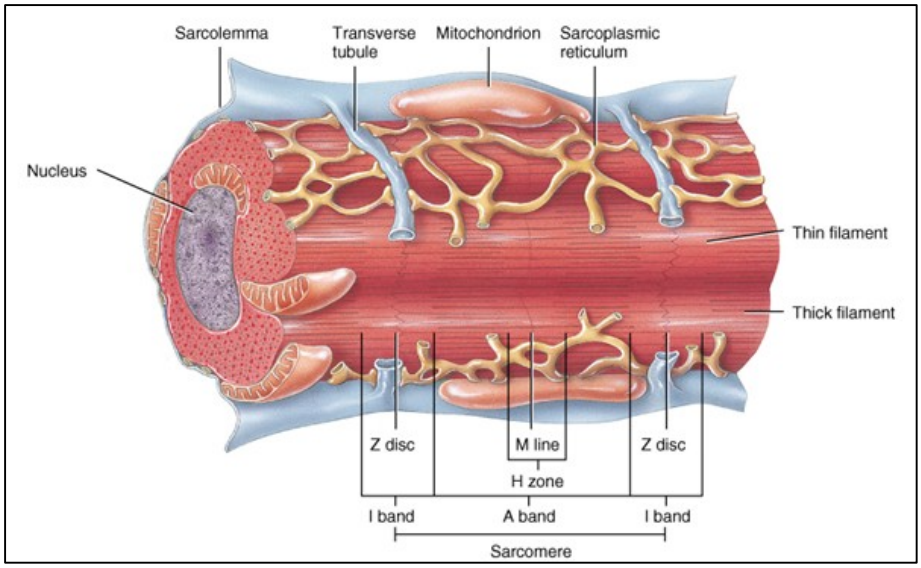

Figure III: *Structure of a cardiac myofiber (Grazia).*

Plasma membrane of CM is called *sarcolemma* and it possesses particular invaginations called *transverse tubules* (*t-tubules*) that are in contact with extracellular space and are important for cell contraction as described below (**Figure III**).

A specialized form of *endoplasmic reticulum* is present in muscle cells which is called *sarcoplasmic reticulum* (SR) or *sarcoendoplasmic reticulum* (SER) with the specialized function of regulation of cytosolic calcium Ca^{2+} concentration[16].

Excitation-contraction coupling

In the heart the process whereby an action potential triggers the CM to contract is called Excitation-Contraction Coupling (ECC)[17]. CM contraction is triggered by an action potential (AP) that opens voltage-gated L-type Ca^{2+} channels located in the t-tubules. The resulting Ca^{2+} influx in the cytoplasm activates a much larger release of Ca^{2+} from the sarcoplasmic reticulum (SR), the intracellular Ca^{2+} store. The massive release of Ca^{2+} from SR is due to Ryanodine Receptor-2 Ca^{2+} channels (RyR-2) opening, these channels are located in the sarcoplasmic reticulum membrane and are very sensitive to changes in $[Ca^{2+}]$ in the cytosol[18].

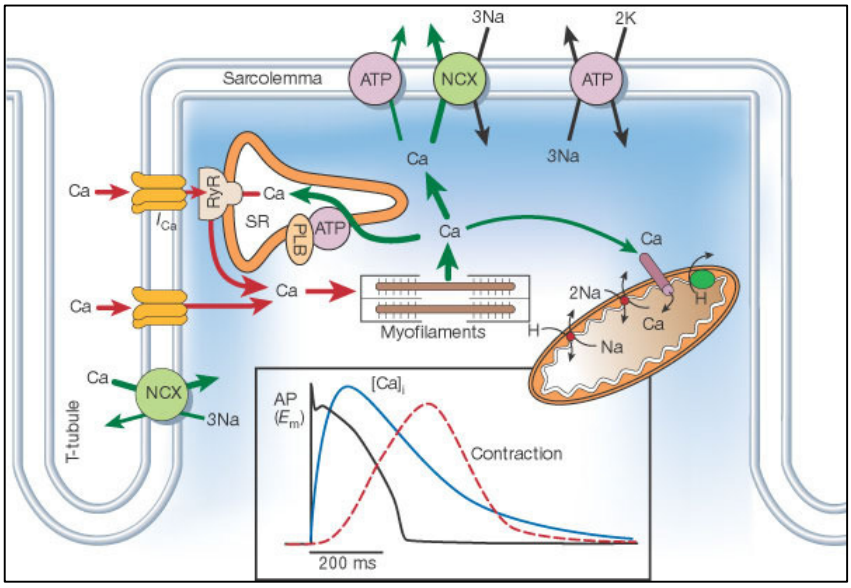

Figure IV: *Excitation contraction coupling model in the cardiomyocyte (Bers 2002).*

When Ca^{2+} binds to the cytosolic part of RyR-2 this opens and creates a Ca^{2+} release as a

passive flux along the concentration gradient, since the [Ca^{2+}] in the SR is several order of magnitude larger than [Ca^{2+}] in the cytosol, and is called calcium-induced-calcium-release (CICR)[19].The elevated [Ca^{2+}] in the cell is thus able to trigger sarcomere shortening. Then RyR-2 immediately closes and the cytosolic [Ca^{2+}] is restored by the activity of *sarcoendoplasmic reticulum calcium atp-ase pump* (SERCA) that pumps it back into the SR. A minor part of cytosolic Ca^{2+} is extruded from the cell via the *sodium-calcium exchanger* (NCX) located in the sarcolemma and also a little amount is taken up by mitochondria (**Fig.IV**). When cytosolic [Ca^{2+}] comes back to original levels, troponins complex rearrange, tropomyosin reattach to actin and contraction is terminated.

Electrical conduction of the heart

The myocardium is a functional syncytium, where CMs, although maintaining an individual identity, are tightly connected each other, mechanically and electrically, by specialized structures called *intercalated disks*[20-23]. The mechanical tethering is provided by *fascia adherens*, a region in which sarcomeric actin is linked to cytoskeletal one, and by *desmosomes*, structures where *intermediate filaments* of adjacent CMs are bound together[24].

The electrical connection between adjacent CMs is operated by *gap junctions*, nonselective channels that allows ions and small molecules to diffuse freely between cytosol of two connected CMs. These channels reduce internal electrical resistance thus creating a functional syncytium in which all CMs are electrically coupled[25 21](**Fig. V**).

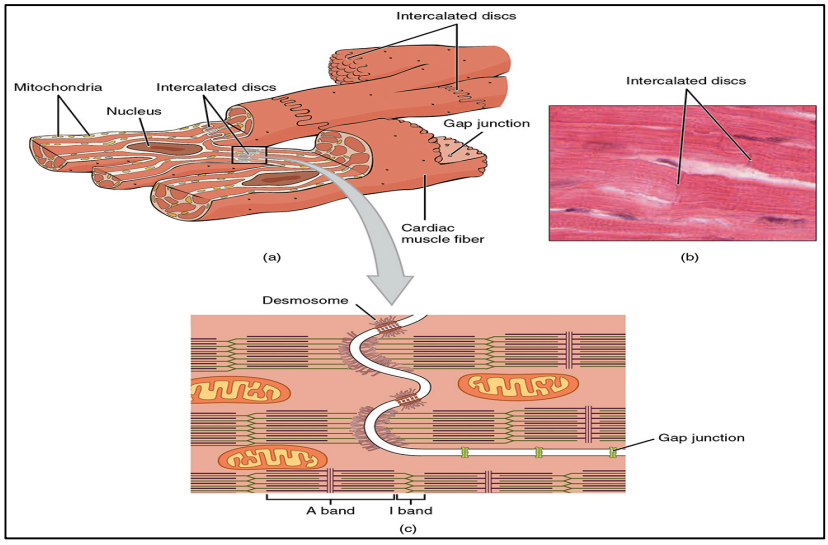

Figure V: *Complex arrangement of cardiomyocytes in the myocardium: structural and mechanical connections between them.*

Gap junctions are constituted by a family of proteins called *connexins* (Cx), which are arranged in esamers at the sarcolemma to form a non selective channel[24] (**Fig. VI**). In the heart many different isoforms of connexins are described, the most abundant being: connexin 43 (Cx43), connexin 40 (Cx40) and connexin 45 (Cx45). Gap junctions formed by the different isoforms of connexin present different permeability to ions and so conduce electrical impulse with different efficiency, and since gap junctions are the links between each single CM, this means that the speed of propagation of electrical stimulus is affected by the isoform of connexin present at the gap junction. Cx40 is the isoform that confers the highest speed of impulse propagation, then there is Cx43 and finally Cx45, which is the slowest[26]. Cx43 is the most abundant since it is expressed by all the working CMs and the distal Purkinje fibers, while Cx40 is expressed in atrial working CMs, in coexistence with Cx43, and in Purkinje fibers, and Cx45 is expressed almost exclusively in SAN and AV node, while a very low expression was also detected in PFs[27-29].

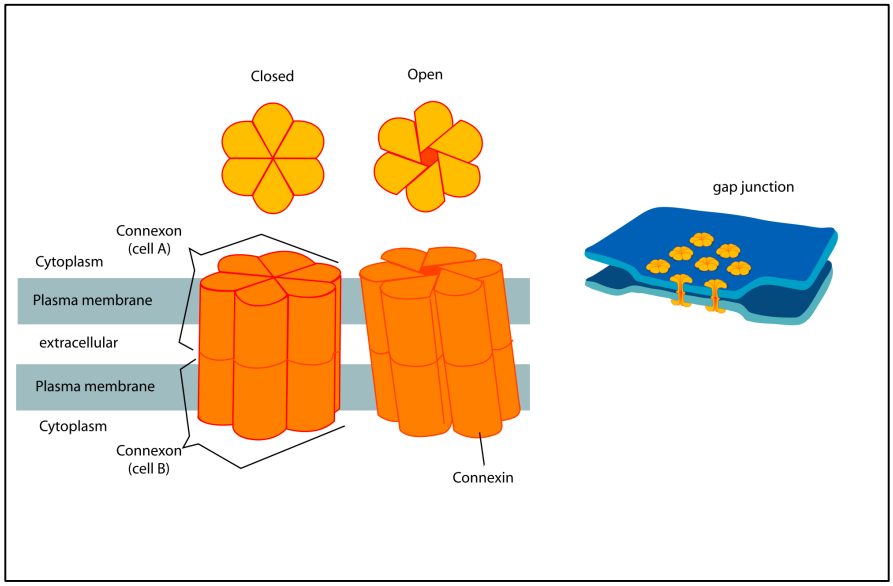

Figure VI: *Structure of the gap junctions formed by the connexins.*

Every heartbeat is preceded by the spontaneous depolarization of sinoatrial node cells, raising an action potential that is spread, through the other cells of the conduction system of the heart, to all the working CMs. This wave of depolarization opens the voltage gated calcium channels in the sarcolemma of working CMs and starts the ECC, culminating in the systolic contraction. The cardiac action potential (AP) is the result of the ordered opening and closing of the several different ion channels present at the sarcolemma of working and conductive CM. AP characteristics are different between each cell type of the heart, and this

depends on the different array and expression level of the ion channels involved. Purkinje fiber AP can be divided into five phase: a rapid and large upstroke (phase 0), due to the inward I_{Na} current, a transient fast repolarization (phase 1), due to the outward I_{kto} current, a plateau (phase 2), due to the balance of different inward I_{Ca} and different outward I_k currents, a repolarization (phase 3), due to the closure of I_{Ca} and different I_k currents and a steady state when membrane potential is at its resting level (phase 4). The AP of ventricular CMs differs between each region of the ventricular wall, is similar in the morphology to the one of the Purkinje fibers in the midmyocardium, is shorter, with almost no phase 2 in the subepicardium (EPI) region and a little bit longer in the subendocardium (ENDO)[30]. The AP of sinoatrial node cells, instead, is more slowly rising, lack phase 1 and 2 and during phase 4 exhibits gradual spontaneous depolarization (**Fig. VII**).

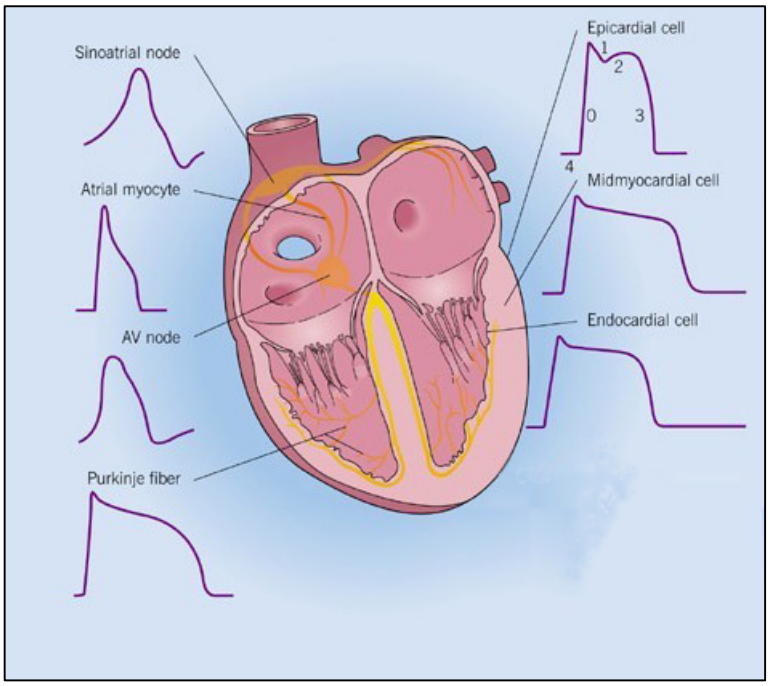

Figure VII: *AP characteristics of the different myocardial cells.*

SAN is the physiologic pacemaker of the heart and it is located in the RA. Every conductive cardiomyocyte possess an intrinsic capacity of spontaneous depolarization, which is called *automaticity*. Since SAN cells exhibits the fastest spontaneous depolarization rate among all conductive CMs, this structure usually takes the lead and initiate the depolarization wave that spreads throughout the heart. SAN cells, as described above, expresse the slowest isoform of connexin in order to allow a unidirectional propagation of

the depolarization wave to the surrounding atrial myocardium, which instead expresses Cx40 and Cx43 and so propagate more rapidly the electrical stimulus.

After been propagated to both atria the depolarization wave reaches the AV insulating region (see above) and can only propagate through the AV node, where it is slowed by the Cx45 expressing nodal cells. The delay that the depolarization wave encounters before passing to the ventricles is fundamental for the correct sequence of contraction of atria and ventricles. Once passed through the AV node the depolarization wave reaches AV bundle in the IVS where it divides into the right (RBB) and left bundle branches (LBB) that propagate the electrical impulse to the distal part of Purkinje fiber network that in turn are interspersed throughout the subendocardium and contacts the working ventricular CMs[31] (**Fig.VIII**).

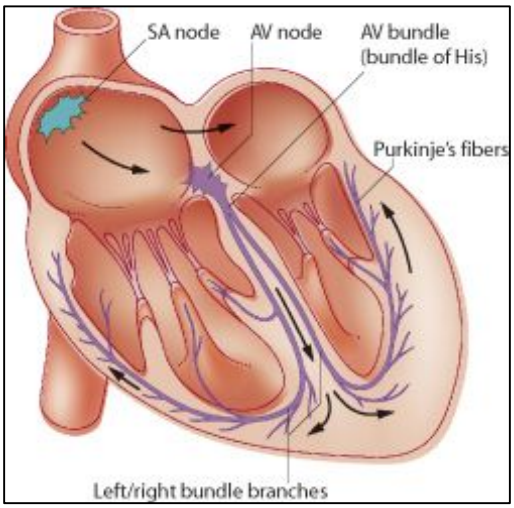

Figure VII: *Central conduction system of the heart (Cunningham 2002).*

Inside the ventricles, the depolarization wave propagates first throughout the Cx40-expressing ventricular conduction system (AV bundle, bundle branches and Purkinje fibers) because of its faster conduction and then it propagates to the remaining working CMs. This allows the correct and simultaneous depolarization, and subsequent contraction, of the ventricles. After the depolarization process the action potential of each heart cell is ended by the action of a complex set of repolarizing currents, that restore the membrane potential at its baseline negative value[2].

The rhythmic depolarization of the heart, described above, precedes every heart beat and it is defined *sinus rhythm*. A depolarization wave that follows a different path than the

one described above generate a so called *arrhythmic beat* also known as *ectopic beat* or *extrasystole*, that becomes an *arrhythmia* if this aberrant depolarization wave is able to self renew and thus overcome the sinus rhythm. Generally, these arrhythmic beats are the result of the abnormal depolarization of a group of CMs. The myocardium is protected by these events by the *source-sink mismatch*, which is the intrinsic capacity of the electrically coupled myocardium (*sink*) to buffer an ectopic current arising from depolarization of a small group of CMs (*source*), by distributing it to all the other repolarized cells coupled. For this reason a depolarizing current to be able to propagate throughout the myocardium needs to be sufficiently higher to overcome this protective factor[32,33]. The minimal number of synchronously depolarizing CMs, sufficient to generate this propagating current is referred to as *critical mass*[34]. This depends on the type of CMs involved (working or conducting) and their location and it is an important parameter in the genesis of arrhythmia, although its calculation is difficult and so far it is only estimated using mathematical modeling[35]. Arrhythmias can be divided, based on their location, into *supraventricular* (arising from atria and nodal cells) and *ventricular* and, based on their effect on heart rate, into *tachycardia* (increasing heart rate) and *bradycardia* (decreasing heart rate) (**Fig.IX**). The most important in terms of epidemiology and severity of symptoms are tachycardia and, especially the ones with ventricular origin are the principal cause of death in many acquired and genetic cardiac disease[36].

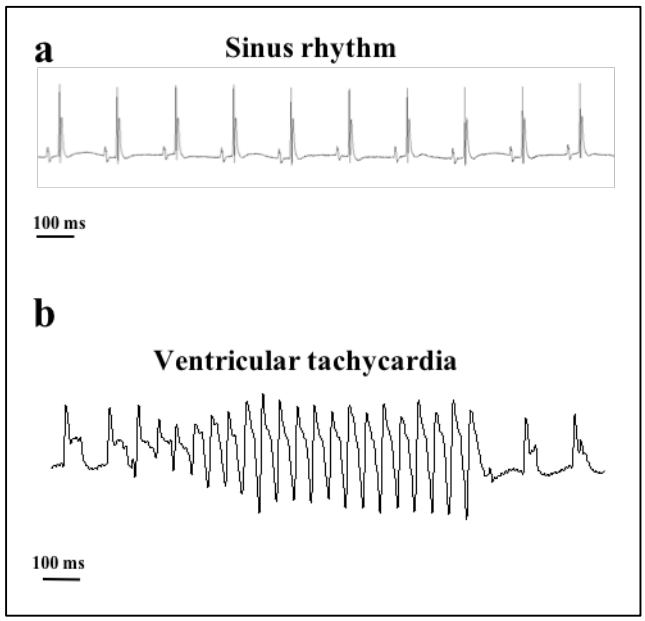

Figure IVIII: *ECG traces of a mouse heart showing an example of sinus rhythm (**a**) and ventricular tachycardia (**b**).*

The electrocardiography

The electrocardiography is the technique that allows to record the electrical activity of the heart and is among the most useful diagnostic tests in clinical medicine, since it is routinely used to investigate disorders of the cardiac rhythm and detect heart diseases such as acquired or inherited cardiomyopathy among others. Electrocardiogram (ECG) is the trace that arises from the recording of heart electrical activity, in terms of voltage over time, through the use of electrodes placed on the skin. It provides information about the heart rate and also other important parameters of the electrical activity of the heart. The typical appearance of an ECG trace, is constituted by the cyclic repetition of specific deflections which represent the depolarization and repolarization of different heart regions. The first, in chronological order, is the so called "*p wave*" which is the manifestation of the current arising from the depolarization of the atria, then comes the "QRS complex", which represents the depolarization of the ventricles and the interventricular septum and then at the end there is the "T wave", which is the sign of the repolarization of the ventricles (**Fig. X**). Electrical currents arising from the depolarization or repolarization of other sites of the heart, SAN or AV node for example, cannot be recorded because of their little intensity, due to the small amount of cells involved. These typical deflections were first described for the human heart but this classification is applicable also to the ECG of different mammals, indeed the morphology of the principal deflections in the ECG is similar, although, mainly due to size differences, the amplitude of each deflection and the length of the intervals between them are very different, in particular in the case of rodent heart, the interval between the end of the QRS complex and the start of the T wave is so reduced that the T wave appears on top of the final part of the QRS (**Fig.X**).

The amplitude of each deflection realizes the intensity of the underlying current, while the length realizes the conduction velocity. For example, defects in the conduction of the depolarization wave throughout the ventricular myocardium, as it happens for example after myocardial infarction when necrotic myocardium is substituted with an electrical inert fibrotic scar, result in the prolongation of the QRS complex. Wide QRS complexes are also feature of an ectopic arrhythmic beat arising from the ventricles. The longer duration of the QRS complex of an arrhythmic beat is explained by its origin, indeed, it arises from the focal depolarization of a small group of CMs, that generates a depolarizing wave that spreads throughout the ventricles, this event is slower than the physiologic depolarization of the

ventricles, which occurs due to the simultaneous activation of CMs in multiple sites of contact between the distal part of the Purkinje fibers network, and so it results in a wider QRS complex (**Fig.IX**). When the heart is in its sinus rhythm every p wave is followed by a QRS at a precise distance, reflecting the delaying filter of the AV node. When AV node or AV bundle are impaired, the normal conduction from the atria to the ventricles is hampered and this phenomenon is called AV block. Based on the severity is classified into three types, I, II and III. The last is called also complete AV block, meaning that heart rhythm is no more controlled by the SAN and ventricular contractions depends on the automaticity of ventricular conduction system cells. In the ECG this condition is seen as p waves completely uncorrelated with QRS complexes, the latter being abnormally wide due to their ventricular origin.

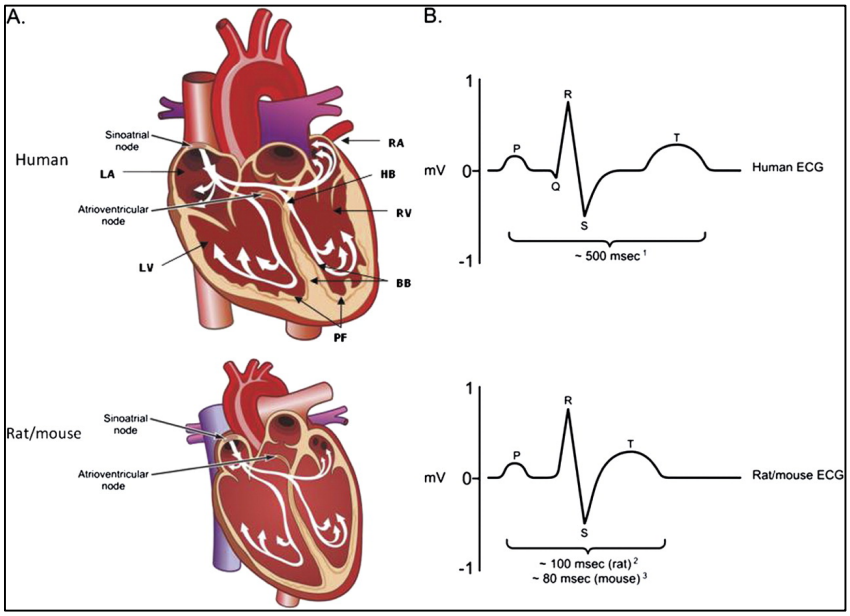

Figure X: (a) *Comparison between the anatomy of human and rodent heart and (**b**) respective deflections seen in the ECG.*

Innervation of the heart

Anatomy of heart innervation

The heart is densely innervated by *autonomic nervous system* (ANS), which comprises *sympathetic* (SNS) and *parasympathetic nervous system*, and at a lower extent also by *sensory nervous system* (**Fig.XI**). Parasympathetic and sympathetic branch of the ANS work in a reciprocal fashion to modulate heart activity by acting on heart rate (*chronotropy*) and conduction velocity (*dromotropy*) at the level of central conduction system. In addition, SNS modulates heart contractility, by acting on the force of contraction (*inotropy*) and relaxation (*lusitropy*) at the level of working myocardium[37]. Parasympathetic neurons are derived from cardiac neural crest cells which migrate into the developing heart and forms cardiac ganglia located in the base of the atria. From these ganglia postganglionic cardiac parasympathetic nerves extend to SAN, AV node, atria and heart's blood vessels, while the innervation of ventricular myocardium is limited. Parasympathetic neurons use mainly *acetylcholine* as neurotransmitter. Sensory neurons, located in the dorsal root ganglia, project their processes into the myocardium and are responsible for pain perception and initiation of feedback mechanism after myocardial injury.

The developmental origin of sympathetic neurons (SNs) is from trunk neural crest cells that migrate and form sympathetic ganglia where they proliferate and differentiate into mature neurons. Postganglionic SNs that innervate the heart have nearly all of their cell bodies in the middle-cervical and stellate ganglia, with the superior cervical and the 4th to 6th thoracic ganglia contributing to a little extent. From these ganglia SN extend their projections from the base of the heart throughout all the myocardium[38-40] (**Fig.XI**). SN processes in the myocardium have a peculiar structure which is quite different from other peripheral neurons such as the motoneuron for example. When reaching their targets SN terminals show the typical "*pearl and necklace*" morphology, with regular varicosities corresponding to the neurotransmitter releasing sites that contacts the target cell. Although SNs release a number of molecules (e.g. adenosine triphosphate, serotonin and histamine), the two main sympathetic neurotransmitters are *norepinephrine* (NE) and *neuropeptide Y* (NPY) that are stored in vesicles, abundant in the neuronal varicosities. Effects of SN activation on CMs involve mainly NE, with NPY that seems to have a minor impact in the short term while it seems to have a role, in the long term, in the regulation of CM ion currents,

through the modulation of ion channel expression[41-43] although its functions are not completely elucidated.

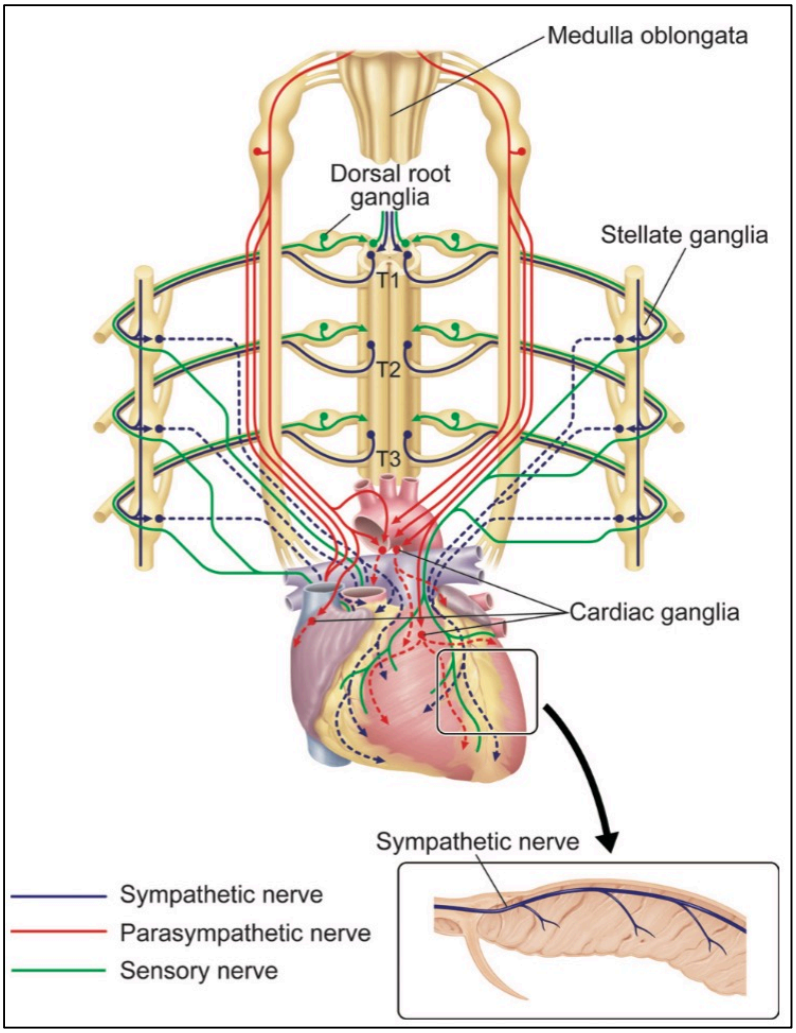

Figure XI: *Anatomy of heart innervation (Kimura 2012).*

Sympathetic innervation pattern

The myocardium starts to be innervated by sympathetic neurons in the early post-natal weeks and axonal sprouting is guided by the balance between chemoattractant neurotrophins (e.g. nerve growth factor, NGF) and chemorepellent factors (e.g. semaphorin-3a) released by the target cells of SN. SN axons penetrate into myocardium, following blood vessels, an intermediate target, that express the neurotrophin-3 (NT-3). The neurotrophins NGF and NT-3 signal through the same receptors: tropomyosin receptor kinase A (TrkA) and p75 neurotrophin receptor (p75), to coordinate distinct stages of sympathetic neuron

development[44]. NT-3 derived from vascular smooth muscle cells activates TrkA on sympathetic axons, allowing axonal extension along the vasculature. As axons approach heart, and begin to acquire CMs-derived NGF, the ensuing retrograde NGF/TrkA signaling promotes survival, anabolic responses, and expression of p75. The increase in p75, in turn, diminishes axonal responsiveness of TrkA to NT-3, enabling NGF to become the dominant axonal growth factor and so to establish a stable contact between CM and SN.

Chemorepellent factors, such as semaphorin-3A, instead interfere with neuronal process growth, causing their retraction, and inhibit the interaction of the neuron with the target cells[43]. In the mouse heart, it is described that in the embryonic stages semaphorin-3A is expressed homogeneously by CMs of the nascent ventricles, while during the postnatal development, instead, it was observed a gradual decrease in the expression of semaphorin-3A that starts in the subepicardial CMs and progresses to subendocardial ones. It has been demonstrated, indeed, that mice lacking semaphorin-3A showed an hyperinnervation of the myocardium and an unbalance of the innervation pattern, while mice overexpressing semaphorin-3A showed an almost denervated myocardium and are subjected to increased mortality due to sudden cardiac death[45].

When the developmental process is completed, the balance between chemoattractant and chemorepellent factors generate a well defined pattern of innervation in the heart. In the murine heart this pattern is well described and shows a heterogeneous distribution among the four chambers. In detail, the highest density of nerve fibers is found in the atria, followed by the RV and LV, moreover inside the ventricular walls there is a decreasing gradient of SN density from the EPI region to the ENDO region. Regarding other mammalian species, although it is described a peculiar organization of the SN, the innervation pattern is not so well characterized. In the case of the human heart, regional differences in innervation have been reported, mainly based on observational EM studies, and similarly to the rodent heart, higher innervation density was observed in the atria compared to the ventricles, while on the contrary, no differences between the RV and LV have been reported. It has to be clarified, however, that these data come from post-mortem samples of patients undergone prolonged medical treatments that might alter the SN patterning and further ad hoc studies are needed to define the SN distribution in normal human hearts [43].

Modulation of cardiomyocyte activity by sympathetic neurons

Cardiac SNs exert a positive effect on force (*inotropy*) and frequency (*chronotropy*) of heart contraction, by the release of NE and the consequent activation of *β-adrenergic receptors* (β-ARs) on CMs. β-ARs, are G protein-coupled receptor (GPCR) localized on the membrane of the CM. GPCRs contain seven transmembrane α-helices and a large cytosolic C-terminal loop. The ligand-binding sites include hydrophobic regions of α-helices, while the G proteins-binding sites include both transmembrane α-helices and the intracellular domain[2,46,47]. G proteins or *heterotrimeric GTP-binding proteins*, that mediate the response of these receptors, are composed of one member of each of three different protein families: Gα, Gβ and Gγ, organized as two separate units, one monomer of Gα and a dimer of Gβ-Gγ. Moreover, two types of Gα subunit are present in CMs: $G\alpha_s$ and $G\alpha_I$ exerting different functions. CMs express two major β-AR subtypes: β1 and β2. Both are members of the GPCR family of proteins, but, although are activated by the same agonist, the selective stimulation of one subtype leads to different downstream responses. Indeed β1-ARs are coupled to $G\alpha_s$ stimulatory subunit only, and mediate the acute inotropic and chronotropic functional response while β2-AR seems to be coupled to $G\alpha_s$, mediating regulatory responses that are weaker than those initiated by β1-ARs and $G\alpha_i$, mediating counter-regulatory responses and anti-apoptotic effects[48,49].

The increase in the force of contraction of CMs is exerted by SN at the level of working myocardium through the release of NE that interacts with β-ARs. This leads to a cascade of downstream events: first there is the activation of $G\alpha_s$, which in turns activates *adenylyl cyclase* (AC), which is the enzyme responsible for the production of the second messenger *cyclic-AMP* (cAMP). cAMP activates its main effector, *protein kinase A* (PKA), that phosphorylates L-type Ca^{2+} channel and the RyR-2, enhancing the CICR and resulting in the increase of the cytoplasmic Ca^{2+} content. This increase leads finally to an augmented sarcomere contraction during systole. PKA activity is also essential in the control of Ca^{2+} reuptake in the SR during diastole, indeed, through the phosphorylation of *phospholamban* (PLB), a protein that positively modulates the activity of SERCA, PKA increase the speed of cytosolic Ca^{2+} clearance, thus resulting in shortening of Ca^{2+} transient (**Fig.XII**)[50]. This allows CMs also to be prone to an increase in the frequency of contraction.

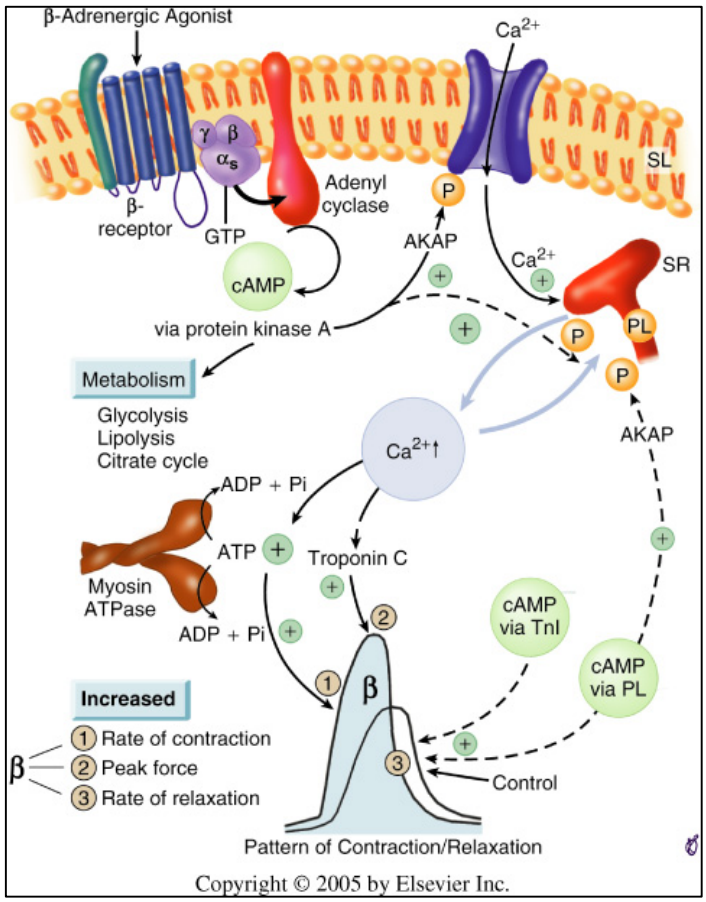

Figure XII: *Sympathetic nervous system positive modulation of CM contraction force (inotropy) (Opie 2004).*

The frequency of heart contraction, that is dictated by SAN depolarization, is positively modulated by SNs innervating SAN cells. SAN is the physiological pacemaker of the heart and SAN cells spontaneously depolarize through the activation of a number of different ion channels. The depolarization of these cells starts with the opening of non specific cation channels called *hyperpolarization activated cyclic-nucleotide gated channels* (HCN), which open when the membrane potential is below a specific negative value and carry an inward depolarizing current called I_f, then the L type Ca^{2+} channels open and contribute to depolarize the cell. Moreover, the Ca^{2+} entered in the cytosol is extruded by NCX that, by exchanging each Ca^{2+} with 3 molecules of Na^+, generate an additional inward current. The repolarization, instead, is ensured by two potassium channels, which carry I_k and $I_{k,Ach}$ currents. $I_{k,Ach}$ is modulated by parasympathetic nervous, while I_k is controlled by SNS.

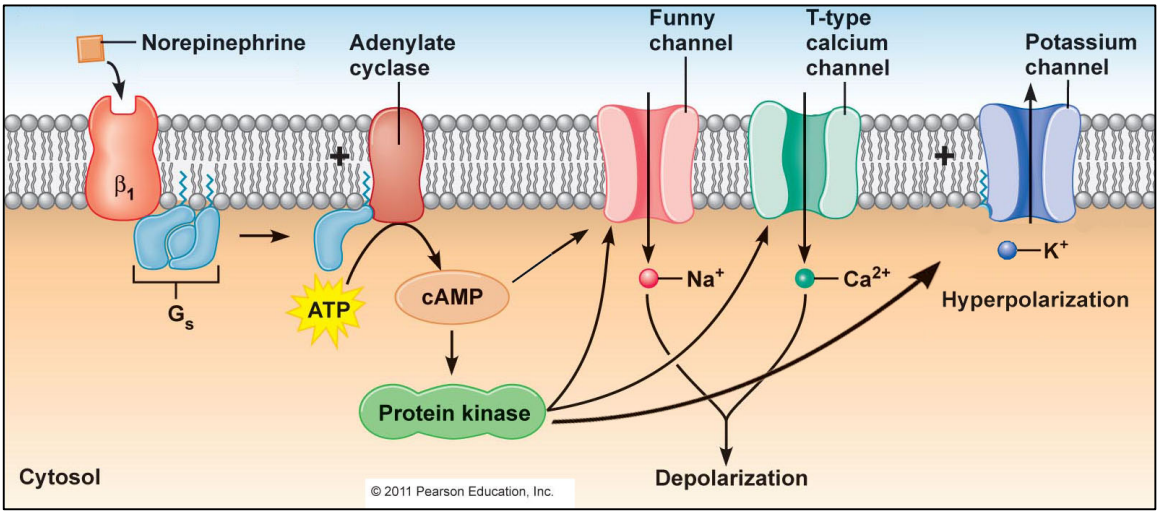

Figure XIII: *Sympathetic nervous system positive modulation of heart frequency at the level of sinoatrial node (chronotropy).*

SNs innervating the SAN, accelerates its depolarization rate through the release of NE and activation of β-ARs in nodal cells. This leads to the increase of cAMP through the $G\alpha_s$/AC pathway that is able directly to positively modulate HCN opening and thus increase I_f. Moreover, cAMP mediated activation of PKA results in the phosphorylation of L type Ca^{2+} channels and I_k channels, which increase depolarization and repolarization currents respectively, leading to the shortening of nodal cell action potential duration. This effects ultimately result in the increase of depolarization frequency of SAN that determines an increase in heart rate (**Fig.XIII**).

The activation of the autonomic nervous system (both sympathetic and parasympathetic branches) generates changes in heart rate, that are seen in the ECG as variations in the distance between two consecutive QRS complexes, a phenomenon which is defined *heart rate variability* (HRV). The measure of HRV offers the possibility to quantify the amount of activation of the autonomic nervous system in a specific situation.

Another important extrinsic modulator of heart activity is constituted by the release of catecholamines from the adrenal glands into the circulatory system, which reach the heart and activate β-ARs of CMs exerting a positive inotropic and chronotropic effect. This is the result of an endocrine signaling, which simultaneously targets various organs eliciting a systemic response in cases of elevated stress. SN modulation of heart activity, instead, is highly selective and is able to finely tune heart function with gradual responses to different stress conditions and also to physiological situations such as postural changes or exercise.

The cardiac sympathetic nervous system plays a key role in the regulation of the myocardial mass

The protein degradation systems

The myocardium is traditionally defined as a post mitotic tissue, CMs, indeed, stop to divide few days after birth. Nevertheless, myocardium is a dynamic tissue that needs to adapt to intrinsic and extrinsic stresses. Thus to ensure the integrity and the viability of CMs, protein quality control needs to be tightly regulated to ensure the correct turnover of proteins. This is regulated through the synthesis of new proteins and the degradation of damaged or misfolded ones. Removal of damaged, misfolded/unfolded proteins, is operated by two main systems: the Ubiquitin Proteasome System (UPS) and the Autophagy-Lysosome System (ALS) (**Fig.XIV**).

The UPS is responsible for the degradation of almost 90% of the sarcomeric proteins, thus ensuring the removal of misfolded or damaged proteins[51]. UPS degrades single proteins that are marked for degradation with a specific signal in a highly controlled manner [52] (**Fig.XIV**). UPS is made of two functional units: a targeting unit and a degradation unit. The first is composed of 3 families of enzymes called E1, E2 and E3 that mediate the recognition of proteins to be degraded and their targeting to the second unit, the proteasome, which performs the degradation of the proteins into their constituents. The proteins to be degraded are labeled by the addition of a small protein, called ubiquitin, in the form of polymeric chains. These chains are assembled on the substrate by a cascade of enzymes, which starts with the activation of ubiquitin by the binding of it to the first enzyme which is called E1, or activator, and then continues with the formation of the polyubiqutin chain by the action of E2 conjugator enzyme. Finally, E3 enzyme, also called ubiquitin ligase, mediates the transfer of the polyubiquitin chain formed to a lysine residue of the substrate[54,55]. With only few exceptions, this lysine residue is constant for all proteins to be degraded and it is the lysine 48. E1 and E2 family of enzymes are composed of only a few number of members, while almost 650 types of E3 ubiquitin ligases are found so far in the human genome, and this occur because E3 is the enzyme which confers the specificity to the system, each E3 selectively targets only a small number of proteins[56]. The screening of gene expression in different models of atrophy in skeletal muscle, lead to identification of a common group of genes which are overexpressed in all the different models and so these were called *atrogenes*.

Among these genes two of the main upregulated and represented are two ubiquitin ligases, which are also muscle specific: *atrogin-1* and *MuRF1*[57,58].

Atrogin-1, also known as MAFbx (muscle atrophy F-box), was also found in cardiac muscle, which appeared to be a key regulator of myocardial remodeling[59,60]. Recent studies have shown that high levels of atrogin-1 suppress the hypertrophy of CMs induced by adrenergic stimulation and increased pressure load, respectively, *in vitro* and *in vivo*. Atrogin-1 prevent CM hypertrophy by regulating the degradation of *calcineurin*, a calcium-activated phosphatase that well described as involved in pathological hypertrophy[61-63].

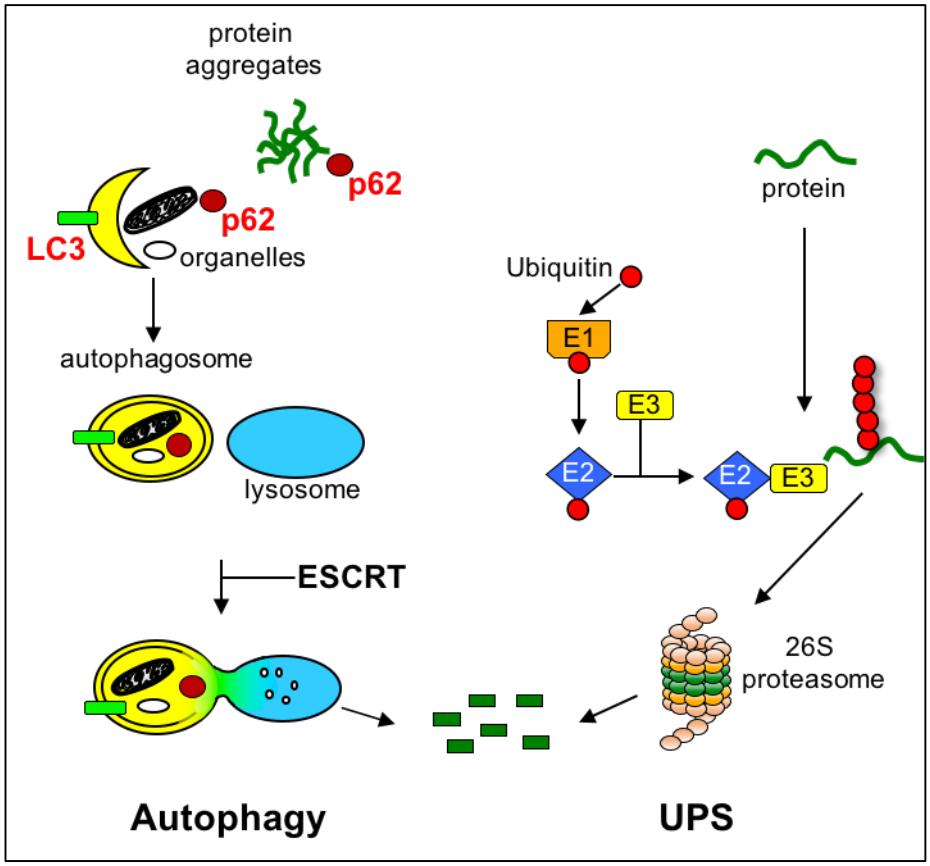

Figure XIV: *Protein degradation systems: Autophagy Lysosome System (ALS) and Ubiquitin Proteasome System (UPS).*

MuRF1 (muscle-specific RING finger 1), is present at the level of skeletal and cardiac muscle[64-66]. Its involvement in cardiac atrophy was demonstrated in different studies: its overexpression was found in isolated cardiac tissues from patients that underwent implantation of a left ventricular assist device, a condition associated to myocardial atrophy[67]; is up-regulated also in heart failure[68] and in an animal model of induced atrophy with administration of dexamethasone[67,69]. The molecular targets of MuRF1 in the CMs are

sarcomeric proteins, such as for example cardiac troponin I (cTnI)[70] or myosin heavy chain (MyHC)[69].

The other main system for protein degradation is ALS (**Fig.XIV**). ALS is a highly conserved process, mediating the degradation of complex cytoplasmic structures such as protein aggregates and organelles. There are various types of autophagy that differ in their mechanisms of action and functions[75,76]: the *chaperone-mediated autophagy*, which is characterized by the selective degradation of cytosolic proteins which expresses a particular aminoacidic domain[77]; the *microautophagy*, which is an aspecific mechanism of direct uptake of cytosolic components into the lysosome membrane through invagination[78]; and the *macroautophagy*, hereafter called just *autophagy*, the most important one, which is characterized by the formation of a compartment delimited by a double membrane, named *autophagosome*, engulfing the cytoplasmic material and delivering it to the lysosome where this material is finally degraded[79]. Among the player of ALS the most known are LC3 and p62, which are used as universal markers of ALS activation. At the beginning of autophagic process there is the binding of cytoplasmic form of LC3 (LC3 I) to a phospholipid creating its lapidated form (LC3 II) that participates in the formation of the autophagosome, so the amount of LC3 II can be used as marker of autophagy activation[80]. p62 is instead involved in the recognition of targets to be degrade and delivery of them to the nascent autophagosome[81]. p62 is retained into the autophagosome and then degraded into the lysosome, so its decrease is used as a marker of autophagy activation.

UPS and ALS have been considered for a long time two completely independent mechanisms, but in a study that we recently published in JCI we provided some evidence of a role of atrogin-1 in the modulation of UPS and ALS cross-talk[82] (see **Appendix**). In detail we described that the loss of atrogin-1, directly causes an impairment in the ALS due to the defective elimination of one of its previously unknown target: CHMP2B (*Charged Multivesicular Body protein 2B*), a member of the ESCRTIII family of proteins which are involved in the last stages of ALS. Moreover, in literature there are evidence a block of autophagy results in increased levels of ubiquitinated proteins[82,83]. UPS and ALS impairments are associated to various pathologies, such as neurodegenerative diseases and cancer[71-74] and recently also to some cardiovascular diseases, such as hypertrophic cardiomyopathy and heart failure [53].

Protein synthesis and degradation: central role of Akt pathway

Among the molecular mechanisms involved in the regulation of the synthesis of new proteins, the signaling pathway PI3K/Akt is among the most important in controlling cell size. The protein kinase Akt, also known as protein kinase B (PKB), belongs to the family of serine/threonine kinases[84]. Akt is the mediator of a large amount of anabolic and catabolic stimuli, activating the synthesis of new proteins, blocking at the same time the proteolysis of existing ones. Akt is also responsible for the phosphorylation and activation of mTOR (mammalian Target Of Rapamycin)[85], another serine/threonine kinase, which has been proven to have a crucial role in the integration of a large number of hypertrophic stimuli, from simple nutritional stimulation to the activation of protein growth factors, which lead to protein synthesis[86]. Both Akt and mTOR phosphorylation levels were demonstrated to be increased in muscle hypertrophy[87]. It was demonstrated, mainly in skeletal muscle, that Akt regulates transcription factors belonging to the family of FOXO (Forkhead box O). In particular, the phosphorylation of FOXO3 mediated by Akt exerts a negative modulation of its function, indeed is able to block its nuclear translocation. On the contrary, a reduced activity of Akt, and so a reduced phosphorylation of FOXO3, promotes its nuclear translocation and consequently leads to increased transcription of a set of genes expressing protein mediators of proteolysis, for example in the case of skeletal muscle the E3 ubiquitin-ligases Atrogin-1 and MuRF1, leading to atrophy[88].

The balance between protein degradation and protein synthesis: the proteostasis

Although myocardium is a post mitotic tissue, it possesses a high plasticity and can adapt its mass in response to mechanical, metabolic and neurohormonal stimuli only through the modulation of CM size. CM size is the result of the balance between protein synthesis and protein degradation, which is called *proteostasis*[89]. The unbalance in proteostasis, as in the case where protein synthesis prevails on degradation, leads to myocardial hypertrophy, while, if protein degradation is increased and protein synthesis is decreased leads to myocardial atrophy.

Cardiac hypertrophy occurs in physiologic conditions, such as post-natal growth, pregnancy and exercise, where it mediates the needs for higher perfusional demands and it results in a more powerful and efficient heart activity, so it is defined as *adaptive hypertrophy*. On the other hand, hypertrophy can occur also in response to pathological stimuli, such as pressure overload due to hypertension, overactivation of SNS as in the case of heart failure and some type of familial cardiomyopathies associated to the accumulation

of misfolded proteins. This hypertrophic remodeling, initiated to reduce myocardial stress, then leads to an abnormal increase in heart size, reprogramming of CMs to an embryonic gene program and ultimately leading to decreased cardiac activity[90-92]; for this reason, is defined as *maladaptive hypertrophy*.

Cardiac atrophy, instead, can be induced by a great variety of stimuli, such as a reduced hemodynamic load, nutrient deprivation and cancer cachexia. Conditions in which CMs optimize energy expenditure by degrading or recycling sarcomeric components, thus leading to a decrease in CM size. Recent studies have shown a complex scenario, in which the two catabolic pathways (UPS and ALS) modulate each other and are often interconnected at various levels[82].

Novel role for sympathetic innervation of working myocardium in the regulation of cardiomyocyte proteostasis

In the heart adrenergic stimulation has a well described role in the post-natal hypertrophic growth[45,93], acting through the stimulation of α-ARs in CMs, while in the adult heart its role is not completely elucidated. There are evidence in literature, that hyper-innervated hearts are hypertrophic and animals chronically treated with β-blockers develop myocardial atrophy[94,95], moreover, in the case of the *neuromuscular junction* (NMJ), it is already described that the adrenergic innervation of the muscle fiber is essential for the regulation of its trophism, through a β2-AR signaling pathway[96]. These data suggest that a role of the adrenergic signaling in the modulation of myocardial mass is plausible and in favor of this hypothesis, we recently published a study[1] (see **Appendix**) in which we demonstrate that SNs modulate CM trophism by acting through the regulation of proteostasis. In this work we used an experimental model of cardiac SN ablation in normal adult mice, obtained by the administration of 6-hydroxy-dopamine (6-OH-DA), an analogue of dopamine, that once internalized by neurons through its transporter causes neurodegeneration due to the production of reactive oxygen species, without affecting CMs. Adrenergic denervation of the heart resulted in an atrophic remodeling, with a reduction in the heart weight normalized to body weight (HW/BW) of 8% and 14% at 8 and 30 days after the denervation, respectively. This reduction was not due to the loss of the CMs, since no signs of CM death were detected, it was instead due to a reduction in the CM size. Moreover, we demonstrated that this denervation induced atrophy was the result of two parallel processes: i) the activation of the protein degradation systems, as demonstrated by the up-

regulation of the ubiquitin ligases MuRF1 and atrogin-1 and ii) the reduction of protein synthesis, as shown by the reduction of activated form of AKT and of its substrate S6. The key role of MuRF1, in particular, was confirmed by the fact that MuRF1 knock-out are protected from denervation induced atrophy. *In vitro* analysis on primary cultures of CMs shown that NE modulates the levels of ubiquitin ligases via β2-AR, moreover, we observed that denervated mice treated with the β2-AR specific agonist clenbuterol, were protected from atrophy after ablation of cardiac SN and that β2-AR knock-out mice had atrophic hearts compared to age and sex matched controls.

Using various experimental approaches, pharmacological, molecular and biochemical as well as several experimental animal models, it has been shown that the SNS in addition to having a role in the regulation of cardiac activity under stress conditions, it is also essential for the determination of the correct cardiac mass.

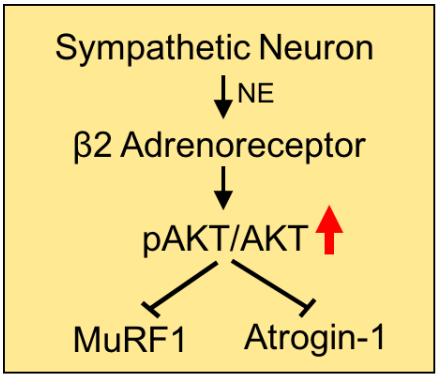

Figure IXV: *Molecular pathway through which SNs regulate CM size.*

Optogenetics

Exciting cells with light: first approaches

The idea of stimulating excitable cells with light dates back to the early years of 21st century, with seminal works on "caged" neurotransmitters, which consisted in the delivery to the neurons of neurotransmitters bound to inactivating molecules, that upon illumination changed conformation and restored the functionality of neurotransmitter[97,98]. This approach had some drawbacks, such as the lack of specificity, in fact, this depend on the type of neurotransmitter used that does not allow the specific activation of only a certain type of neuron. Moreover, the spatial control of activation required a stationary substrate and this maked almost impossible to use it for *in vivo* studies. These problems were circumvented by the pioneering studies of Miesenböck's group[99] in 2005 who inserted the gene of an ATP-gated cation channel from the rat into the genome of *Drosophila*, in which the channel did not exist, and engineered the system so that this was expressed only in specific neurons of the fly. Then was given to the fly a "caged ATP", which works in the same way of caged neurotransmitters. In this way the researchers succeeded in controlling membrane potential of specific classes of neurons in the fly, *in vivo*, with just the delivery of a flash of light.

ChannelRhodopsin: a new member of the rhodopsin family

Rhodopsins, are a family of proteins that can be found from prokaryotes, where they are involved in ionic homeostasis, to monocellular *algae* where they control the flagellar movement and thus *phototaxis*, till animal cells, like retina cells, where they are implicated in the process of vision. All these proteins have in common that they are light-activated and once active they are able to change the membrane potential of the cell[100].

Channelrhodopsin-2 (ChR2) is a new member of the rhodopsin family of proteins, discovered by Nagel and Hegemann's group in 2002, in the green alga *Chlamydomonas*[101]. ChR2 is a light-gated cation channel, sensitive to 470 nm light, composed of seven trans-membrane helices that form the ion channel and a long C-terminal extension of unknown function, which is omitted in the recombinant form of ChR2. The light-absorbing chromophore *retinal*, a vitamin A derivative, is buried within the hydrophobic center of the seven helices (**Fig.XV**). Light absorption by retinal leads to isomerization, followed by a protein conformational change and opening of the ion pore[101,102]. It was immediately clear,

when these proteins were discovered, that their structural simplicity, with light sensor element and actuator channel linked and transcribed by a single gene, and their fast kinetic could turn them into a useful biotechnological tool.

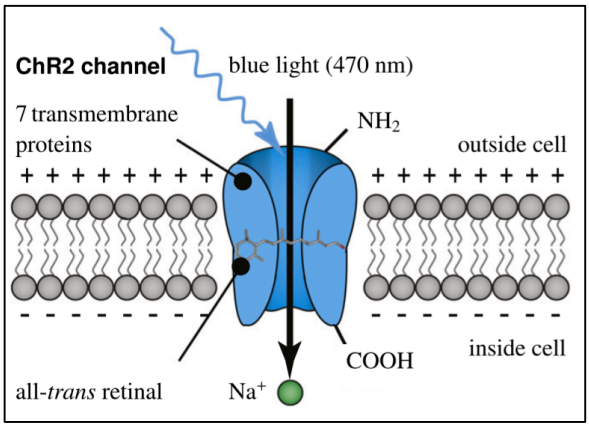

Figure XVI: *ChannelRhodopsin-2 (ChR2) is a light gated cation channel (Nagel 2013).*

Optogenetics: a new field of study rises

At the same time of Miesenböck experiments, the group of Carl Deisseroth in Stanford[103], decided to express ChR2, which was recently discovered by Nagel's group, in specific neurons of the mouse brain, in order to control the membrane potential of these cells with the simple delivery of flashes of light. This approach simplified a lot the system, since once the channel has been inserted into the genome of the cell of interest, then no more molecules are to be added, a part from the co-factor retinal which is already present in many tissue. Moreover, by exploiting genetic tools for tissue-specific expression, such as the *Cre-Lox system*, expression of the channel only in a specific type of neurons inside a complex tissue such as the brain can be achieved.

To describe these experiments later was coined the term: "optogenetics", which combines the two aspects of this technique: the use of photo-activated channel to depolarize a cell and the selective exogenous expression of this channel in a specific cell type of interest[104]. The innovative aspects of this technique, compared with the conventional electrophysiological methods, based on electrical stimulation, are the specificity of the stimulation, its non-invasiveness and its spatial-temporal accuracy. The specificity is particularly important when a stimulation of only a desired marker-expressing neuron is needed, in a complex tissue with a lot of other cells intermingled, such as the brain. This

made possible to study the functionality of peculiar regions of the brain or even the single neural circuit, without affecting the others[105].

Moreover, the possibility to stimulate such cells multiple times and for a long period, without perturbing or damaging them, is an incredible advancement for electrophysiological studies in neuroscience. Later the optogenetic toolbox expanded with the exploitation of different rhodopsins, such as *Halorhodopsin* [106]which is a chloride channel that upon illumination iperpolarize the cell and offered the possibility to "switch off" single neurons or entire neural circuits (**Fig.XVI**).

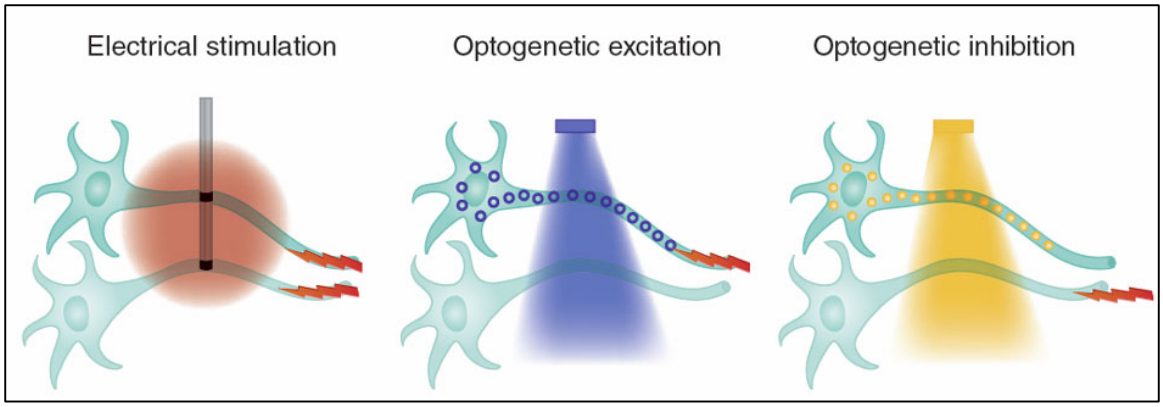

Figure XVII: *Advantages of optogenetics compared to electrical stimulation (Deisseroth 2011).*

Cardiac optogenetics

Some years after the birth of optogenetics and its application to the neuroscience field, the pioneering studies of Bruegmann et al.[107] and Arrenberg et al.[108] demonstrated that this technique could be applied also for the study of heart electrophysiology. In particular, Arrenberg and colleagues managed to express halorhodopsin and ChR2 in *zebrafish* CMs and with the light sheet microscopy technology succeeded in controlling the heart rate of the animal *in vivo*, evoking episodes of tachycardia, bradycardia and also cardiac arrest[108]. Bruegmann and colleagues, instead, generated a stable mouse embryonic stem cell line (ESC) expressing ChR2 under the constitutive synthetic promoter CAG and, after having characterized the cells *in vitro*, they generate from them a transgenic mouse[107]. With the use of light emitted from the objective of a confocal microscope, they were able to influence heart rhythm by evoking ectopic heart beats *in vivo*.

Despite these firsts proof of principle studies opened various fascinating perspectives, advancements in the new field of cardiac optogenetics lagged behind the following years,

with only sparse studies involving especially in vitro models or computational approaches[109-111]. In particular, the group of Entcheva demonstrated *in vitro* the feasibility of obtaining optogenetic stimulation of CMs, through the delivery of non-excitable cells, expressing ChR2, that are capable of forming electrical coupling with CMs and conferring to them the ability to be light stimulated[112]. Other *in vitro* studies tried different approaches to obtain ChR2 expression in CMs, using electroporation to express ChR2 in atrial cell line HL-1[113] or lentiviral infection of human ESC that are then differentiated into CMs[114]. Bingen and colleagues used the same approach of lentiviral transduction of ChR2 in isolated neonatal atrial CMs, and used optogenetics to study, in a monolayer of CMs, the possible mechanisms to obtain light-driven termination of spiral wave arrhythmia, responsible for atrial fibrillation in the intact heart[115]. Moreover, Boyle and colleagues in 2013 provided a computational simulation of cardiac optogenetics, that took into account opsin channel kinetics, delivery mode and spatial distribution of light sensitive cells inside the heart, to study how these variables can be modulated to obtain low energy optical defibrilaltion of the heart[116]. Beyond the use in membrane potential modulation, some studies showed that optogenetics can be used to investigate, with unprecedented detail, intracellular signaling in CMs[117,118]. Beiert and colleagues, for example, demonstrated that G proteins signaling can be optically modulated in CMs, in detail they used *melanopsin*, a light sensitive G protein-coupled receptor, to modulate intracellular Ca^{2+} in HL-1 cells and ES-derived CMs[119].

In this thesis are presented the results of a study, published in Proceedings of the National Academy of Science (PNAS) by our group, that showed the set up and characterization of a cardiac optogenetic experiment in the *in vivo* animal model and exploited this to investigate the tissue requirements for the development of ectopic beats in the normal heart and the electrophysiology of Purkinje fibers and their involvement in the generation of life-threatening ventricular arrhythmia in the ischemic heart[120].

Results

The results section of this thesis is composed of four research articles, organized in introduction, results, discussion and material and methods sections, figure panels are at the endo of the discussion section:

- **Sympathetic innervation locally modulates cardiomyocyte proteolysis inside the working myocardium**

- **Optogenetic determination of the myocardial requirements for extrasystoles by cell type-specific targeting of ChannelRhodopsin-2** *(PNAS (2015) Aug 11;112(32):E4495-504)*

- **Optogenetic interrogation of cardiac sympathetic neurons shed light on the "neuro-cardiac junction"**

- **Cardiac optogenetics as an alternative to electrical pacemaking and cardioversion: insights from an *in vivo* animal model**

Sympathetic innervation locally modulates cardiomyocyte proteolysis inside the working myocardium
(manuscript in preparation)

Collaborators: *Valentina Prando, Mauro Franzoso, Anna Di Bona, Marina Campione, Marco Sandri, Tania Zaglia and Marco Mongillo*

ABSTRACT

Purpose: The myocardium is highly innervated by Sympathetic Neurons (SNs), that distribute within the tissue with a well-defined pattern. We have previously shown that neuronal input to cardiomyocytes (CMs) represses proteolysis and activates protein synthesis, through the β2-AR dependent signaling. We here test the hypothesis that SNs perform a local modulation on CM size, acting through differential modulation of proteolysis. **Results**: In the mouse heart, SNs are predominantly found in the outer myocardial cell layers, and, consistently, CMs in the outer layers (EPI) are significantly larger than the similarly oriented ones in the innermost (ENDO) layers (SNs/CM: EPI 0.45±0.06 vs ENDO 0.15±0.02; CM volume: EPI 8590±2121 *vs* ENDO 4697±1433, in μm^3). Such differences disappear upon SN ablation in the adult mouse, and never establish when SNs are ablated before the postnatal period in which sympathetic innervation of myocardium occurs (P3 to P21). Furthermore, systemic delivery of a β2-AR agonist, or antagonist, which diffuse throughout the myocardium resulting in hypertrophic and atrophic remodeling respectively, abolishes CM heterogeneity, suggesting that SNs act with a limited spatial range on neighboring CMs. In support of this we demonstrated, by ISH and RT-qPCR, that CM size heterogeneity is the result of local control on proteolysis operated by SNs. This concept holds true regardless of the innervation pattern as in the heart of other mammals, including humans, characterized by different SN distribution, CM size follows neuronal density. **Conclusion**: This is the first evidence, to the best of our knowledge, of an otherwise homogeneous tissue, shaped, after development, by a superimposed innervation network, through the modulation of cellular protein turnover.

INTRODUCTION

The mammalian ventricular myocardium is a highly heterogeneous tissue, with transmural differences in cytoarchitecture and electrophysiology of cardiomyocytes (CMs). Based on these different properties, two regions can be defined across the ventricular wall: an outer region of CMs that is called subepicardium (EPI) and an inner region, which is called subendocardium (ENDO)[5,7,121]. Between these two regions a third type of CMs can be defined, the so-called "M cells", whose identity and function is still debated[122-124]. Moreover, the level of complexity inside the ventricular wall is increased by the presence of sympathetic nervous system (SNS) innervation. SNS is the principal regulator of heart activity during stress conditions, and in particular at the level of the working myocardium modulates the contraction force of CMs[43].

Our group recently uncovered a novel role for cardiac SNs, in the modulation of CMs proteostasis. Indeed, we demonstrated that a constitutive sympathetic stimulus is required to maintain the correct CM size by modulating the balance between protein synthesis and protein degradation, through β2-adrenoceptor (β2-AR) activation and AKT dependent phosphorylation of FOXO3 transcription factor, that lead to down-regulation of ubiquitin proteasome system (UPS) activity[1].

The SNS abundantly innervates the working myocardium with a well-defined pattern inside the ventricular walls, forming a transmural gradient of sympathetic neurons (SNs) that in the murine myocardium decreases from the epicardium to the endocardium, while in other mammalian species, including human, the distribution of SNS inside myocardium has not been characterized yet[45,125]. It has been demonstrated, that sympathetic innervation of the myocardium is a process starts immediately after birth, and continues for the first post-natal weeks[40,45]. Moreover, it was proved, in mouse heart, that the peculiar pattern of SNs inside the ventricular myocardium is guided by the balance between chemoattractant neurotrophins (e.g. nerve growth factor, NGF) and chemorepellent factors (e.g. semaphorin-3a) released by cardiac cells with a well defined topology [126].

In this work, based on our published evidence, we aim to asses if the peculiar ventricular pattern of SNs might reflect in a transmural modulation of CMs size, suggesting the hypothesis of a regional activity of SNs in modulating CM properties. Indeed, in literature are present evidence of a close interaction between SNs and CMs coming from studies involving electron microscopy analysis[127] and *in vitro* models of co-culture of SNs and CMs where was also proved that stimulation of SNs induced an increase in the

contraction rate of co-cultured CMs [128-131]. However, to date, whether SNs interacts with CMs in a local environment or if the interaction is mediated by the diffuse release of norepinephrine (NE) in the interstitium is still an open question.

To understand the role of SN patterning inside the ventricular myocardium in the local modulation of CMs properties is of great relevance since many pathological conditions are associated to an impairment in the autonomic innervation of the heart and the main pharmacological treatment for this pathologies is indeed β-AR blockage.

RESULTS

1. Sympathetic neuron innervation pattern reflects in local heterogeneity in CM size in the mammalian heart.

Cardiac sympathetic neurons (SNs) abundantly innervate the murine ventricular myocardium with a well defined pattern (**Figure 1a**). We used an antibody specific for tyrosine hydroxylase (TOH) to identify SN, since this enzyme is the rate limiting step in the biosynthesis of norepinephrine (NE). Consistently with published data[38], we observed that SNs, mainly concentrate in the outer part of the ventricular wall, the subepicardium (EPI), and SN density progressively decreases till reaching the inner part of the ventricle, the subendocardium (ENDO) (EPI: 0.45±0.06 vs ENDO: 0.15±0.02, TOH+ fibre/CM) (**Fig. 1a-b**). The EPI-to-ENDO SN density gradient is present at the level of the apex, the mid ventricles and the heart base (data not shown).

Based on our finding that SNs are able to modulate CM size[1], we evaluated whether the heterogeneity in cardiac SN distribution parallels with regional differences in CM size throughout the myocardium. To this purpose, we evaluated CM size in both the EPI and the ENDO of the left ventricle (LV) of adult mouse hearts (see Method section). Morphometric analyses on heart sections stained with an antibody to dystrophin and performed by both a blinded operator and an automate software developed in the laboratory (**Fig.1e**), demonstrated that the mean cross-sectional area of EPI CMs is almost two-fold, as compared to the ENDO ones (**Fig. 1c-e**). The same heterogeneity in the cross-sectional area of EPI and ENDO CMs was detected at the level of the cardiac apex, mid ventricles and heart base (data not shown). Moreover, no significant differences in the long axis length of CMs was observed between EPI and ENDO CMs. we evaluated the long axis length of EPI and ENDO

CMs (**Fig. 2b**). To exclude that the differences in CM size are a consequence of the different tissue vascularization, we measured the density of capillaries inside the two regions. We performed IF co-staining on mouse cryosections, with an antibody for dystrophin, to identify CM membrane, and isolectin-B4 to detect capillary vessels and we found no significant differences in the capillary density between the two regions (0,981±0,054 *vs* 0,957±0,044; number of capillary / number of CMs) (**Fig. 2a**).

All these data suggest that there is a spatial correlation between SN density and CM size in the ventricular myocardium of the mouse heart. To assess if this feature is conserved among other mammals we analyzed SN distribution and CM size in the hearts from rats, rabbits and also humans. In all these species, SN density resulted slightly higher in the ENDO region compared to the EPI, an opposite situation to that described for the mouse heart (**Fig. 3a**). Consistently, the size of CMs resulted higher in the ENDO region than in the EPI. Thus demonstrating that the correlation between the density of SNs and CM size, is conserved regardless of the different innervation present among different species (**Fig. 3b)**

In all the experiments described later we decided to analyze in better detail this correlation focusing on the mouse heart, given the well known advantages of this animal model in terms of genetic, pharmacology and handling, moreover, the mouse heart shows the highest heterogeneity in cardiac innervation pattern among the species analyzed.

2. Cardiac sympathetic innervation determines the transmural heterogeneity in CM size during the postnatal development.

The causal role of the SN innervation patterning in shaping the transmural heterogeneity in CM size was asses by measuring CM size at different stages during the progression of cardiac sympathetic innervation. The process of myocardial innervation starts immediately after birth, in the early post-natal weeks[40,45]. What we found is that in P1 hearts rare SNs are detectable only on the epicardial surface and interestingly, at this stage, no significant differences in EPI and ENDO CM size were observed. As SN sprouting proceeds, during the following postnatal phases, the transmural heterogeneity in the size of CMs becomes more evident and increases independently from the overall progressive postnatal CM hypertrophic growth. To further asses this hypothesis, we treated neonatal mice with 6-hydroxy-dopamine (6-OH-DA): a well known pharmacological treatment that induces the SN degeneration, without any side effects on CMs. Then we compared the cross–sectional

areas of EPI and ENDO CMs of denervated hearts to control mice treated with the 6-OH-DA vehicle. Consistently with our hypothesis, in P7, P21 and adult (3 mo. old) denervated hearts the postnatal CM hypertrophic growth appeared significantly reduced as compared to controls and the transmural EPI-to-ENDO CM size heterogeneity totally disappeared. (**Fig.4**).

These results support a causal role for cardiac SNS in the establishment, during the postnatal development, of the transmural patterning of CM size observed in the adult heart.

3. Sympathetic neurons locally modulate cardiomyocyte size during the adulthood.

To address whether SN activity is also required for the maintenance of the transmural patterning of CM size in the adulthood, we evaluated EPI-to-ENDO CM size differences in the hearts from mice of two study group: i) mice subjected to denervation in the adulthood and ii) mice treated with β2-AR antagonist and agonist. As expected, denervated mice developed heart atrophy due to a reduction in CM size, that affected mostly the EPI region, resulting in the abolishment of CM size heterogeneity inside the ventricle (**Fig. 5a**). Such alterations were peculiar of denervation-induced atrophy, since the analysis of a mouse model of caloric restriction, which induced a significant decrease in cardiac mass, with no changes in SN distribution, resulted in an overall decrease of CM size, but a preserved EPI-ENDO heterogeneity (**Fig. 5a**). In line with this, the interference with β2-AR activity by the systemic continuous delivery of either: β2-AR agonist (i.e. clenbuterol) or β2-AR antagonist (i.e. ICI 118,551), although inducing cardiac hypertrophy (heart weight/body weight: clenbuterol: 5.5±0.3 vs controls: 4.5±0.2, in mg/g) and atrophy (heart weight/body weight: ICI: 4.0±0.1 vs controls: 4.3±0.3 in mg/g), respectively, in both cases resulted in the loss of CM size heterogeneity (**Fig. 5b**). In these hearts SN patterning was unaltered, but consistently with our hypothesis, its regional control over CM size was by-passed by the diffuse action of the drug. Interestingly, while the EPI-to-ENDO difference in CM size was reduced upon ICI 118,551 treatment, an inversion of CM size distribution occurred in clenbuterol-treated hearts with the mean cross-sectional area of ENDO CMs appearing bigger as compared to the EPI one. This result could be explained by the *supersensitization* effect experienced by ENDO CMs (see discussion)[132,133]. Consistently, analysis of β2-AR mRNA levels by RT-qPCR on tissue extracts from EPI and ENDO regions revealed that at baseline the receptor is differentially transcribed between the two regions, being upregulated

in the ENDO. After denervation it increases in the EPI region reaching the same level of expression of the ENDO region (**Fig. 5c**). Altogether these data demonstrate that SN pattern is essential to maintain the physiologic CM size differences inside the myocardium during the adult life, moreover, these finding suggest that SNs operate a local control over CM size.

4. Alterations in the β2-AR signalling pathway associate to a failure in the physiological cardiomyocyte size patterning.

To investigate the role of the β2-ARs/AKT/MuRF1 pathway[1] in the establishment of the physiological transmural patterning of cardiomyocyte size, we measured the size of EPI and ENDO CMs in mouse models lacking β2-ARs and MuRF1. No significant changes in the SN patterning were detected in hearts from β2-ARs$^{-/-}$ mice, which displayed heart atrophy (heart weight/body weight: β2-AR$^{-/-}$: 3.0±0.02 vs controls: 3.8±0.4 in mg/g), accompanied, in accordance with our previous results, with the disappearance of CM size heterogeneity (**Fig. 6a**). In particular, EPI CMs were smaller in size as the ENDO ones. MuRF1$^{-/-}$ hearts, instead, were hypertrophic (heart weight/body weight: MuRF1$^{-/-}$: 5.2±0.2 vs WT: 4.6±0.3 in mg/g) but with no sign of on overt cardiomyopathy. MuRF1$^{-/-}$ hearts, although displaying a normal SN innervation pattern, do not show CM size heterogeneity in the LV, suggesting a fundamental role for this ubiquitin ligase in the process of denervation-induced cardiac atrophy[1] (**Fig.6b**).

These results suggest that the transmural CMs differences are dictated by a spatial heterogeneity in the activation of the β2-AR/AKT/MuRF1 pathway.

5. The cardiac sympathetic neuron patterning reflects in local changes in cardiomyocyte proteolytic activity.

To assess if SNs are able to modulate locally proteolysis rate of CMs, we evaluated changes in the mRNA expression level of the ubiquitin ligase MuRF1. To achieved this goal, we performed in situ hybridization (ISH) in control and denervated adult mouse hearts (30d after the denervation). In WT hearts we observed a homogeneous distribution of MuRF1 mRNA among CMs, while in denervated hearts, we found that it was more expressed in the EPI region compared to the ENDO one (**Fig.7a**). To quantify this difference, we set up a protocol for the surgical dissection of the two regions of the heart and performed RT-qPCR

on tissue extracts. To verify the quality of our dissection procedure we evaluated the mRNA expression level of a subunit of the voltage gated potassium channel (K_V4.2), which is reported to be upregulated in the EPI region, obtaining the same results (**Fig.7c**). With this approach we observed that in normal condition mRNA levels of MuRF1 were comparable between EPI and ENDO, but when we perturbed this equilibrium by the ablation of SNs we found an upregulation of MuRF1 significantly more pronounced in the EPI region compared to the ENDO (**Fig.7b**).

These results suggest that cardiac SNs are able to modulate CM size by acting on their proteolysis rate and thus that the pattern of SN inside ventricular myocardium reflects in a related CM size heterogeneity.

ONGOING EXPERIMENTS

All the data described support the notion that SNs control CM proteostasis through a local action, to address this point the following experiments are in progress: I) the regional denervation of the myocardium *in vivo*, II) the 3D reconstruction of SN-CM interaction and III) the set up of an *in vitro* co-culture system mimicking SN-CM interaction occurring *in vivo*.

Regional denervation of myocardium

We set up a protocol for the denervation of a small portion of the myocardium, through the application of phenol on the epicardium. Phenol epicardial painting is described in literature as an efficient method to obtain neuronal death, without affecting significantly CMs viability[146,147]. We have performed a first experiment in which we applied phenol to the epicardial surface of the LV with a cotton fiber tip with a diameter of 2 mm and obtained the denervation of this limited region of the myocardium, as assessed through IF staining for TOH, without apparent damage to the tissue. Now we are designing a DNA construct which harbors the promoter of MuRF1 fused to GFP, later we will use an adeno-associated viral vector to deliver this construct to the heart. With this approach we will assess, from *ex vivo* heart section, if the denervation of a small region of the myocardium results in the upregulation of MuRF1, appreciated by the increase in the fluorescence signal, only in this confined region.

3D reconstruction of SN-CM interaction

We will also take advantage by the use of the multiphoton microscopy to analyze in great detail the structure of the contact between a single SN and its target CM. With this technology, already used in literature for the 3D characterization of cardiac SN sprouting [148], we will investigate the the close contact between SNs and CMs in the normal heart and also the activation of MuRF1 following regional denervation. To characterize the interaction between SNs and CMs we need to fluorescently mark CM membrane and SNs in intact thick heart tissue samples, to achieve that we set up a protocol for the IF staining of thick myocardial tissue samples (1 mm^3) and we have collected some preliminary results showing that it is possible to mark CMs and SNs in sections of up to 400 μm thickness (**Fig.S1**).

***In vitro* co-culture to study SN-CM interaction**

We have set up an *in vitro* model of co-culture between CMs and PC12 cells (**Fig.S2**). PC12 cells are a cell line derived from pheochromocytoma of the rat adrenal medulla, that upon treatment with NGF, terminally differentiate into NE secreting neurons[149]. In a parallel project, in which we analyzed *in vitro* SN-CM co-culture (see **Results**), we observed, upon SN stimulation, acute changes in cAMP levels only in CMs directly innervated by SNs and not in the adjacent ones. These results suggest a functional contact between SNs and CMs. Based on these evidence we evaluated the effect of a chronic stimulation of PC12 cells, in the PC12-CM co-culture, on CM size. We treated co-culture 7 days after their plating, since it is described in literature [96], and confirmed also by our data (see **Results**), that this time is sufficient for neurons to establish functional contacts with CMs. We used nicotine, to stimulate neurotransmitter release, with different conditions: a short stimulation (1-hour treatment 3 times a day for 5 consecutive days) and a longer stimulation (8-hour treatment each day for 5 consecutive days) and different concentrations: 1-10-500 μM. We focused on clusters of CMs in which only some of them are directly contacted by neuronal processes, and we found that, in the condition with longer stimulation and 500 μM of nicotine, only CMs innervated showed a hypertrophic remodeling, compared to non-innervated ones. To achieve an even more controlled and precise stimulation of the neurons we are setting up a PC12 cell line that stably express ChannelRhodopsin-2. Then we will perform a chronic stimulation of PC12 cells co-cultured with CMs and we will asses if this results in changes

in the size of CMs directly contacted by PC12 cells compared with the other CMs present in culture.

DISCUSSION

This study provides evidence in favor of the hypothesis of a local interaction between SNs and CMs, rather than the model of a non specific diffusion of neurotransmitter released by SNs into the interstitium. One consideration that arises from this work is that the different effects of SNS innervation of the heart could be operated through the activation of different receptors in CMs, a hypothesis suggested also by other studies in literature[134-136]. In particular, parallel to the well known acute effect of increase in heart contraction operated through activation of β1-AR, there is a more long-term effect acting through β2-AR that modulates CMs size[1,137]. How these two effects are discriminated at the level of SN-CM interaction is not completely understood, although in literature there are evidence of a different localization and response to stimulation of the two receptor subtypes. In particular, it was demonstrated that the two receptor subtypes have different compartmentalization, β1-ARs are enriched in specialized zone that surround contacting axon, in close proximity of scaffold protein such as AKAPs and SAP97[131] and remain at the plasma membrane upon stimulation, while β2-ARs undergo endocytosis and recycling upon stimulation. Moreover, it is well described in literature, in fact, that the continuous activation of β-AR result in the decrease in numbers of the receptors, a physiological process called *desensitization*[133]. While chronic treatment with a β2-AR antagonist, impedes the desensitization process and a sudden discontinuation of this treatment was shown to be deleterious since the effects of neurotransmitters on CMs were then exacerbated, a process called *supersensitization*, and could give raises to arrhythmic events[138,139]. Our data obtained from pharmacological activation of β2-AR through the systemic delivery of clenbuterol, are consistent with the supersensitization effect since ENDO region, which is physiologically less innervated by SN and thus is supposed to have more β2-AR compared to the more innervated EPI (which we demonstrated at the level of transcript mRNA), shows a higher response in terms of hypertrophic remodeling. This result implies that in a normal situation there is a local control of CM size exerted by SN, which cannot be achieved otherwise if the neurotransmitter is released broadly into the interstitium as it can occur for example with circulating

catecholamines, and this is a further proof in favor of the model of the direct interaction between SNs and CMs.

The importance of this study is given by the presence of many pathological conditions that are associated to autonomic innervation impairment of the heart, where in many of them the main pharmacological treatment is indeed β-AR blockage. One of these situation is heart failure, where an hyperactivation of SNS is demonstrated. Another important pathologic condition in which heterogeneous distribution of the sympathetic innervation is observed is myocardial infarction, where hyperinnervated, denervated and normally innervated area are present[140]. Moreover, in literature are present studies that provides evidence that stimulation of a small fraction of cardiac cells is sufficient to trigger a premature ventricle complex raising the hypothesis that local adrenergic activation is involved in triggering arrhythmia[32,120] (see **Appendix**).

Furthermore, another important clinical implication for this study regards heart transplantation, this condition, in fact, is inevitably associated to heart denervation and during time also to the process of reinnervation, however, although the importance of heart innervation in physiologic modulation of heart activity and in pathological triggering of arrhythmic events is clearly demonstrated, there is a lack of studies regarding these aspects in transplanted hearts[141-145].

In conclusion, beyond the specific context of heart, this study provides, to the best of our knowledge, the first example of an otherwise homogeneous tissue whose cells are shaped in terms of their size by a superimposed pattern of neurons.

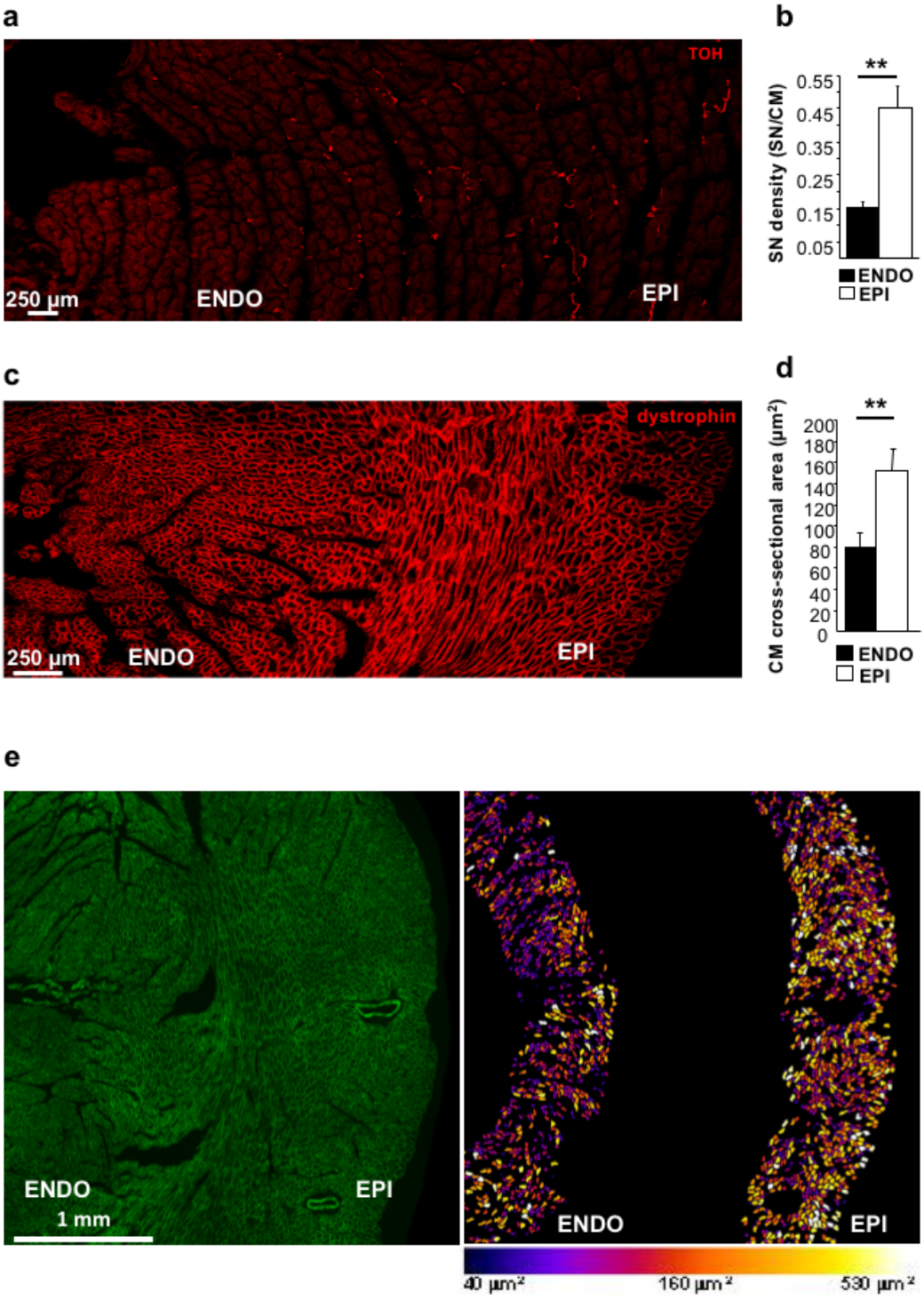

Figure 1. (**a**) IF staining for TOH of a mouse ventricular cryosection, detail of the LV showing the distribution of SNs. (**b**) Quantification of SN density in the LV of mouse heart. (**c**) IF staining for dystrophin, identifying CM membrane, of a mouse ventricular cryosection, detail of the LV. (**d**) Morphometric measurement of CM cross sectional area in the LV of mouse heart. (**e**) Pseudocolor map based on the IF staining for dystrophin (left panel), obtained with the software developed in this study, detail of the LV of a mouse heart cyosection showing each CM with a color code that is based on its cross sectional area.

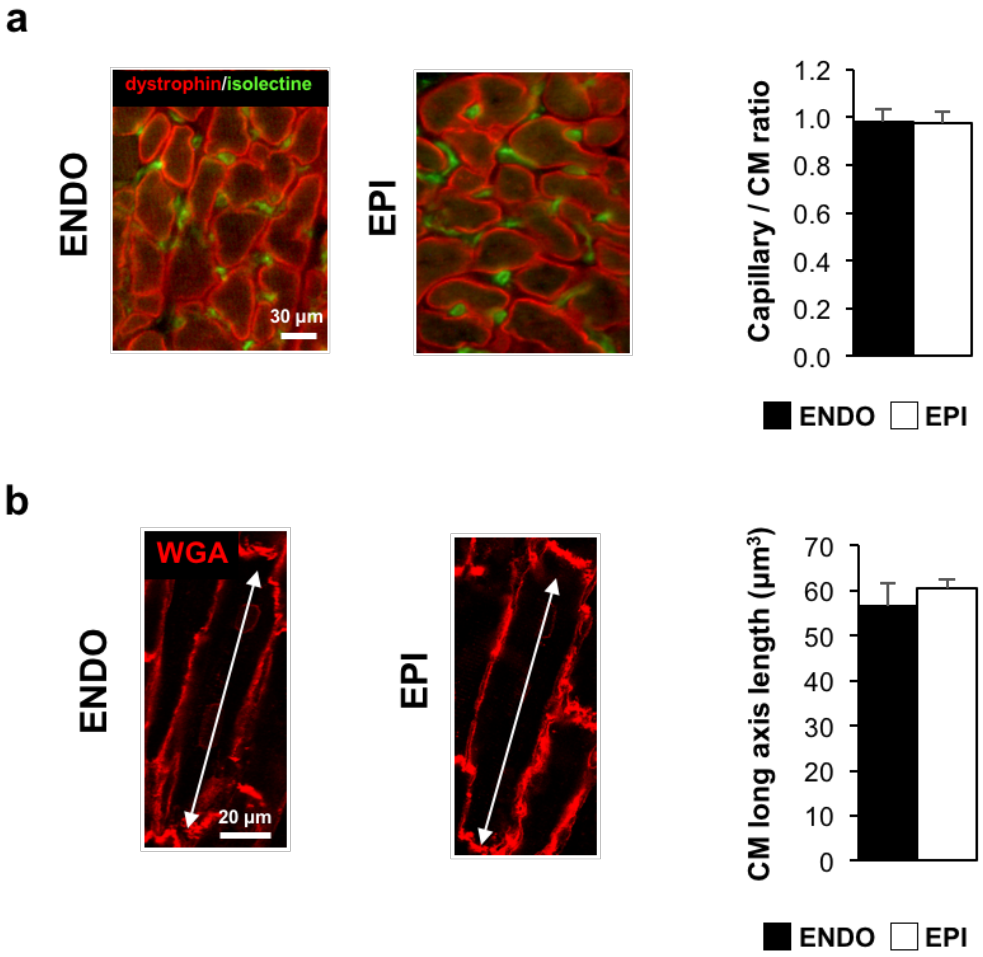

Figure 2. (**a**) IF double staining for dystrophin (CM membrane) and isolectine (capillary membrane) in the ENDO and EPI region of mouse heart and quantification of the ratio between the number of capillary and the number of CMs. No significant changes were detected. (**b**) Details of a IF staining for wheat germ agglutinin (WGA) showing CM membrane, the arrows highlight the long axis of CM form ENDO and EPI regions. Graph showing the quantification of CM long axis length of the ENDO and EPI CMs. No significant changes were detected**.**

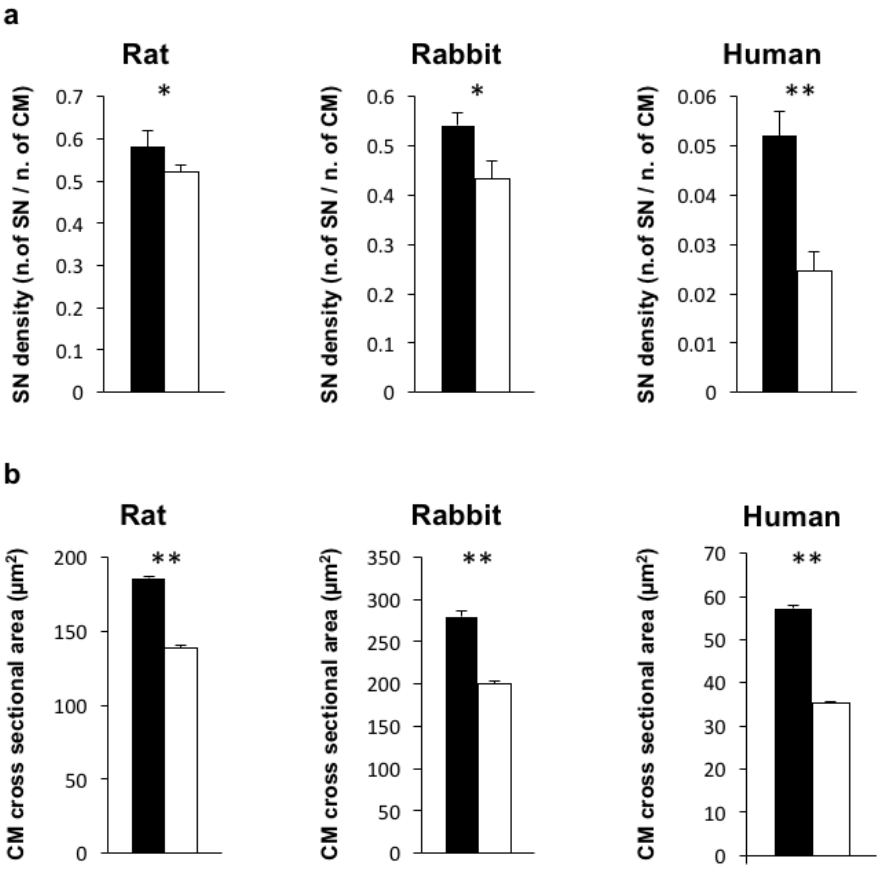

Figure 3. (a) Quantification of SN density in the LV of rat, rabbit and human heart. (**b**) Morphometric analysis of CM cross sectional area in the LV of rat, rabbit and human heart.

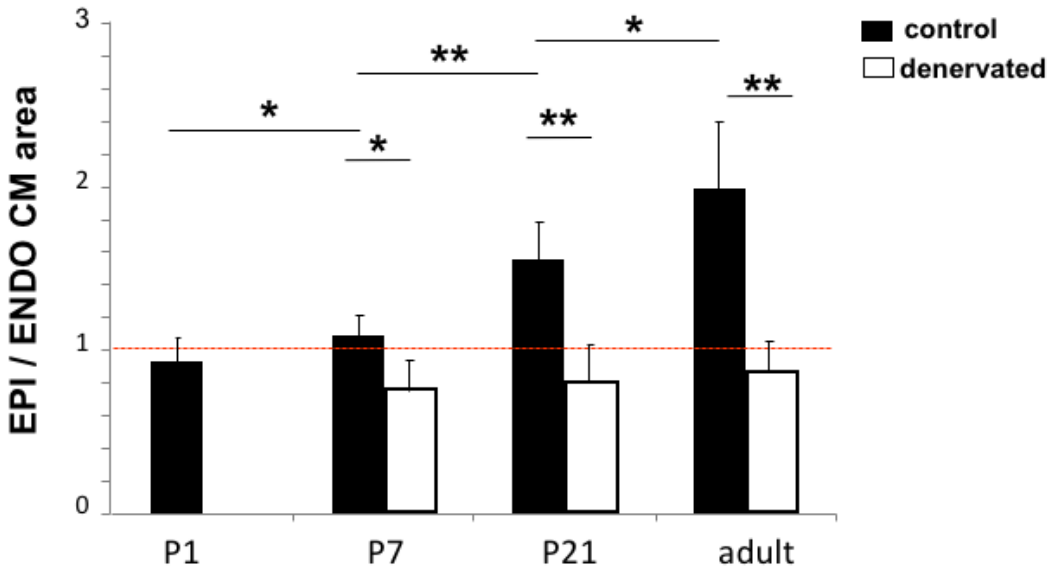

Figure 4. Graph showing the ratio between the cross sectional area of CMs from EPI and ENDO regions of neonatal mouse hearts at 1,7 and 21 days after birth. Black bars indicate normal hearts, white bars indicate hearts denervated at birth. Red dashed line highlight the ratio value of 1, which corresponds to the situation of cells with an equal size. The white bar at P1is absent because the heart is not yet innervated.

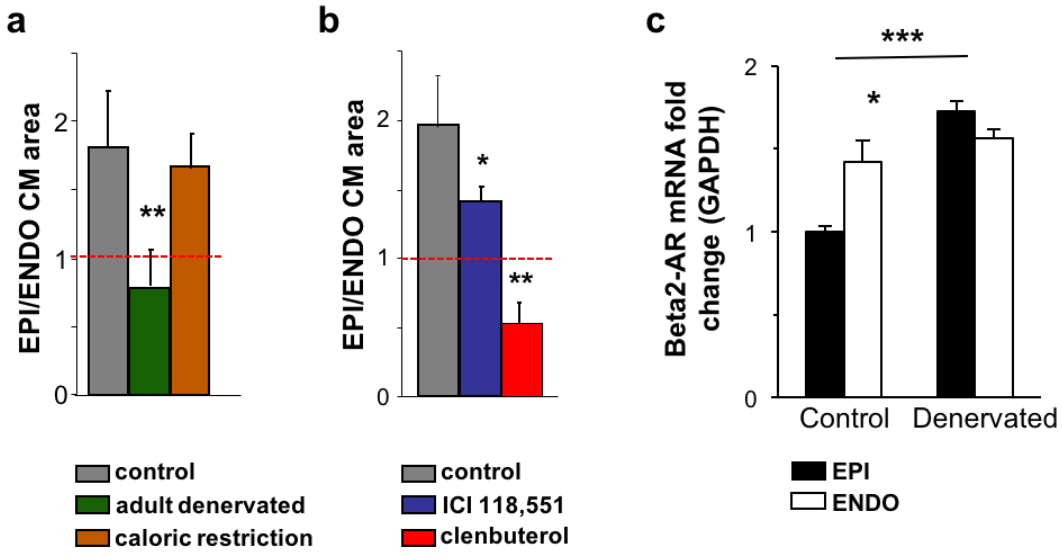

Figure 5. (**a**) Graph showing the ratio between the cross sectional area of CMs from EPI and ENDO regions in hearts of control, adult denervated and subjected to caloric restriction mice. (**b**) Graph showing the ratio between the cross sectional area of CMs from EPI and ENDO regions in hearts of control, β2-AR antagonist (ICI 118,551) and β2-AR agonist (clenbuterol) treated mice. (**c**) Quantification of RT-qPCR performed on heart extracts from EPI and ENDO regions of control and denervated mice which shows the mRNA levels of β2-AR relative to housekeeping gene GAPDH.

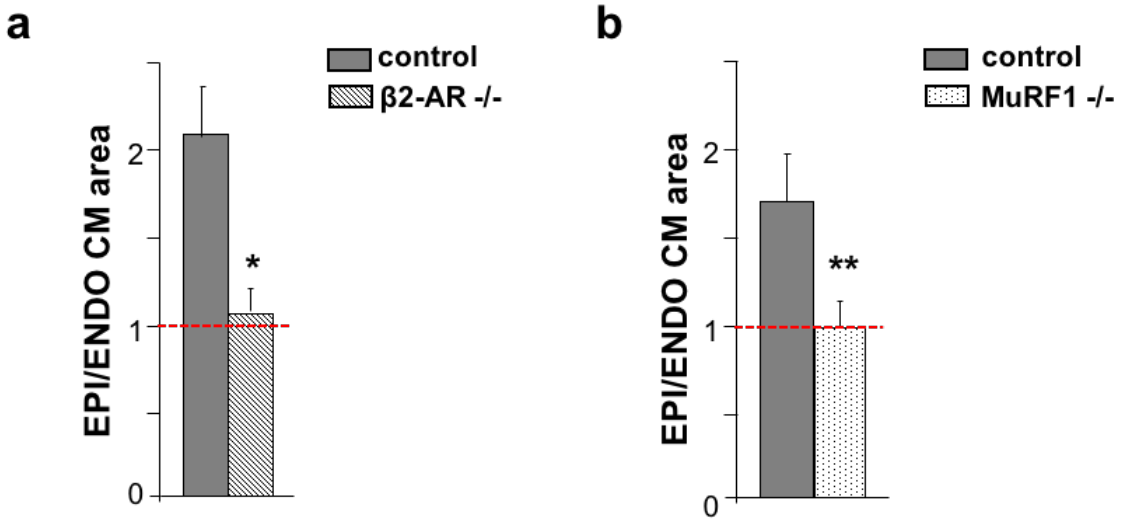

Figure 6. (**a**) Graph showing the ratio between the cross sectional area of CMs from EPI and ENDO regions in hearts of control and β2-AR$^{-/-}$ mice. (**b**) Graph showing the ratio between the cross sectional area of CMs from EPI and ENDO regions in hearts of control and MuRF1$^{-/-}$ mice.

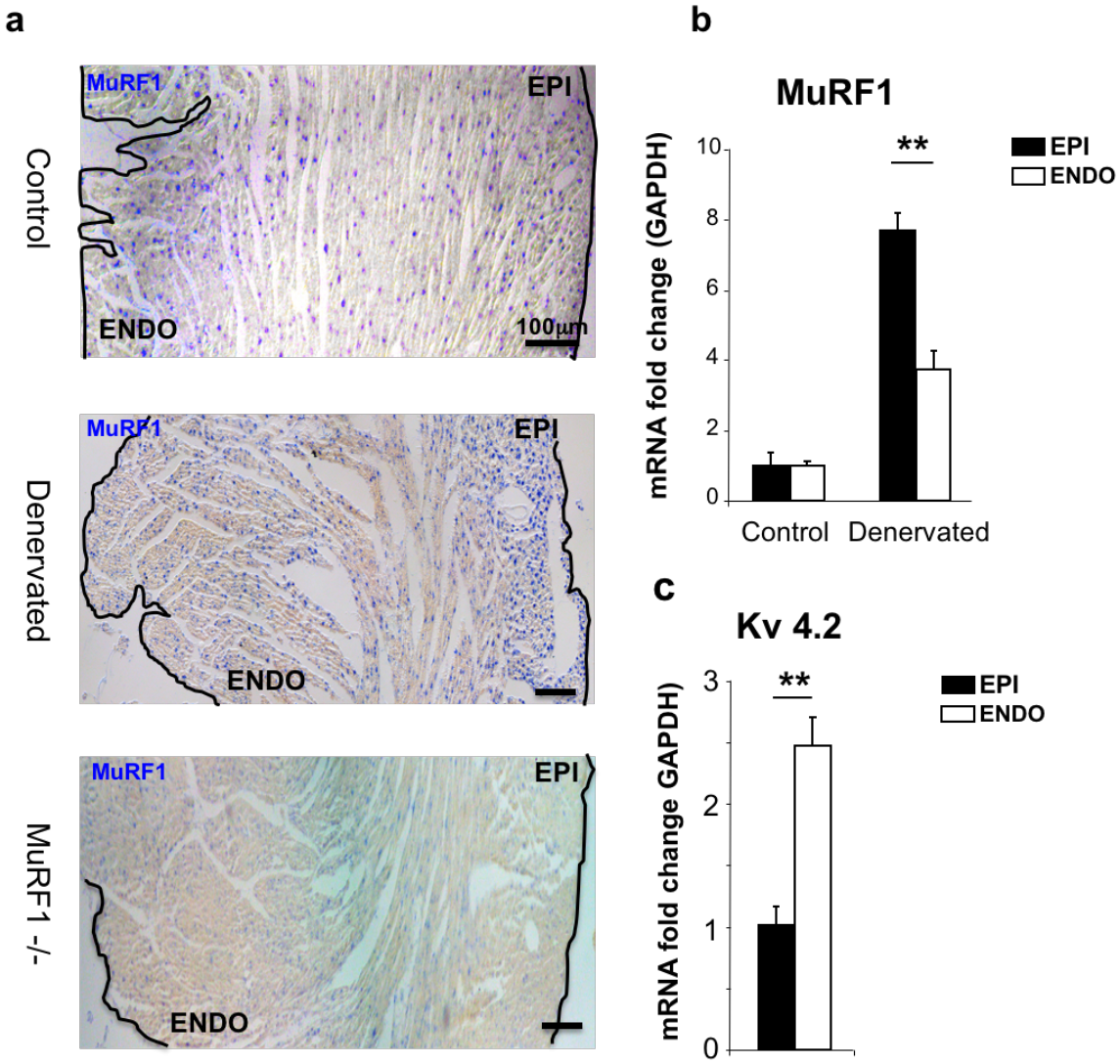

Figure 7. (**a**) ISH on LV sections of hearts from control, denervated and MuRF1$^{-/-}$ mice, showing the localization and intensity of mRNA expression of MuRF1as blue signal. (**b**) Quantification of RT-qPCR performed on heart extracts from EPI and ENDO regions of control and denervated mice which shows the mRNA levels of MuRF1 relative to housekeeping gene GAPDH. (**c**) Quantification of RT-qPCR performed on heart extracts from EPI and ENDO regions of control mice which shows the mRNA levels of Kv4.2 relative to housekeeping gene GAPDH.

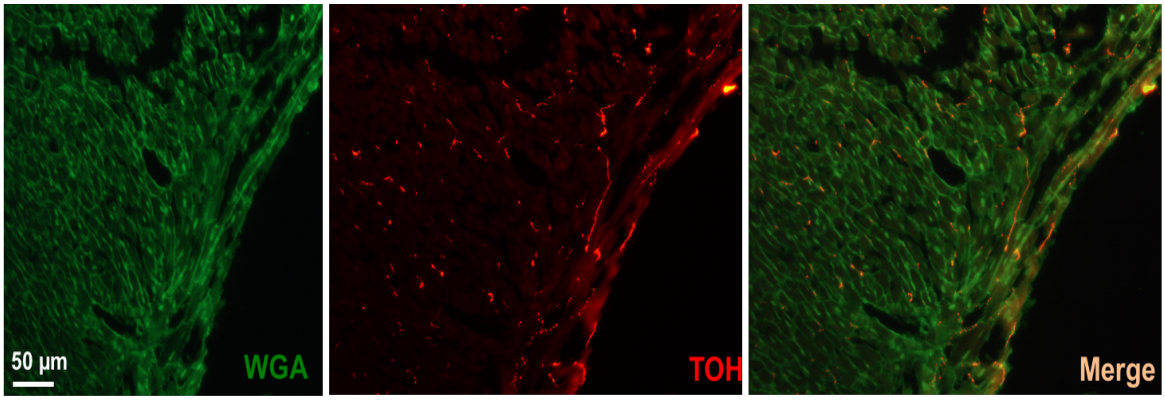

Figure S1. IF images of a 10 µm section cut from a myocardial tissue sample of 1 mm^3 stained with the protocol described in the text for wheat germ agglutinin (WGA) that stains CM membrane and tyrosine hydroxylase (TOH) that marks SNs. The section was cut at a depth of 400 µm inside the sample, showing the penetration of the antibody and the dye into the tissue.

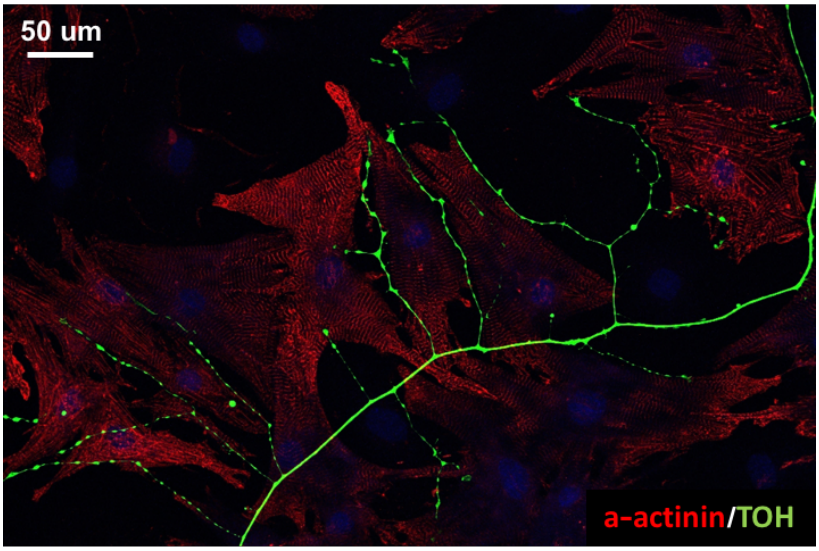

Figure S2. Confocal IF image of the co-culture CM-PC12 stained for a-actinin to mark CM sarcomeres and TOH to mark neuron processes. In this picture is evident the "perl and necklace" morphology of the neurons and their varicosities at the contact site with CMs.

MATERIALS AND METHODS

Animal models. In this study we analyzed hearts from: P1, P7 and P21 CD1 mice, as well as C57BL/6J, FVB (all from Charles River, Milan, Italy), MuRF1$^{-/-}$ (Dr David J. Glass, Regeneron Pharmaceuticals, Tarrytown, NY.) and β2-Adenoceptors$^{-/-}$ (β2-AR, P.C. Brum, University of São Paulo, Sao Paulo) adult male mice. Hearts from Sprague-Dawley adult male rats, rabbits (all from Harlan, Milan, Italy) were also evaluated. All experimental procedures described in this manuscript have been approved by the local ethical committee (Authorization number C54) and communicated to the relevant Italian authority (Ministero della Salute, Ufficio VI), in compliance of Italian Animal Welfare Law (Law n 116/1992 and subsequent modifications).

Histological and immunofluorescence analyses. Hearts were harvested from mice and immediately placed in a fixative solution. This solution contained 1% (v/v) paraformaldehyde (Sigma Aldrich) diluted in PBS 1x, with a concentration of KCl (Sigma Aldrich) of 25mM to allow the relaxation of the heart muscle fibers. After fixation hearts were washed in PBS 1x and allowed to dehydrate and equilibrate in an aqueous solution containing 30% Sucrose (w/v) (Sigma Aldrich) overnight at 4°C. The next day hearts were embedded in OCT matrix (Vetrotecnica) and frozen in the vapor phase of liquid nitrogen and stored at -80°C. For histological and immunofluorescence analysis heart slices of 10 μm were obtained using a cryostat (Leica 1860). For immunofluorescence analyses heart slices were incubated with the primary antibody diluted in PBS 1x supplemented with 1% BSA (Sigma Aldrich) and 0.5% Triton-X100 (Sigma Aldrich) and secondary antibody diluted in PBS 1x supplemented with 1% BSA and mounted using Elvanol solution. The following primary antibodies were used: anti-TOH (Millipore), anti-dystrophin (Abcam) and revealed using secondary antibody conjugated with fluorophores: Alexafluor-488 or Alexafluor-cy3 (Jackson). Wheat Germ Agglutinin conjugated with Alexafluor-555 fluorophore and Isolectine conjugated with Alexafluor-488 fluorophore(Invitrogen) were also used.

RNA extraction and RT-qPCR. Total RNA was extracted from heart tissue using the SV Total RNA Isolation System Z3100 (Promega), according to the manufacturer's protocol. RNA was reverse-transcribed using SuperScript III enzyme (Invitrogen), according to the manufacturer's protocol. RT-qPCR was performed with Power SYBR Green PCR Master Mix (Applied Biosystems) and run on a GeneAmp 7900HT thermal cycler (Applied

Biosystems). Relative RNA abundance was evaluated according to the method described by Pfaffl[150] with GAPDH as reference housekeeping gene, whose levels were unchanged in the experimental conditions analyzed. Primers were designed using primer-BLAST software (NCBI) and their sequences are: GAPDH fw CACCATCTTCCAGGAGCGAG rv CCTTCTCCATGGTGGTGAAGAC; MuRF1 fw ACCTGCTGGTGGAAAACATC rv CTTCGTGTTCCTTGCACATC; Kv4.2 fw CCTGGAGAAAACCACGAACC rv GACTGTGACTTGATGGGCGA; β2-AR fw TGTGTCTTTCTACGTGCCCC rv GGGCGTGGAATCTTCCTTCA.

Pharmacological sympathectomy. Pharmacological sympathectomy was obtained with 6-hydroxy-dopamine (6-OH-DA) (100 mg/kg, ip) (Sigma Aldrich). The drug was delivered at days 0, 2, and 7. Animals were sacrificed 8 and 30 days after the first 6-OH-DA injection using excess anesthesia. Control mice were treated with the vehicle (0.9% NaCl and 0.1% ascorbic acid).

Chronic treatment with drugs *in vivo*. *In vivo* drug delivery of the β2-adrenoceptor antagonist: ICI 118,551 (Sigma), at a concentration of 1 mg/kg/day, and agonist: clenbuterol (Sigma), at a concentration of 3 mg/kg/day, was achieved through the implant of osmotic mini-pumps (Alzet 1004, Alzet) in the abdominal cavity of mice. These mini-pumps were used to deliver continuously the drug for 14 days, then the mice were sacrificed and the hearts were harvested and processed as described above for histology and immunofluorescence analysis.

Evaluation of sympathetic neuron density. SNs were recognized using an antibody to Tyrosine Hydroxylase (TOH). TOH is a well-accepted marker of adrenergic cardiac neurons, since it is a rate limiting step enzyme in the biosynthesis of noradrenaline. The number of SNs per cardiomyocyte (CM) was evaluated through co-staining of TOH, to identify SN, and Wheat Germ Agglutinin (WGA), to identify CM membrane. This analysis was performed in six non-consecutive 10 μm section at the level of the heart base, the mid-portion of the ventricles and the apex.

Human samples: Human autoptic samples were provided by Prof. Cristina Basso from the Cardiovascular Pathological Anatomy department already anonymized and used in accordance with the relevant authority. The sample analyzed in this study derives from a 2-month old patient died for non cardiac related causes. The region that we used for the

morphometric analysis is the medial part of the LV. We captured the image of random fields from EPI and ENDO region of the LV and measured the cross sectional area of 1650 CMs for the EPI region and 950 CMs for the ENDO region. Measurement of SN density was performed on 3 non consecutive 5 μm sections.

Caloric restriction. Both CD1 and C57BL/6J adult male mice underwent caloric restriction for 7 days (3 gr of normal chow food/day)[1]. At day 8th mice were sacrificed, hearts harvested and processed for morphometric and molecular analyses.

Morphometric evaluation of EPI and ENDO cardiomyocyte size. The cross-sectional area of the LV EPI and ENDO CMs was evaluated in cryosections stained with an antibody specific for dystrophin. The images of six 10μm non-consecutive transversal cryosections, distributed in 600 μm, at three anatomical levels around the mid portion of the ventricles, were acquired at the fluorescence microscopy (Leica DC130, Leica Microsystems) and the image composite was performed with the software *AdobePhotoshop8.0.* For this analysis, we considered only CMs characterized by the same fiber orientation, as evaluated by the eccentricity index and the cross-sectional areas were measured both manually, by using the software *Image J* [151], and by an automatized program developed in *MatLab* (The MathWorks Inc., Natick, MA, 2000). All CMs from the posterior, lateral and anterior LV wall were evaluated and the distribution of the values of CM areas was fitted with a Gaussian approximation, considering only the values included in a 99% confidence interval. Six hearts for each study group were analyzed. Longitudinal heart cryosections were also obtained from additional subsets of animals, processed for IF as previously described and used to measure the long axis of EPI and ENDO CM.

Pseudocolor heart maps and eccentricity index. We developed heart area maps through a semi-automated program implemented in *Matlab*: the program analyses images of the whole slice of the mouse heart, segmenting and measuring the area of CMs; then the resulting image is displayed on the screen, enabling the user to specifically select the ENDO and EPI area and to remove incorrectly segmented CMs. Finally, CM area are calculated (using *regionprops* function) and at every CM is given a grayscale value that is directly proportional to its area. Images were recolored using the *Lookup Table* function in the software *Image J*. The software calculates also the eccentricity index of the segmented CMs and showed no

significant differences between the two heart zones (EPI vs ENDO: 0.771 ±0.047 vs 0.779 ±0.046).

Myocardial tissue micro-dissection. To obtain myocardial tissue separately from the EPI and ENDO regions, the LV free wall was surgically separated the from the rest of the heart, deprived of the papillary muscles, flattened and fixed on a support using 29G needles and immediately frozen in liquid nitrogen. Then using a cryostat (LEICA 1860) 20 cryosections of the thickness of 20 μm were cut and collected from the EPI region, discarding the pericardium and epicardium, and the same number from the ENDO region, here excluding endocardium. On these tissue extracts RNA and protein extraction was performed as described in the relative sections.

In Situ Hybridization. Complementary RNA probe to full length mouse MuRF1 (Trim63) was generated using standard protocols. Non-radioactive in situ hybridization (ISH) on paraffin-embedded heart sections, was performed as previously described[152]. Images were taken using a Leica DC300 digital camera and a Leica DMR microscope. All patterns in wild-type, MuRF1 KO and denervated hearts were observed in at least 3 samples.

Statistical analysis. All data are expressed as the mean±s.e.m. Comparison between the experimental groups was made by using the non-paired Student's *t* and Anova tests, with Bonferroni correction, with $p<0.05$ being considered statistically significant. * stands for $p<0.05$, ** stands for $p<0.01$, *** stands for $p<0.001$, NS stands for not significant.

PNAS PNAS

CrossMark click for updates

PNAS PLUS

Optogenetic determination of the myocardial requirements for extrasystoles by cell type-specific targeting of ChannelRhodopsin-2

Tania Zaglia[a,b,1], Nicola Pianca[a,b,1], Giulia Borile[a,b], Francesca Da Broi[b], Claudia Richter[c], Marina Campione[a,d], Stephan E. Lehnart[e,f], Stefan Luther[c,e,f,g], Domenico Corrado[h], Lucile Miquerol[i], and Marco Mongillo[a,b,d,2]

[a]Department of Biomedical Sciences, University of Padova, 35122 Padova, Italy; [b]Venetian Institute of Molecular Medicine, 35129 Padova, Italy; [c]Research Group Biomedical Physics, Max Planck Institute for Dynamics and Self-Organization, 37077 Gottingen, Germany; [d]Neuroscience Institute, Consiglio Nazionale delle Ricerche, 35121 Padova, Italy; [e]Heart Research Center Göttingen, Clinic of Cardiology and Pulmonology, University Medical Center, 37077 Gottingen, Germany; [f]German Centre for Cardiovascular Research, partner site Göttingen, 37077 Gottingen, Germany; [g]Institute for Nonlinear Dynamics, Georg-August-Universität Göttingen, 37077 Gottingen, Germany; [h]Department of Cardiologic, Thoracic and Vascular Sciences, University of Padova, 35128 Padova, Italy; and [i]Aix Marseille University, CNRS Institut de Biologie du Développement de Marseille UMR 7288, 13288 Marseille, France

Edited by David E. Clapham, Howard Hughes Medical Institute, Boston Children's Hospital, Boston, MA, and approved June 5, 2015 (received for review May 18, 2015)

This article is a PNAS Direct Submission.

[1]T.Z. and N.P. contributed equally to this work.

ABSTRACT

Extrasystoles lead to several consequences, ranging from uneventful palpitations to lethal ventricular arrhythmias, in the presence of pathologies, such as myocardial ischemia. The role of working *versus* conducting cardiomyocytes (CMs), as well as the tissue requirements (minimal cell number) for the generation of extrasystoles, and the properties leading ectopies to become arrhythmia triggers (topology), in the normal and diseased heart, have not been determined directly *in vivo*. Here, we used optogenetics in transgenic mice expressing ChannelRhodopsin-2 selectively in either CMs or the conduction system, to achieve cell-type specific, non-invasive control of heart activity with high spatial and temporal resolution. By combining measurement of optogenetic tissue activation *in vivo* and epicardial voltage mapping in Langendorff-perfused hearts, we demonstrated that focal ectopies require, in the normal mouse heart, the simultaneous depolarization of at least 1300-1800 working CMs or 90-160 Purkinje fibers. The optogenetic assay identified specific areas in the heart that were highly susceptible to forming extrasystolic foci, and such properties were correlated to the local organization of the Purkinje fiber network, which was imaged in the three-dimensions using optical projection tomography. Interestingly, during the acute phase of myocardial ischemia, focal ectopies arising from this location, and including both Purkinje fibers and the surrounding working CMs, have the highest propensity to trigger sustained arrhythmias. In conclusion, we used cell-specific optogenetics to determine with high spatial resolution and cell type specificity, the requirements for the generation of extrasystoles, and the factors causing ectopies to be arrhythmia triggers during myocardial ischemia.

INTRODUCTION

Aberrant heartbeats, caused by the ectopic depolarization of a group of cardiomyocytes (CMs), are associated with a wide range of consequences, from the commonly experienced feeling of 'palpitation' to the triggering of potentially lethal ventricular arrhythmias in diseased hearts. Physiological conduction of normal heartbeats is orchestrated by the interaction of at least two functionally and anatomically distinct population of CMs: the working CMs and the conduction system (i.e. Purkinje fibers at the ventricular level) [153]. The electrotonic coupling of myocardial cells protects the heart from abnormal excitation, allowing the effect of spontaneous activity in sparse CMs to be 'sunk' by the surrounding myocardium. As a result, a minimal 'critical' number of CMs needs to simultaneously depolarize to prevail over such protective mechanism and generate conducted beats [20,32,33,154]. When this occurs, the source-sink mismatch (abnormal depolarization current/myocardial electrotonic sink) is focally overcome, resulting in a premature ventricular contraction (PVC) that, in the presence of arrhythmogenic substrates may evolve into chaotic and self sustained ventricular arrhythmias [155,156]. In fact, ventricular tachycardia (VT) and fibrillation (VF) frequently occur in coronary artery disease during both the acute ischemic phase and the infarct evolution phase, and are responsible for most cases of sudden cardiac death (SCD) occurring yearly in the United States of America (USA) [157-159].

The tissue determinants of a focal arrhythmic source (i.e. critical cell number, topology) have so far only been estimated using biophysical modeling, suggesting that almost one million cells are required to generate ventricular ectopies in the rabbit heart [33]. Moreover, while pharmacologic approaches and single cell electrophysiological studies have suggested that abnormal activation of the Purkinje fiber network is a likely arrhythmia trigger in both acquired (e.g. myocardial ischemia) and inherited (LQTS, CPVT) arrhythmias [160-165], the role of the cardiac conduction system has not been addressed directly in the intact animal so far, mainly due to methodological constraint [166-169]. In fact, the experimental technique most commonly used to investigate cardiac electrophysiology *in vivo* is based on the delivery of electrical pulses to the epicardial surface during ECG recording [170,171]. The method, however, cannot discriminate the specific role of the conduction system cells, as they are embedded in the myocardium and not easily accessible to invasive electrophysiological investigation [169,172-174]. Optogenetics exploits the targeting

of photoactivatable ion channels in specific cell types to achieve non invasive control of membrane potential [175].

Channelrhodopsin-2 (ChR2) is a microbial derived cation channel, that, in a similar way to visual rhodopsin and bacteriorhodopsin, undergoes a conformational change upon illumination resulting in an immediate increase in ionic permeability, with high conductance to Na^+ [103,176]. ChR2 exhibits fast and reversible activation kinetics (in the order of milliseconds), that is instrumental to drive reliable trains of high frequency action potentials *in vivo*. Optogenetics is widely used in neuroscience to modulate neuronal circuits in *in vivo* models [177-179] and has been proposed as an attractive tool to control cardiomyocyte membrane potential [107,108,180-182]. In cardiac research, optogenetics is still in very early stages and has mainly been applied to *in vitro* and regenerative medicine studies [112,116,119,183,184].

We have applied optogenetics in transgenic mice with cardiac specific ChR2 expression to determine the critical cell mass necessary to generate focal ectopic beats *ex vivo*, in the isolated heart, and *in vivo*. In addition, we addressed the vulnerability of the ischemic heart to ventricular arrhythmias, in relation to the characteristics of the focal trigger. Furthermore, we exploited genetic targeting of ChR2 to Purkinje cells to interrogate the role of this cellular network in cardiac electrophysiology and arrhythmogenesis.

RESULTS

1. Non-invasive generation of cardiac ectopies *in vivo* using cardiomyocyte specific expression of ChannelRhodopsin-2.

To achieve ChR2 expression in CMs, we crossed B6.Cg-Gt (ROSA) 26Sortm27.1 $^{(CAG-COP4*H134R/tdTomato)\ Hze}$/J expressing mice with a transgenic strain encoding Cre-recombinase under the control of cardiac-specific α-Myosin Heavy Chain (α-MyHC) promoter. The resulting offspring had the STOP cassette deleted in CMs, driving the expression of ChR2 (hChR2 (H134R)-*tdTomato* fusion protein) (**Fig.S1a**). ChR2 expression was uniformly detected in heart cryosections by *tdTomato* fluorescence, and was localised at the sarcolemma and t-tubules of CMs (**Fig.1a,b** and **Fig.S1b**). ChR2-expressing mice had normal heart size, morphology, and gross electrophysiology (Heart Rate, α-MyHC-ChR2: 340±39 *vs* control: 322±9, in bpm; n=10 mice for each group, under anesthesia) (QRS interval, α-MyHC-ChR2: 12.43±0.63 *vs* control: 13.05±0.87, in ms; n=10 mice for each

group) (**Fig.S1c-d**). To obtain timely and spatially controlled photostimulation of ChR2 hearts *in vivo*, we used a fiber optic delivering 470 nm light pulses, generated by a time-controlled Light Emitting Diode (LED), in open-chest anesthetized mice during continuous ECG monitoring (**Fig.1c**). The effect of local cardiac photostimulation was mapped by delivering brief (5 ms) light pulses with the fiber tip placed close to the epicardium of different heart regions (**Fig.1d-e**). Atrial stimulation evoked supraventricular paced beats with normal QRS and wider P waves (P wave duration, basal: 14.28±0.26 *vs* left atrium photostimulation: 27.90±0.63, ms; n=15 mice). Ventricular stimulation from the heart base to the apex, in both the right and left sections, triggered beats with wider QRS complexes (QRS interval: basal 12.43±0.63 *vs* left ventricle photostimulation: 21.82±0.90, ms; n=10 mice for each group) (**Fig.1d**). Repetitive stimulation of the same myocardial focus, produced paced heartbeats that, consistent with the fixed ventricular origin, had enlarged and identical QRS morphology (**Fig.1e**). Photo-pacing could be maintained for several minutes, and sinus rhythm started promptly when illumination was interrupted, suggesting that no functional or structural damage resulted from the activation protocol. In addition, disconnection of the fiber optics tip from the light source on the epicardial surface, as well as photostimulation of WT littermates did not cause any alteration in the sinus rhythm (data not shown).

We thus demonstrated that experimentally induced ectopies can be evoked, using optogenetics, with high spatial and temporal resolution and implemented such methodology for the non-invasive investigation of cardiac electrophysiology.

2. Voltage mapping of cardiac activation in optogenetically-paced ChR2 hearts.

To address the effect of light pulses on ChR2 hearts directly at the local tissue level, cardiac optogenetics was combined with high speed optical mapping of membrane voltage, in Langendorff-perfused heart preparations. To achieve this, isolated hearts from α-MyHC-ChR2-tg mice were loaded with a voltage-sensitive membrane dye (RH1691), and additionally monophasic action potentials were also recorded by a contact electrode from the heart surface (**Fig.2a,b** and **Fig.S2**). Light pulses achieved with the same optics used for *in vivo* experiments, caused reproducible local depolarizations that, strictly within the time window of the light pulse, were confined to a tissue area corresponding precisely to the optical fiber physical diameter. Moreover, the radial intensity distribution of photostimulation light applied was overall symmetric, and well-confined within the radius

of the optical fiber, with no appreciable fluorescence changes at the margins of the photostimulation area. Further considering the dynamic range of the voltage dye and the Signal/Noise ratio of the detection system, voltage changes at the edge of the region directly irradiated were below 1 mV. Above a light intensity threshold comparable to that observed *in vivo*, optical pacing resulted in an activation pattern that was initially radial symmetric, and subsequently spread by physiological, anisotropic propagation as shown in **Fig.2c-f**. Taken together, combined measurement of optogenetic tissue activation and epicardial voltage mapping demonstrates that local light delivery to ChR2 expressing hearts activates a relatively small tissue volume, that precisely correlated with the light source, and triggers focal ectopic beats or tertiary pacemakers. These results support as a proof of principle in *ex vivo* experiments the all-optical approach to simultaneously control and record cardiac electrophysiology.

3. Direct optogenetic assessment of Purkinje fiber function *in vivo* using Cx40 driven expression of ChannelRhodopsin-2.

The Purkinje fiber network constitutes the distal ventricular conduction system, branching throughout the subendocardial cell layers of both ventricles, with a high density in the right ventricular wall. *In vitro* studies and mathematical modelling indicate that Purkinje fiber cells have unique structural and electrophysiological properties, but the direct assessment of their function *in vivo*, with conventional approaches (i.e. electrical stimulation), is limited by their subendocardial location and proximity to surrounding working CMs. To interrogate the specific role of Purkinje fiber myocytes in heart physiology, we genetically targeted ChR2 expression to the ventricular conduction system cells. Double-floxed *ChR2-tdTomato* mice were crossed with Cx40-Cre mice, previously shown to drive transgene expression throughout the conduction system cells, including Purkinje fibers, and atrial myocardium [185](**Fig.3a**). ChR2 expression was assessed by confocal imaging of the red fluorescence of *td-Tomato*, and its specific expression by Cx40 expressing cells was confirmed by immunofluorescence. ChR2 was thus detected in atrial CMs and Purkinje fibers, consistent with the expression of Cx40 (**Fig.3b-d** and **Fig.S3**). Hearts from Cx40-ChR2 mice had normal morphology and function (Heart Rate, Cx40-ChR2: 351±20 *vs* control: 335±15, in bpm; n=10 mice for each group) (QRS interval, Cx40-ChR2: 12.82±0.25 *vs* control: 12.35±0.47, in ms; n=10 mice for each group), indistinguishable from control littermates (**Fig.S4a,b**). We therefore used the photoactivation protocol described above

(**Fig.1c**) to selectively stimulate, by illuminating the epicardial surface, discrete foci of Purkinje fibers in the intact heart *in vivo*, and analyze the effects on cardiac electrical activation. Consistent with the ubiquitous expression of ChR2 in atrial cells, photoactivation of the right and left atria resulted in supraventricular pacing, with ECG morphology superimposable to that obtained in the α-MyHC-ChR2 transgenic hearts at corresponding pacing sites (**Fig.3e and Fig.S4c**). By scanning the heart surface with the fiber optic tip, the ventricular conduction system was activated at different sites, corresponding to proximal (septal) and distal regions of the Purkinje fiber network, both in the RV and LV. Consistent with the physiological characteristics of the different conduction system regions, ectopies triggered by photoactivation of the AV bundle had QRS duration identical to the spontaneous complex (Cx40-ChR2 basal QRS: 12.82±0.25 *vs* photostimulated QRS: 13.04±0.33, in ms; n=10 mice for each group) (**Fig.3f**). While stimulation of the distal Purkinje fibers of the RV yielded ectopic beats with enlarged QRS duration (photostimulated QRS duration: 23.2±0.52, in ms; n=10 mice for each group), light pulses failed to activate ectopies when delivered to the much thicker LV wall (**Fig.3e,f**).

In contrast to the uniform response to photoactivation of the α-MyHC-ChR2 ventricles, Purkinje fibers stimulation yielded highly variable effects depending on the illumination site. Ectopies were in general evoked with the stimulation of all RV regions, however, successfully coupled light pulses were almost 100% in a small (about 2 mm^2 wide) region of the lateral RV free wall (**Fig.3e,f** and **Fig.4a**), corresponding to the origin of the right ventricular outflow tract (RVOT). We thus used confocal immunofluorescence and Optical Projection Tomography in intact Cx40-GFP mouse hearts to investigate the relationship between the geometry of Purkinje fibers arborization and the response to photostimulation. The small RV hyperactivable region identified functionally with optogenetics (**Fig.4a**) was characterized by the presence of Purkinje fibers arranged in multiple cell layers (**Fig.4b**). Moreover the 3-D reconstruction of the ventricular conduction system network showed that in this region, Purkinje fibers of the RV free wall connect to the right septal branch (**Fig.4c-f**), suggesting that the increased responsiveness to local activation might be explained by the high degree of interconnection between sectors of the conduction system. Regardless of the photoactivation site or intensity, the response to RV photoactivation of Cx40-ChR2 hearts was abolished by intracavital injection of iodine/potassium iodide solution (Lugol's solution), a common strategy used to ablate Purkinje fibers [160,186-190], further proving the specificity of the Cx40-ChR2 mouse model

(**Fig.4g**). Intracavital injection of physiologic solution did not alter heart responsiveness to photostimulation (data not shown, n=5 mice for each group).

Our results show that the Cx40-ChR2 model represents a unique tool to investigate the role of the cardiac conduction system *in vivo*, using a simple experimental setup that allows accuracy and flexibility without requiring invasive approaches, i.e. endocardiac electrophysiology.

4. Selective electrophysiological study of Purkinje fibers *in vivo*.

To assess the maximal ventricular pacing rate, we photostimulated hearts with trains of light pulses delivered at incrementally shorter cycle repetition rate, from 10 to 25 Hz, and determined the threshold for 1:1 capture by analyzing the ECG trace. The α-MyHC-ChR2 hearts were responsive up to 18 Hz (1080 bpm) (n=5 mice), while the Cx40-ChR2 mice responded with 1:1 capture up to about 15 Hz (900 bpm) (n=5 mice), and above this threshold, stimulation was effective in a variable percentage of activation flashes (**Fig.5a**). These results are compatible with the increased refractoriness reported for conduction system cells with respect to working CMs. However, the Effective Refractory Period (ERP) of Purkinje fibers, has only been determined in *ex vivo* preparations [164,188,191-194], or inferred using intracavital microelectrodes to deliver electrical pulses to an area that includes, but is not limited to, the conduction system [172-174,195,196]. We thus performed non-invasive epicardial optical programmed stimulation to determine selectively the ERP of Purkinje fibers and that of the working CMs *in vivo*. The standard electrophysiological protocol of 'extrastimulus' (see **methods** and **Fig.5b**), was used for optical stimulation. In agreement with the data acquired using *ex vivo* preparations, the ERP of Purkinje fibers, measured directly *in vivo,* was significantly longer than that of the working myocardium (ERP, RV Cx40-ChR2: 59.7±1.2 *vs* α-MyHC-ChR2: 38.4±2.6, in ms; n=5 Cx40-ChR2 mice and n=10 α-MyHC-ChR2 mice) (**Fig.5c**). This latter values was indistinguishable from those obtained with conventional electrical stimulation [197].

5. Requirement for afterdepolarizations to trigger ectopies in the working *vs* conducting myocardium.

Propagation of focal arrhythmic beats in the heart occurs when the current density generated by the abnormally depolarizing CMs (current source) is sufficient to overcome the

electrotonic sink of the surrounding polarized tissue. The critical cell number needed to bring the sink to its activation threshold has never been determined directly in the intact heart. Similarly, the individual contribution of the two distinct myocyte populations (i.e. working *vs* Purkinje myocytes) has not been elucidated. Here, we exploited the ability of optogenetics to specifically control a distinct myocardial cell population, in a well-defined volume, to determine the tissue requirements for the generation of a globally spreading wavefront causing arrhythmic beats *in vivo*.

Calculation of blue light attenuation by the myocardium. The optogenetics experiments were based on the local photoactivation of ChR2 in confined myocardial volumes. Therefore, to calculate the tissue depth irradiated by light at sufficient intensity to activate ChR2, we first sought to determine the blue light attenuation coefficient of the myocardium. To this aim, the fiber optic illuminator was placed on one side of a myocardial slice and light intensity emerging across the slice was measured with a radiometer (Thorlabs GmbH, Germany). The fractional light absorption was estimated for slices of incrementally higher thickness, from 25 to 800 μm. This allowed determination of the light attenuation coefficient of the myocardium, by fitting the experimental data to the commonly used light-matter interaction model, Lambert law: $\boldsymbol{I(h) = I_o e^{-h/\delta}}$ [116,198,199], where I_0 is the light intensity at the source, h the depth in the tissue and δ is the scattering length (**Fig.6a**). Data fitting gave us a scattering length δ of 240 μm with a good coefficient of determination ($R^2 > 0.9$). The experimental data obtained for light attenuation were fitted to another light-matter interaction model, the Kubelka-Munk model [200,201] (data not shown), resulting in the estimate of the scattering parameter S = 14-20 mm^{-1} (S parameter previously calculated for the brain is 12 mm^{-1} [200]). Based on ChR2 activation threshold values, obtained by us and confirmed by others in isolated cells (1-0.5 mW/mm^2) [107,116], we were thus able to determine the depth of photoactivated ChR2 into the myocardium in each experimental condition.

The physical features of the optic fibers define an emerging light cone with an a very narrow opening angle, around 15°, which was calculated from the NA of the fiber (0.39 for all fibers with the exception of the 100 μm diameter fiber which was 0.22) and the refractive index of the myocardium (1.44, [202]). Subsequently, to experimentally assess the degree of lateral delimitation of the incident light beam and the effect of tissue light scattering, we captured the image of the light, as emerging from the myocardial slices. The analysis of the beam intensity profile indicates that, although the beam shape has the tendency to diverge

with distance from the light source, over the 90% of total light intensity was confined in a volume that can be approximated to a cylinder (**Fig.6b** and **Suppl. Fig.5**).

Optogenetic assay of the minimal myocardial volume to obtain PVCs. To quantify the relationship between the number of activated cells and the ability to generate ectopies, we then implemented an optogenetic assay based on gradually increasing the photoactivation light intensity (at the fiber tip) in differently-sized fiber optics (light intensity: 0.36 to 27 mW/mm^2; fiber tip diameter: 100 to 1500, μm).

We were thus able to control the light penetration depth (h) and width (d), respectively, thus shaping the volume of illuminated myocardium as shown in **Fig.6c**. When all CMs were photoactivated (α-MyHC-ChR2, n=10 mice), ventricular beats were triggered upon illumination of a minimal tissue volume of 12.6-18 nL (d: 200; h: 400-570, in μm) in the LV, and 5.1-5.7 nL (d: 100; h: 650-720, in μm) in the RV, that would result, when considering the average cardiomyocyte volume (10 pL) and orientation in the different cell layers, to about 1300-1800 (LV) and 511-570 (RV) cells, respectively (**Fig.6d,e**). It is likely that the differences observed in the critical tissue mass in the two ventricles may reflect the contribution of Purkinje fibers, mainly found in the subendocardial layers, to the photoactivation of the thinner RV; although a role played by the different electrophysiological properties of RV and LV CMs cannot be excluded. To more specifically establish the critical tissue requirements to generate premature ventricular contractions (PVC) upon RV stimulation, we chemically ablated Purkinje fibers using intracardiac injection of Lugol's solution in α-MyHC-ChR2 mice. In these conditions, the minimal photoactivated cell number, in the RV, increased to values comparable to those measured in the LV (RV+Lugol's solution: 1800-2300 working myocytes: d: 200, h: 570-740, in μm, n=5 mice) (**Fig.6e**). Due to the higher thickness of the LV wall, Purkinje fibers failed to be photoactivated with epicardial photostimulation. Consistently, LV intracavital Lugol's solution injection did not cause significant changes in susceptibility to photoactivation, and consequently in the minimal tissue volume required for generating an ectopic beat.

It is well established that Purkinje fibers are prone to develop early or delayed afterdepolarizations that, in turn, represent common trigger mechanisms of ventricular arrhythmias. How many Purkinje fiber cells are needed to simultaneously fire, for successful propagation of their AP into the myocardium, has not been determined so far. Thus, we calculated the minimal volume to be irradiated to evoke Purkinje fiber driven PVCs in the most responsive regions of the RV, which resulted of about (d: 200; h: 570-740, μm),

corresponding, based on our immunohistochemical quantification to about 90-160 cells (n=8 Cx40-ChR2 mice).

Collectively, our results demonstrate that ectopies can be triggered *in vivo* by the afterdepolarization of either a substantial number of working CMs, or a much lower quantity of Purkinje fibers. Although with disparities in the cell number presumably due to species differences, our findings support the concept suggested by computational modelling of the rabbit heart, whereby afterdepolarizations arising in Purkinje fibers are more likely to overcome the source-sink mismatch and trigger ectopic beats [33].

6. Optogenetic discrimination of arrhythmia trigger sites during myocardial ischemia.

Sudden cardiac death (SCD) caused by ventricular arrhythmias in the early phase of acute myocardial ischemia accounts for a large number of fatalities [157]. Ischemia induces heterogeneities in excitability, refractoriness and/or conduction that generate a permissive myocardial environment (substrate) upon which abnormal depolarizations, although uneventful in the healthy heart, may act as a trigger for self-sustained arrhythmias. What are the factors, i.e. location relative to the ischemic area, size and cell type (i.e. working *vs* Purkinje myocytes), that characterize an efficient focal trigger for sustained ventricular arrhythmias during ischemia has not been addressed directly.

To explore this, optogenetics was used during the acute phase of experimental ischemia in α-MyHC-ChR2 and Cx40-ChR2 mice. Myocardial ischemia was obtained by ligating the left anterior descending (LAD) coronary artery, during continuous ECG monitoring. The associated myocardium became immediately pale and within the first fifteen minutes, ischemia caused the expected alterations in the QRS complex (**Fig.S6**).

The susceptibility to focal arrhythmia triggering was assessed using a phostostimulation protocol consisting of a burst of ten light pulses (5 ms), at repetition rates from 10 to 20 Hz (cycle length from 100 ms to 50 ms), that was applied to a series of reference epicardial sites of the left and right ventricles (1: LV anterior, 2: LV septal, 3: lateral; 4: RV free wall, 5: septal; at basal, mid and apical regions). In both the α-MyHC-ChR2 (n=10 mice) and the Cx40-ChR2 (n=8 mice) hearts, responses to focal photostimulation were, in the initial phase (0-15 min.), similar to non-ischemic controls, with the exception of the anterior LV region, that became progressively unresponsive due to the direct effect of ischemia. Local burst activation at none of the cardiac foci resulted in sustained arrhythmias (**Fig.7a-b**) (0 out of 10 mice for α-MyHC-ChR2 and 0 out of 8 mice

for Cx40-ChR2). Fifteen-to-thirty minutes after ischemia, in α-MyHC-ChR2 mice, the identical photostimulation protocol, applied to a restricted area of the RV basal free wall, (corresponding to the junctional region between the septal and RV conduction system (see **Fig.4**)) evoked frequent episodes of non-sustained runs of polymorphic ventricular tachycardia (VT), lasting few beats after pacing in all animals analyzed (**Fig.7c, top panel**). Such behaviour was never evoked by applying the identical stimulation protocol in the Cx40-ChR2 mice (**Fig.7c, bottom panel**) (n=6 mice for each group). Interestingly, during the transitional phase to irreversible ischemic damage (45-60 min. after LAD ligation, 59-61), photostimulation of the same region of the RV triggered sustained polymorphic VT and VT/VF, lasting up to 50 s, in 8 out of 10 of the α-MyHC-ChR2 mice analyzed (**Fig.7d, top**). On the contrary, the same protocol applied to all other myocardial areas explored, outside this region, failed to evoke sustained VT/VF. Moreover, the arrhythmia protocol applied to stimulate the Purkinje fibers of ischemic Cx40-ChR2 hearts never induced sustained arrhythmias, regardless of the stimulation frequency and location (**Fig.7d, bottom**). In sham-operated mice (n=4), photostimulation, either in single pulses or in bursts, never triggered sustained arrhythmias (data not shown).

These results indicate that, during LV myocardial ischemia, the propensity of focal ectopic beats to trigger arrhythmias varies with the anatomical sites, as identical ectopies had remarkably different effect, ranging from single stimulated beats to the triggering of sustained arrhythmias. The highest arrhythmogenic potential was found for ectopies occurring in the region corresponding to the root of the RVOT, and involving both Purkinje fibers and working CMs. The depolarization of the sole Purkinje fibers was, in fact, not able to trigger sustained arrhythmias.

DISCUSSION

Most ventricular arrhythmias are caused by the combined effect of factors creating a *substrate* in the heart tissue favouring electrical instability, with events of localized depolarization in the CMs serving as *trigger* [32,33]. While great progress has been made in the identification of the mechanisms determining the pro-arrhythmogenic substrate (e.g. genetic mutations altering the single cell electrophysiology or cell-cell communication, myocardial fibrosis) [25,155,156], the fundamental requirements of arrhythmia triggers are as yet poorly understood. Cardiac optogenetics was used to define such requirements, by determining the

minimal cell number of working *vs* conducting CMs that characterize a trigger focus of ectopic heartbeats in the normal heart. The arrhythmogenic potential of such ectopies was explored during acute myocardial ischemia, a condition associated with increased arrhythmia susceptibility [158,161,162]. In this study, the optogenetic approach discriminated with high precision the location of arrhythmia trigger sites in the heart and the different cell systems involved (working *vs* conducting CMs).

Critical determinants of arrhythmogenic foci

Ectopic heartbeats are common disturbances of the heart rhythm whereby the untimely depolarization of groups of CMs, mainly due to early- or delayed-afterdepolarizations, disrupts the physiologic sequence of impulse formation resulting in premature contractions. The electrotonic coupling of the myocardium protects from the propagation of arrhythmogenic action potentials triggered by afterdepolarizations, only after a sufficient number of CMs are activated simultaneously to overcome the source-sink mismatch, an ectopic beat will occur [32,33]. Here we quantitatively studied the critical determinants of arrhythmogenic focal sources, including the minimal cell number, their cardiac topology and the type of cells involved. These aspects have, thus far, only indirectly been estimated in *ex vivo* preparations or with simulation modeling based on cellular data [32,33]. We used optogenetics that allowed the direct activation of selective cardiac cell populations expressing the photoactivable channels (i.e. ChR2 in this study) in confined regions of the heart wall, thus mimicking focal spontaneous electrical activity. As a prerequisite to our experimentation, we determined the attenuation of the blue light across the myocardial wall, by combining light penetrance data in tissue, with mathematical modelling, and were thus able to accurately control the three dimensional size of the ectopic foci. Our data demonstrated that the minimal number of CMs required to form a focal ectopic site of ventricular activation is, in the mouse heart, in the order of few thousand (from 1300 to 1800) cells. When premature depolarization was selectively induced in the Purkinje fiber cells, a much lower number of simultaneously depolarizing cells (about 100) was needed to trigger ventricular activation. This observation is in agreement with the prediction of simulation modelling [33] suggesting that, irrespective of their sensitivity to develop afterdepolarizations, a working CMs to overcome the protective effect of myocardial current *sinks,* solely due to their quasi mono-dimensional arrangement. Notably, when light pulses were delivered to this region at supra-threshold intensity, the success rate in the activation of ectopic heartbeats was close to 100%. Taken together, these results demonstrate that the

selective optogenetic interrogation of the Purkinje fibers, combined with the topological study of their distribution, informs on the structure/function relationship of this cardiac sub-system with unprecedented detail.

Triggered arrhythmias during myocardial ischemia.

Acute myocardial ischemia is a major cause of sudden cardiac death (SCD) [158,159]. The sudden cessation of myocardial blood flow causes heterogeneities in excitability, refractoriness and/or conduction. All of these factors contribute to creating the pro-arrhythmogenic myocardial *substrate* that, in the presence of ectopic excitation from focal sources, may *trigger* the lethal ventricular arrhythmias [161,203,204]. Having established the tissue determinants for the generation of focal ectopic beats, we ascertained the characteristics of focal ectopic triggers of ventricular arrhythmias potentially causing SCD, by coupling optogenetic investigation to the experimental model of acute myocardial ischemia. Central to such experimental design, the optogenetic investigation is non-invasive, and does not associate to heterogeneity in myocardial depolarization nor to tissue damage that might be caused by the production of damaging gases (Cl_2, H_2, O_2) and pH alterations, during conventional electric stimulation [205,206], especially during prolonged experiments. Focal ventricular pacing at various regions in the healthy heart could be performed even at elevated rate and for a prolonged period of time (up to 30 min), and never triggered arrhythmic episodes. Local deep tissue pacing during myocardial ischemia triggered instead several arrhythmia types, progressing from short runs of extra beats to sustained ventricular tachycardia/fibrillation, along with ischemia time. Remarkably, the longer and more complex arrhythmias were triggered by local pacing in correspondence of the right ventricular portion showing a complex organization in the terminal Purkinje fibers. Interestingly, the same structure has been identified in the human heart [207,208], and it is tempting to speculate that such anatomical organization of the cardiac conduction system network might contribute to the generation of arrhythmias triggered by ectopies arising from the RVOT, as well reported in the literature [209].

Limitations and perspectives of the study.

The study applies cardiac optogenetics to a murine model of cardiovascular pathology (i.e. myocardial ischemia) and describes the focal arrhythmia trigger determinants. The main limitation of the study is that, although the genetic restriction of ChR2 expression to atrial and conduction system cells allowed to selectively interrogate the Purkinje fiber

function, in the alternative model used the α-MyHC promoter drives ChR2 expression to all cardiomyocyte types, and not solely to the working CMs. We aimed to overcome such disadvantage by combining optogenetics with the conventional pharmacologic strategy used to ablate Purkinje fibers, in a subset of experiments. Such approach, however, could not be applied to the *in vivo* assessments during ischemia, due to the complex adverse effects of the treatment. The study methodology and the accuracy of the estimates of the cell number needed to generate PVCs relies centrally on the measurements of tissue light absorption. One limitation of such measures is that they have been performed using cardiac slices that, although freshly cut, are not physiologically perfused by the blood, which may have a modest but noticeable effect on tissue light penetration. The protocols developed in the current investigation can potentially be combined to emerging methods of voltage imaging of the heart *in vivo*, to define in higher detail the electrophysiologic effect of local photoactivation and the mechanisms of arrhythmia dynamics. We have used here a rather simple hardware setup for the photoactivation experiments in the mouse, but our preliminary investigations indicate that technical strategies allowing complex light patterns, e.g. multiple photopacing foci or delivery of complex spatial illumination patterns, can be used to mimic relevant arrhythmogenic phenotypes, including bidirectional ventricular tachycardias or spiral depolarization wavefronts. In addition, stable implant of miniaturized LED in the mouse thorax can be pursued to achieve optical stimulation of PVCs in the freely moving animal, allowing the investigation of the effects of focal ectopies in chronic disease models and the longitudinal study of drug effects.

Conclusions.

In essence, our study extended the cardiac optogenetics toolkit with a novel murine model with ChR2 expression restricted to the conduction system, and developed experimental protocols to address physiological and pathological mechanisms relevant to the understanding of cardiac arrhythmias. In perspective development, optogenetics can be employed for the study of other arrhythmia-linked genetic (e.g. LQTS, CPVT) or acquired arrhythmogenic conditions and for pharmacological research aimed at the identification and testing of antiarrhythmic compounds.

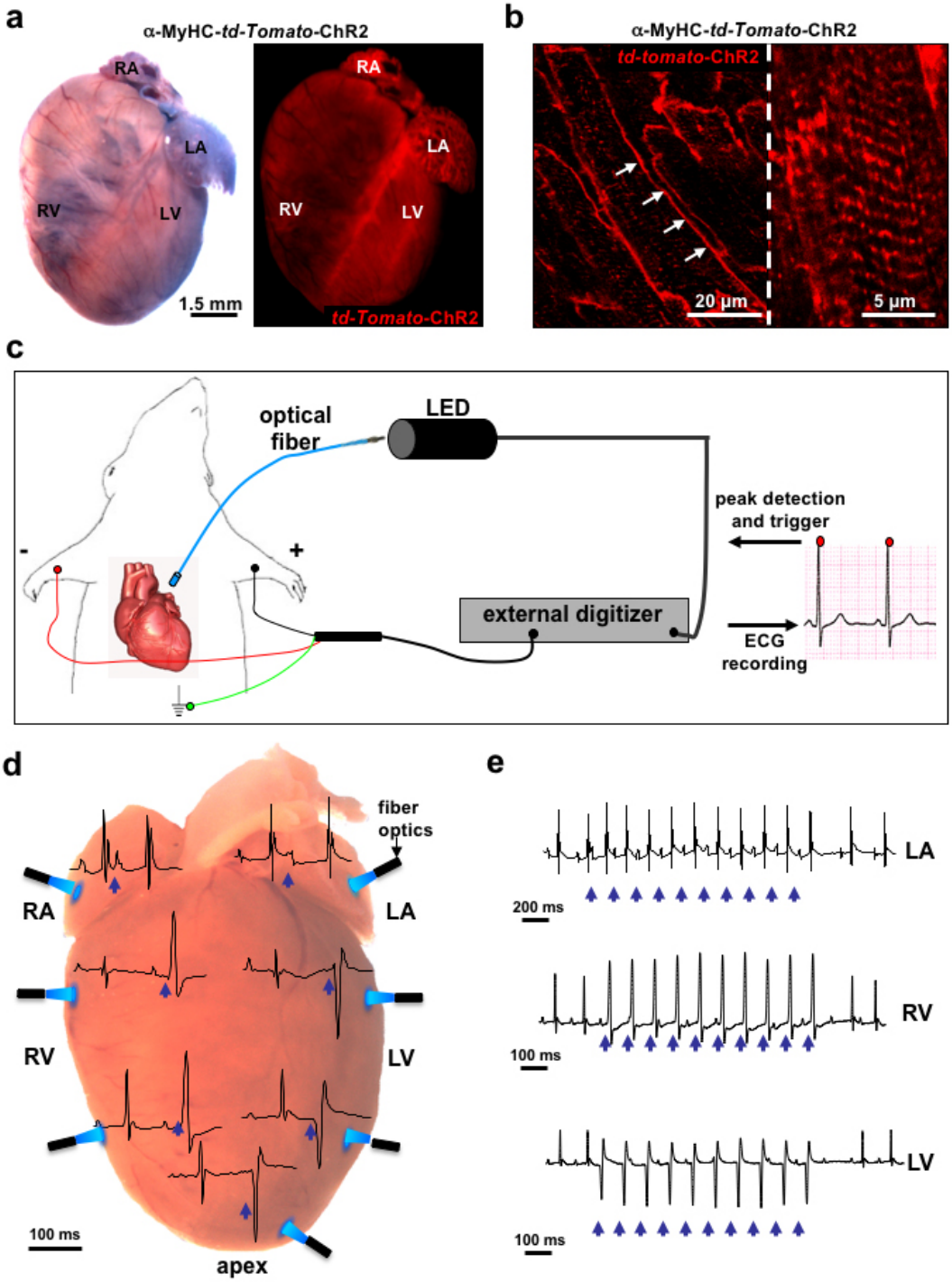

Figure 1. Cardiac optogenetics allows non-invasive investigation of heart electrophysiology *in vivo*.
(**a**) Bright field (left panel) and fluorescence (right panel) images of α-MyHC-*tdTomato*-ChR2 heart. The right image of *tdTomato* fluorescence shows expression of ChR2 in both atria and ventricles. RA, right atrium; LA, left atrium; RV, right ventricle; LV, left ventricle. (**b**) Confocal image of ventricular cryosections from α-MyHC-*tdTomato*-ChR2 transgenic hearts showing ChR2 localization at the level of cardiomyocyte sarcolemma (white arrows) and t-tubuli. (**c**) Set up used for epicardial photostimulation in open-chest anesthetized mice. LED stimulation occurred through fiber optics delivering time-controlled pulses of 470 nm blue light. (**d-e**) Representative ECG traces of ectopic beats originated by epicardial light-stimulation of different regions of the myocardium from α-MyHC-ChR2 mice (n=10 mice). Blue arrows in (**d**) and (**e**) indicate light pulses. LA, RV and LV photostimulation originates ectopic beats with different QRS shape.

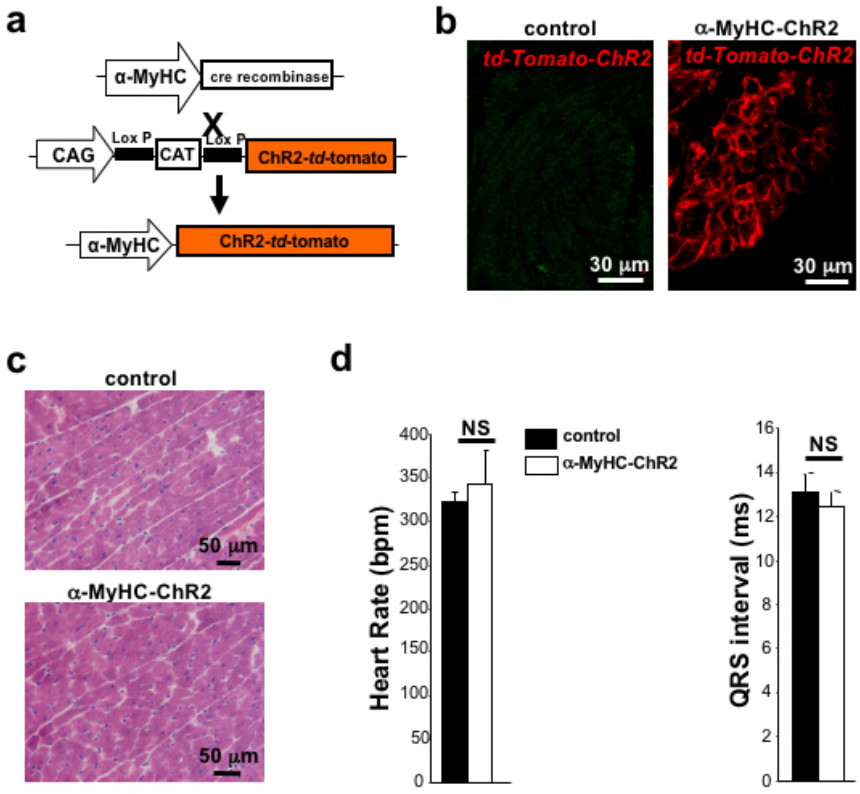

Supplementary Figure 1. Tissue specific expression of ChR2 in the heart by using the cre-lox genetic system.

(**a**) Transgenic mice expressing cre-recombinase under the control the cardiomyocyte specific promoter, α -Myosin Heavy Chain (α-MyHC), were crossed with B6.Cg-Gt (ROSA) 26Sortm27.1 $^{(CAG-COP4*H134R/tdTomato)Hze}$/J. The resulting offspring had the STOP cassette deleted in CMs, driving the expression of the hChR2 (H134R)-*tdTomato* fusion protein. (**b**) Confocal image analysis of atrial cryosections from control (left panel) and α-MyHC-ChR2 transgenic mice (right panels). (**c**) Haematoxilin-eosin staining on ventricular cryosections from control (top panel) and α-MyHC-ChR2 transgenic mice (bottom panel), showing no significant alterations in myocardial histology in ChR2 expressing hearts. (**d**) Evaluation of heart rate (in beat per minute, bpm) (left panel) and QRS interval (in ms, right panel) in control (black bars) and α-MyHC-ChR2 transgenic mice (white bars). Bars represent s.e.m. (NS, not significant; n=10 mice for each group).

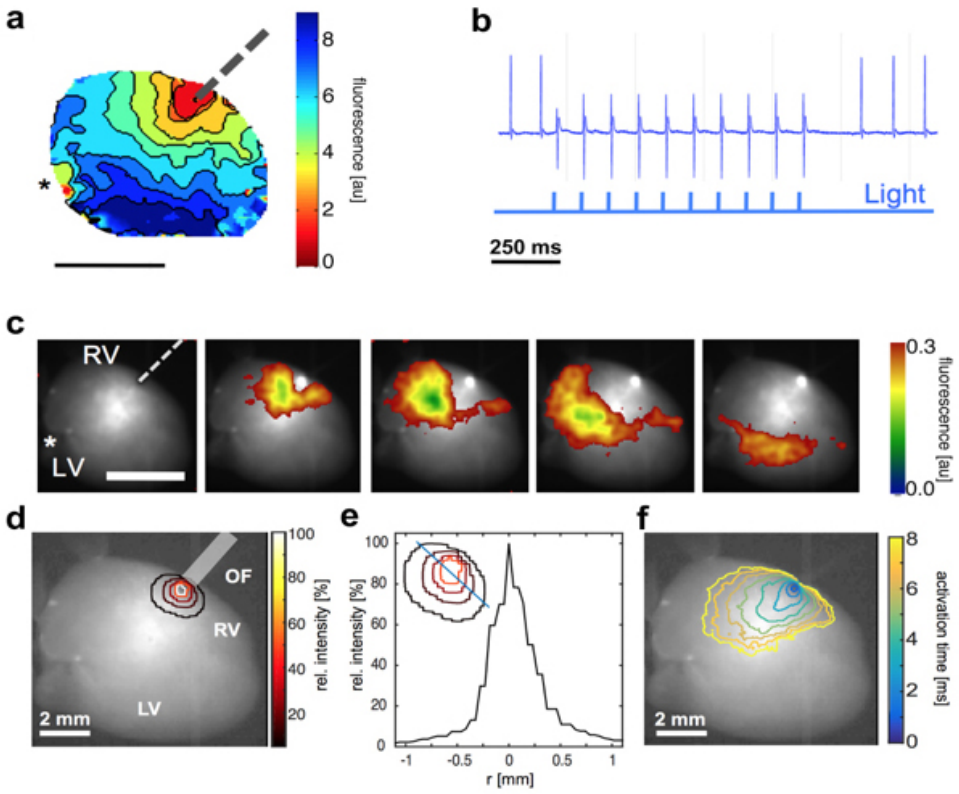

Figure 2. Optogenetics based investigation of heart electrophysiology *ex vivo*.
(**a**) Activation map of one photostimulation pulse on the RV. The dashed line indicates the stimulation fiber position. Scale bar: 0.5 cm, colorbar in (ms). (**b**) Example of monophasic potential (MAP) signal during photostimulation. (**c**) Optical mapping (Vm) of one light pulse. The fiber position is adumbrated in the first snapshot by the grey dashed line. All propagation showing snapshots are separated in time by 2 ms. Scale bar: 0.5 cm. The asterisk shows the MAP electrode position. (**d-f**) Optical measurement of photostimulation and spread of activation in a Langendorff-perfused intact mouse heart. **(d)** Intensity distribution of photostimulation using an optical fiber (OF, diameter 0.4 mm). The position of the fiber tip is indicated by the gray-shaded rectangle. The isochrones indicate the relative intensity (colors of the isochrones correspond to colorbar). RV = right ventricle, LV = left ventricle. (**e**) Cross section of the intensity distribution. The intensity profile is given along the blue line shown in the inset. (**f**) Activation map showing the propagation of wave fronts following photostimulation.

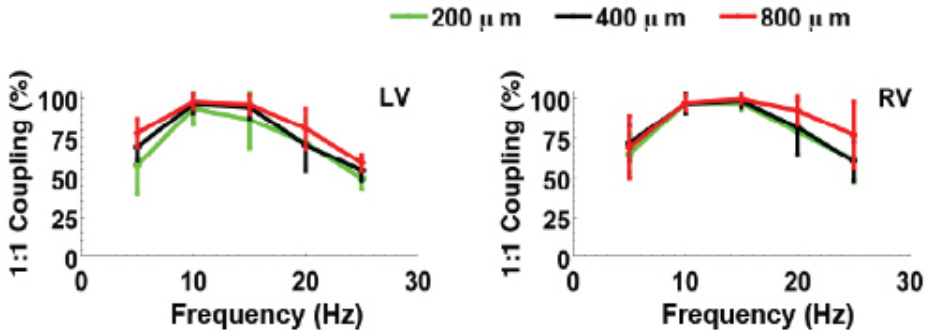

Supplementary Figure 2. *Ex vivo* photostimulation of α-MyHC-ChR2 hearts.
(**a**) Percentage of successful coupling on the left (LV, left panel) and right (RV, right panel) ventricles at different stimulation frequencies and with different sized fibers (200 µm, green; 400 µm, black and 800µm, red).

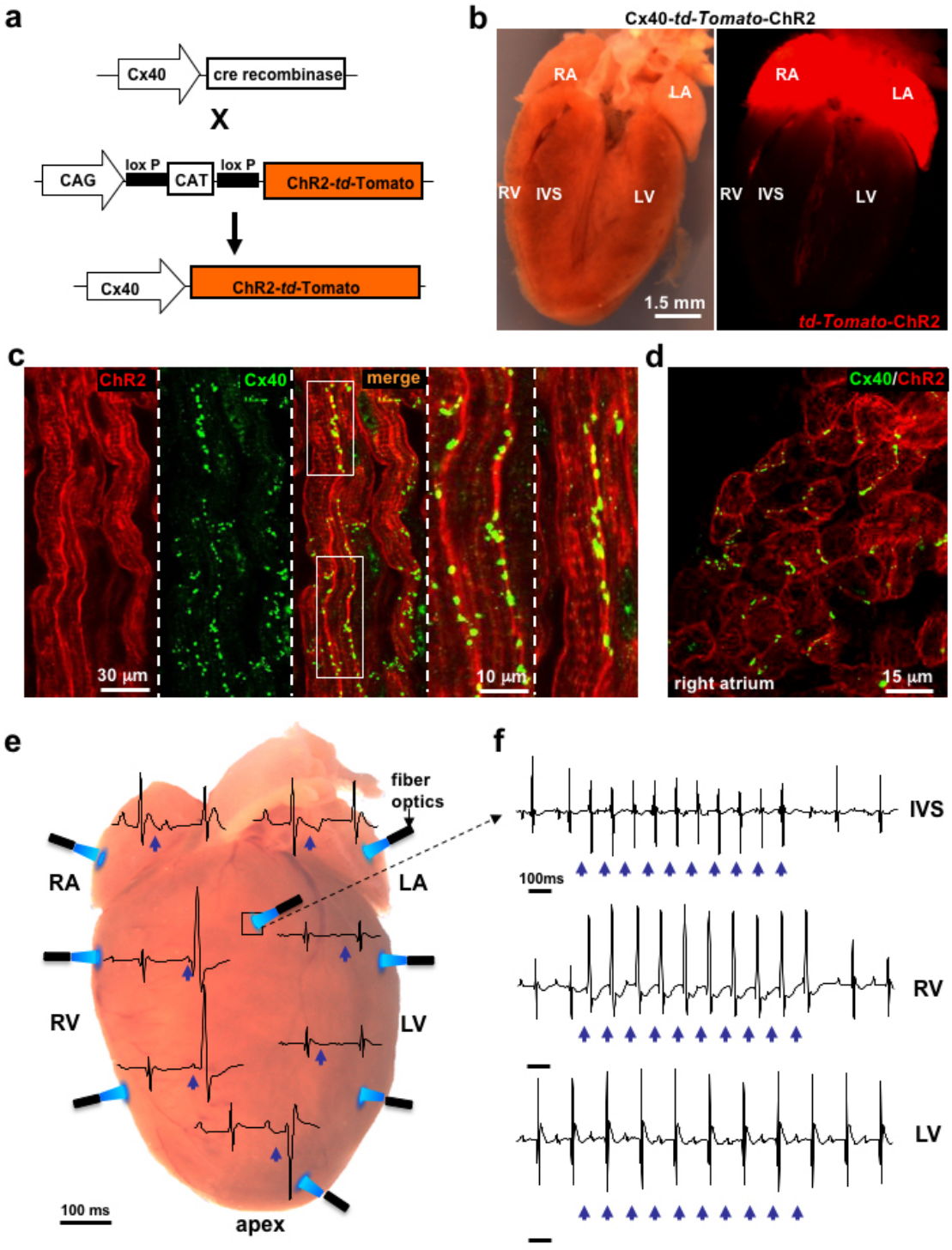

Figure 3. Direct optogenetic assessment of Purkinje fiber function *in vivo*.
(**a**) Scheme of the generation of the transgenic mouse expressing the fused protein, *tdTomato*-ChR2, under the control of Connexin-40 (Cx40) promoter, (Cx40-ChR2). (**b**) Bright field (left panel) and fluorescence (right panel) images of a longitudinally sectioned whole Cx40-ChR2 heart. The right image shows specific expression of ChR2 in the atria and the conduction system. RA, right atrium; LA, left atrium; RV, right ventricle; LV, left ventricle. (**c-d**) Confocal immunofluorescence analysis on ventricular (**c**) and atrial (**d**) cryosections from red fluorescent Cx40-ChR2 mice stained with an antibody specific for Cx40 (green signal). (**e-f**) Representative ECG traces of ectopic beats originated by epicardial photostimulation of different regions of the myocardium from Cx40-ChR2 mice (n=8 mice). Blue arrows indicate light pulses. RV and IVS photostimulation originates ectopic beats with different QRS shape in all mice, while LV epicardial stimulation always failed to induce ectopies.

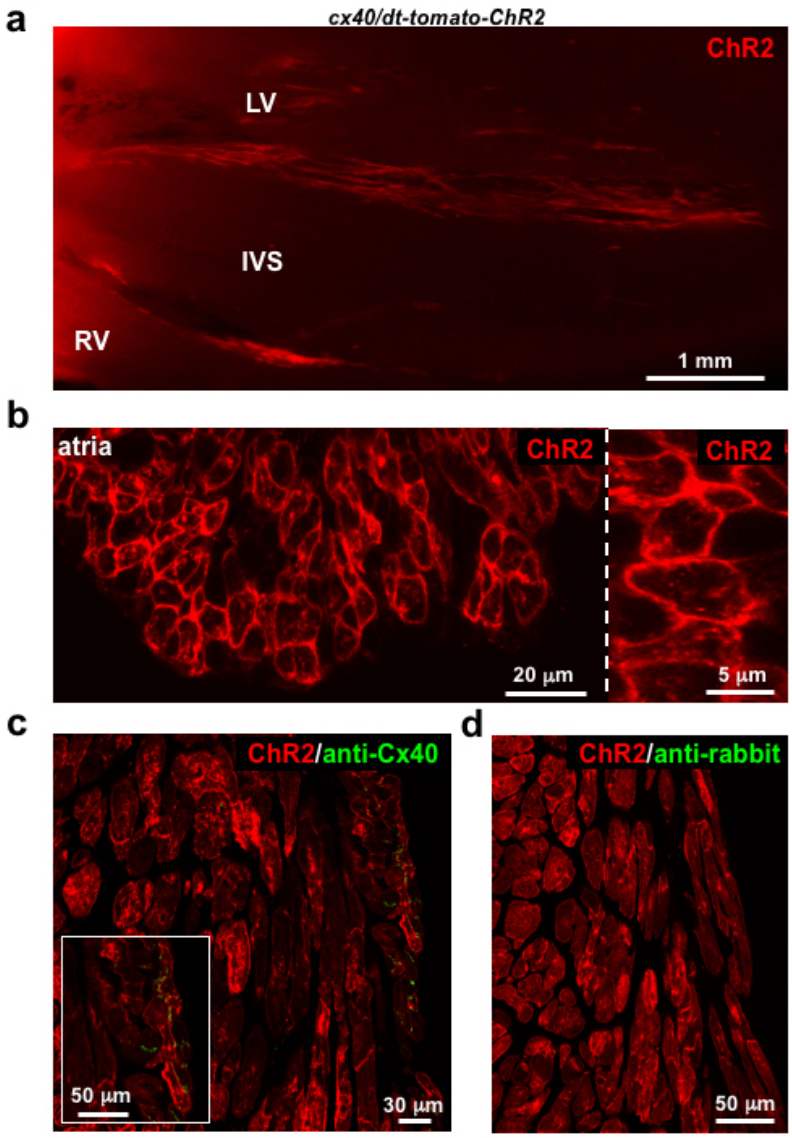

Supplementary Figure 3. Selective expression of ChR2 in conducting cardiomyocytes.
(**a**) Hearts from a Cx40-ChR2 transgenic mouse were cut longitudinally and slices were analyzed at the fluorescence stereomicroscope. The image evidences the presence of ChR2 expressing bundles in the interventricular septum (IVS), as well as in the right ventricle (RV) subendocardium. ChR2 positive fibers can be detected in the left ventricular (LV) wall. (**b**) Confocal image analysis of atrial cryosections from Cx40-ChR2 transgenic mice. (**c**) Confocal immunofluorescence analysis on ventricular cryosections from a α-MyHC-ChR2 transgenic mouse stained with an antibody to Cx40. The red signal is the fluorescence of *td-Tomato-ChR2* expressing cells. The green signal, indicating the expression of Cx40, is specifically restricted to the subendocardial layers of Purkinje Fibers. (**d**) Confocal immunofluorescence analysis on ventricular cryosections from a α-MyHC-ChR2 transgenic mouse stained with a 488-conjugated anti-rabbit secondary antibody. The red signal is the fluorescence of *td-Tomato-ChR2* expressing cells. The absence of the green signal indicates no a-specific staining of the secondary antibody.

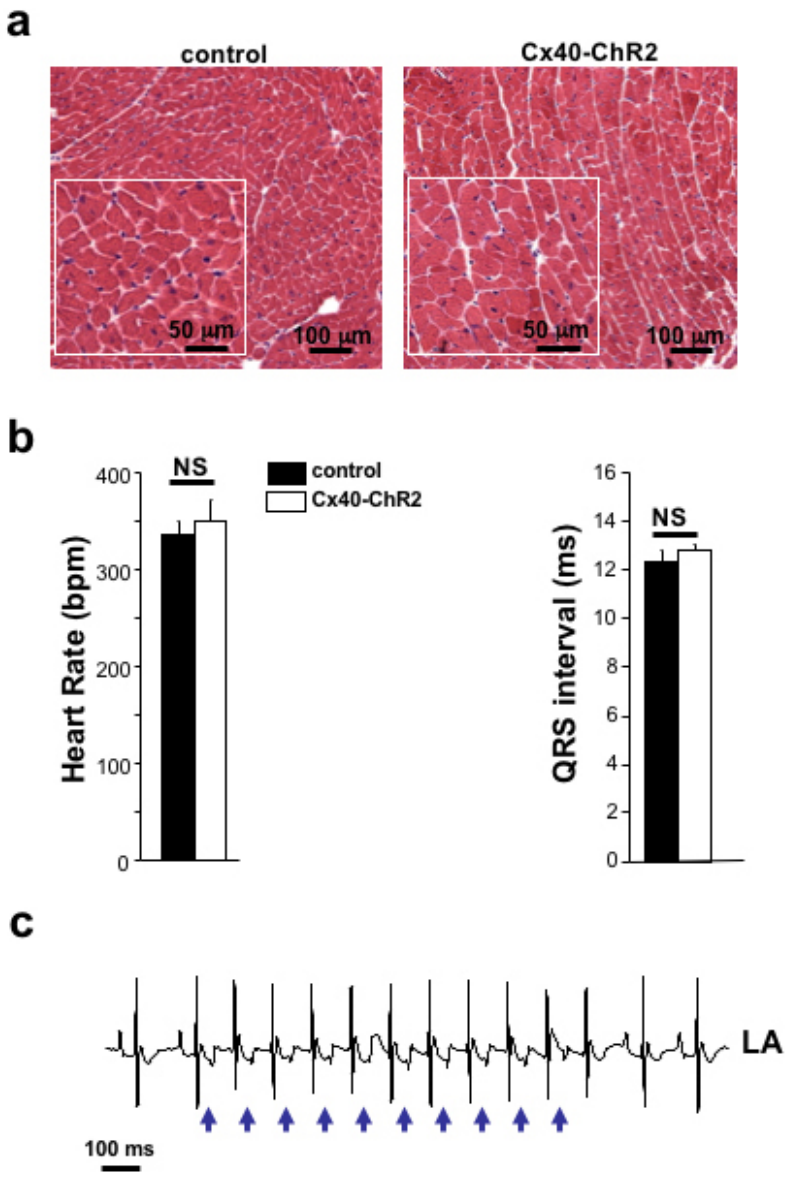

Supplementary Figure 4. ChR2 expression in the cardiac conduction system does not affect heart morphology and function.
(**a**) Haematoxilin-eosin staining on ventricular cryosections from control (left panel) and Cx40-ChR2 transgenic mice (right panel). (**b**) Evaluation of heart rate (in beat per minute, bpm) (left panel) and QRS interval (in ms, right panel) in control (white bars) and Cx40-ChR2 transgenic mice (black bars). Bars represent s.e.m. (NS, not significant; n=8 mice for each group). (**c**) Representative ECG trace of ectopic beats originated by epicardial light-stimulation (10 Hz) of the left atrium (LA) from Cx40-ChR2 mice (n=8 mice). Blue arrows indicate light pulses (5 ms).

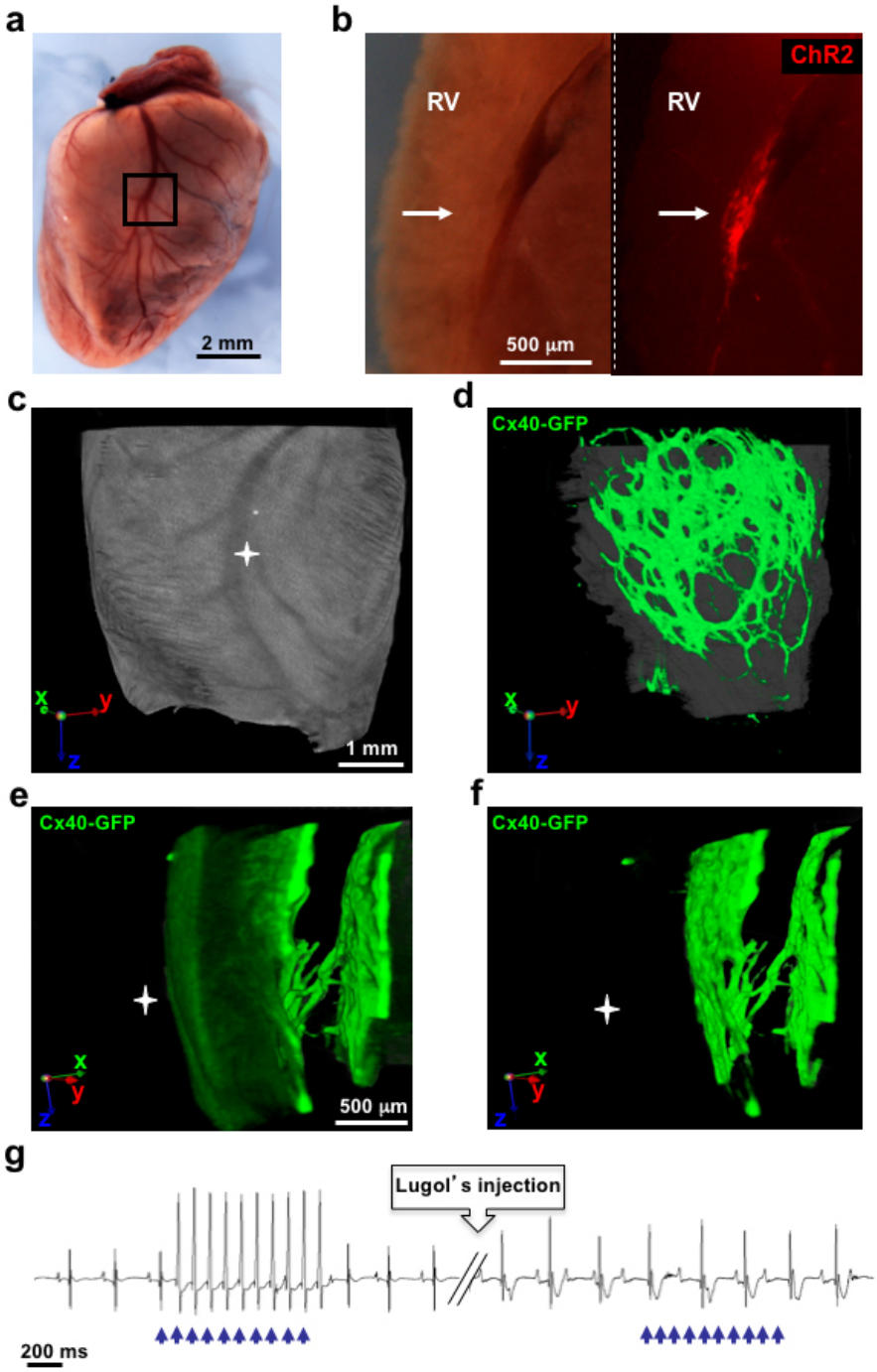

Figure 4. Correlation between distribution and function of the Purkinje fiber network in the right ventricle.

(a) RV epicardial surface of Cx40-ChR2 heart. The black box indicates the RV region with the highest responsiveness to photostimulation. (**b**) Bright field (left panel) and fluorescence (right panel) images of the RV section at the anatomical level enclosed in the black box in (**a**). (**c-f**) Three-dimensional reconstruction of the RV Purkinje fiber arborization obtained in Cx40-GFP transgenic mice by optical projection tomography. Images in (**e,f**) highlight the connecting bundle between septal and the right ventricular branches of PF. **(g**) Representative ECG traces of ectopic beats originated by epicardial light-stimulation of the RV from Cx40-ChR2 mice before and after (15 min) RV intracavital Lugol's solution injection (n=5 mice). Blue arrows indicate the light pulses. Lugol's solution treatment caused enlargement of the QRS complex and abolished light induced ectopies in all mice analyzed.

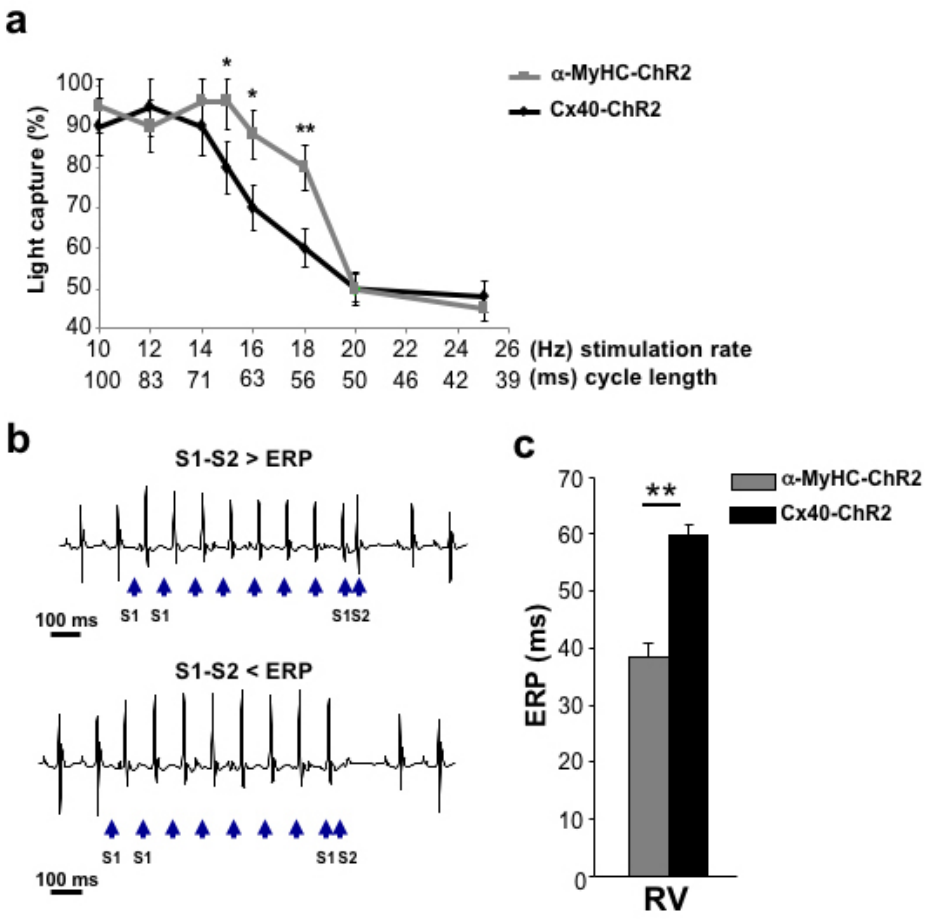

Figure 5. Optogenetics allows selective interrogation of Purkinje fiber electrophysiology *in vivo*.
(**a**) Stimulation rate/cardiac capture relationship obtained in α-MyHC-ChR2 and Cx40-ChR2 mice. Bars represent s.e.m. (*, $p<0.05$, **, $p<0.01$; n=5 mice for each group). (**b**) Optical programmed stimulation using the extrastimulus (S1-S2) protocol to measure the effective refractory period (ERP). Blue arrows indicate the light pulses. (**c**) Evaluation of the ERP in the RV of both α-MyHC-ChR2 (grey bar) and Cx40-ChR2 (black bar) mice. Bars represent s.e.m. (**, $p<0.01$; n=10 α-MyHC-ChR2 mice and n=5 Cx40-ChR2 mice).

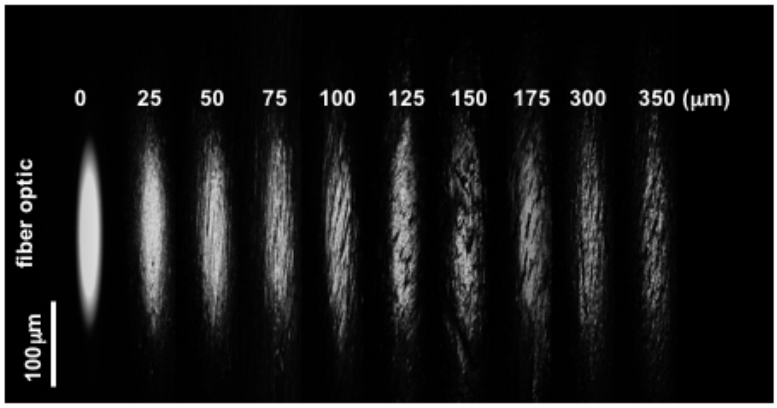

Supplementary Figure 5. Estimation of the shape of the light penetrating the myocardial tissue.
Shape of the light emitted by a 200 μm optical fiber as it emerges from myocardial slices of different thickness.

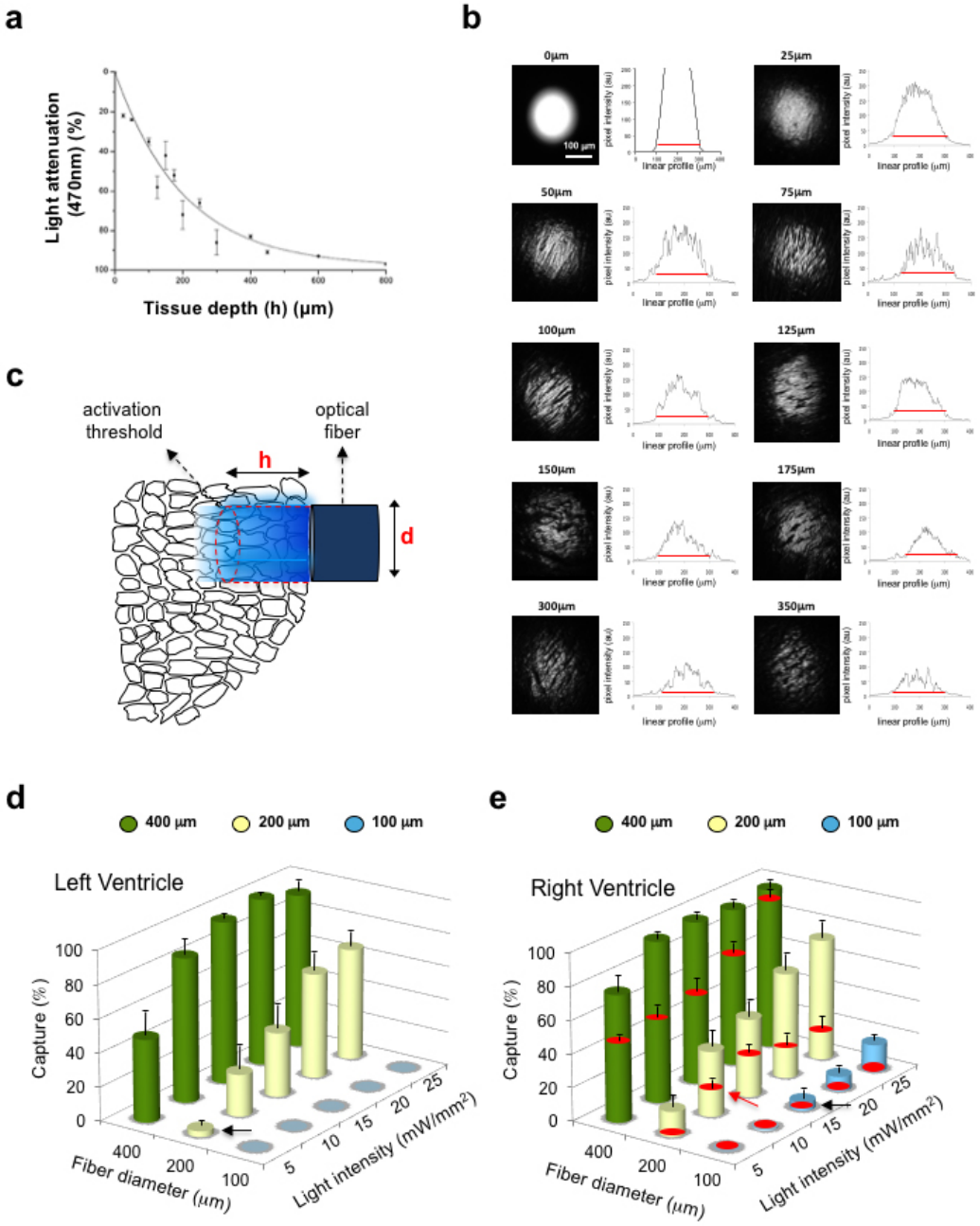

Figure 6. Optogenetic assay of the minimal myocardial volume required to trigger focal ectopic beats in the normal myocardium.

(**a**) Measure of 470nm light penetrance into the ventricular myocardium upon epicardial illumination. Experimental data were fitted to a monoexponential decay function (R^2>0.9) [200], shown with solid line. Bars represent s.e.m. (n=10). (**b**) Images of the optical fiber's light beam, as emerging from myocardial slices of incremental thickness. For each image the beam intensity profile is shown; the red bar indicates the diameter of the optical fiber (**c**) Modulation of light intensity and fiber diameter shapes depth (h) and width (d), respectively, of the illuminated myocardial cylinder. (**d-e**) Optogenetic assay of minimal myocardial volume required for successful trigger of ectopies in the LV (**d**) and RV (**e**). The red circle in the columns in (**e**) indicates the percentage of successfully captured beats after Purkinje fiber ablation with Lugol's solution. Black arrows in (**d**) and (**e**) indicate the liminal tissue volume to be irradiated to evoke ectopic beats. Red arrow in (**e**) indicates the liminal tissue volume after Lugol's solution injection in the RV. Bars represent s.e.m. (measures repeated in triplicate, in n=10 mice).

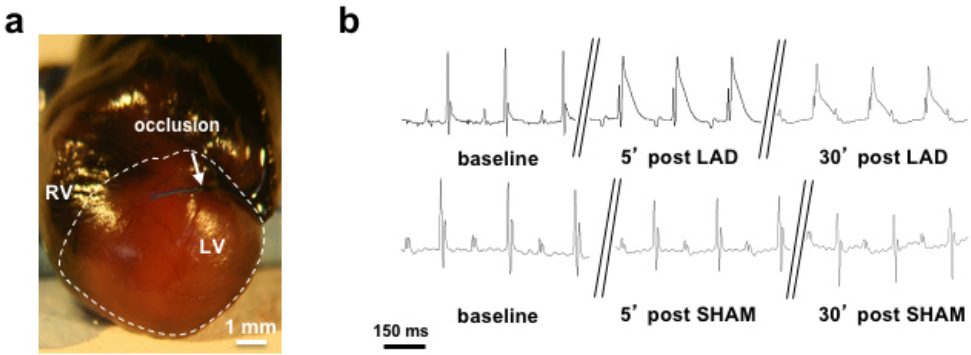

Supplementary Figure 6. Left descending coronary artery ligation in α-MyHC-ChR2 mice.
(**a**) Image of a whole heart from a α-MyHC-ChR2 undergone left anterior descending (LAD) coronary artery ligation and subsequent intravenous injection of Evans Blue, to identify the ischemic pale area. White arrow indicates the coronary ligation. LV: left ventricle; RV: right ventricle. Scale bar: 1 mm. (**b**) Representative ECG traces from α-MyHC-ChR2 transgenic mouse at baseline, 5 and 30 minutes after LAD ligation. ECG recording evidences alterations of the QRS complex upon ischemia, which are absent in sham operated mice at the same time point.

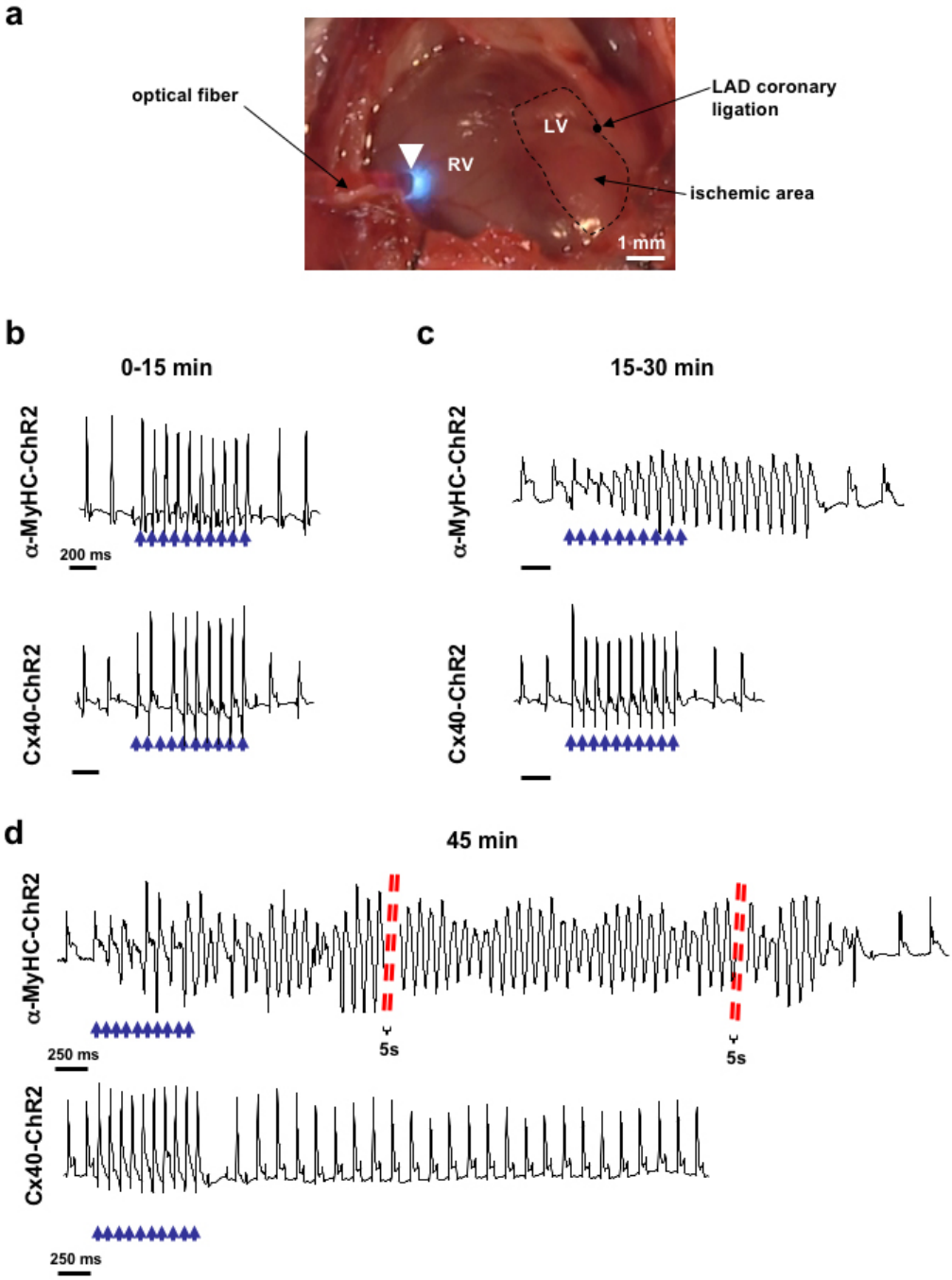

Figure 7. Induction of sustained ventricular arrhythmias by optical stimulation in the advanced post ischemic phase.

(**a**) Photograph of the optogenetic experiment, picturing the heart of the anesthetized mouse, seen through the toracotomic window, during delivery of a light pulse to the RV epicardium via the optical fiber. The white arrowhead shows the region described in **Fig.4c-f**. (**b**) ECG traces of RV photostimulation during the first 15 minutes after LAD ligation in α-MyHC-ChR2 (top panel) and Cx40-ChR2 (bottom panel) hearts (n=10 and n=8 mice, respectively). (**c**) ECG trace recorded between 15 and 30 minutes after LAD ligation in α-MyHC-ChR2 (top panel). Photostimulation of the origin of the RVOT induced episodes of un-sustained polymorphic ventricular tachycardia. (bottom panel) ECG trace recorded 15 to 30 minutes after LAD ligation in Cx40-ChR2 mouse. (**d**) (top panel) ECG trace of sustained arrhythmias originated by light-stimulation of the RV, at the site indicated above, in α-MyHC-ChR2 during post-ischemic phase 2. Sustained arrhythmias were induced in 8 out of 10 mice. The same photostimulation protocol failed to trigger sustained arrhythmias in Cx40-ChR2 mice (n= 8 mice) (bottom panel). Blue arrows indicate the light pulses**.**

MATERIALS AND METHODS

Mouse models. For *ex vivo* study, we used transgenic adult (3 mo.) male mice expressing the hChR2(H134R)-*td*Tomato fusion gene under the control of alpha-Myosin Heavy Chain α-MyHC) promoter; mice were backcrossed into the C57B6J background. For in vivo study, transgenic adult male mice, with a genetic background C57B6J, expressing cre-recombinase under the control of either α-MyHC or Connexin-40 (Cx40) promoter were bred with B6.Cg-Gt(ROSA)26Sor$^{tm27.1(CAG-COP4*H134R/tdTomato)Hze}$/J expressing mice (Jackson Lab. Bar Harbor, Maine, USA). The resulting offspring has the STOP cassette deleted in the heart, resulting in cardiomyocyte (α-MyHC-ChR2) or Purkinje fibers (Cx40-ChR2) expression of the hChR2(H134R)-*td*Tomato fusion protein. Both α-MyHC-cre$^{+/-}$ and Cx40-cre$^{+/-}$ lines were used to maintain the colonies. Hearts from cx40-GFP transgenic mice were also analyzed [210]. All experimental procedures described in this manuscript have been approved by the local ethical committee (Authorization number C54) and communicated to the relevant Italian authority (Ministero della Salute, Ufficio VI), in compliance of Italian Animal Welfare Law (Laws n 116/1992, D.Lgs 26/2014 and subsequent modifications).

Optical Mapping. The electrical activity of hearts of transgenic channelrhodopsin-2 (ChR2) mice was visualized in Langendorff isolated perfused hearts, via epicardial voltage mapping. To eliminate cross-talk between stimulating light and fluorescence emission the dye RH1691 [40 μM] was used, which has a deep red emission spectrum. The recording system consisted of the commercially available microscope MVX10 (Olympus, Germany) and the MiCam camera system, which allows to record with a framerate of up to 1 kHz at a spatial resolution of 100 × 100 pixel. As light source for the photostimulation a High Power LED with an emitting peak wavelength of 470 nm was coupled to multimode optical fibers (Thorlabs GmbH, Germany) with decreasing diameters (∅ 1000 μm, 800 μm, 400 μm and 200 μm). The LED was triggered via a high power, 1-channel LED driver with pulse modulation (Thorlabs GmbH, Germany).

***In vivo* epicardial photostimulation.** Adult ChR2 expressing transgenic male mice and littermate controls were anesthetized by isoflurane administration (1,5%-3%), secured to the table in supine position and intubated with a 24G needle for ventilation (tidal volume 0.4

ml; 120 strokes/min) from an artificial ventilator (SAR-830). Body temperature was monitored constantly during the experiment. The skin was dissected by a lateral sub-ascellary 1.5 cm cut, subcutaneous muscles were removed and a 0.5 cm incision was performed at the level of the 4th intercostal space. Self-retaining microretractors were then used to separate the 3rd and 4th ribs enough to get adequate exposure of the operating region. The heart was exposed and different epicardial regions from the atria and the left and right ventricles were stimulated by differently-sized (from 100 to 1500 diameter, in μm) fiber optics (Thorlabs, Germany), coupled to a 470 nm LED (Thorlabs, Germany), controlled by an ECG-coupled recording system (Powerlab 8/30, LabChart 7.1 software; AD Instruments). Trains of 5 ms light pulses were delivered with a cycle-length of 100 ms, with the exception of the burst stimulation used for the study of arrhythmia triggering.

ECG recording and analysis. A standard lead I ECG was recorded (Powerlab 8/30, Bioamp; AD Instruments) during the experiment. ECG parameters (QRS, PR interval and heart rate) were calculated by using LabChart 7.1 software (AD Instruments).

Measurement of The Ventricular Effective Refractory Period (VERP). The VERP of both the working CMs and Purkinje fibers was evaluated in α-MyHC-ChR2 and cx40-ChR2, respectively, by using the extrastimulus technique [211,212]. The epicardial surface of the right ventricle was photostimulated by a train of 10 light pulses (5 ms), at a frequency of 10 Hz (cycle length = 100 ms) (**S1**), followed by a premature optical stimulus (**S2**) at progressively shorter coupling interval until the S2 failed to trigger an ectopy at the VERP (see **Fig. 5b**).

Burst photoactivation protocol. Brief trains of 5 ms light pulses were delivered to a fixed epicardial region with repetition rates ranging from 10 Hz to 25 Hz (cycle length: 100 ms to 40 ms). For each experiment, stimulation was delivered to five reference regions at the heart base and mid portion, that specifically were: 1: LV anterior, 2: LV septal, 3: lateral; 4: RV free wall, 5: septal. The apex was considered separately.

Pharmacological Purkinje fibers ablation. Ten μl of Lugol's solution (5% (wt/v) iodine and 10% (wt/v) potassium iodide, in distilled water) supplemented with an equal volume of Heparin (all from SIGMA), was carefully injected into either the RV or the LV cavity by using a Hamilton syringe supporting a 34G needle. To increase permanence of Lugol's

solution in the ventricles, the pulmonary artery or the aorta were transiently clamped (about 10 s).

Optical Projection Tomography. Hearts from Cx40-GFP transgenic mice were analyzed as previously described in [28].

Left anterior descending (LAD) coronary artery ligation. The main trunk of the LAD coronary artery was ligated under microscope guidance, by using a 7/0 polypropylene suture [213]. Epicardial photostimulation was performed at different time points (from 5 to 90 minutes) after coronary occlusion, during constant ECG recording.

Measurement of blue light attenuation in the myocardium. Hearts from both control and ChR2 expressing mice were harvested and the left and right ventricular walls dissected. Intact ventricles, as well as longitudinally cut ventricular slices of different thickness were placed in contact with the light sensor of a power meter (Thorlabs, PM100D). The same fiber optics used in the *in vivo* experiments were used to determine tissue light attenuation, by illuminating the slices while measuring the emerging light intensity with the power meter. Emerging light intensity was measured for each fiber diameter (from 100 to 1500 μm), at varying light intensities (from 0.36 to 27 mW/mm^2), and all these measures were performed in slices of different thickness (from 25 to 800 μm) . Myocardial light attenuation was modelled by adapting previous studies made in the brain [200]. Briefly, values of light intensity experimentally determined using the tissue phantoms described above were fitted to a monoexponential decay curve to extrapolate light intensity as a function of the depth from the epicardial surface. Light intensity threshold for ChR2 activation were obtained from [107,116]. To determine the lateral discrimination of the illuminating beam in the myocardium, slices were imaged through a modified inverted microscope (Nikon eclipse 200) equipped with a 2048x1024 pixel CCD detector (Hamamatsu, Japan), to acquire the image of the fiber optic carried 470 nm light, as emerging through myocardial tissue samples of incremental thickness. In each image the shape, brightness, pixel intensity distribution, intensity linear profile were calculated using image analysis software (ImageJ, Wayne Rasband, NIH, Bethesda, USA).

Tissue samples and immunofluorescence analysis. The hearts were harvested from transgenic, as well as control mice, fixed in 2% paraformaldehyde (PFA) (Sigma) for 1 hour

at room temperature, equilibrated in sucrose gradient at 4°C, embedded in OCT and frozen in liquid nitrogen. Ten-micron myocardial sections were obtained with a cryostat (Leica CM1860) and processed for histological and immunofluorescence analyses. Immunofluorescence analysis was performed as described in [1] . Rabbit anti-cx40 (1:200, Invitrogen) and AlexaFluo antirabbit-488 (Jackson) was used. Sections were analyzed with a Leica TCS SP5 confocal microscope.

Tamoxifen treatment. Adult (3 month) Cx40-ChR2 transgenic mice were injected with Tamoxifen (Sigma) (100 mg/kg, ip.) for 5 consecutive days. Mice underwent *in vivo* ChR2 photostimulation two weeks after the conclusion of the pharmacological treatment. Tamoxifen delivery was also performed in a subset of α-MyHC-ChR2 mice leading to exclude that such treatment causes *per se* alterations in cardiac activity or affects arrhythmias susceptibility.

Evans blue staining. A subset of control and ChR2 transgenic mice were injected, upon LAD coronary ligation, with 1% Evans Blue (Sigma) (w/v) in phosphate-buffered saline (PBS, pH 7.5) sterilised by passage through a 0.22 μm filter (Millipore). Intravenous injections were made to either of the dorsal veins of the tail. Thirty minutes upon injection, mice were sacrificed, the hearts were harvested and fixed in 4% paraformaldehyde (PFA) o.n. at 4°C.

Statistical analysis. All data are expressed as the mean±s.e.m. Comparison between the experimental groups was made by using the non-paired Student's *t* and Anova tests followed by Bonferroni correction, with $P<0.05$ being considered statistically significant.

Optogenetic interrogation of cardiac sympathetic neurons shed light on the "neuro-cardiac junction".

(manuscript in preparation)

Collaborators: *Tania Zaglia, Francesca Da Broi, Anna Pia Plazzo, Valentina Prando Mauro Franzoso and Marco Mongillo*

ABSTRACT

Rationale: The heart is innervated by sympathetic neurons that regulate cardiac function during exercise or stress through the release of norepinephrine (NE) activating β-adrenergic receptors. Abnormal sympathetic activity is involved in the development and progress of cardiovascular disease. In this context, it is important to understand whether and how sympathetic neurons (SNs) communicate with cardiomyocytes (CMs).

Objective: To investigate the characteristics of the interaction between SNs and CMs and its functional outcome in the context of the physiological role of SNs in the modulation of heart rate in the intact heart.

Methods and Results: Co-cultures between rat neonatal sympathetic neurons and ventricular CMs were set up as an *in vitro* model of neuro-cardiac interaction. Neurons develop adrenergic phenotype, in the presence of NGF, and extend processes forming synapsin1-enriched varicosities contacting different CMs. By means of a live imaging FRET-based approach we observed that neuronal depolarization lead to intracellular cAMP and PKA activity increase specifically in innervated CMs. A single neuron action potential released an amount of NE sufficient to initiate cAMP signaling, that remained confined in the coupled cardiomyocyte. Optogenetic stimulation of SN innervating sinoatrial node *in vivo* resulted in an increase in heart rate with fast and repeatable kinetics, supporting the hypothesis of a specialized interaction SN-CM.

Conclusions: SNs develop 'cardiac synapses' with target CMs to provide fast, economic and repeatable modulation of cardiac function.

INTRODUCTION

Sympathetic neurons modulate cardiac function to match the perfusional demand of the organism through the release of NE that, by activating CM β-ARs, triggers the cAMP-dependent increase in heart rate and contraction force, a phenomenon called "fight-or-flight" response. NE activates adenylyl cyclase producing the second messenger cyclic AMP (cAMP) and leading to activation of PKA in the cAMP/PKA pathway. PKA mediates its functional effect by phosphorylating several cytoplasmic and nuclear targets involved in the increase in force and frequency of heart contraction. Thanks to many FRET-based biosensors developed in the recent years, it has been possible to monitor cAMP variations in real time in living cells, highly improving the knowledge of intracellular cAMP dynamics in CMs. This response is characterized by a fast and repeatable outcome and this contrasts with the traditional model of SN modulation of cardiac activity, which relies on the paracrine effect of NE released by SN into the myocardial interstitium. However, whether sympathetic control of heart function occurs through the activation of a fraction of the receptors localized at the neuro-cardiac interaction site or through the activation of all the receptors localized in the cardiomyocyte membrane is still debating. In literature there are growing amount of evidence in favor of a different model, in which a direct contact between SNs and CMs is described, resembling a sort of "neuro-cardiac junction". Electron microscopy analysis demonstrated that in SN-CM co-cultures, neurons form varicosities containing synaptic vesicles along their axons 20-30 nm from the cardiomyocyte surface[127,214], and that SNs activation modulates neighboring CM beating rate[129]. More recently, it has been shown that there is an accumulation of anchoring and signaling proteins at the portion of CM membrane adjacent to sympathetic terminals, supporting a model in which the neuro-cardiac interaction occurs through a well-organized structure similar to the neuromuscular junction[131]. Although these structural evidence point in the direction of a neuro-cardiac junction, the functional implication of this interaction, so far, have been poorly characterized *in vitro* and has never been directly proved *in vivo*.

In this study, we sought to use an *in vitro* model of SN-CM co-cultures, coupled to state-of-the-art live cell imaging to monitor in real time the adrenergic signaling occurring in a single neuron-cardiomyocyte couple. Moreover, we developed a novel optogenetic approach to test the functional implications of this interaction *in vivo*. This tool is based on the expression of the photo-activated cation channel ChannelRhodpsin-2 (ChR2) in the

adrenergic neurons of the heart, under the control of the promoter of tyrosine hydroxylase (TOH) gene.

The understanding of the mechanism of SN-CM interaction is of great clinical relevance since local cardiac innervation impairment has been associated to a growing amount of pathological situations, such as myocardial infarction, diabetes and different types of cardiomyopathies.

RESULTS

1. Intercellular signalling between sympathetic neurons and cardiomyocytes

SNs innervate abundantly the ventricular myocardium of mammals, in particular what we observed from IF analysis on ventricular cryosections of mouse heart is that SN terminals, stained with synapsin-I, are closely juxtaposed to CM membrane, suggesting that a direct contact between SN terminals and CMs occurs (**Figure 1a-c**). Moreover. EM analysis highlighted the presence of some features that suggest the existence of a specialized interaction between SN varicosities and CMs, such as polarization of the neurotransmitter vesicles, thickening of the membrane and reduced intermembrane space (**Fig. 1d-e**). To analyze at single-cell level the dynamics of the intercellular coupling between SNs and CMs, we used co-culture of primary neonatal rat superior cervical ganglia neurons and primary neonatal rat ventricular CMs. SNs in culture extended processes and interacted with surrounding CMs forming discrete contact sites corresponding to synapsin I-enriched neuron varicosities (**Fig. 1g**). Consistent with previous reports, the majority of neurons in the culture were adrenergic, as shown by immunoreactivity for anti-dopamine-β-hydroxylase antibodies, a specific marker of adrenergic neurons, being the last enzyme involved in the biosynthesis of NE (**Fig.1f**). Moreover, EM analysis of SN-CM co-cultures showed the same characteristic features observed in the myocardial sections at the intersection between SN varicosities and CMs (**Fig.1h**). We thus exploited real-time fluorescence imaging of intracellular cAMP in CMs to analyze the dynamics of the response to the activation of the coupled neuron, with the attempt to mimic *in vitro* the interaction occurring *in vivo*. To this aim, CMs in co-culture with SNs were transfected with the FRET-based cAMP sensor Epac1-camps[215] (**Fig.2**). In Epac1-camps expressing CMs, an increase in intracellular [cAMP] is expected to decrease FRET efficiency between the CFP and YFP moieties

flanking the cAMP-binding site in the Epac1-camps protein. Therefore, by monitoring the variation of CFP/YFP emission upon CFP illumination, changes in [cAMP] (*i.e.* upon NE administration, **Fig.2b**) can be estimated in real time, with high spatial and temporal resolution. Epac1-camps expressing CMs had normal cell morphology and spontaneous contraction rate. In the co-culture a number of CMs interacted with neurons that developed axonal varicosities at the contact site (**Fig. 2a.1, arrowheads**), while others were passed over by neuronal processes that did not show apparent changes in morphology (**Fig. 2a.2**). To activate the neurons and elicit NE secretion from sympathetic terminals, the cells were briefly depolarized with a solution containing 50 mmol/L KCl perfused in the bathing solution. Depolarization of SNs in co-culture induced an increase in intracellular [cAMP] in coupled CMs with a $\Delta R/R_0$ = 5.10 % ± 0.42 (n=16) (**Fig. 2c**, *i.e.* a cell as depicted in **Fig. 2a.1**, and **Fig. 2e**) and a $t_{1/2}$ of 20.42 s ± 1.88 (n=16). The same treatment did not activate cAMP signaling in the CMs not interacting directly with neuronal terminals in the co-culture (*i.e.* a cell as depicted in Fig. 2A.2, $\Delta R/R_0$ = 1.62 % ± 0.35, n=7, **Figure 2d and 2e**) as well as in CMs cultured without neurons ($\Delta R/R_0$ = 0.61 % ± 0.17, n=15, not shown). All groups showed comparable cAMP responses to direct application of NE (NE 10 nM, $\Delta R/R_0$: 14.98 % ± 1.54, n=16, coupled to sympathetic neurons; 16.45 % ± 2.59, n=6, uncoupled to sympathetic neurons; 15.59 % ± 1.79, n=12, CMs alone). Addition of the cell bathing solution, collected after neuronal depolarization, to Epac1-cAMPs expressing CMs was not able to induce any cAMP response, indicating that the [NE] in the bulk medium was too low to activate β-ARs (not shown). To investigate whether the cAMP cascade is confined only in the innervated CMs, we focused on small clusters of isolated CMs in the co-culture, that showed a SN process innervating only one CMs of the cluster. Then we stimulated the neuron with KCl and monitored cAMP variation both in the innervated CM and in the adjacent non-innervated ones (**Fig.2f**). Interestingly, only the innervated cell showed intracellular cAMP increase that did not propagate to a coupled CM (**Fig. 2g**).

To probe the efficiency of the cellular neuro-cardiac system, we used shorter neuron stimulation protocols to gradually decrease neuronal activation. To achieve this, a micropipette containing a 50mM KCl solution was placed in proximity to the soma of the SN. By modulating the injection time and pressure, the system was calibrated to obtain a controlled number of action potentials in the neuron (**Fig.3a-b**). Stimulation of a single AP evoked a reproducible cAMP increase in the target cardiomyocyte, with a $\Delta R/R_0$ of 1.56 % ± 0.20 (mean ± SEM, n=6), a rapid onset (2.08 s ± 0.74) (**Fig.3c-d**), and fast kinetics (time to half maximal amplitude: 3.43 s ± 0.59 (n=6)).

Collectively, these results indicate that SNs establish functional contacts with CMs and suggest that communication between the two cell types is exerted at the contact site.

2. Generation of the transgenic mouse expressing ChannelRhodopsin-2 in sympathetic neurons: *in vivo* and *in vitro* characterization

To investigate the functional implications of the direct contact between SNs and CMs *in vivo* we exploited the specificity and selectivity of cardiac optogenetics, through the generation of a transgenic mice expressing ChR2 in SNs. To achieve the expression of ChR2 selectively in adrenergic neurons of the heart we crossed transgenic mice expressing *Cre* recombinase under the control of the promoter of TOH (B6.129X1-$Th^{tm1(cre)Te}$/Kieg) with transgenic mice harboring in their genome the ChR2 variant H134R flanked by *LoxP* sites (B6.Cg-Gt(ROSA)26Sortm27.1(CAG-COP4*H134R/tdTomato)Hze/J). The resulting offspring expressed ChR2 only in SN expressing TOH. We characterized the animals for basal heart activity parameters (ECG) and histology and they showed a phenotype undistinguishable from control littermates (TOH-$Cre^{+/-}$). Moreover, also the morphology and pattern of SN expressing ChR2 is undistinguishable from control littermates (**Fig. 4**)

Before moving to *in vivo* photostimulation experiment, we characterized SNs from transgenic mice by culturing them *in vitro*. SNs were isolated from the superior cervical ganglia of TOH-ChR2 mice, and maintained in culture for several days, their morphology was undistinguishable from that of cultured SNs, isolated from WT mice. SNs isolated from transgenic mice expressed ChR2 at a high level and with a correct membrane localization, as shown by of tdTomato fluorescence (**Fig.5a-b**). Whole cell voltage clamp demonstrated activation of the typical ChR2 photocurrent upon illumination of the cells with 470nm light focused on the cells through the microscope objective (**Fig.5c**). The effect of optical stimulation on the neuronal membrane potential was assessed using the current clamp configuration. The activation of ChR2 inward current by a brief (10 ms) light flash, caused SN membrane depolarization, sufficient to trigger a neuronal action potential, with identical kinetics of a spontaneous occurring one (**Fig.5d**). These results indicate that ChR2 is successfully expressed in peripheral sympathetic neurons in the TOH-ChR2 mouse, enabling the control of neruonal activation using non-invasive optical stimulation with 470nm light.

2. Photostimulation of sympathetic neurons innervating sinoatrial node *in vivo*

The experimental setup used for optogenetic stimulation of SN innervating the heart, is similar to the one described in our previous study[120] (see **Results**), where we used optogenetics to interrogate working and conducting CMs. Briefly, we anesthetized the mouse, attached it to an artificial ventilator and opened a surgical window between the 1st and 2nd ribs with thoracotomy, through which the optical fiber was inserted into the thorax. The illumination site was identified with the help of the surgical stereo-microscope. Continuous ECG recording was maintained during the stimulation, for real time measurement of HR. The optical fiber was coupled to an LED emitting 470 nm light. Brief flashes of light (10 ms) were used to photostimulate the neurons, in the forms of a single pulse, multiple pulses or trains of pulses characterized by a different inter-pulse distance, that we defined as frequency of stimulation.

We decided to stimulate SN processes directly at the level of sinoatrial node (SAN), not at their cell bodies in the ganglia, in order to dissect only the effect of SN activation on heart rate, among the various effects of SNs on heart activity. SAN is the pacemaker of the heart and it is highly innervated by SNs (**Fig.6a**), whose activation determines an increase in SAN automaticity, which outcome is an increase in HR. To test the feasibility of our approach, we performed a first proof-of-principle photostimulation of SNs using a train of light pulses with 20 Hz frequency, based on our previous *in vitro* data. This attempt resulted in an increase in HR, which lasted the duration of the stimulation and then rapidly went back to the HR showed before stimulation (**fig.6b top panel**). To asses if this response was due to the induction of an aspecific arrhythmic event, we analyzed the ECG parameters during photostimulation (QRS duration, p wave-QRS correlation) and we demonstrated that these are compatible with a standard increase in the frequency of sinus rhythm (chronotropy). Having demonstrated the feasibility of our approach, we decided to screen different types of photostimulations to characterize SN modulation of HR. First we used trains of light pulses with fixed-number of pulses and gradually decreased the frequency of stimulation, from 20 Hz to 5 Hz. What we observed is that we were always able to elicit an increase in HR with all the different stimulation, and that the kinetics was only slightly different (**Fig.6b**). Then we wanted to find out which was the minimal number of stimulations needed to elicit a change in the HR, and to do that we fixed the frequency of stimulation and we gradually reduced the number of pulses. The result obtained was that just 2 light pulses are sufficient to generate a single shorter sinus beat (**Fig.7a**). This result showed that only 2 depolarizing

stimuli in the SNs are sufficient to trigger an increase in the automaticity of target SAN cells, consistently with our findings in the *in vitro* model. This result demonstrates the high efficiency and precision of SN modulation of heart frequency, having the possibility to interfere with HR at the level of the single beat.

Based on these evidence, and on IF analysis on SAN innervation, that showed how SNs are closely associated to pacemaker cells (**Fig.6a**), what we would expect from *in vivo* photostimulation experiments, is that the delay between the light pulse and the onset of the first shorter sinus beat (measured at the start of the p wave) was short (**Fig.7a**). Indeed, we measure a mean value of 44±3 ms, which is fully compatible with the hypothesis that the sympathetic-releasing terminals are in direct contact with the 'postsynaptic' cardiomyocyte membrane, much faster than the activation time that would require the simple release and diffusion of the neurotransmitter, that would be almost an order of magnitude higher[214]. Moreover, we found that trains of photostimulations made of 20-40 pulses, can be repeated up to 10 times during a time window of 2 minutes, without apparent changes in the kinetics of the hear rate increase (**Fig.7b**). This result is a clear sign of the highly repeatable nature of this mechanism, which could be possible only if the release of the NE is limited to a restricted space between SN releasing site and CM membrane and the mechanisms for avoiding its spillover into the myocardial interstitium are tightly regulated, as in the case of a specialized junctional site.

DISCUSSION

The adrenergic neurons innervating the heart are responsible for the continuous adjustment of cardiac performance, through activation of β-ARs, occurring in both the daily activities and in acute stress as part of the *fight-or-flight* response. Whether the neuronal control of heart activity occurs through a direct coupling between the NE-releasing varicosities along the neuronal axon and the target CMs remains a debated topic in the literature (REF). Indeed, although it has been shown in SNs-CMs co-cultures that the distance between synaptic terminal and CM membrane is in the order of 80 nm[127] and that the junctional site between the two cells is characterized by specialization of both the pre- and post-synaptic membranes[131], the functional role of the apposition of the two membranes in the signal transmission from the SN to the CM remains largely unexplored.

In this study we examined SN-CM interaction signaling, performing real-time live imaging with FRET-based biosensors, to explore the effects of this interaction at the subcellular level. We demonstrated that minimal activation of sympathetic neurons (*i.e.* one action potential) triggers cAMP pathway exclusively in the target CMs, leading to cAMP elevation and PKA phosphorylation. We did not observe significant increase of cAMP in non-innervated CMs, suggesting that β-ARs activation in coupled cardiac cells is due to NE released by the innervating neuron and not to NE released in the bathing solution by all depolarized-neurons in culture. This hypothesis was confirmed by stimulating CMs with neuronal-conditioned medium, where any intracellular cAMP increase was detected (data not shown), suggesting that the concentration of NE released by stimulated neuron in the culture medium is too low to lead an β-AR activation sufficient to elicit a cAMP rise, essential in the modulation of cardiac contraction. Our model shows that the neuro-cardiac interaction forms a structure that allow to control cardiomyocyte intracellular signaling with high efficiency, where only one releasing event (i.e. one action potential, **Fig.3c**) is sufficient to evoke a repeatable cAMP increase in the coupled cardiomyocyte (**Fig.3d**). Such event remained confined only in the innervated cell (**Fig.2g**), supporting the hypothesis that neuron/cardiomyocyte interaction is specialized contact, and the regulation of heart activity by sympathetic nervous system occurs through a specific cell-to-cell signalling.

Then to test the functional outcome of a direct interaction between SNs and CMs *in vivo*, we exploited a novel optogenetic approach. The results of the optogenetic stimulation of SNs innervating SAN showed a rapid increase in HR upon stimulation and a rapid decrease after the end of stimulation, a short delay between the stimulation and the response and that multiple subsequenet stimulation are possible resulting always in HR increase with the same kinetics. These results are consistently with our *in vitro* data and demonstrate, in the intact heart, the existence of a *quasi-synaptic* interaction between SNs and CMs, that allows a fast, repeatable and efficient control of heart rate at the level of SAN.

In this study, we provided the first example, to the best of our knowledge, of *in vivo* optogenetic stimulation of SN processes innervating the heart. The only other example of optogenetic stimulation of cardiac SNs present in literature, is a work recently published by the group of Kay[216] in which they used the *ex vivo* model of Langendorff isolated and perfused heart. They observed that isolated heart responded to optogenetic stimulation of SN processes with an increase in HR and contraction force, however this system is highly questionable since in isolated hearts, the SN processes are deprived from their cell bodies that are located in sympathetic ganglia.

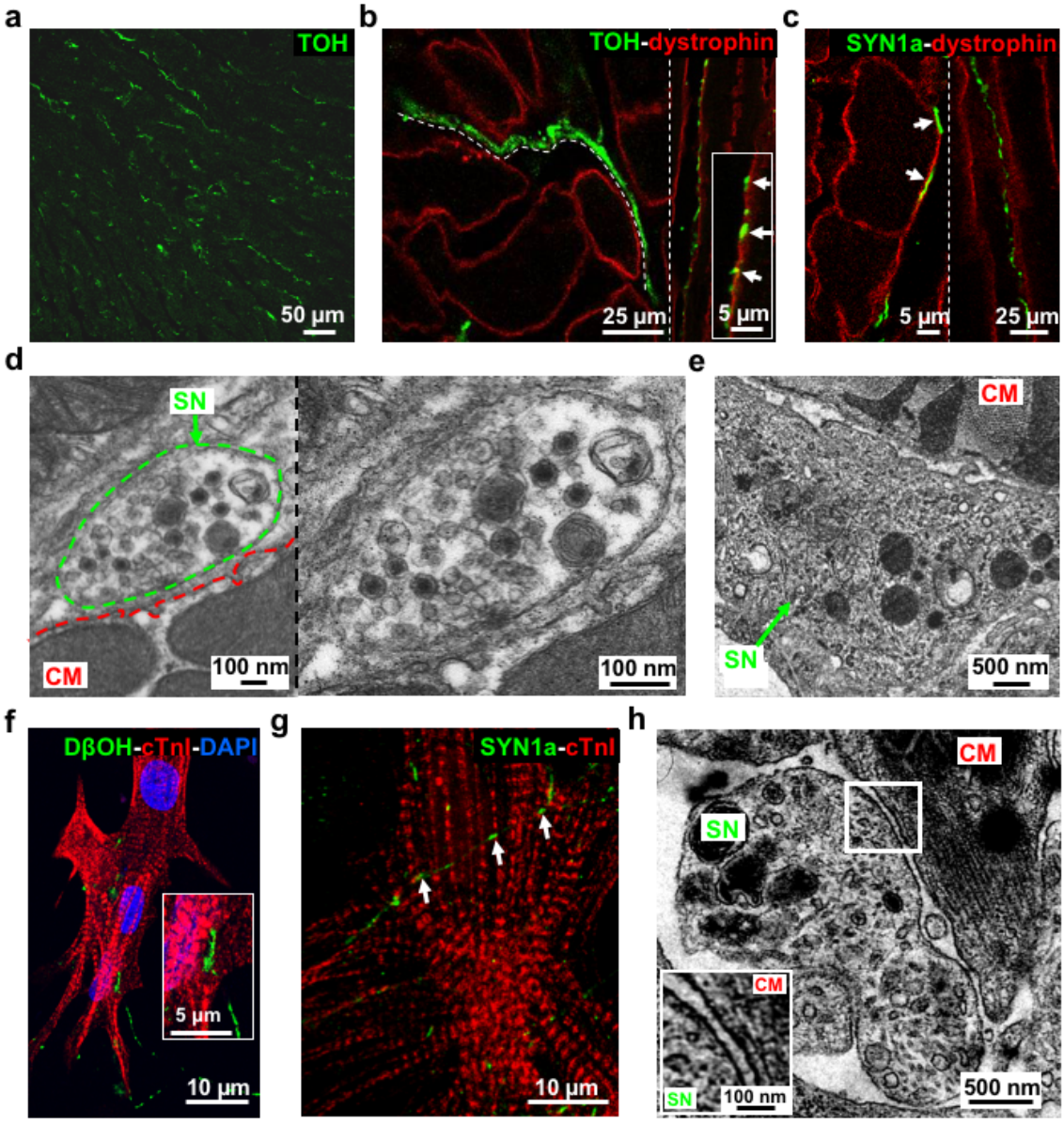

Figure 1. Sympathetic neurons establish close interactions with target cardiomyocytes both *in vivo* and *in vitro*.

(**a**) Confocal immunofluorescence analysis on ventricular cryosections from adult mouse heart stained with an antibody to tyrosine hydroxylase (TOH, green signal). The image shows a detail from the left ventricular wall. (**b-c**) Confocal immunofluorescence analysis on ventricular cryosections from adult mouse heart co-stained with an antibody to dystrophin (red signal) and either TOH (**b**) or synapsin1a (**c**, SYN1a) (all green signals). Arrows evidence the close contact between cardiac SN varicosities and CM membrane. (**d-e**) Electron microscopy analysis on semi-thin ventricular sections from adult normal mouse heart. The images highlight the strict interaction between SN varicosities (green line) and target CMs. The red line indentifies the CM membrane. (**f-g**) Confocal immunofluorescence analysis on seven-day SN-CM co-cultures. CMs were stained with an antibody to cardiac troponin-I (cTnI, red signal), while SNs were identified by antibodies specific for: dopamine-β-hydroxylase (**f**, DβOH) and SYN1a (**g**) (all green signals). Nuclei in (**f**) were counterstained with DAPI (blue signal). The high magnification in (**f**) shows the SN-CM strict contact. White arrows in (**g**) evidence SN varicosities interacting with a target CM. (**h**) Electron microscopy analysis on semi-thin sections from SN-CM co-cultures, showing that SNs establish a close contact with CMs, similar to that observed in heart sections.

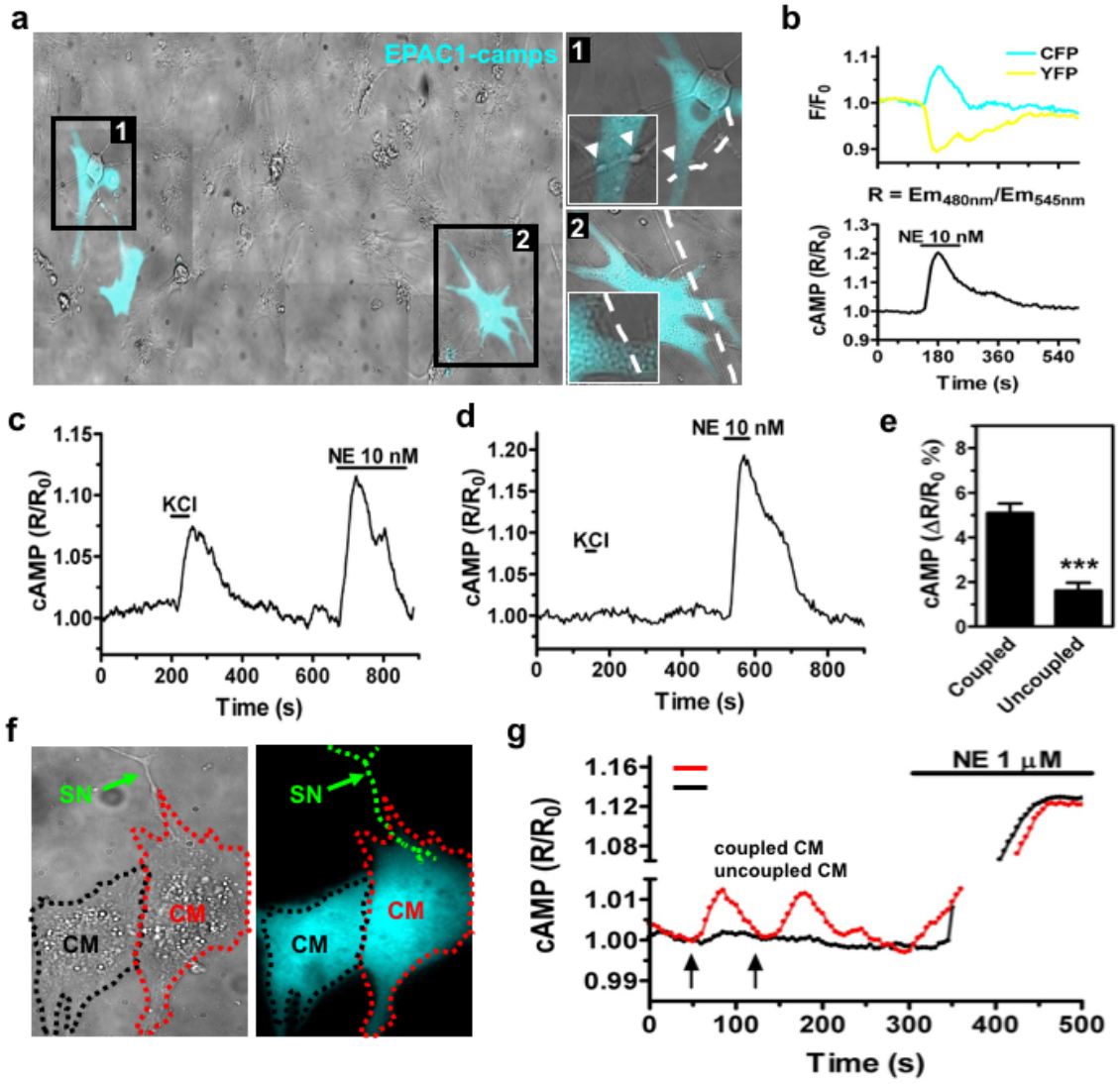

Figure 2. Norepinephrine released upon sympathetic neuron depolarization initiates cAMP signaling selectively in target cardiomyocytes.

(a) Bright field and fluorescence image analysis of a SN-CM co-culture in which CMs were transfected with the FRET-based cAMP sensor Epac1-camps (light blue signal). The higher magnifications show, respectively, a CM contacted by SN process varicosities (1, arrows), and a non-innervated CM (2). The white lines in (1 and 2) show the SN processes. Note in (2) that the CM is passed by a SN which does not establish a structural contact with the CM. (**b**) EPAC1-camps expressed in neonatal CMs allowed to monitor intracellular cAMP variation. Upon NE administration, binding of intracellular cAMP induces a decrease in FRET efficiency expressed as ratio between the 480 nm/535 nm emission signals (R) over the value at t =0 s (R_0). (**c-d**) Evaluation of cAMP increase in the Epac1-camps expressing CMs, upon SN depolarization induced by 50 mmol/L KCl. The trace in (**c**) refers to the CM contacted by a SN shown in panel A1, while the trace in (**d**) shows the response of the not-contacted cell in A2. SN depolarization induced an increase in cAMP concentration only in the innervated CM (**c**). NE (10 nM) addition to the cell bath was performed at the end of the experiment, as positive control, and evoked the same response in both the CMs analyzed. (**e**) Quantification of cAMP increase observed in coupled and non-innervated CMs in co-culture with SNs upon neuronal depolarization. (**f**) Bright-field (left) and fluorescence (right) images of two adjacent EPAC1-camps expressing CMs. The green line indicates a SN contacting only one of these two cells. The innervated CM is surrounded by a red line, while the not innervated one is identified by a black line. (**g**) Selective stimulation of the SN innervating the CM in (**f**, red line) was obtained by a puff of KCl (black arrows). Variations in cAMP concentration were evaluated in both coupled and uncoupled cells. Interestingly, increase in cAMP concentration occurred only in the innervated CM. NE was administered at the end of the experiment as positive control. Bars indicate s.e.m. (***$p<0.001$; n=20 CMs for each group).

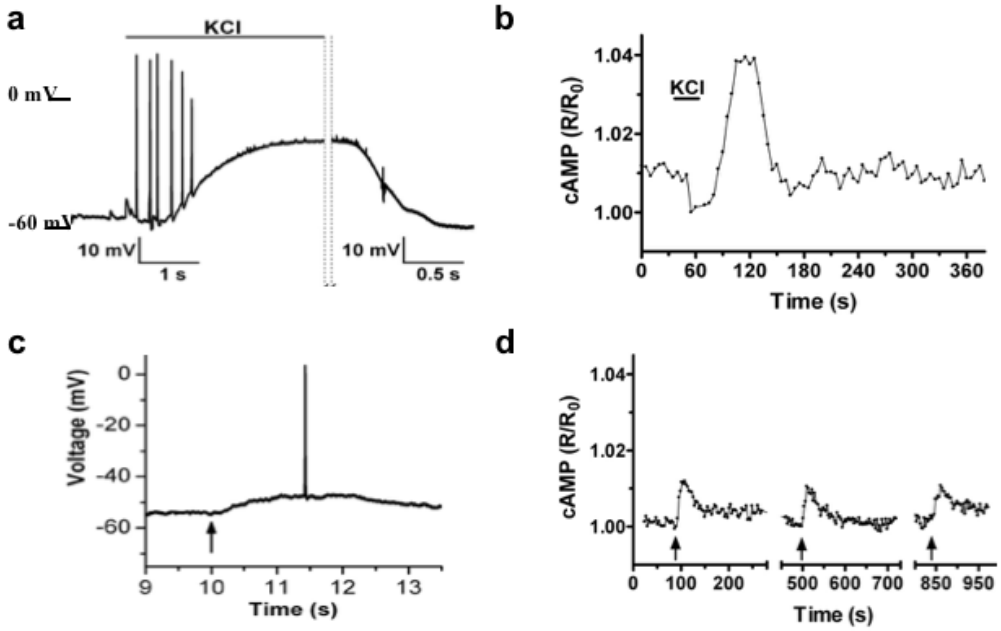

Figure 3. A single action potential in sympathetic neurons is sufficient to trigger cAMP signaling in coupled cardiomyocytes.

(**a-b**) Depolarization of SNs, innervating CMs, were induced by 50 mmol/L KCl for 30s and changes in membrane potential were evaluated by patch clamp (**a**). The corresponding effects in coupled CMs were estimated as cAMP increase (**b**). The traces in (**a**) and (**b**) are representative of the responses obtained. (**c-d**) A single action potential was generated in SNs by brief pulses of KCl applied to the SN soma via the tip of a picospritzer pipette (5-10 psi for up to 10 s) (**c**). cAMP variations, upon the brief SN activation, were evaluated in the innervated CMs. Arrows in (**d**) indicate the time in which a single action potential was induced in a SN. The representative trace in (**d**) demonstrates that a single action potential is sufficient to trigger a cAMP response in the innervated CM.

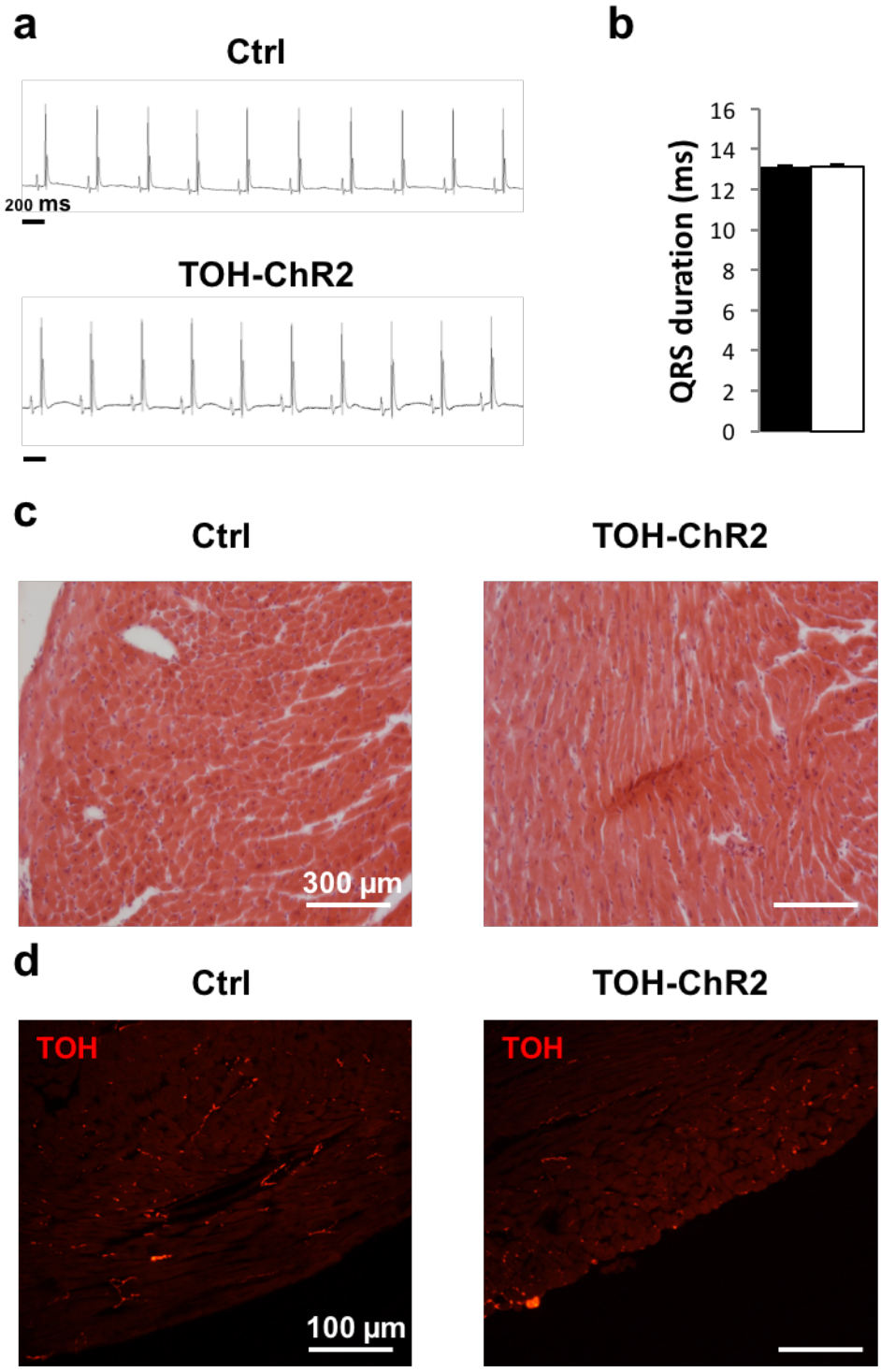

Figure 4. TOH-ChR2 hearts have a normal morphology and function as well as a normal innervation pattern.
(**a**) ECG traces from controls and TOH-ChR2 mouse heart, showing no alterations in the transgenic model. (**b**) QRS values of controls and TOH-ChR2 hearts are undistinguishable, demonostrating no defects in the ventricular conduction in the transgenic model. (**c**) Haematoxylin and Eosin staining shows no difference in the histology between controls and TOH-ChR2 hearts. (**d**) IF staining with an antibody to TOH showing that TOH-ChR2 hearts present a normal innervation pattern of sympathetic neurons, whose morphology is identical to the one of the controls.

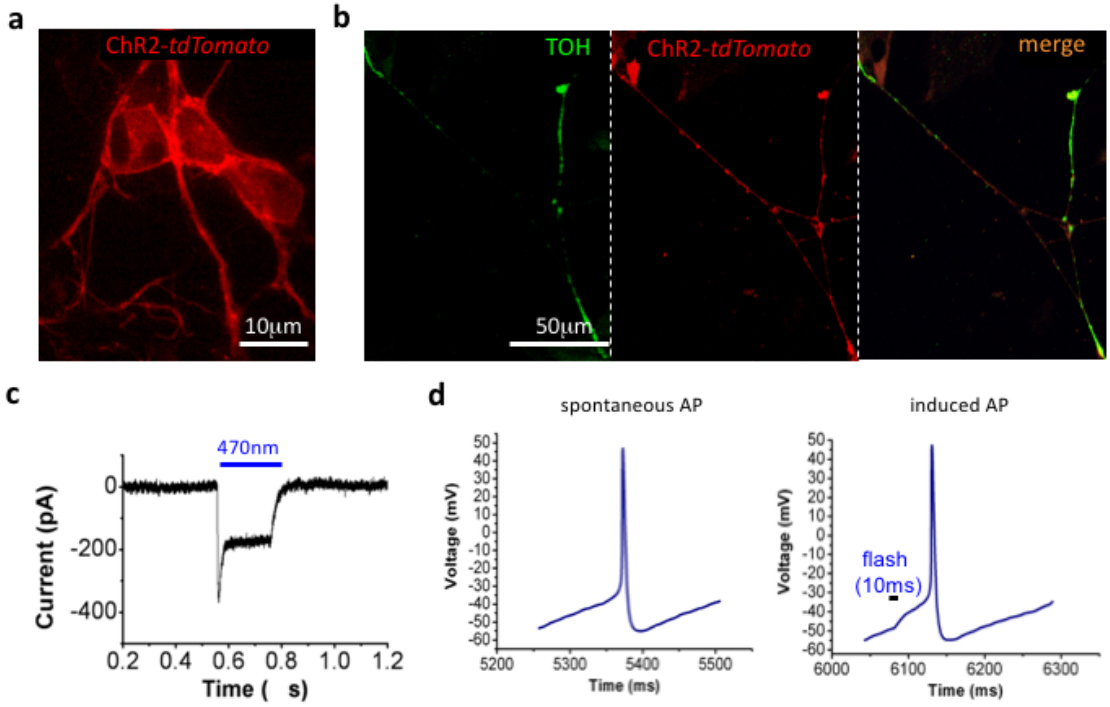

Figure 5. Channelrhodopsin-2 allows modulation of sympathetic neuron activity *in vitro*.
(**a**) Confocal immunofluorescence analysis on cultured SNs, isolated from the superior cervical ganglia of TOH/ChR2 neonatal mice, showing ChR2 localization at the level of the SN membrane and neuritic processes. (**b**) Confocal immunofluorescence analysis on cultured SNs stained with an antibody to TOH (left panel, green signal). The middle panel shows ChR2 expression (red signal) while the right panel is the merge of the two signals. ChR2 expressing ganglionic cells differentiate into SNs in culture. (**c**) Patch clamp was performed in cultured TOH/ChR2 SNs to measure changes in the membrane potential upon 470nm blue light photostimulation. The light pulse (blue bar) causes an inward current which started with the cell illumination and stopped immediately after cell photostimulation cessation. (**d**) Comparison of spontaneous (left panel) and light-induced (10ms, 470nm light pulse) (right panel) action potentials (AP) in cultured SNs isolated from TOH/ChR2 mice. The images show no differences in the kinetics of both APs.

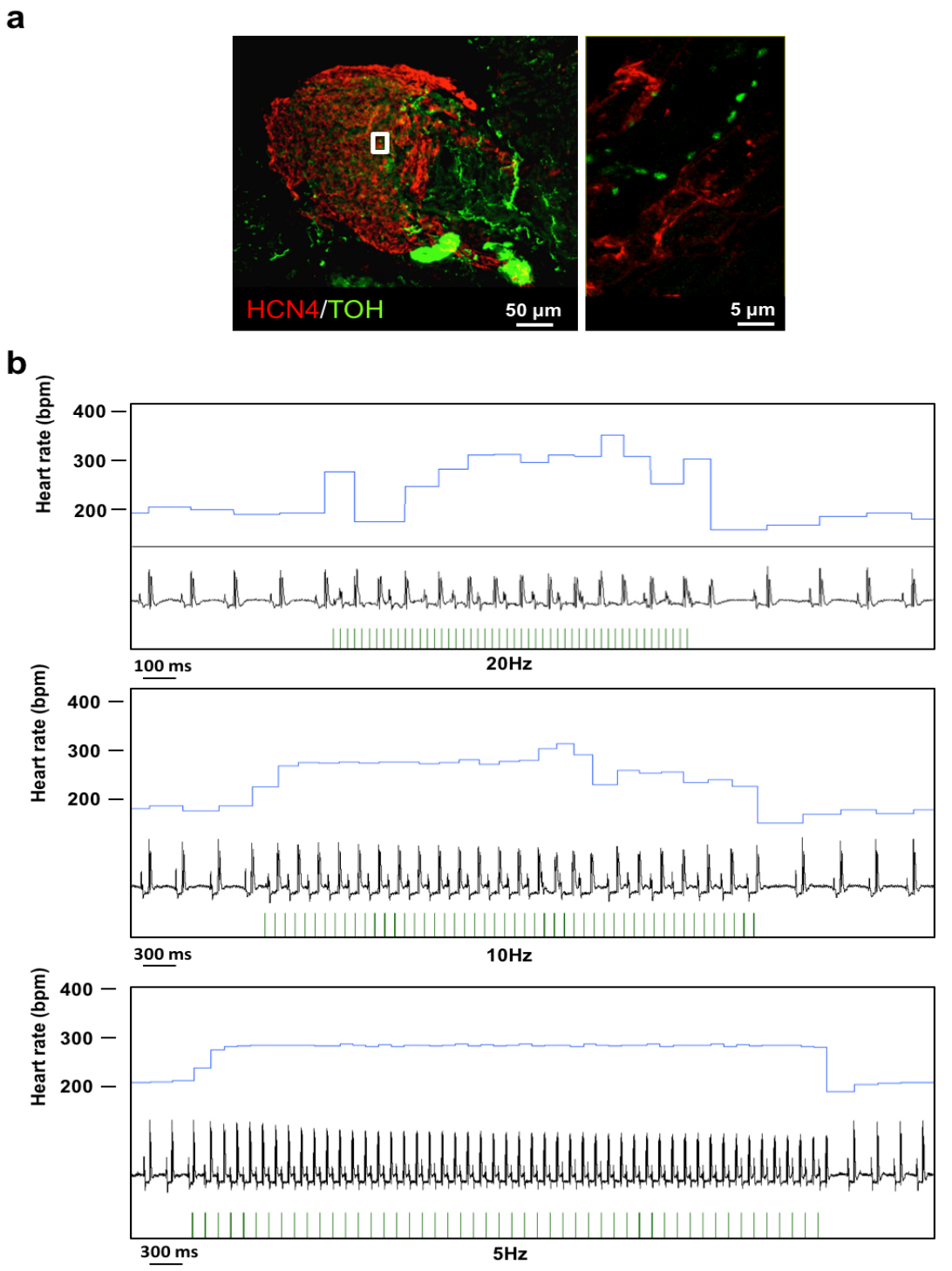

Figure 6. SNs are tightly coupled to SAN cells and respond to photostimulation with an increase in HR. (**a**) Confocal immunofluorescence analysis on a cryosection of the sino-atrial node (SAN), from an adult control mouse, stained with antibodies to HCN4 (green signal), to identify the SAN cells, and TOH (red signal). The high magnification (right panel) evidences the strict contact between SN and the targeted HCN4 positive cells. (**b**) Representative ECG traces of TOH-ChR2 heart photostimulation with trains of different frequency. The black trace represents the ECG, the blue trace the heart rate and the green dashes the light pulses.

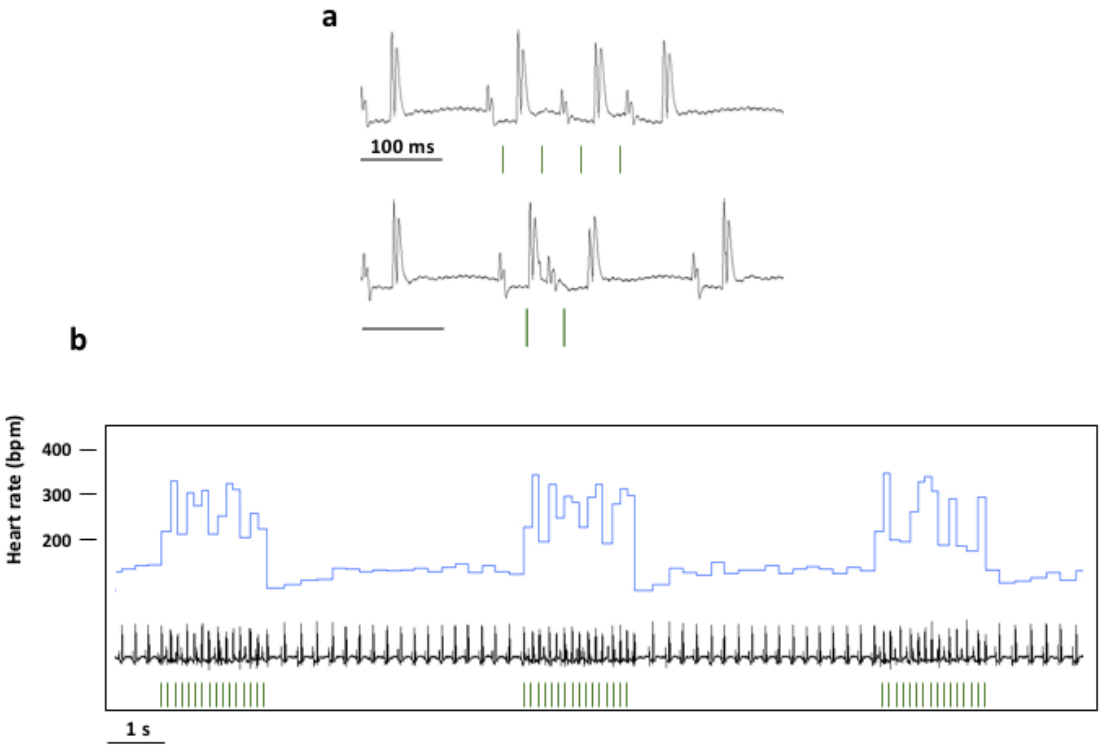

Figure 7. SN mediated increase in heart rate is highly efficient and repeatable.
(**a**) Representative ECG traces of TOH-ChR2 heart photostimulation showing the minimum number of light pulses needed to evoke a shorter sinus beat. (**b**) Representative ECG traces of TOH-ChR2 heart photostimulation showing multiple photostimulation of SNs in a short time window. The black trace represents the ECG, the blue trace the heart rate and the green dashes the light pulses.

MATERIALS AND METHODS

Mouse models. Transgenic mice expressing cre-recombinase under the control of tyrosine hydroxylase (TOH) promoter B6.129X1-Th$^{tm1(cre)Te}$/Kieg (Hemma Laboratories, KCTT/EMMA/Johannes Wilbertz Stockholm SWEDEN) were bred with B6.Cg-Gt(ROSA)26Sortm27.1(CAG-COP4*H134R/tdTomato)Hze/J expressing mice (Jackson Lab. Bar Harbor, Maine, USA). The resulting offspring has the STOP cassette deleted in dopaminergic and adrenergic neurons, thus expressing the hChR2(H134R)-tdTomato fusion protein. TOH-CRE+/- lines were used to maintain the colonies. All experimental procedures described in this manuscript have been approved by the local ethical committee (Authorization number C54) and communicated to the relevant Italian authority (Ministero della Salute, Ufficio VI), in compliance of Italian Animal Welfare Law (Law n 116/1992 and subsequent modifications).

Neonatal cardiomyocyte isolation and culture. Primary cultures of cardiac myocytes (NRVMs) were prepared from P1-P3 Sprague Dawley rats, as previously described[217]. Briefly, hearts were removed, minced in ADS (5 mM glucose, 106 mM NaCl, 5.3 mM KCl, 20 mM Hepes, 0.8 mM Na2HPO4, and 0.4 mM MgSO4, pH7.4) and enzimatically dissociated with collagenase A (0.4 mg/ml, Roche) and pancreatine (1.2 mg/ml, Sigma). Cells were plated onto laminin-coated (10 μg/cm^2, BD Biosciences) round glass coverslips, at a density of 60000 cells/cm^2, in culture medium containing: 75% D-MEM-Hepes, 17% M199, 5% horse serum, 0.5% newborn calf serum, 200 mM glutamine, 50 μg/ml penicillin-streptomycin, (all from Invitrogen) and maintained in a humidified atmosphere (5% CO_2) at 37°C. Twenty-four hours after seeding, VRVMs were transfected with the appropriate FRET based sensor, GcAMPs (for cAMP accumulation measurements, courtesy of Dr. Martin Lohse) or the fluorescent PKA activity reporter AKAR3 (for PKA activity, kind gift of Dr. Jin Zhang) using transfectin (Bio Rad) as recommended by the manufacturer.

Sympathetic neuron isolation and co-culture with CMs. Sympathetic neurons (SNs) were isolated from either P1-P3 Sprague Dawley rats or P1-P3 TOH/ChR2 mice, by adapting the procedure of Zareen and Greene[218]. Superior cervical ganglia were minced in complete medium (RPMI supplemented with 10% horse serum, both from Invitrogen) and then enzimatically dissociated in 0.25% Trypsin with no EDTA (Invitrogen) for 30 min at 37°C. Cells were plated onto laminin-coated round glass coverslips. ChR2 expressing SNs were

cultured alone, while rat SNs were seeded at a density of 1500 cells/cm^2 with NRVMs. Cells were maintained in cardiomyocyte medium supplemented with 100 ng/ml NGF (Sigma). Half of the medium was replaced every two days.

Stimulation of sympathetic neurons and FRET imaging of co-cultured CMs. FRET imaging experiments were performed 7-10 days after the establishment of the co-culture. Cells were maintained in Hepes-buffered Ringer-modified saline (in mmol/L, 125 NaCl, 5 KCl, 1 Na_3PO_4, 1 $MgSO_4$, 5.5 glucose, 1.8 $CaCl_2$, 20 Hepes, pH 7.4) at room temperature and imaged on an inverted Olympus IX50 microscope coupled to a CCD camera (Sensicam QE, PCO) and a beam-splitter optical device (Microimager). Images were acquired using custom-made software and processed using ImageJ (National Institutes of Health). Variations in FRET efficiencies were measured by drawing a region of interest (ROI) in the cell cytosol and by monitoring changes in the 480 nm/545 nm fluorescence emission signals (R) on excitation at 430 nm after background subtraction. FRET values were expressed as $\Delta R/R_0$, where R_0 is the ratio at t = 0 s and $\Delta R = R - R_0$. The beginning of FRET variations, indicative of intracellular cAMP concentration, was defined as the time of the first frame after which two consecutive values fell outside the standard deviation of values in basal condition. Membrane depolarization of sympathetic neurons was obtained by applying high potassium solution (in mmol/L, 80 NaCl, 50 KCl, 1 Na_3PO_4, 1 $MgSO_4$, 5.5 glucose, 1.8 $CaCl_2$, 20 Hepes, pH 7.4) either via a perfusion system or via pulses delivered by means of a software-controlled pressurized micropipette in proximity of the analyzed cell.

Electrophysiology Whole cell current-clamp experiments were performed at room temperature (~23°C) on single cells visualized with an inverted microscope (Olympus IX50, Tokyo, Japan). Data were recorded using a EPC-7 amplifier (HEKA electronic, Lambrecht, Germany) and Axon Instruments pClamp10 software. Data were sampled at 10 kHz. Patch pipettes were prepared by pulling borosilicate glass capillaries (1.5 mm outer diameter and 1.16 mm inner diameter, Harvard Apparatus LTD, Massachusetts, United States) using a micropipette puller (Narishige, Japan). Pipette resistance was 2-4 MΩ when filled with intracellular solution. Extracellular solutions contained (in mmol/L): 125 NaCl, 5 KCl, 1 Na_3PO_4, 1 $MgSO_4$, 20 Hepes, 5.5 Glucose, 1.8 $CaCl_2$, pH 7.4 with NaOH. Intracellular solution was (in mmol/L): 100 K-gluconate, 20 KCl, 10 Hepes, 10 phosphocreatine, 4 Mg-ATP, 0.3 GTP, pH 7.3 with KOH. All membrane potential values were corrected for liquid junction potential, calculated as -14.5 mV.

In vivo SN photostimulation in TOH/ChR2 mice. Adult wild-type and TOH/ChR2 male mice were anesthetized by avertin administration (Tribromoethanol 2,5%, Sigma), secured to the table in supine position and intubated with a 24G needle for ventilation (tidal volume 0.4ml; 120 strokes/min) from an artificial ventilator (SAR-830). Body temperature was monitored constantly during the experiment. The skin was dissected by a lateral sub-ascellary 1.5 cm cut, subcutaneous muscles were removed and a 0.5 cm incision was performed at the level of the 1^{th} to 2^{nd} intercostal space. Self-retaining microretractors were then used to separate the 1rd and 2th ribs enough to get adequate exposure of the operating region. The sinoatrial node have been exposed, and stimulated by differently-sized (from 800 to 1500 diameter, in μm) fiber optics (Thorlabs, Germany), coupled to a 470 nm LED (Thorlabs, Germany), controlled by an ECG-coupled recording system (Powerlab 8/30, Bioamp and LabChart 7.1 software; AD Instruments).

ECG recording and analysis. A standard lead I ECG recording was performed (Powerlab 8/30, Bioamp; AD Instruments) during the experiment. ECG parameters (QRS, PR interval and heart rate) were calculated using LabChart 7.1 software (AD Instruments).

Statistics. Data are shown as mean ± s.e.m., unless differently indicated. For the analysis of significance, unpaired Student's t-test was used, with p-values < 0.05 (*), < 0.005 (**) and < 0.001 (***) considered statistically significant.

Cardiac optogenetics as an alternative to electrical pacemaking and cardioversion: insights from an *in vivo* animal model
(manuscript in preparation)

Collaborators: *Giulia Borile, Tania Zaglia and Marco Mongillo.*

INTRODUCTION

The use of electronic devices for the treatment of heart rhythm disturbances is a well established therapeutic intervention, in heart diseases with either dysfunctional cardiac activation (bradyarrhythmia), or increased risk of sudden cardiac death due to arrhythmias (ventricular tachyarrhythmia)[219-221].

In particular, in the former case, the most popular device is the electronic pacemaker, which is constituted by a generator of the electrical impulse with a battery and usually two electric lead that are inserted into the atrial and ventricular cavity. Low energy electrical currents are delivered to the heart to substitute the physiologic nodal pacemaker and achieve continuous and sequential depolarization and regulate the timing of cardiac activation[222]. For the treatment of ventricular tachyarrhythmias, including fibrillation, the device used is the implantable cardioverter defibrillator (ICD), which has a similar structure, but a more complex functioning, that is based on: i) monitoring and real-time of analysis of ECG to detect abnormal heart rhythms and ii) delivery of electrical stimulation, using either a single high-energy impulse to terminate a ventricular fibrillation (VF), or a train of low energy stimuli synchronized to the QRS, called *overdrive pacing* or *anti-tachycardia pacing*, to terminate ventricular tachycardia[221].

Although these approaches are the only therapeutic option in a subset of drug resistant arrhythmias, in severe conditions of heart rhythm impairment or in cardiac pathologies where no other approaches are available, they present some disadvantages: I) invasive procedure of intra-cavity catheter implantation, II) interference of the catheter leads with cardiac valve leaflets, thus leading to increased risk of endocarditis[223], III) interference with other electronic devices and IV) possible tissue damage due to frequent electrical currents imposed to the same site and due to the constant physical contacts with the lead[224]. Evidence of a detrimental effect of ICD implantation in the follow-up of patients that received multiple electrical shocks have been clearly showed in two important clinical trial:

Multicenter Automatic Defibrillator Implantation Trial (MADIT II)[225] and Sudden Cardiac Death in Heart Failure (SCD-HeFT)[226], in which it was reported that patients who undergone ICD implantion and received electrical shocks had a greater mortality index in the long term follow up period[225-230].

For these reasons, the use of cardiac optogenetic was suggested in many studies as an attractive alternative to standard electrical techniques[231].

The distinctive features of the optogenetic approach, which are instrumental for the use in cardiac therapies are certainly cell type selectivity and the ability to precisely control the activated tissue volume. These properties derive from the biophysics at the basis of optogenetic control of membrane potential in cells. Indeed, optogenetic tissue depolarization does not depend on the presence of factors causing discontinuities in tissue conductivity, such as blood vessels, changes in fiber orientation, fatty tissue and intercellular clefts, all of which can influence the propagation of electric fields in the tissue. As a result of such factors, in conventional electrical stimulation, the site of direct contact of the electrode with the tissue is the point source of depolarization that may cause irregular conductance and heterogeneous dispersion of the cardiac activation wave current. Optogenetics, by contrast, has the potential to overcome the drawbacks of conventional electrical stimulation, given its capacity to obtain the depolarization of myocardial tissue without physical contact, with cell-type specificity and a high spatial-temporal resolution.

Moreover, with the development of miniaturized devices for light stimulation[232] and detection[233] and the development of cardiomyocyte (CMs)-specific genetic targeting of voltage-sensitive dyes[234], the perspective of an all-optical (sensor and actuator) optogenetic system for the treatment of heart rate disturbances seems plausible[235].

Although these characteristics seem promising, only few studies investigate the translational potential of cardiac optogenetics and are based on *in vitro* or computational models[111]. In a previous study, we demonstrated the potential of cardiac optogenetics as a tool to investigate the electrophysiological properties of different cell-type of the heart, and their involvement in arrhythmogenesis, in the intact heart[120] (see **Results**).

In this study, we used mouse models to provide a proof-of-principle of the clinical applicability of cardiac optogenetics.

PRELIMINARY RESULTS

1. Cardioversion with light: optogenetic termination of ventricular tachycardia

To assess the feasibility of cardiac optogenetics in obtaining the termination of VT, we set up an anesthetized open-chest mouse model, expressing light-gated cation channel ChannelRhodospin-2 (ChR2) specifically in CMs, under the control of α-MyHC promoter. We delivered light stimulation pulses using an optical fiber coupled to an LED emitting 470 nm light (the model is characterized in detail in Zaglia and Pianca et al[120], see **Results**). To deliver the light pulses at precise moments in the cardiac cycle, we used a digitizer device that allowed us to record ECG and to automatically control the delivery of light pulses based on the ECG trace. In order to obtain a clinically relevant condition associated to the development of ventricular arrhythmias, we induced left ventricle (LV) myocardial ischemia through ligation of left anterior descending coronary artery (LAD), a well defined condition creating a tissue substrate prone to the development of arrhythmic events[158]. Ventricular arrhythmias were triggered by photostimulation of a specific heart region in correspondence of the origin of right ventricular outflow tract, that we previously demonstrated to be highly arrhythmogenic[120] (see **Results**). VT was reproducibly induced by bursts of light flashes at high frequency.

In the attempt to terminate the VT, we mimicked the overdrive pacing approach used by conventional ICD. To this aim, we synchronized light pulses with the QRS of VT, to achieve a paced heart rate faster than the one imposed by VT (overdrive pacing). When optical stimulation was 'captured', i.e. when optical pacing was successful, we were able to stop the VT, that occurred (**Fig. 1**) in 4 out of 6 mice.

2. Optogenetic pacing

With the same set up described above, we tested the possibility of using the optogenetic approach to perform prolonged cardiac pacing, from atria and ventricles. As stated above, the main disadvantages of electrically-stimulated pacing, caused by the physical contact of cathethers with the tissue and the damage produced by electrical currents, are intrinsically avoided using contactless photostimulation. We demonstrated that epicardial photostimulation is able to produce a stable ventricular paced rhythm, carried on

for up to 30 minutes, without any structural or functional alteration (**Fig.2a**).

Atrioventricular (AV) block is a condition in which the depolarization wave is not correctly spread from the atria to the ventricles, because of an impairment in the AV node. Transient AV block is a commonly observed consequence of myocardial ischemia, and consistently, we recorded the ECG characteristics of AV block in experiementally induced ischemia following LAD ligation. We thus used light assisted stimulation to assess whether optical pacing was able to restore sinusal rhythm during complete AV block. Short term ventricular pacing was successful in overcoming the electrophysiologic abnormalities as shown in **Fig.2b**.

3. Simulation of reversible bundle branch block

In addition to provide a proof of principle of optogenetic-based cardioversion and pacing, we here wanted to assess whether the flexibility and ease of optical stimulation could be used to experimentally mimic, in the animal model, clinically relevant situations like the bundle branch block (BBB), a clinical condition caused by abnormal function of a part of the cardiac conduction system (i.e. the bundle branch). Given the cell-type specific nature of this pathologic condition, such investigation would not be feasible with conventional electrophysiologic techniques. For this experiments, we used a mouse model in which ChR2 is expressed specifically in the ventricular conduction system, under the control of Connexin-40 promoter. With the same experimental set up described above, we illuminated the epicardial surface of the anterior region of interventricular septum at the intersection with LV wall, in anesthetized mouse, with an optical fiber of 1500 μm diameter, by delivering a continuous light stimulation of 2 s duration. Such stimulation protocol resulted in the refractoriness to depolarization of the cells in the illuminated area, corresponding to the left bundle branch (LBB) and caused their reversible inability to conduct the endogenous depolarization wave coming from SA node/AV bundle, thus mimicking in mice the effects of left bundle branch block (LBBB) (**Fig.3**). This condition is reversible, in fact, if light stimulus is turned off BB recover its function. In human pathology, BBB occurs as a result of structural or functional damage to the conduction system cells[236]. The possibility to mimic BBB in an animal model is fundamental to understand its effects on cardiac dynamics, and it is achievable only thank to the specificity of the optogenetic approach.

DISCUSSION

Optogenetics offers the possibility of non invasive, cell type specific and contactless stimulation of heart depolarization. These features make this technique a promising alternative to conventional electrical depolarization methods, used to control heart rate. Our recent work[120] (see **Results**) showed the feasibility of the simultaneous optical detection, using Ca^{2+} sensitive dye, and stimulation using optogenetics in *ex vivo* preparations, and this approach was also tried by the group of Nussinovitch at the same time[237]. Moreover, in recent reports described the development of genetically-encoded voltage sensitive sensors[234], that offer the possibility, combined with gene or cell therapy, to perform the study of single cell electrophysiology in the intact heart, *in vivo*. In addition, recent advances in LED miniaturization, led to the development of flexible meshes of micron-scale LED, that could be used to achieve complex geometrical stimulations on the heart surface[232]. These methodologies could be exploited to directly investigate common arrhythmia mechanisms, including, e.g. cardiac 'rotors', atrial and ventricular flutter, or polymorphic ventricular arrhythmias, all of which are characterized by complex spatial and temporal depolarization pattern. The combination of the aforementioned tools with miniaturized sensing optical elements[238], would predictably pave the way to the all-optical sensor-stimulator control of heart rate, with important implications in the study of arrhythmogenic mechanisms.

Moreover, thank to the cell-type selectivity of optogenetics, stimulation of selected parts of the central conduction system can be achieved, prospecting the possibility of even more precise and specific ways to control heart electrical activity.

To achieve the goal of optogenetic control of heart rate *in vivo*, however, some problems need to be solved: like methods for a stable implantation of illumination and sensing elements, that were solved in the neuroscience field using stable implantation of optrodes on the skull bone, but for the use in cardiology will require to deal with the continuous movement during the heart cycle.

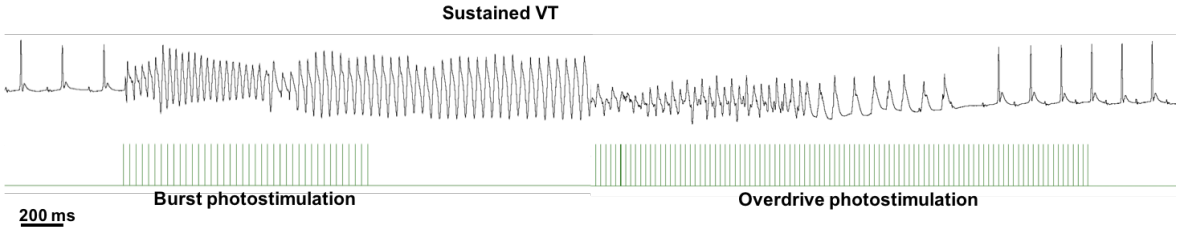

Figure 1. Representative ECG trace showing the photostimulation of a sustained VT and the subsequent light-induced overdrive cardioversion. Green lines show the light flashes, each one 5 ms long.

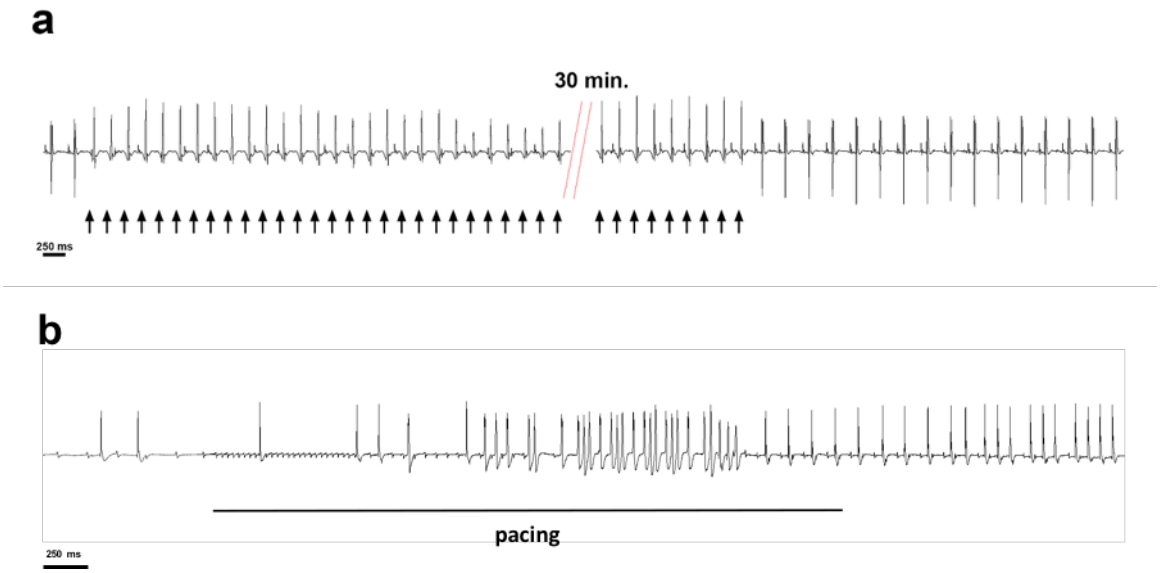

Figure 2. (**a**) ECG representative trace showing that optogenetic pacing for up to 30 minutes causes no damage. (**b**) ECG trace showing the recovery from AV block with photostimulation.

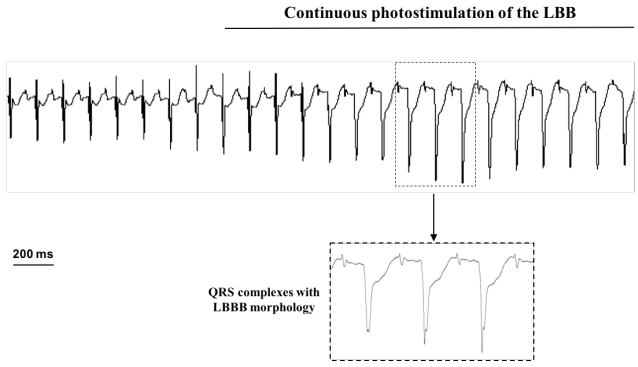

Figure 3. ECG representative trace of the continuous photostimulation of LBB of a Connexin-40-ChR2 heart, showing that this led to the inability of LBB to conduce electrical stimuli and thus resulting in LBBB.

MATERIALS AND METHODS

Mouse models. Transgenic adult male mice, with a genetic background C57B6J, expressing cre-recombinase under the control of either α-MyHC or Connexin-40 (Cx40) promoter were bred with B6.Cg-Gt(ROSA)26Sor$^{tm27.1(CAG-COP4*H134R/tdTomato)Hze}$/J expressing mice (Jackson Lab. Bar Harbor, Maine, USA). The resulting offspring has the STOP cassette deleted in the heart, resulting in cardiomyocyte (α-MyHC-ChR2) or Purkinje fibers (Cx40-ChR2) expression of the hChR2(H134R)-*td*Tomato fusion protein. Both α-MyHC-cre$^{+/-}$ and Cx40-cre$^{+/-}$ lines were used to maintain the colonies. All experimental procedures described in this manuscript have been approved by the local ethical committee (Authorization number C54) and communicated to the relevant Italian authority (Ministero della Salute, Ufficio VI), in compliance of Italian Animal Welfare Law (Laws n 116/1992, D.Lgs 26/2014 and subsequent modifications).

***In vivo* epicardial photostimulation.** Adult ChR2 expressing transgenic male mice and littermate controls were anesthetized by isoflurane administration (1,5%-3%), secured to the table in supine position and intubated with a 24G needle for ventilation (tidal volume 0.4 ml; 120 strokes/min) from an artificial ventilator (SAR-830). Body temperature was monitored constantly during the experiment. The skin was dissected by a lateral sub-ascellary 1.5 cm cut, subcutaneous muscles were removed and a 0.5 cm incision was performed at the level of the 4th intercostal space. Self-retaining microretractors were then used to separate the 3rd and 4th ribs enough to get adequate exposure of the operating region. The heart was exposed and different epicardial regions from the atria and the left and right ventricles were stimulated with 1500 μm diameter fiber optic (Thorlabs, Germany), coupled to a 470 nm LED or directly with the bare LED (Thorlabs, Germany), controlled by an ECG-coupled recording system (Powerlab 8/30, Bioamp and LabChart 7.1 software; AD Instruments).

ECG recording and analysis. A standard lead I ECG was recorded (Powerlab 8/30, Bioamp; AD Instruments) during the experiment. ECG parameters (QRS, PR interval and heart rate) were calculated by using LabChart 7.1 software (AD Instruments).

Burst photoactivation protocol. Brief trains of 5 ms light pulses were delivered to a fixed epicardial region with repetition rates ranging from 10 Hz to 25 Hz (cycle length: 100 ms to 40 ms).

Left anterior descending (LAD) coronary artery ligation. The main trunk of the LAD coronary artery was ligated under microscope guidance, by using a 7/0 polypropylene suture[120] .Epicardial photostimulation was performed in the time window of 30-90 minutes after coronary occlusion, during constant ECG recording.

Conclusions

During my PhD training I had the opportunity to learn important techniques at the cutting edge in molecular biology, cell biology and also to participate in the development of new a scientific tool: cardiac optogenetics.

With the use of the techniques learned and the interaction with other collaborators and my supervisors, I had the possibility to carry on my scientific research project which brought to the discovery of a novel role for sympathetic innervation of the heart in the locally modulation of the proteostasis of CMs; to the aforementioned implementation of cardiac optogenetics on CMs and Purkinje fibers, that allowed to propose the first *in vivo* determination of the critical mass of working and conducting CMs needed to obtain an extrasystole and the characterizion of Purkinje fibers physiology *in vivo* with unprecedented detail and specificity. Moreover, the achievement of the first example of *in vivo* optogenetic stimulation of sympathetic efferents to the heart, allowed to add a further prove of that control of heart rate by sympathetic neurons is achieved through a *quasi-synaptic* interaction between sympathetic neurons and CMs. Finally, I provided a proof-of-principle study for the application of cardiac optogenetics in clinical relevant conditions, as an alternative to current therapies based on electrical stimulation of the heart.

Future perspectives

This thesis opens the way to various future perspectives, in particular regarding the physiologic relevance of the SN-CM interaction. We are following this path by investigating the possible implications of SN modulation of CM size, through the combination of cardiac optogenetics and molecular biology. Indeed, we have collected preliminary data, obtained through the denervation of α-MyHC-ChR2 hearts, that showed how denervated hearts are prone to develop sustained arrhythmia after optogenetic focal stimulation (**Fig.P1**), moreover we observed that after denervation there is a change in the expression level of the voltage gated potassium channel $K_v4.2$ (**Fig.P1**). These findings suggest that SNs could be determinant in modulating the electrophysiological properties of CMs, through the regulation of the expression level of proteins involved in the AP, for this reason in the next future we will explore the putative molecular players involved in the SN-mediated control of CM electrophysiology.

We will implement cardiac optogenetics in the conscious freely moving mice through the permanent implantation of a LED in the thorax of mice. This will allow to perform a chronic stimulation of SNs, offering the possibility to analyze, with unprecedented detail, the effects of chronic SN activation in the heart of living animal. This is of great relevance since many pathological situations are associated to a continuous iperactivation of SNS during time, such as heart failure, moreover this approach also will allow to study SN activation during functional studies (*i.e.* exercise). Moreover, this approach will allow to investigate the genesis of arrhythmias in the conscious mice and the involvement of the SN in the triggering of arrhythmia.

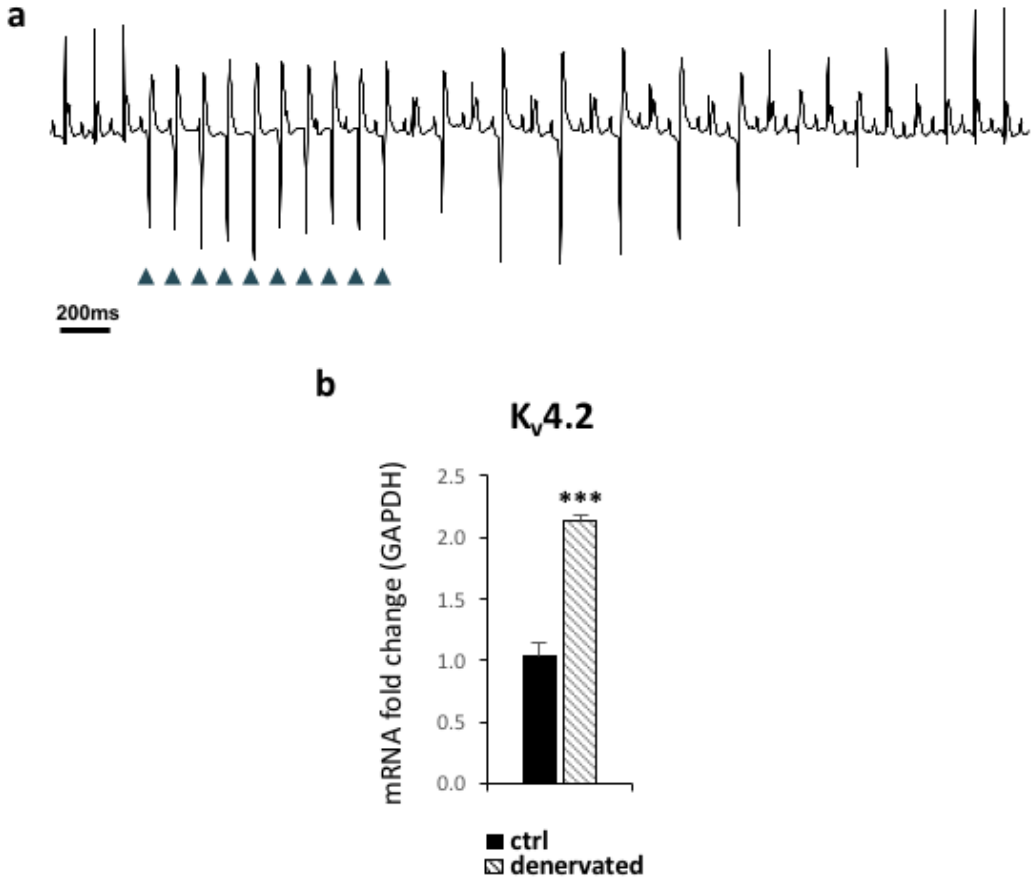

Figure P1. (**a**) ECG representative trace showing an example of sustained ventricular tachycardia, induced with photostimulation in α-MyHC-ChR2 denervated heart. (**b**) mRNA levels of $K_v4.2$ in the heart of control and denervated mice. ***: $p<0.001$

References

1 Zaglia, T. *et al.* Cardiac sympathetic neurons provide trophic signal to the heart via beta2-adrenoceptor-dependent regulation of proteolysis. *Cardiovasc Res* **97**, 240-250, doi:10.1093/cvr/cvs320 (2013).

2 Katz, A. *Physiology of the heart*. 5th edn, (Lippincot Williams and Wilkins, 2011).

3 Becker, A. E. & De Wit, A. P. Mitral valve apparatus. A spectrum of normality relevant to mitral valve prolapse. *Br Heart J* **42**, 680-689 (1979).

4 Brutsaert, D. L. The endocardium. *Annu Rev Physiol* **51**, 263-273, doi:10.1146/annurev.ph.51.030189.001403 (1989).

5 Antzelevitch, C. *et al.* Heterogeneity within the ventricular wall. Electrophysiology and pharmacology of epicardial, endocardial, and M cells. *Circ Res* **69**, 1427-1449 (1991).

6 Antzelevitch, C. Heterogeneity and cardiac arrhythmias: an overview. *Heart Rhythm* **4**, 964-972, doi:10.1016/j.hrthm.2007.03.036 (2007).

7 Liu, D. W., Gintant, G. A. & Antzelevitch, C. Ionic bases for electrophysiological distinctions among epicardial, midmyocardial, and endocardial myocytes from the free wall of the canine left ventricle. *Circ Res* **72**, 671-687 (1993).

8 Moseley, M. E., de Crespigny, A. J., Roberts, T. P., Kozniewska, E. & Kucharczyk, J. Early detection of regional cerebral ischemia using high-speed MRI. *Stroke* **24**, I60-65 (1993).

9 Basser, P. J., Mattiello, J. & LeBihan, D. MR diffusion tensor spectroscopy and imaging. *Biophys J* **66**, 259-267, doi:10.1016/S0006-3495(94)80775-1 (1994).

10 Healy, L. J., Jiang, Y. & Hsu, E. W. Quantitative comparison of myocardial fiber structure between mice, rabbit, and sheep using diffusion tensor cardiovascular magnetic resonance. *J Cardiovasc Magn Reson* **13**, 74, doi:10.1186/1532-429x-13-74 (2011).

11 Jiang, Y., Pandya, K., Smithies, O. & Hsu, E. W. Three-dimensional diffusion tensor microscopy of fixed mouse hearts. *Magn Reson Med* **52**, 453-460, doi:10.1002/mrm.20191 (2004).

12 Schmitt, B. *et al.* Three-dimensional alignment of the aggregated myocytes in the normal and hypertrophic murine heart. *J Appl Physiol (1985)* **107**, 921-927, doi:10.1152/japplphysiol.00275.2009 (2009).

13 Angeli, S. *et al.* A high-resolution cardiovascular magnetic resonance diffusion tensor map from ex-vivo C57BL/6 murine hearts. *J Cardiovasc Magn Reson* **16**, 77, doi:10.1186/s12968-014-0077-x (2014).

14 Sands, G. B., Smaill, B. H. & LeGrice, I. J. Virtual sectioning of cardiac tissue relative to fiber orientation. *Conf Proc IEEE Eng Med Biol Soc* **2008**, 226-229, doi:10.1109/iembs.2008.4649131 (2008).

15 Hanson, J. & Huxley, H. E. Structural basis of the cross-striations in muscle. *Nature* **172**, 530-532 (1953).

16 Grazia, A. in *Anatomy and physiology* Ch. 20, 486-8332.

17 Bers, D. M. Cardiac excitation-contraction coupling. *Nature* **415**, 198-205, doi:10.1038/415198a (2002).

18 Zalk, R. *et al.* Structure of a mammalian ryanodine receptor. *Nature* **517**, 44-49, doi:10.1038/nature13950 (2015).

19 Fabiato, A. & Fabiato, F. Use of chlorotetracycline fluorescence to demonstrate Ca2+-induced release of Ca2+ from the sarcoplasmic reticulum of skinned cardiac cells. *Nature* **281**, 146-148 (1979).
20 Hoyt, R. H., Cohen, M. L. & Saffitz, J. E. Distribution and three-dimensional structure of intercellular junctions in canine myocardium. *Circ Res* **64**, 563-574 (1989).
21 Veeraraghavan, R., Poelzing, S. & Gourdie, R. G. Intercellular electrical communication in the heart: a new, active role for the intercalated disk. *Cell Commun Adhes* **21**, 161-167, doi:10.3109/15419061.2014.905932 (2014).
22 Weidmann, S. Cardiac muscle: the functional significance of the intercalated disks. *Ann N Y Acad Sci* **137**, 540-542 (1966).
23 Weingart, R. The permeability to tetraethylammonium ions of the surface membrane and the intercalated disks of sheep and calf myocardium. *J Physiol* **240**, 741-762 (1974).
24 Franke, W. W., Borrmann, C. M., Grund, C. & Pieperhoff, S. The area composita of adhering junctions connecting heart muscle cells of vertebrates. I. Molecular definition in intercalated disks of cardiomyocytes by immunoelectron microscopy of desmosomal proteins. *Eur J Cell Biol* **85**, 69-82, doi:10.1016/j.ejcb.2005.11.003 (2006).
25 Peters, N. S. New insights into myocardial arrhythmogenesis: distribution of gap-junctional coupling in normal, ischaemic and hypertrophied human hearts. *Clin Sci (Lond)* **90**, 447-452 (1996).
26 Gros, D. *et al.* Restricted distribution of connexin40, a gap junctional protein, in mammalian heart. *Circ Res* **74**, 839-851 (1994).
27 Kirchhoff, S. *et al.* Abnormal cardiac conduction and morphogenesis in connexin40 and connexin43 double-deficient mice. *Circ Res* **87**, 399-405 (2000).
28 Miquerol, L. *et al.* Biphasic development of the mammalian ventricular conduction system. *Circ Res* **107**, 153-161, doi:10.1161/circresaha.110.218156 (2010).
29 Van Kempen, M. J. *et al.* Developmental changes of connexin40 and connexin43 mRNA distribution patterns in the rat heart. *Cardiovasc Res* **32**, 886-900 (1996).
30 Antzelevitch, C. & Fish, J. Electrical heterogeneity within the ventricular wall. *Basic Res Cardiol* **96**, 517-527 (2001).
31 Cunningham, J. G. *Textbook of veterinary physiology*. (Saunders, 2002).
32 Myles, R. C., Wang, L., Kang, C., Bers, D. M. & Ripplinger, C. M. Local beta-adrenergic stimulation overcomes source-sink mismatch to generate focal arrhythmia. *Circ Res* **110**, 1454-1464, doi:10.1161/circresaha.111.262345 (2012).
33 Xie, Y., Sato, D., Garfinkel, A., Qu, Z. & Weiss, J. N. So little source, so much sink: requirements for afterdepolarizations to propagate in tissue. *Biophys J* **99**, 1408-1415, doi:10.1016/j.bpj.2010.06.042 (2010).
34 Park, S. A. & Gray, R. A. Optical Mapping of Ventricular Fibrillation Dynamics. *Adv Exp Med Biol* **859**, 313-342, doi:10.1007/978-3-319-17641-3_13 (2015).
35 Boyle, P. M., Park, C. J., Arevalo, H. J., Vigmond, E. J. & Trayanova, N. A. Sodium current reduction unmasks a structure-dependent substrate for arrhythmogenesis in the normal ventricles. *PLoS One* **9**, e86947, doi:10.1371/journal.pone.0086947 (2014).
36 Priori, S. G. *et al.* 2015 ESC Guidelines for the management of patients with ventricular arrhythmias and the prevention of sudden cardiac death: The Task Force for the Management of Patients with Ventricular Arrhythmias and the Prevention of Sudden Cardiac Death of the European Society of Cardiology (ESC)Endorsed by:

Association for European Paediatric and Congenital Cardiology (AEPC). *Eur Heart J*, doi:10.1093/eurheartj/ehv316 (2015).
37 Zipes, D. P. Heart-brain interactions in cardiac arrhythmias: role of the autonomic nervous system. *Cleve Clin J Med* **75 Suppl 2**, S94-96 (2008).
38 Kimura, K., Ieda, M. & Fukuda, K. Development, maturation, and transdifferentiation of cardiac sympathetic nerves. *Circ Res* **110**, 325-336, doi:10.1161/circresaha.111.257253 (2012).
39 Fukuda, K., Kanazawa, H., Aizawa, Y., Ardell, J. L. & Shivkumar, K. Cardiac innervation and sudden cardiac death. *Circ Res* **116**, 2005-2019, doi:10.1161/CIRCRESAHA.116.304679 (2015).
40 Hasan, W. Autonomic cardiac innervation: development and adult plasticity. *Organogenesis* **9**, 176-193, doi:10.4161/org.24892 (2013).
41 Protas, L. & Robinson, R. B. Neuropeptide Y contributes to innervation-dependent increase in I(Ca, L) via ventricular Y2 receptors. *Am J Physiol* **277**, H940-946 (1999).
42 Protas, L. *et al.* Neuropeptide Y is an essential in vivo developmental regulator of cardiac ICa,L. *Circ Res* **93**, 972-979, doi:10.1161/01.RES.0000099244.01926.56 (2003).
43 Franzoso, M., Zaglia, T. & Mongillo, M. Putting together the clues of the everlasting neuro-cardiac liaison. *Biochim Biophys Acta*, doi:10.1016/j.bbamcr.2016.01.009 (2016).
44 Kuruvilla, R. *et al.* A neurotrophin signaling cascade coordinates sympathetic neuron development through differential control of TrkA trafficking and retrograde signaling. *Cell* **118**, 243-255, doi:10.1016/j.cell.2004.06.021 (2004).
45 Ieda, M. *et al.* Sema3a maintains normal heart rhythm through sympathetic innervation patterning. *Nat Med* **13**, 604-612, doi:10.1038/nm1570 (2007).
46 Clapham, D. E. & Neer, E. J. G protein beta gamma subunits. *Annu Rev Pharmacol Toxicol* **37**, 167-203, doi:10.1146/annurev.pharmtox.37.1.167 (1997).
47 Luttrell, L. M. Transmembrane signaling by G protein-coupled receptors. *Methods Mol Biol* **332**, 3-49, doi:10.1385/1-59745-048-0:1 (2006).
48 Chruscinski, A. J. *et al.* Targeted disruption of the beta2 adrenergic receptor gene. *J Biol Chem* **274**, 16694-16700 (1999).
49 Bernstein, D. *et al.* Differential cardioprotective/cardiotoxic effects mediated by beta-adrenergic receptor subtypes. *Am J Physiol Heart Circ Physiol* **289**, H2441-2449, doi:10.1152/ajpheart.00005.2005 (2005).
50 Opie, L. H. *Heart physiology, from cell to circulation*. (Lippincott Williams and Wilkins, 2004).
51 Bucciantini, M. *et al.* Inherent toxicity of aggregates implies a common mechanism for protein misfolding diseases. *Nature* **416**, 507-511, doi:10.1038/416507a (2002).
52 Glickman, M. H. & Ciechanover, A. The ubiquitin-proteasome proteolytic pathway: destruction for the sake of construction. *Physiol Rev* **82**, 373-428, doi:10.1152/physrev.00027.2001 (2002).
53 Powell, S. R. The ubiquitin-proteasome system in cardiac physiology and pathology. *Am J Physiol Heart Circ Physiol* **291**, H1-h19, doi:10.1152/ajpheart.00062.2006 (2006).
54 Frescas, D. & Pagano, M. Deregulated proteolysis by the F-box proteins SKP2 and beta-TrCP: tipping the scales of cancer. *Nat Rev Cancer* **8**, 438-449, doi:10.1038/nrc2396 (2008).
55 Jung, T., Catalgol, B. & Grune, T. The proteasomal system. *Mol Aspects Med* **30**, 191-296, doi:10.1016/j.mam.2009.04.001 (2009).

56 Sacheck, J. M. *et al.* Rapid disuse and denervation atrophy involve transcriptional changes similar to those of muscle wasting during systemic diseases. *FASEB J* **21**, 140-155, doi:10.1096/fj.06-6604com (2007).
57 Willis, M. S. & Patterson, C. Into the heart: the emerging role of the ubiquitin-proteasome system. *J Mol Cell Cardiol* **41**, 567-579, doi:10.1016/j.yjmcc.2006.07.015 (2006).
58 Baehr, L. M., Tunzi, M. & Bodine, S. C. Muscle hypertrophy is associated with increases in proteasome activity that is independent of MuRF1 and MAFbx expression. *Front Physiol* **5**, 69, doi:10.3389/fphys.2014.00069 (2014).
59 Li, H. H. *et al.* Atrogin-1 inhibits Akt-dependent cardiac hypertrophy in mice via ubiquitin-dependent coactivation of Forkhead proteins. *J Clin Invest* **117**, 3211-3223, doi:10.1172/jci31757 (2007).
60 Baskin, K. K. *et al.* MAFbx/Atrogin-1 is required for atrophic remodeling of the unloaded heart. *J Mol Cell Cardiol* **72**, 168-176, doi:10.1016/j.yjmcc.2014.03.006 (2014).
61 Carrier, L., Schlossarek, S., Willis, M. S. & Eschenhagen, T. The ubiquitin-proteasome system and nonsense-mediated mRNA decay in hypertrophic cardiomyopathy. *Cardiovasc Res* **85**, 330-338, doi:10.1093/cvr/cvp247 (2010).
62 Gomes, M. D., Lecker, S. H., Jagoe, R. T., Navon, A. & Goldberg, A. L. Atrogin-1, a muscle-specific F-box protein highly expressed during muscle atrophy. *Proc Natl Acad Sci U S A* **98**, 14440-14445, doi:10.1073/pnas.251541198 (2001).
63 Li, H. H. *et al.* Atrogin-1/muscle atrophy F-box inhibits calcineurin-dependent cardiac hypertrophy by participating in an SCF ubiquitin ligase complex. *J Clin Invest* **114**, 1058-1071, doi:10.1172/jci22220 (2004).
64 Bodine, S. C. *et al.* Identification of ubiquitin ligases required for skeletal muscle atrophy. *Science* **294**, 1704-1708, doi:10.1126/science.1065874 (2001).
65 Willis, M. S. *et al.* Muscle ring finger 1, but not muscle ring finger 2, regulates cardiac hypertrophy in vivo. *Circ Res* **100**, 456-459, doi:10.1161/01.res.0000259559.48597.32 (2007).
66 Maejima, Y. *et al.* Muscle-specific RING finger 1 negatively regulates pathological cardiac hypertrophy through downregulation of calcineurin A. *Circ Heart Fail* **7**, 479-490, doi:10.1161/CIRCHEARTFAILURE.113.000713 (2014).
67 Willis, M. S. *et al.* Muscle ring finger 1 mediates cardiac atrophy in vivo. *Am J Physiol Heart Circ Physiol* **296**, H997-H1006, doi:10.1152/ajpheart.00660.2008 (2009).
68 Willis, M. S. *et al.* Cardiac muscle ring finger-1 increases susceptibility to heart failure in vivo. *Circ Res* **105**, 80-88, doi:10.1161/CIRCRESAHA.109.194928 (2009).
69 Clarke, B. A. *et al.* The E3 Ligase MuRF1 degrades myosin heavy chain protein in dexamethasone-treated skeletal muscle. *Cell Metab* **6**, 376-385, doi:10.1016/j.cmet.2007.09.009 (2007).
70 Kedar, V. *et al.* Muscle-specific RING finger 1 is a bona fide ubiquitin ligase that degrades cardiac troponin I. *Proc Natl Acad Sci U S A* **101**, 18135-18140, doi:10.1073/pnas.0404341102 (2004).
71 Morselli, E. *et al.* Autophagy mediates pharmacological lifespan extension by spermidine and resveratrol. *Aging (Albany NY)* **1**, 961-970 (2009).
72 Kiffin, R., Bandyopadhyay, U. & Cuervo, A. M. Oxidative stress and autophagy. *Antioxid Redox Signal* **8**, 152-162, doi:10.1089/ars.2006.8.152 (2006).
73 Yorimitsu, T., Nair, U., Yang, Z. & Klionsky, D. J. Endoplasmic reticulum stress triggers autophagy. *J Biol Chem* **281**, 30299-30304, doi:10.1074/jbc.M607007200 (2006).

74 Zhu, K., Dunner, K., Jr. & McConkey, D. J. Proteasome inhibitors activate autophagy as a cytoprotective response in human prostate cancer cells. *Oncogene* **29**, 451-462, doi:10.1038/onc.2009.343 (2010).
75 Klionsky, D. J. The molecular machinery of autophagy: unanswered questions. *J Cell Sci* **118**, 7-18, doi:10.1242/jcs.01620 (2005).
76 Massey, A. C., Zhang, C. & Cuervo, A. M. Chaperone-mediated autophagy in aging and disease. *Curr Top Dev Biol* **73**, 205-235, doi:10.1016/S0070-2153(05)73007-6 (2006).
77 Bandyopadhyay, U., Sridhar, S., Kaushik, S., Kiffin, R. & Cuervo, A. M. Identification of regulators of chaperone-mediated autophagy. *Mol Cell* **39**, 535-547, doi:10.1016/j.molcel.2010.08.004 (2010).
78 Sahu, R. *et al.* Microautophagy of cytosolic proteins by late endosomes. *Dev Cell* **20**, 131-139, doi:10.1016/j.devcel.2010.12.003 (2011).
79 Dargemont, C. & Ossareh-Nazari, B. Cdc48/p97, a key actor in the interplay between autophagy and ubiquitin/proteasome catabolic pathways. *Biochim Biophys Acta* **1823**, 138-144, doi:10.1016/j.bbamcr.2011.07.011 (2012).
80 McLeland, C. B., Rodriguez, J. & Stern, S. T. Autophagy monitoring assay: qualitative analysis of MAP LC3-I to II conversion by immunoblot. *Methods Mol Biol* **697**, 199-206, doi:10.1007/978-1-60327-198-1_21 (2011).
81 Myeku, N. & Figueiredo-Pereira, M. E. Dynamics of the degradation of ubiquitinated proteins by proteasomes and autophagy: association with sequestosome 1/p62. *J Biol Chem* **286**, 22426-22440, doi:10.1074/jbc.M110.149252 (2011).
82 Zaglia, T. *et al.* Atrogin-1 deficiency promotes cardiomyopathy and premature death via impaired autophagy. *J Clin Invest* **124**, 2410-2424, doi:10.1172/JCI66339
66339 [pii] (2014).
83 Wang, C. & Wang, X. The interplay between autophagy and the ubiquitin-proteasome system in cardiac proteotoxicity. *Biochim Biophys Acta* **1852**, 188-194, doi:10.1016/j.bbadis.2014.07.028 (2015).
84 Robertson, G. P. Functional and therapeutic significance of Akt deregulation in malignant melanoma. *Cancer Metastasis Rev* **24**, 273-285, doi:10.1007/s10555-005-1577-9 (2005).
85 Nave, B. T., Ouwens, M., Withers, D. J., Alessi, D. R. & Shepherd, P. R. Mammalian target of rapamycin is a direct target for protein kinase B: identification of a convergence point for opposing effects of insulin and amino-acid deficiency on protein translation. *Biochem J* **344 Pt 2**, 427-431 (1999).
86 Glass, D. J. Signalling pathways that mediate skeletal muscle hypertrophy and atrophy. *Nat Cell Biol* **5**, 87-90, doi:10.1038/ncb0203-87 (2003).
87 Reynolds, T. H. t., Bodine, S. C. & Lawrence, J. C., Jr. Control of Ser2448 phosphorylation in the mammalian target of rapamycin by insulin and skeletal muscle load. *J Biol Chem* **277**, 17657-17662, doi:10.1074/jbc.M201142200 (2002).
88 Sandri, M. *et al.* Foxo transcription factors induce the atrophy-related ubiquitin ligase atrogin-1 and cause skeletal muscle atrophy. *Cell* **117**, 399-412 (2004).
89 Sandri, M. & Robbins, J. Proteotoxicity: an underappreciated pathology in cardiac disease. *J Mol Cell Cardiol* **71**, 3-10, doi:10.1016/j.yjmcc.2013.12.015 (2014).
90 Frey, N., Katus, H. A., Olson, E. N. & Hill, J. A. Hypertrophy of the heart: a new therapeutic target? *Circulation* **109**, 1580-1589, doi:10.1161/01.CIR.0000120390.68287.BB (2004).
91 Oparil, S. Pathogenesis of ventricular hypertrophy. *J Am Coll Cardiol* **5**, 57B-65B (1985).

92 Barry, S. P., Davidson, S. M. & Townsend, P. A. Molecular regulation of cardiac hypertrophy. *Int J Biochem Cell Biol* **40**, 2023-2039, doi:10.1016/j.biocel.2008.02.020 (2008).
93 Anversa, P., Ricci, R. & Olivetti, G. Quantitative structural analysis of the myocardium during physiologic growth and induced cardiac hypertrophy: a review. *J Am Coll Cardiol* **7**, 1140-1149 (1986).
94 Kiriazis, H. *et al.* Preserved left ventricular structure and function in mice with cardiac sympathetic hyperinnervation. *Am J Physiol Heart Circ Physiol* **289**, H1359-1365, doi:10.1152/ajpheart.01010.2004 (2005).
95 Nayler, W. G., Slade, A., Vaughan Williams, E. M. & Yepez, C. E. Effect of prolonged beta-adrenoceptor blockade on heart weight and ultrastructure in young rabbits. *Br J Pharmacol* **68**, 363-371 (1980).
96 Lockhart, S. T., Turrigiano, G. G. & Birren, S. J. Nerve growth factor modulates synaptic transmission between sympathetic neurons and cardiac myocytes. *J Neurosci* **17**, 9573-9582 (1997).
97 Volgraf, M. *et al.* Allosteric control of an ionotropic glutamate receptor with an optical switch. *Nat Chem Biol* **2**, 47-52, doi:10.1038/nchembio756 (2006).
98 Banghart, M., Borges, K., Isacoff, E., Trauner, D. & Kramer, R. H. Light-activated ion channels for remote control of neuronal firing. *Nat Neurosci* **7**, 1381-1386, doi:10.1038/nn1356 (2004).
99 Lima, S. Q. & Miesenbock, G. Remote control of behavior through genetically targeted photostimulation of neurons. *Cell* **121**, 141-152, doi:10.1016/j.cell.2005.02.004 (2005).
100 Zhang, F. *et al.* The microbial opsin family of optogenetic tools. *Cell* **147**, 1446-1457, doi:10.1016/j.cell.2011.12.004 (2011).
101 Nagel, G. *et al.* Channelrhodopsin-2, a directly light-gated cation-selective membrane channel. *Proc Natl Acad Sci U S A* **100**, 13940-13945, doi:10.1073/pnas.1936192100 (2003).
102 Hegemann, P. & Nagel, G. From channelrhodopsins to optogenetics. *EMBO Mol Med* **5**, 173-176, doi:10.1002/emmm.201202387 (2013).
103 Boyden, E. S., Zhang, F., Bamberg, E., Nagel, G. & Deisseroth, K. Millisecond-timescale, genetically targeted optical control of neural activity. *Nat Neurosci* **8**, 1263-1268, doi:10.1038/nn1525 (2005).
104 Miller, G. Optogenetics. Shining new light on neural circuits. *Science* **314**, 1674-1676, doi:10.1126/science.314.5806.1674 (2006).
105 Deisseroth, K. Optogenetics. *Nat Methods* **8**, 26-29, doi:10.1038/nmeth.f.324 (2011).
106 Zhao, S. *et al.* Improved expression of halorhodopsin for light-induced silencing of neuronal activity. *Brain Cell Biol* **36**, 141-154, doi:10.1007/s11068-008-9034-7 (2008).
107 Bruegmann, T. *et al.* Optogenetic control of heart muscle in vitro and in vivo. *Nat Methods* **7**, 897-900, doi:10.1038/nmeth.1512 (2010).
108 Arrenberg, A. B., Stainier, D. Y., Baier, H. & Huisken, J. Optogenetic control of cardiac function. *Science* **330**, 971-974, doi:10.1126/science.1195929 (2010).
109 Wong, J., Abilez, O. J. & Kuhl, E. Computational Optogenetics: A Novel Continuum Framework for the Photoelectrochemistry of Living Systems. *J Mech Phys Solids* **60**, 1158-1178, doi:10.1016/j.jmps.2012.02.004 (2012).
110 Williams, J. C. *et al.* Computational optogenetics: empirically-derived voltage- and light-sensitive channelrhodopsin-2 model. *PLoS Comput Biol* **9**, e1003220, doi:10.1371/journal.pcbi.1003220 (2013).

111 Boyle, P. M., Karathanos, T. V., Entcheva, E. & Trayanova, N. A. Computational modeling of cardiac optogenetics: Methodology overview & review of findings from simulations. *Comput Biol Med* **65**, 200-208, doi:10.1016/j.compbiomed.2015.04.036 (2015).
112 Jia, Z. *et al.* Stimulating cardiac muscle by light: cardiac optogenetics by cell delivery. *Circ Arrhythm Electrophysiol* **4**, 753-760, doi:10.1161/circep.111.964247 (2011).
113 Hofmann, B. *et al.* Light induced stimulation and delay of cardiac activity. *Lab Chip* **10**, 2588-2596, doi:10.1039/c003091k (2010).
114 Abilez, O. J. *et al.* Multiscale computational models for optogenetic control of cardiac function. *Biophys J* **101**, 1326-1334, doi:10.1016/j.bpj.2011.08.004 (2011).
115 Bingen, B. O. *et al.* Light-induced termination of spiral wave arrhythmias by optogenetic engineering of atrial cardiomyocytes. *Cardiovasc Res* **104**, 194-205, doi:10.1093/cvr/cvu179 (2014).
116 Boyle, P. M., Williams, J. C., Ambrosi, C. M., Entcheva, E. & Trayanova, N. A. A comprehensive multiscale framework for simulating optogenetics in the heart. *Nat Commun* **4**, 2370, doi:10.1038/ncomms3370 (2013).
117 Airan, R. D., Thompson, K. R., Fenno, L. E., Bernstein, H. & Deisseroth, K. Temporally precise in vivo control of intracellular signalling. *Nature* **458**, 1025-1029, doi:10.1038/nature07926 (2009).
118 Ye, H., Daoud-El Baba, M., Peng, R. W. & Fussenegger, M. A synthetic optogenetic transcription device enhances blood-glucose homeostasis in mice. *Science* **332**, 1565-1568, doi:10.1126/science.1203535 (2011).
119 Beiert, T., Bruegmann, T. & Sasse, P. Optogenetic activation of Gq signalling modulates pacemaker activity of cardiomyocytes. *Cardiovasc Res* **102**, 507-516, doi:10.1093/cvr/cvu046 (2014).
120 Zaglia, T. *et al.* Optogenetic determination of the myocardial requirements for extrasystoles by cell type-specific targeting of ChannelRhodopsin-2. *Proc Natl Acad Sci U S A* **112**, E4495-4504, doi:10.1073/pnas.1509380112
1509380112 [pii] (2015).
121 Di Diego, J. M. *et al.* Optical and electrical recordings from isolated coronary-perfused ventricular wedge preparations. *J Mol Cell Cardiol* **54**, 53-64, doi:10.1016/j.yjmcc.2012.10.017 (2013).
122 Wilson, L. D., Jennings, M. M. & Rosenbaum, D. S. Rebuttal to M cells are not present in the ventricular myocardium. Point. *Heart Rhythm* **8**, 1099, doi:10.1016/j.hrthm.2011.04.029 (2011).
123 Wilson, L. D., Jennings, M. M. & Rosenbaum, D. S. Point: M cells are present in the ventricular myocardium. *Heart Rhythm* **8**, 930-933, doi:10.1016/j.hrthm.2011.01.026 (2011).
124 Janse, M. J., Coronel, R. & Opthof, T. Counterpoint: M cells do not have a functional role in the ventricular myocardium of the intact heart. *Heart Rhythm* **8**, 934-937, doi:10.1016/j.hrthm.2010.10.048 (2011).
125 Randall, W. C., Szentivanyi, M., Pace, J. B., Wechsler, J. S. & Kaye, M. P. Patterns of sympathetic nerve projections onto the canine heart. *Circ Res* **22**, 315-323 (1968).
126 Ieda, M. & Fukuda, K. Cardiac innervation and sudden cardiac death. *Curr Cardiol Rev* **5**, 289-295, doi:10.2174/157340309789317904 (2009).
127 Landis, S. C. Rat sympathetic neurons and cardiac myocytes developing in microcultures: correlation of the fine structure of endings with neurotransmitter function in single neurons. *Proc Natl Acad Sci U S A* **73**, 4220-4224 (1976).

128 Potter, D. D., Landis, S. C., Matsumoto, S. G. & Furshpan, E. J. Synaptic functions in rat sympathetic neurons in microcultures. II. Adrenergic/cholinergic dual status and plasticity. *J Neurosci* **6**, 1080-1098 (1986).
129 Zaika, O., Zhang, J. & Shapiro, M. S. Functional role of M-type (KCNQ) K(+) channels in adrenergic control of cardiomyocyte contraction rate by sympathetic neurons. *J Physiol* **589**, 2559-2568, doi:10.1113/jphysiol.2010.204768 (2011).
130 Ogawa, S. *et al.* Direct contact between sympathetic neurons and rat cardiac myocytes in vitro increases expression of functional calcium channels. *J Clin Invest* **89**, 1085-1093, doi:10.1172/JCI115688 (1992).
131 Shcherbakova, O. G. *et al.* Organization of beta-adrenoceptor signaling compartments by sympathetic innervation of cardiac myocytes. *J Cell Biol* **176**, 521-533, doi:10.1083/jcb.200604167 (2007).
132 Tenner, T. E., Jr., Mukherjee, A. & Hester, R. K. Reserpine-induced supersensitivity and the proliferation of cardiac beta-adrenoceptors. *Eur J Pharmacol* **77**, 61-65 (1982).
133 Luttrell, L. M. & Gesty-Palmer, D. Beyond desensitization: physiological relevance of arrestin-dependent signaling. *Pharmacol Rev* **62**, 305-330, doi:10.1124/pr.109.002436 (2010).
134 Khamssi, M. & Brodde, O. E. The role of cardiac beta1- and beta2-adrenoceptor stimulation in heart failure. *J Cardiovasc Pharmacol* **16 Suppl 5**, S133-137 (1990).
135 Bartel, S., Krause, E. G., Wallukat, G. & Karczewski, P. New insights into beta2-adrenoceptor signaling in the adult rat heart. *Cardiovasc Res* **57**, 694-703 (2003).
136 Richter, W. *et al.* Signaling from beta1- and beta2-adrenergic receptors is defined by differential interactions with PDE4. *Embo j* **27**, 384-393, doi:10.1038/sj.emboj.7601968 (2008).
137 Rybin, V. O., Pak, E., Alcott, S. & Steinberg, S. F. Developmental changes in beta2-adrenergic receptor signaling in ventricular myocytes: the role of Gi proteins and caveolae microdomains. *Mol Pharmacol* **63**, 1338-1348, doi:10.1124/mol.63.6.1338 (2003).
138 Inoue, H. & Zipes, D. P. Results of sympathetic denervation in the canine heart: supersensitivity that may be arrhythmogenic. *Circulation* **75**, 877-887 (1987).
139 Stanton, M. S. & Zipes, D. P. Modulation of drug effects by regional sympathetic denervation and supersensitivity. *Circulation* **84**, 1709-1714 (1991).
140 Chen, L. S., Zhou, S., Fishbein, M. C. & Chen, P. S. New perspectives on the role of autonomic nervous system in the genesis of arrhythmias. *J Cardiovasc Electrophysiol* **18**, 123-127, doi:10.1111/j.1540-8167.2006.00590.x (2007).
141 Guzzetti, S. *et al.* Non-linear dynamics and chaotic indices in heart rate variability of normal subjects and heart-transplanted patients. *Cardiovasc Res* **31**, 441-446 (1996).
142 Kaye, D. M. *et al.* Functional and neurochemical evidence for partial cardiac sympathetic reinnervation after cardiac transplantation in humans. *Circulation* **88**, 1110-1118 (1993).
143 Donald, D. E. Myocardial performance after excision of the extrinsic cardiac nerves in the dog. *Circ Res* **34**, 417-424 (1974).
144 Constant, I. *et al.* Spectral analysis of systolic blood pressure and heart rate after heart transplantation in children. *Clin Sci (Lond)* **88**, 95-102 (1995).
145 Donald, D. E. Capacity for exercise after denervation of the heart. *Circulation* **38**, 225-226 (1968).

146 Barber, M. J., Mueller, T. M., Davies, B. G. & Zipes, D. P. Phenol topically applied to canine left ventricular epicardium interrupts sympathetic but not vagal afferents. *Circ Res* **55**, 532-544 (1984).
147 Weksler, N. *et al.* Phenol neurolysis for severe chronic nonmalignant pain: is the old also obsolete? *Pain Med* **8**, 332-337, doi:10.1111/j.1526-4637.2006.00228.x (2007).
148 Freeman, K., Tao, W., Sun, H., Soonpaa, M. H. & Rubart, M. In situ three-dimensional reconstruction of mouse heart sympathetic innervation by two-photon excitation fluorescence imaging. *J Neurosci Methods* **221**, 48-61, doi:10.1016/j.jneumeth.2013.09.005 (2014).
149 Bothwell, M. A., Schechter, A. L. & Vaughn, K. M. Clonal variants of PC12 pheochromocytoma cells with altered response to nerve growth factor. *Cell* **21**, 857-866 (1980).
150 Pfaffl, M. W. A new mathematical model for relative quantification in real-time RT-PCR. *Nucleic Acids Res* **29**, e45 (2001).
151 Schneider, C. A., Rasband, W. S. & Eliceiri, K. W. NIH Image to ImageJ: 25 years of image analysis. *Nat Methods* **9**, 671-675 (2012).
152 Ammirabile, G. *et al.* Pitx2 confers left morphological, molecular, and functional identity to the sinus venosus myocardium. *Cardiovasc Res* **93**, 291-301, doi:10.1093/cvr/cvr314 (2012).
153 Sedmera, D. & Gourdie, R. G. Why do we have Purkinje fibers deep in our heart? *Physiol Res* **63 Suppl 1**, S9-18 (2014).
154 Rohr, S., Kucera, J. P., Fast, V. G. & Kleber, A. G. Paradoxical improvement of impulse conduction in cardiac tissue by partial cellular uncoupling. *Science* **275**, 841-844 (1997).
155 Wilders, R. *et al.* Effects of anisotropy on the development of cardiac arrhythmias associated with focal activity. *Pflugers Arch* **441**, 301-312 (2000).
156 Peters, N. S. & Wit, A. L. Myocardial architecture and ventricular arrhythmogenesis. *Circulation* **97**, 1746-1754 (1998).
157 Goldberger, J. J. *et al.* American Heart Association/American College of Cardiology Foundation/Heart Rhythm Society scientific statement on noninvasive risk stratification techniques for identifying patients at risk for sudden cardiac death: a scientific statement from the American Heart Association Council on Clinical Cardiology Committee on Electrocardiography and Arrhythmias and Council on Epidemiology and Prevention. *Circulation* **118**, 1497-1518 (2008).
158 Campbell, R. W., Murray, A. & Julian, D. G. Ventricular arrhythmias in first 12 hours of acute myocardial infarction. Natural history study. *Br Heart J* **46**, 351-357 (1981).
159 Zheng, Z. J., Croft, J. B., Giles, W. H. & Mensah, G. A. Sudden cardiac death in the United States, 1989 to 1998. *Circulation* **104**, 2158-2163 (2001).
160 Cerrone, M. *et al.* Arrhythmogenic mechanisms in a mouse model of catecholaminergic polymorphic ventricular tachycardia. *Circ Res* **101**, 1039-1048, doi:10.1161/circresaha.107.148064 (2007).
161 Bogun, F. *et al.* Role of Purkinje fibers in post-infarction ventricular tachycardia. *J Am Coll Cardiol* **48**, 2500-2507, doi:10.1016/j.jacc.2006.07.062 (2006).
162 Hayashi, M. *et al.* Novel mechanism of postinfarction ventricular tachycardia originating in surviving left posterior Purkinje fibers. *Heart Rhythm* **3**, 908-918, doi:10.1016/j.hrthm.2006.04.019 (2006).
163 Herron, T. J., Milstein, M. L., Anumonwo, J., Priori, S. G. & Jalife, J. Purkinje cell calcium dysregulation is the cellular mechanism that underlies catecholaminergic

polymorphic ventricular tachycardia. *Heart Rhythm* **7**, 1122-1128, doi:10.1016/j.hrthm.2010.06.010 (2010).
164 Boyden, P. A., Hirose, M. & Dun, W. Cardiac Purkinje cells. *Heart Rhythm* **7**, 127-135, doi:10.1016/j.hrthm.2009.09.017 (2010).
165 Kang, G. *et al.* Purkinje cells from RyR2 mutant mice are highly arrhythmogenic but responsive to targeted therapy. *Circ Res* **107**, 512-519, doi:10.1161/circresaha.110.221481 (2010).
166 Scheinman, M. M. Role of the His-Purkinje system in the genesis of cardiac arrhythmia. *Heart Rhythm* **6**, 1050-1058, doi:10.1016/j.hrthm.2009.03.011 (2009).
167 Li, P. & Rudy, Y. A model of canine purkinje cell electrophysiology and Ca(2+) cycling: rate dependence, triggered activity, and comparison to ventricular myocytes. *Circ Res* **109**, 71-79, doi:10.1161/circresaha.111.246512 (2011).
168 Syed, F. F., Hai, J. J., Lachman, N., DeSimone, C. V. & Asirvatham, S. J. The infrahisian conduction system and endocavitary cardiac structures: relevance for the invasive electrophysiologist. *J Interv Card Electrophysiol* **39**, 45-56, doi:10.1007/s10840-013-9858-7 (2014).
169 Davidenko, J. M. & Antzelevitch, C. Electrophysiological mechanisms underlying rate-dependent changes of refractoriness in normal and segmentally depressed canine Purkinje fibers. The characteristics of post-repolarization refractoriness. *Circ Res* **58**, 257-268 (1986).
170 Wellens, H. J. Forty years of invasive clinical electrophysiology: 1967-2007. *Circ Arrhythm Electrophysiol* **1**, 49-53, doi:10.1161/circep.108.770529 (2008).
171 Saba, S., Wang, P. J. & Estes, N. A., 3rd. Invasive cardiac electrophysiology in the mouse: techniques and applications. *Trends Cardiovasc Med* **10**, 122-132 (2000).
172 Ward, D. E. & Camm, A. J. Methodologic problems in the use of atrial pacing studies for the assessment of A-V conduction. *Clin Cardiol* **3**, 155-162 (1980).
173 Peters, R. W., Scheinman, M. M., Raskin, S. & Desai, J. Determination of His-Purkinje refractoriness in man with His bundle pacing. *Circulation* **60**, 956-959 (1979).
174 Pang, B. J., Kumar, S., Tacey, M. A. & Mond, H. G. Capturing the His-Purkinje system is not possible from conventional right ventricular apical and nonapical pacing sites. *Pacing Clin Electrophysiol* **37**, 724-730, doi:10.1111/pace.12331 (2014).
175 Fenno, L., Yizhar, O. & Deisseroth, K. The development and application of optogenetics. *Annu Rev Neurosci* **34**, 389-412, doi:10.1146/annurev-neuro-061010-113817 (2011).
176 Plazzo, A. P. *et al.* Bioinformatic and mutational analysis of channelrhodopsin-2 protein cation-conducting pathway. *J Biol Chem* **287**, 4818-4825, doi:10.1074/jbc.M111.326207 (2012).
177 Zhang, F., Aravanis, A. M., Adamantidis, A., de Lecea, L. & Deisseroth, K. Circuit-breakers: optical technologies for probing neural signals and systems. *Nat Rev Neurosci* **8**, 577-581, doi:10.1038/nrn2192 (2007).
178 Zhang, F. *et al.* Multimodal fast optical interrogation of neural circuitry. *Nature* **446**, 633-639, doi:10.1038/nature05744 (2007).
179 Chow, B. Y., Han, X. & Boyden, E. S. Genetically encoded molecular tools for light-driven silencing of targeted neurons. *Prog Brain Res* **196**, 49-61, doi:10.1016/b978-0-444-59426-6.00003-3 (2012).
180 Abilez, O. J. Cardiac optogenetics. *Conf Proc IEEE Eng Med Biol Soc* **2012**, 1386-1389, doi:10.1109/embc.2012.6346197 (2012).

181 Entcheva, E. Cardiac optogenetics. *Am J Physiol Heart Circ Physiol* **304**, H1179-1191, doi:10.1152/ajpheart.00432.2012 (2013).
182 Boyle, P. M., Entcheva, E. & Trayanova, N. A. See the light: can optogenetics restore healthy heartbeats? And, if it can, is it really worth the effort? *Expert Rev Cardiovasc Ther* **12**, 17-20, doi:10.1586/14779072.2014.864951 (2014).
183 Sasse, P. Optical pacing of the heart: the long way to enlightenment. *Circ Arrhythm Electrophysiol* **4**, 598-600, doi:10.1161/circep.111.965400 (2011).
184 Nussinovitch, U., Shinnawi, R. & Gepstein, L. Modulation of cardiac tissue electrophysiological properties with light-sensitive proteins. *Cardiovasc Res* **102**, 176-187, doi:10.1093/cvr/cvu037 (2014).
185 Beyer, S., Kelly, R. G. & Miquerol, L. Inducible Cx40-Cre expression in the cardiac conduction system and arterial endothelial cells. *Genesis* **49**, 83-91, doi:10.1002/dvg.20687 (2011).
186 Cha, Y. M. *et al.* Effects of chemical subendocardial ablation on activation rate gradient during ventricular fibrillation. *Am J Physiol* **269**, H1998-2009 (1995).
187 Chen, P. S., Wolf, P. L., Cha, Y. M., Peters, B. B. & Topham, S. L. Effects of subendocardial ablation on anodal supernormal excitation and ventricular vulnerability in open-chest dogs. *Circulation* **87**, 216-229 (1993).
188 Damiano, R. J., Jr. *et al.* The effect of chemical ablation of the endocardium on ventricular fibrillation threshold. *Circulation* **74**, 645-652 (1986).
189 Uhley, H. N. & Rivkin, L. M. Visualization of the left branch of the human atrioventricular bundle. *Circulation* **20**, 419-421 (1959).
190 Taufic, M., Bashour, F. A. & Lewis, F. J. Production of heart block in dogs, under direct vision. *Surg Forum* **5**, 96-101 (1955).
191 Robinson, R. B., Boyden, P. A., Hoffman, B. F. & Hewett, K. W. Electrical restitution process in dispersed canine cardiac Purkinje and ventricular cells. *Am J Physiol* **253**, H1018-1025 (1987).
192 Bailey, J. C., Lathrop, D. A. & Pippenger, D. L. Differences between proximal left and right bundle branch block action potential durations and refractoriness in the dog heart. *Circ Res* **40**, 464-468 (1977).
193 Carmeliet, E. Electrophysiological effects of encainide on isolated cardiac muscle and Purkinje fibers and on the Langendorff-perfused guinea-pig heart. *Eur J Pharmacol* **61**, 247-262 (1980).
194 Persson, F., Andersson, B., Duker, G., Jacobson, I. & Carlsson, L. Functional effects of the late sodium current inhibition by AZD7009 and lidocaine in rabbit isolated atrial and ventricular tissue and Purkinje fibre. *Eur J Pharmacol* **558**, 133-143, doi:10.1016/j.ejphar.2006.11.040 (2007).
195 Denker, S., Lehmann, M., Mahmud, R., Gilbert, C. & Akhtar, M. Effects of alternating cycle lengths on refractoriness of the His-Purkinje system. *J Clin Invest* **74**, 559-570, doi:10.1172/jci111453 (1984).
196 Denker, S., Shenasa, M., Gilbert, C. J. & Akhtar, M. Effects of abrupt changes in cycle length on refractoriness of the His-Purkinje system in man. *Circulation* **67**, 60-68 (1983).
197 Martin, C. A., Grace, A. A. & Huang, C. L. Refractory dispersion promotes conduction disturbance and arrhythmias in a Scn5a (+/-) mouse model. *Pflugers Arch* **462**, 495-504, doi:10.1007/s00424-011-0989-3 (2011).
198 Deng, W., Goldys, E. M., Farnham, M. M. & Pilowsky, P. M. Optogenetics, the intersection between physics and neuroscience: light stimulation of neurons in physiological conditions. *Am J Physiol Regul Integr Comp Physiol* **307**, R1292-R1302, doi:10.1152/ajpregu.00072.2014 (2014).

199 Hall, G., Jacques, S. L., Eliceiri, K. W. & Campagnola, P. J. Goniometric measurements of thick tissue using Monte Carlo simulations to obtain the single scattering anisotropy coefficient. *Biomed Opt Express* **3**, 2707-2719, doi:10.1364/BOE.3.002707 (2012).
200 Aravanis, A. M. *et al.* An optical neural interface: in vivo control of rodent motor cortex with integrated fiberoptic and optogenetic technology. *J Neural Eng* **4**, S143-156, doi:10.1088/1741-2560/4/3/s02 (2007).
201 Roy, A., Ramasubramaniam, R. & Gaonkar, H. A. Empirical relationship between Kubelka-Munk and radiative transfer coefficients for extracting optical parameters of tissues in diffusive and nondiffusive regimes. *J Biomed Opt* **17**, 115006 (2012).
202 Mesradi, M. *et al.* Experimental and analytical comparative study of optical coefficient of fresh and frozen rat tissues. *J Biomed Opt* **18**, 117010, doi:10.1117/1.jbo.18.11.117010 (2013).
203 Clements-Jewery, H., Hearse, D. J. & Curtis, M. J. Phase 2 ventricular arrhythmias in acute myocardial infarction: a neglected target for therapeutic antiarrhythmic drug development and for safety pharmacology evaluation. *Br J Pharmacol* **145**, 551-564, doi:10.1038/sj.bjp.0706231 (2005).
204 Takahashi, Y., Takahashi, A. & Isobe, M. Ventricular fibrillation initiated by premature beats from the ventricular myocardium not associated with the Purkinje system after myocardial infarction. *Heart Rhythm* **5**, 1458-1460, doi:10.1016/j.hrthm.2008.06.008 (2008).
205 Merrill, D. R., Bikson, M. & Jefferys, J. G. Electrical stimulation of excitable tissue: design of efficacious and safe protocols. *J Neurosci Methods* **141**, 171-198, doi:10.1016/j.jneumeth.2004.10.020 (2005).
206 Wikswo, J. P., Jr., Lin, S. F. & Abbas, R. A. Virtual electrodes in cardiac tissue: a common mechanism for anodal and cathodal stimulation. *Biophys J* **69**, 2195-2210, doi:10.1016/s0006-3495(95)80115-3 (1995).
207 Atkinson, A. *et al.* Anatomical and molecular mapping of the left and right ventricular His-Purkinje conduction networks. *J Mol Cell Cardiol* **51**, 689-701, doi:10.1016/j.yjmcc.2011.05.020 (2011).
208 Tusscher, K. H. & Panfilov, A. V. Modelling of the ventricular conduction system. *Prog Biophys Mol Biol* **96**, 152-170, doi:10.1016/j.pbiomolbio.2007.07.026 (2008).
209 Dobrzynski, H. *et al.* Structure, function and clinical relevance of the cardiac conduction system, including the atrioventricular ring and outflow tract tissues. *Pharmacol Ther* **139**, 260-288, doi:10.1016/j.pharmthera.2013.04.010 (2013).
210 Miquerol, L. *et al.* Architectural and functional asymmetry of the His-Purkinje system of the murine heart. *Cardiovasc Res* **63**, 77-86, doi:10.1016/j.cardiores.2004.03.007 (2004).
211 Han, J. & Moe, G. K. Nonuniform Recovery of Excitability in Ventricular Muscle. *Circ Res* **14**, 44-60 (1964).
212 Burton, F. L. & Cobbe, S. M. Dispersion of ventricular repolarization and refractory period. *Cardiovasc Res* **50**, 10-23 (2001).
213 Ahn, D. *et al.* Induction of myocardial infarcts of a predictable size and location by branch pattern probability-assisted coronary ligation in C57BL/6 mice. *Am J Physiol Heart Circ Physiol* **286**, H1201-1207, doi:10.1152/ajpheart.00862.2003 (2004).
214 Furshpan, E. J., Landis, S. C., Matsumoto, S. G. & Potter, D. D. Synaptic functions in rat sympathetic neurons in microcultures. I. Secretion of norepinephrine and acetylcholine. *J Neurosci* **6**, 1061-1079 (1986).

215 Nikolaev, V. O., Bunemann, M., Hein, L., Hannawacker, A. & Lohse, M. J. Novel single chain cAMP sensors for receptor-induced signal propagation. *J Biol Chem* **279**, 37215-37218, doi:10.1074/jbc.C400302200 (2004).
216 Wengrowski, A. M. *et al.* Optogenetic release of norepinephrine from cardiac sympathetic neurons alters mechanical and electrical function. *Cardiovasc Res* **105**, 143-150, doi:10.1093/cvr/cvu258 (2015).
217 Castaldi, A. *et al.* MicroRNA-133 modulates the beta1-adrenergic receptor transduction cascade. *Circ Res* **115**, 273-283, doi:10.1161/CIRCRESAHA.115.303252 (2014).
218 Zareen, N. & Greene, L. A. Protocol for culturing sympathetic neurons from rat superior cervical ganglia (SCG). *J Vis Exp*, doi:10.3791/988 (2009).
219 Yousuf, O. & Spragg, D. ICD Therapy - Can We Make a Life-saving Device Less Lethal? *J Cardiovasc Electrophysiol*, doi:10.1111/jce.12883 (2015).
220 Tomzik, J., Koltermann, K. C., Zabel, M., Willich, S. N. & Reinhold, T. Quality of Life in Patients with an Implantable Cardioverter Defibrillator: A Systematic Review. *Front Cardiovasc Med* **2**, 34, doi:10.3389/fcvm.2015.00034 (2015).
221 Mirowski, M. *et al.* Termination of malignant ventricular arrhythmias with an implanted automatic defibrillator in human beings. *N Engl J Med* **303**, 322-324, doi:10.1056/NEJM198008073030607 (1980).
222 Parsonnet, V. History of cardiac pacing - II. *Am J Cardiol* **41**, 615 (1978).
223 Glavis-Bloom, J. *et al.* Candida and cardiovascular implantable electronic devices: a case of lead and native aortic valve endocarditis and literature review. *Mycoses* **58**, 637-641, doi:10.1111/myc.12391 (2015).
224 Conti, S. *et al.* Electrical storm: A clinical and electrophysiological overview. *World J Cardiol* **7**, 555-561, doi:10.4330/wjc.v7.i9.555 (2015).
225 Moss, A. J. *et al.* Long-term clinical course of patients after termination of ventricular tachyarrhythmia by an implanted defibrillator. *Circulation* **110**, 3760-3765, doi:10.1161/01.CIR.0000150390.04704.B7 (2004).
226 Poole, J. E. *et al.* Prognostic importance of defibrillator shocks in patients with heart failure. *N Engl J Med* **359**, 1009-1017, doi:10.1056/NEJMoa071098 (2008).
227 Daubert, J. P. *et al.* Inappropriate implantable cardioverter-defibrillator shocks in MADIT II: frequency, mechanisms, predictors, and survival impact. *J Am Coll Cardiol* **51**, 1357-1365, doi:10.1016/j.jacc.2007.09.073 (2008).
228 Powell, B. D. *et al.* Survival after shock therapy in implantable cardioverter-defibrillator and cardiac resynchronization therapy-defibrillator recipients according to rhythm shocked. The ALTITUDE survival by rhythm study. *J Am Coll Cardiol* **62**, 1674-1679, doi:10.1016/j.jacc.2013.04.083 (2013).
229 Ruwald, A. C. *et al.* Mortality reduction in relation to implantable cardioverter defibrillator programming in the Multicenter Automatic Defibrillator Implantation Trial-Reduce Inappropriate Therapy (MADIT-RIT). *Circ Arrhythm Electrophysiol* **7**, 785-792, doi:10.1161/CIRCEP.114.001623 (2014).
230 Sweeney, M. O., Sherfesee, L., DeGroot, P. J., Wathen, M. S. & Wilkoff, B. L. Differences in effects of electrical therapy type for ventricular arrhythmias on mortality in implantable cardioverter-defibrillator patients. *Heart Rhythm* **7**, 353-360, doi:10.1016/j.hrthm.2009.11.027 (2010).
231 Ambrosi, C. M. & Entcheva, E. Optogenetics' promise: pacing and cardioversion by light? *Future Cardiol* **10**, 1-4, doi:10.2217/fca.13.89 (2014).
232 Abilez, O. J. Optogenetic LED array for perturbing cardiac electrophysiology. *Conf Proc IEEE Eng Med Biol Soc* **2013**, 1619-1622, doi:10.1109/embc.2013.6609826 (2013).

233 Klimas, A. & Entcheva, E. Toward microendoscopy-inspired cardiac optogenetics in vivo: technical overview and perspective. *J Biomed Opt* **19**, 080701, doi:10.1117/1.jbo.19.8.080701 (2014).
234 Chang Liao, M. L. *et al.* Sensing Cardiac Electrical Activity With a Cardiac Myocyte-Targeted Optogenetic Voltage Indicator. *Circ Res* **117**, 401-412, doi:10.1161/circresaha.117.306143 (2015).
235 Park, S. A., Lee, S. R., Tung, L. & Yue, D. T. Optical mapping of optogenetically shaped cardiac action potentials. *Sci Rep* **4**, 6125, doi:10.1038/srep06125 (2014).
236 Cardenas, N., Dreifus, L. S. & Kimbiris, D. Block in the divisions of the bundle branch systems: recognition and significance of bilateral bundle branch block. *Cardiovasc Clin* **2**, 87-99 (1970).
237 Nussinovitch, U. & Gepstein, L. Optogenetics for in vivo cardiac pacing and resynchronization therapies. *Nat Biotechnol* **33**, 750-754, doi:10.1038/nbt.3268 (2015).
238 Kim, T. I. *et al.* Injectable, cellular-scale optoelectronics with applications for wireless optogenetics. *Science* **340**, 211-216, doi:10.1126/science.1232437 (2013).

Appendix

Research article

Atrogin-1 deficiency promotes cardiomyopathy and premature death via impaired autophagy

Tania Zaglia,[1,2] Giulia Milan,[3] Aaron Ruhs,[4] Mauro Franzoso,[1,2] Enrico Bertaggia,[3] Nicola Pianca,[1,2] Andrea Carpi,[5] Pierluigi Carullo,[6] Paola Pesce,[7] David Sacerdoti,[7] Cristiano Sarais,[8] Daniele Catalucci,[6] Marcus Krüger,[4] Marco Mongillo,[1,2,9] and Marco Sandri[1,3,9,10]

[1]Department of Biomedical Sciences, University of Padova, Padova, Italy. [2]Molecular Cardiology and [3]Muscle Signaling Lab, Venetian Institute of Molecular Medicine, Padova, Italy. [4]Max Planck Institute for Heart and Lung Research, Bad Nauheim, Germany. [5]European Institute of Oncology, Milano, Italy. [6]National Research Council (CNR), Institute of Genetic and Biomedical Research — UOS of Milan, Milan, Italy, and Humanitas Clinical and Research Center, Milan, Italy. [7]Department of Clinical and Experimental Medicine and [8]Department of Cardiac, Thoracic and Vascular Sciences, University of Padova, Padova, Italy. [9]CNR Institute of Neuroscience, Padova, Italy. [10]Telethon Institute of Genetics and Medicine (TIGEM), Napoli, Italy.

Cardiomyocyte proteostasis is mediated by the ubiquitin/proteasome system (UPS) and autophagy/lysosome system and is fundamental for cardiac adaptation to both physiologic (e.g., exercise) and pathologic (e.g., pressure overload) stresses. Both the UPS and autophagy/lysosome system exhibit reduced efficiency as a consequence of aging, and dysfunction in these systems is associated with cardiomyopathies. The muscle-specific ubiquitin ligase atrogin-1 targets signaling proteins involved in cardiac hypertrophy for degradation. Here, using atrogin-1 KO mice in combination with in vivo pulsed stable isotope labeling of amino acids in cell culture proteomics and biochemical and cellular analyses, we identified charged multivesicular body protein 2B (CHMP2B), which is part of an endosomal sorting complex (ESCRT) required for autophagy, as a target of atrogin-1–mediated degradation. Mice lacking atrogin-1 failed to degrade CHMP2B, resulting in autophagy impairment, intracellular protein aggregate accumulation, unfolded protein response activation, and subsequent cardiomyocyte apoptosis, all of which increased progressively with age. Cellular proteostasis alterations resulted in cardiomyopathy characterized by myocardial remodeling with interstitial fibrosis, with reduced diastolic function and arrhythmias. CHMP2B downregulation in atrogin-1 KO mice restored autophagy and decreased proteotoxicity, thereby preventing cell death. These data indicate that atrogin-1 promotes cardiomyocyte health through mediating the interplay between UPS and autophagy/lysosome system and its alteration promotes development of cardiomyopathies.

Introduction

Cardiac muscle mass adapts as a consequence of functional requirements. Increased workload, such as during exercise or chronic disease stresses causing pressure overload, induces cardiomyocyte hypertrophy, while hemodynamic unloading leads to heart atrophy (1–3). Such changes in cell size depend on the equilibrium between the rates of protein synthesis and degradation, both of which are finely regulated by a number of signaling pathways and require a tight control over protein turnover and protein quality control to avoid accumulation of unfolded/misfolded proteins and subsequent ER stress (4–6). Unfolded/misfolded proteins are degraded by the ubiquitin/proteasome system (UPS) and autophagy/lysosome system (7–9). Proteins degraded via UPS are linked covalently by a polyubiquitin chain through a multistep reaction involving different enzymes, named ubiquitin-activating (E1), ubiquitin-conjugating (E2), and ubiquitin ligase (E3) enzymes, the last of which determines substrate specificity and the rate of ubiquitination (5, 10, 11). Atrogin-1 (also known as MAFbx) is a muscle-specific ubiquitin-ligase (12, 13), originally identified as a mediator of muscle atrophy under the control of FoxO transcription factors (14, 15). Similar to skeletal muscle (12), atrogin-1 upregulation in the heart leads to atrophy (16) and regression from calcineurin-dependent cardiac hypertrophy (17–19). However, it has been proposed recently that atrogin-1 inhibition prevents pressure overload induced cardiac hypertrophy (20).

Parallel to the UPS, autophagy is a conserved mechanism, which is upregulated in response to several stressors (21). Autophagy begins with the engulfment of a portion of cytoplasm by a double membrane to form the autophagosome, which, by fusing to lysosome, culminates in the degradation of the sequestered material. Among the key regulators of autophagy, the endosomal sorting complex required for transport (ESCRT) protein complexes have been reported to affect lysosome-autophagosome fusion (22–24). The functionality of both UPS and autophagy/lysosome system independently and of their interplay is essential for cell and tissue homeostasis. Indeed, both primary (e.g., mutations in autophagy-related genes) and secondary (e.g., unfolded protein accumulation) dysfunction in either the UPS or autophagy/lysosome system have been associated with cardiomyopathies and neurodegenerative diseases (4, 25, 26), mainly because the failure of one of the two systems leads to substrate overload and consequent impairment of the other. A common finding in aging is the reduced exercise tolerance due to cardiac dysfunction, which has been attributed to a number of concurrent mechanisms, including increased oxidative damage, activation of unfolded protein response (UPR), and increased rates of apoptotic cardiomyocyte death (27). All these observations suggest that alterations in the UPS and autophagy might be

Authorship note: Tania Zaglia and Giulia Milan, as well as Marco Mongillo and Marco Sandri, contributed equally to this work.

Conflict of interest: The authors have declared that no conflict of interest exists.

Citation for this article: *J Clin Invest.* 2014;124(6):2410–2424. doi:10.1172/JCI66339.

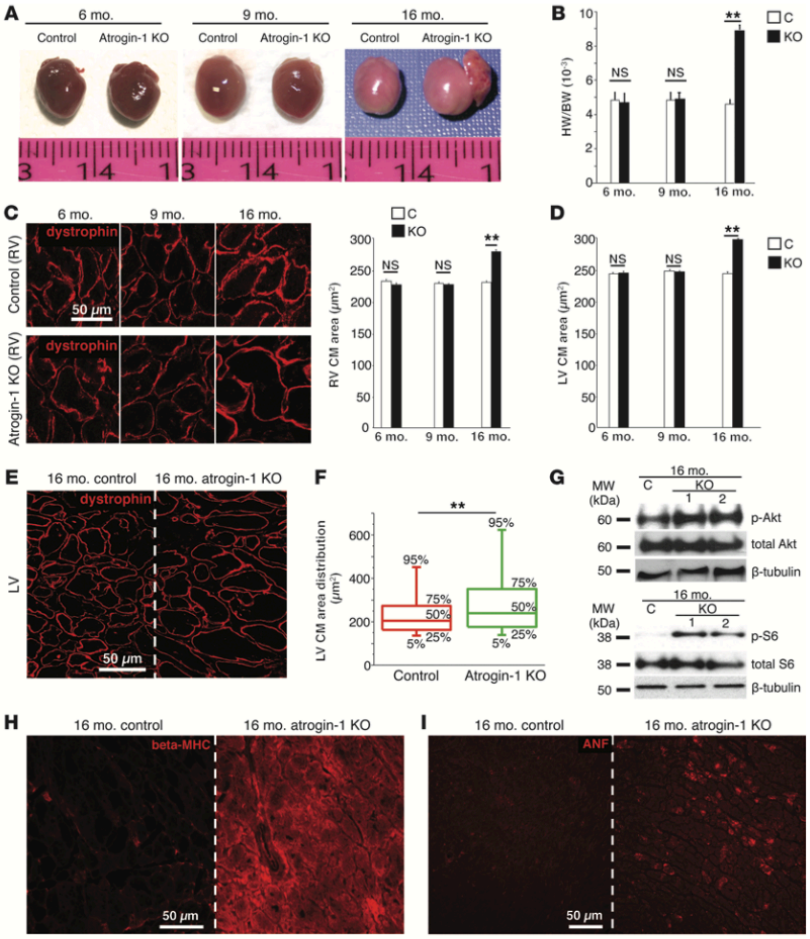

Figure 1

Atrogin-1 KO mice develop an age-related cardiomyopathy. (**A**) Hearts from 6-, 9-, and 16-month-old control and atrogin-1 KO mice. (**B**) Evaluation of the heart weight/body weight (HW/BW) ratio in 6-, 9-, and 16-month-old control (C) and atrogin-1 KO mice. Error bars indicate SEM (**$P < 0.01$; $n = 6$ hearts for each group). (**C**) Confocal immunofluorescence on ventricular cryosections from 6-, 9-, and 16-month-old control and atrogin-1 KO mice stained with an antibody against dystrophin. Images show details from the RV. Scale bar: 50 μm. The morphometric evaluation of RV cardiomyocyte cross-sectional area is also shown. Error bars indicate SEM (**$P < 0.01$; $n = 6$ hearts for each group). (**D**) Evaluation of LV cardiomyocyte area in 6-, 9-, and 16-month-old control and atrogin-1 KO mice. Error bars indicate SEM (**$P < 0.01$; $n = 6$ hearts for each group). (**E**) Confocal immunofluorescence on LV cryosections from aged control and atrogin-1 KO hearts stained with an antibody against dystrophin, showing the mixture of normal sized and hypertrophic cardiomyocytes. Scale bar: 50 μm. (**F**) Evaluation of cardiomyocyte size distribution in the LV of 16-month-old control and atrogin-1 KO hearts. (**G**) Western blotting on ventricular extracts from aged control and atrogin-1 KO hearts. (**H** and **I**) Confocal immunofluorescence analysis of ventricular cryosections from aged control and atrogin-1 KO mice stained with antibodies to (**H**) β-myosin heavy chain and (**I**) atrial natriuretic factor. Scale bar: 50 μm.

centrally involved in cardiac age-related dysfunction. Here, we demonstrate that atrogin-1 mediates the cross-talk between the UPS and autophagy/lysosome system by targeting a key effector of autophagy, the ESCRT-III protein charged multivesicular body protein 2B (CHMP2B), for proteasome degradation. CHMP2B accumulation, in the absence of atrogin-1, causes a block in the autophagy/lysosome system that leads to apoptosis and, with time, to cardiomyopathy and premature death.

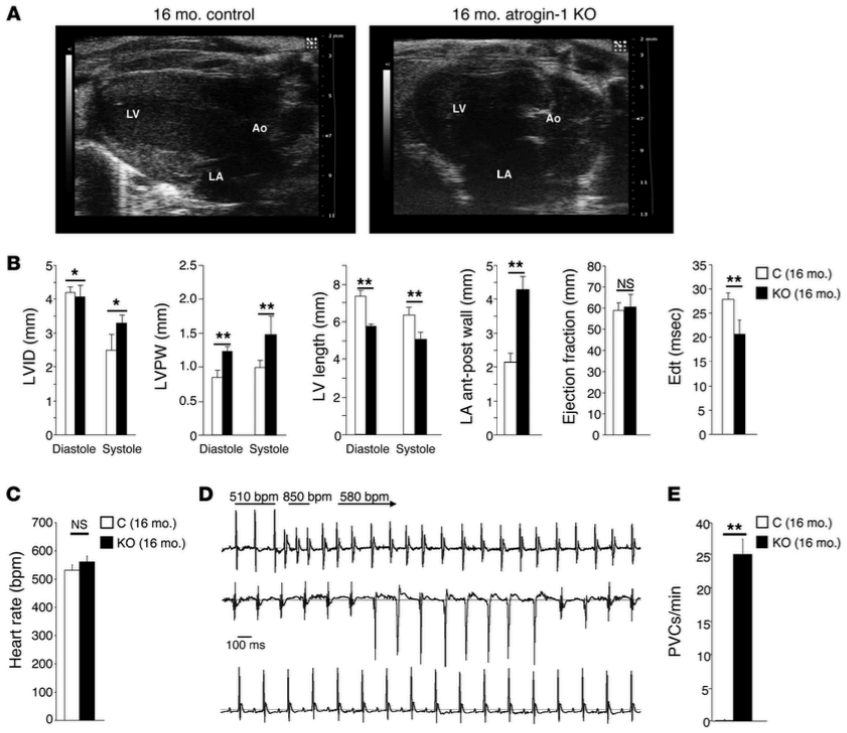

Figure 2

Aged atrogin-1 KO mice show impaired heart function. (**A**) Echocardiographic long-axis view of 16-month-old control and atrogin-1 KO hearts. Ao, aorta. (**B**) Quantification of LV internal diameter (LVID), LV posterior wall (LVPW) thickness, LV length, LA anterior-posterior wall (LA ant-post wall), ejection fraction, and E wave deceleration time (EdT) in 16-month-old control and atrogin-1 KO mice. Error bars indicate SEM (*0.01 < P < 0.05; **P < 0.01; controls, n = 5 mice; atrogin-1 KO, n = 7 mice). (**C**) Quantification of heart rate (bpm) in freely moving aged control and atrogin-1 KO mice. Error bars indicate SEM (n = 4 mice for each group). (**D**) ECG recording in freely moving aged control (bottom) and atrogin-1 KO (top, 2 examples) mice. Atrogin-1 KO mice show runs of ventricular tachycardia. Estimation of heart rate is reported in the first ECG trace from an atrogin-1 KO mouse. (**E**) Quantification of ventricular ectopies per minute in aged control and atrogin-1 KO mice. Error bars indicate SEM (**P < 0.01; n = 4 mice for each group). PVC, premature ventricular complexes.

Results

Genetic ablation of atrogin-1 causes myocardial interstitial fibrosis and cardiomyopathy. Atrogin-1 is a muscle-specific ubiquitin ligase that has been associated with heart diseases, which represents an attractive novel target of cardiovascular therapy. However, the role of atrogin-1 in cardiomyocyte biology as well as its involvement in the molecular mechanism of cardiac dysfunction is largely unexplored. To address the role of atrogin-1 in the regulation of cardiomyocyte proteostasis and function, we monitored the cardiac phenotype of adult atrogin-1 KO mice (6 months old) onward until death and compared it with that of age- and sex-matched atrogin-1 haploinsufficient (atrogin-1$^{+/-}$) mice and C57BL/6J WT controls. At 6 and 9 months old, both cardiac morphology and size were unchanged in atrogin-1 KO mice compared with that in controls (heart weight/body weight: 6 month, atrogin-1 KO vs. controls: 0.0048 ± 0.0004 vs. 0.0047 ± 0.0005; 9 month, atrogin-1 KO vs. controls: 0.0048 ± 0.0004 vs. 0.0047 ± 0.0002) (Figure 1, A and B), and consistently cardiomyocyte cross-sectional areas were identical to those of controls (Figure 1, C and D). At 16 months old, however, hearts of atrogin-1 KO mice appeared abnormal in shape with rounded ventricles, grossly dilated left atrium (LA), and increased heart weight, resulting in higher heart weight/body weight ratios (16 month, atrogin-1 KO vs. controls: 0.0090 ± 0.0003 vs. 0.0046 ± 0.0002) (Figure 1, A and B). In these hearts, cardiomyocyte cross-sectional areas were significantly increased (RV, atrogin-1 KO vs. controls: 279.85 ± 1.52 μm^2 vs. 230.82 ± 1.58 μm^2; LV, atrogin-1 KO vs. controls: 289.34 ± 2.23 μm^2 vs. 236.77 ± 1.64 μm^2) (Figure 1, C and D), and, interestingly, coexistence of hypertrophic and normally sized cardiomyocytes was observed in the LV wall (Figure 1, E and F). Such hypertrophic remodeling in aged atrogin-1 KO hearts was accompanied by an increase in Akt and S6 kinase phosphorylation, both of which regulate protein

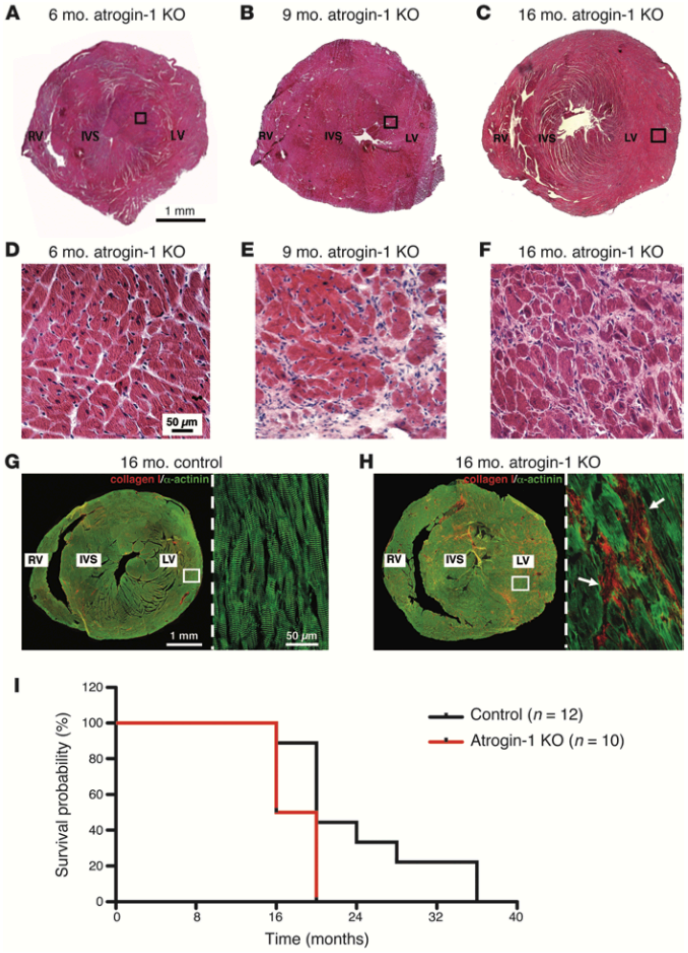

Figure 3
Atrogin-1 KO mice develop myocardial interstitial fibrosis during aging. (**A**–**F**) Hematoxylin-eosin staining on ventricular cryosections from (**A** and **D**) 6-, (**B** and **E**) 9-, and (**C** and **F**) 16-month-old atrogin-1 KO mice, showing the presence of interstitial fibrosis in 9-month-old and 16-month-old atrogin-1 KO hearts. Scale bar: 1 mm (**A**–**C**); 50 μm (**D**–**F**). (**G** and **H**) Confocal immunofluorescence analysis of ventricular cryosections from 16-month-old (**G**) control and (**H**) atrogin-1 KO mice costained with antibodies against collagen I (red signal) and sarcomeric actinin (α-actinin, green signal). The right images in **G** and **H** show high-magnification views of the white boxes in the composite image (left images). White arrows indicate collagen I accumulation in the LV interstitium of atrogin-1 KO hearts. Scale bar: 1 mm (left images); 50 μm (right images). (**I**) Survival probability of male control (black line) and atrogin-1 KO (red line) mice, evaluated by using Kaplan-Meier method. Comparison of control and atrogin-1 KO survival curves was performed by both Mantel-Cox and Gehan-Breslow-Wilcoxon tests. Atrogin-1 KO mice show a significant reduction in the life span, as compared with that of controls ($P < 0.05$).

synthesis (Figure 1G). Reactivation of the fetal isoforms β-myosin heavy chain and atrial natriuretic factor, which is a hallmark of pathologic myocardial hypertrophy (28, 29), was evident in the aged atrogin-1 KO hearts (Figure 1, H and I). Echocardiography demonstrated that 16-month-old atrogin-1 KO hearts had thickened LV wall, without significant systolic dysfunction (ejection fraction, atrogin-1 KO vs. controls: 60.47% ± 10.98% vs. 55.20% ± 12.36%) (Figure 2, A and B, and Supplemental Table 1; supplemental material available online with this article; doi:10.1172/JCI66339DS1). Remarkably, echo-Doppler measurements showed that atrogin-1 KO mice, which had normal diastolic function at 6 and 9 months of age, developed significant impairment in diastolic relaxation at 16 months of age, as demonstrated by a reduction of the E wave deceleration time in the mitral valve inflow pattern measurements (E wave deceleration time, atrogin-1 KO vs. controls: 20.7 ± 2.7 ms vs. 27.8 ± 5.7 ms) (Figure 2B). We next used telemetry monitoring of the ECG to analyze heart rhythm in freely moving mice. Aged atrogin-1 KO mice had unchanged heart rhythm compared with that of controls but showed frequent ventricular ectopies and runs of ventricular tachycardia, both of which indicate increased arrhythmia vulnerability (Figure 2, C–E). These morphological and functional data were well supported by the observation that the myocardial interstitium, which was normal in 6-month-old atrogin-1 KO hearts, showed rare foci of fibrosis at 9 months of age and progressed into diffuse LV and LA fibrosis in the aged KO hearts (Figure 3, A–F, and Supplemental Figure 1, A and B). Such fibrotic remodeling was due to abundant interstitial collagen I and collagen VI deposition, which was predominant in the LV and interventricular septum (IVS) (atrogin-1 KO: collagen I, RV: 5.0% ± 1.4% collagen area per

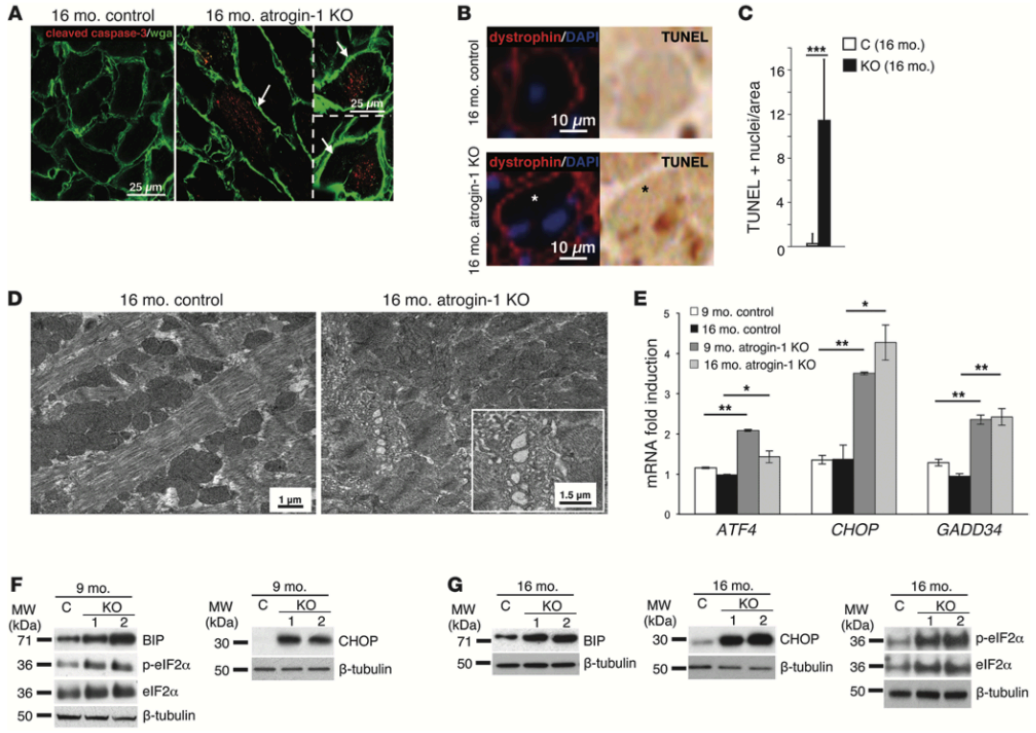

Figure 4
Atrogin-1 KO hearts show increased cardiomyocyte apoptosis and ER stress. (**A**) Confocal immunofluorescence analysis of ventricular cryosections from 16-month-old control and atrogin-1 KO mice costained with wheat germ agglutinin (wga, green signal) and an antibody against the cleaved isoform of caspase-3 (red signal). Arrows indicate apoptotic cardiomyocytes in atrogin-1 KO hearts. Scale bar: 25 μm. (**B**) Immunofluorescence and bright-field images of heart cryosections from aged control and atrogin-1 KO mice simultaneously stained with an antibody to dystrophin and used for TUNEL assay (brown signal). Nuclei were counterstained with DAPI (blue signal). The asterisks indicate an apoptotic cardiomyocyte in an atrogin-1 KO heart. Scale bar: 10 μm. (**C**) Quantification of TUNEL-positive nuclei in aged control and atrogin-1 KO hearts. Error bars indicate SEM (***$P < 0.001$; $n = 6$ hearts for each group). (**D**) Electron micrographs of ventricular thin sections from aged control and atrogin-1 KO mice. The inset shows abnormal ER cisternae in atrogin-1 KO cardiomyocytes. Scale bar: 1 μm; 1.5 μm (inset). (**E**) Real-time quantitative PCR analysis of ventricular extracts from 9- and 16-month-old control and atrogin-1 KO mice demonstrating upregulation of genes involved in ER stress. Error bars indicate SEM (*$0.01 < P < 0.05$; **$P < 0.01$; $n = 5$ hearts for each group). (**F** and **G**) Western blotting on ventricular extracts from (**F**) 9- and (**G**) 16-month-old control and atrogin-1 KO mice, showing a marked increase of ER stress activation markers in atrogin-1 KO hearts.

total area; IVS: 12.0% ± 1.6% collagen area per total area; LV: 16.0% ± 2.3% collagen area per total area; controls: collagen I, RV: 1.2% ± 0.3% collagen area per total area; IVS: 1.5% ± 0.5% collagen area per total area; LV: 1.5% ± 0.5% collagen area per total area) (Figure 3, G and H, and Supplemental Figure 1, A–D). Our findings indicate that atrogin-1 KO mice progressively develop cardiomyopathy with interstitial fibrosis, diastolic dysfunction accompanied by intraventricular conduction defects, and secondary LA and ventricular remodeling, all of which are common features of cardiomyopathies with a restrictive pattern (30). In further support of this, aged atrogin-1 KO mice had reduced tolerance to treadmill exercise compared with that of age-matched controls and shortened life span (Figure 3I and Supplemental Figure 1E).

Increased apoptosis and ER stress in atrogin-1–null hearts. The presence of interstitial fibrosis in atrogin-1 KO hearts prompted us to investigate whether increased apoptosis rates were detectable. The number of apoptotic cardiomyocytes, assessed either using detection of the cleaved form of caspase-3 or performing TUNEL assay, was increased already in 9-month-old hearts, in which myocardial fibrotic remodeling was still moderate (Supplemental Figure 2A). In aged KO mice, apoptotic nuclei were mainly detected within the LV and in the IVS (TUNEL: LV, atrogin-1 KO vs. control: 11.37 ± 5.50 vs. 0.13 ± 0.47 nuclei per field; IVS, atrogin-1 KO vs. control: 7.22 ± 3.58 vs. 0.36 ± 0.60 nuclei per field) (Figure 4, A–C), both regions characterized by the highest degree of fibrosis (Figure 3, G and H). We thus used electron microscopy to investigate

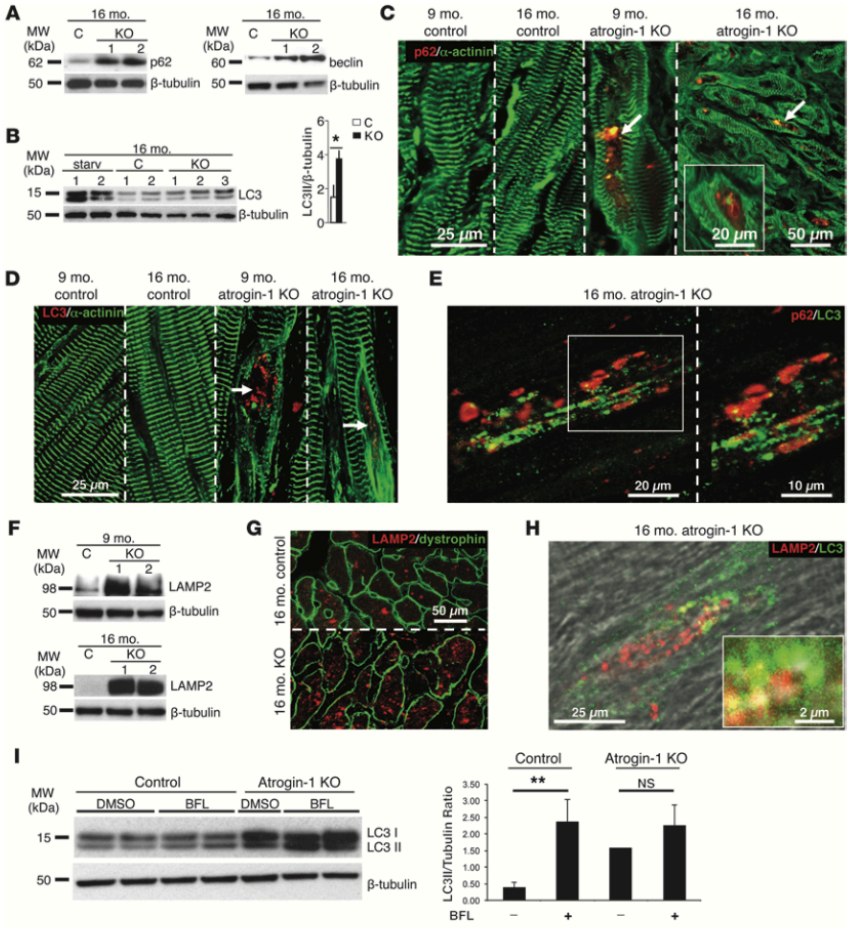

Figure 5

Atrogin-1 ablation leads to impairment in the autophagy flux. (**A** and **B**) Western blotting on ventricular extracts from aged control, atrogin-1 KO, and starved control (starv) mice. The LC3-II/β-tubulin ratio was evaluated in control and atrogin-1 KO hearts. Error bars indicate SEM (*$P < 0.01$; $n = 6$ for each group). (**C** and **D**) Confocal immunofluorescence on ventricular cryosections from 9- and 16-month-old control and atrogin-1 KO mice costained with antibodies against sarcomeric actinin (α-actinin) and (**C**) p62 or (**D**) LC3, showing p62 and LC3 aggregates in both adult and aged atrogin-1 KO cardiomyocytes (arrows). Scale bar: 20 μm (inset in **C**); 25 μm (**C**, 9- and 16-month-old control and 9-month-old atrogin-1 KO, and **D**); 50 μm (**C**, 16-month-old atrogin-1 KO). (**E**) Confocal 3D reconstruction of a ventricular cardiomyocyte from an aged atrogin-1 KO mouse costained with antibodies against p62 and LC3. Scale bar: 20 μm (left image); 10 μm (right image). (**F**) Western blotting on ventricular extracts from 9- and 16-month-old control and atrogin-1 KO hearts, showing LAMP2 accumulation in atrogin-1 KO hearts. (**G**) Confocal immunofluorescence on ventricular cryosections from aged control and atrogin-1 KO mice costained with antibodies against LAMP2 and dystrophin. Scale bar: 50 μm. (**H**) Confocal 3D reconstruction of a ventricular cardiomyocyte from aged atrogin-1 KO mice costained with antibodies against LAMP2 and LC3. Scale bar: 30 μm; 5 μm (inset). (**I**) Western blotting on ventricular extracts from aged control and atrogin-1 KO mice treated either with DMSO or the lysosome inhibitor bafilomycin (BFL). The LC3-II/β-tubulin ratio was evaluated in DMSO- and BLF-treated control and atrogin-1 KO hearts. Error bars indicate SEM (**$P < 0.01$; $n = 6$ for each group).

cardiomyocyte ultrastructure and gain insight into the cellular mechanisms leading to apoptosis in the atrogin-1 KO hearts. This analysis revealed cardiomyocyte areas with diffuse sarcomeric disarray and expansion of ER cisternae. Moreover, within the region of ER proliferation, we found small electron-pale mitochondria (Figure 4D and Supplemental Figure 2B). These ultrastructural features are consistent with activation of the ER stress response, which was evaluated by assessing UPR genes (e.g., *ATF4* and its

Table 1
Proteins involved in intracellular vesicle trafficking and maturation

Protein name	Identification code
Activator of multicatalytic protease subunit 3	P61290
Bmi-1 upstream gene protein	Q63829
NudC domain-containing protein 2	Q9CQ48
NEDD9-interacting protein	Q8VDP3
Regulator of microtubule dynamics protein 3	Q3UJU9
Endoglin	Q63961
Dynein light chain Tctex-type 3	P56387
Coatomer subunit α	Q8CIE6
Adducin 3 (γ)	Q9QYB5
Bcl-2–associated transcription factor 1	Q8K019
Asparaginyl endopeptidase, legumain	O89017
Cytoplasmic FMR1-interacting protein 2	Q5SQX6
Calgranulin-B	P31725
ESCRT-II complex subunit VPS25	Q9CQ80
90-kDa ribosomal protein S6 kinase 3	QSWUT3
Ub-activating enzyme E1 domain-containing protein 1	Q3U8X9
SEC22 vesicle-trafficking protein homolog	O08547
BRISC complex subunit Abro1	Q3TCJ1
Proteasome subunit β type-8	P28063
Fcho2 protein	Q3UQN2
CHMP2B	**Q8BJF9**
Ribosome maturation protein SBDS	P70122
28S ribosomal protein S36	Q9CQX8
Calpain-8	Q91VA3
Calcium/calmodulin-dependent 3,5-cyclic nucleotide phosphodiesterase 1C	Q64338
Isoamyl acetate-hydrolyzing esterase 1 homolog	Q9DB29
Coatomer subunit ε	O89079
5-AMP–activated protein kinase subunit β-1	Q9R078
Haptoglobin	Q61646
Kinectin	Q61595
Hepatoma-derived growth factor-related protein 2	Q3UMU9
Rab4-interacting protein	Q8BIJ7

Proteins that accumulated after 9 months in atrogin-1 KO hearts, as compared with control hearts, are shown. Bold font was used to highlight that, among the proteins accumulated in atrogin-1 KO hearts, we focused our attention on the ESCRT-III protein, CHMP2B.

downstream targets *CHOP* and *GADD34*) and protein markers (e.g., eIF2α, CHOP, and the ER stress chaperone BIP). Interestingly, upregulation of UPR genes, phosphorylation of eIF2α, and BIP and CHOP accumulation were detected in atrogin-1 KO hearts and were already present in 9-month-old animals, prior to the onset of overt myocardial alterations ultimately leading to cardiomyopathy (Figure 4, E–G), strongly supporting that activation of ER stress preceded apoptosis and subsequent myocardial fibrosis.

The autophagy/lysosome machinery is impaired in atrogin-1–null hearts. We have demonstrated previously that, in skeletal muscles, impairment of autophagy leads to intracellular protein accumulation and increased apoptosis (31, 32), and skeletal muscle–specific inhibition of autophagy causes UPR activation (33). Moreover, interplay between UPS and autophagy has been proposed recently in the setting of neurodegenerative diseases (34), indicating that impairment of UPS impinges on the correct function of the autophagy/lysosome system. Interestingly, atrogin-1 KO hearts were characterized by ultrastructural features similar to those of autophagy-defective muscles, such as sarcomeric disarray and changes in mitochondrial morphology (33). Therefore, we assessed the state of the autophagy/lysosome system in adult and aged atrogin-1 KO hearts. Accumulation of Bnip3 (data not shown) and beclin-1 proteins (Figure 5A) indicated that autophagy was induced in the atrogin-1 KO hearts. However, we detected increased levels of p62 and lipidated LC3 proteins (Figure 5, A and B), a finding consistent with autophagy impairment (35). In line with this, immunofluorescence revealed that those atrogin-1 KO cardiomyocytes that showed sarcomeric disruption had abundant p62 aggregates and LC3 puncta (Figure 5, C and D, and Supplemental Figure 3A). Importantly, LC3 and p62 staining did not colocalize (Figure 5E and Supplemental Figure 3, B–D), suggesting that LC3-positive puncta are truly autophagosomes and are not due to LC3 sequestration into p62-positive protein aggregates. Western blot and immunofluorescence analyses revealed an increase in the amount of the lysosomal marker LAMP2 and in lysosome number in atrogin-1–null cardiomyocytes (Figure 5, F and G). We thus sought to determine whether autophagic and lysosomal markers colocalized, using coimmunofluorescence for LC3 and LAMP2, which demonstrated that the majority of autophagosomes were juxtaposed to lysosomes but did not colocalize (Figure 5H and Supplemental Figure 4). To further confirm that ablation of atrogin-1 causes a block of the autophagy flux, we treated adult control and atrogin-1 KO mice with bafilomycin, an inhibitor of autophagosome/lysosome fusion. Consistent with our hypothesis, bafilomycin increased the LC3-II band in control mice, while it did not elicit any significant change in atrogin-1 KO hearts (Figure 5I). Altogether, these results suggest that, in atrogin-1 KO cardiomyocytes, despite normal autophagy induction, autophagosome/lysosome fusion is compromised, culminating in the block of the autophagic flux.

The ESCRT-III protein CHMP2B accumulates in atrogin-1–null hearts. In order to explain how the lack of atrogin-1, a ubiquitin ligase so far associated with the proteasomal function, leads to inhibition of the autophagy/lysosome system, we considered the possibility that atrogin-1 regulates the turnover of proteins involved in the autophagy/lysosome machinery. To address this issue, we used in vivo stable isotope labeling of amino acids in cell culture (SILAC) mass spectrometry analysis to compare heart protein turnover rates in the 9-month-old atrogin-1 KO and control mice. Metabolic protein profiling with labeled amino acids (pulsed SILAC) is a straightforward approach to assess changes in protein turnover. Here, we fed the mice for 2 weeks with a diet containing a labeled isotope of the essential amino acid lysine (^{13}C6 lysine [Lys-6]). Subsequent mass spectrometry in heart tissue extracts allowed, for every protein detected, quantification of both its absolute amount and the Lys-6–incorporating fraction (newly synthesized within the diet period), thus inferring the protein turnover rate. Consistent with the reduced efficiency of autophagy/lysosome system in atrogin-1 KO hearts, pulsed SILAC experiments demonstrated that substrates of lysosomes (36), including Tau, filamin C, GAPDH, and BAG3, had decrease protein turnover and/or increased protein concentration (Supplemental Tables 2 and 3).

Given that our results indicate that the maturation and fusion of autophagosome/lysosome vesicle is impaired in KO hearts, we selected among the proteins accumulated in atrogin-1–null hearts 32 candidate proteins involved in vesicular trafficking (Table 1 and Supplemental Table 4). We further sorted these hits for biological function and focused on the presence of 2 ESCRT proteins, VPS25 and CHMP2B, that belong to ESCRT-II and

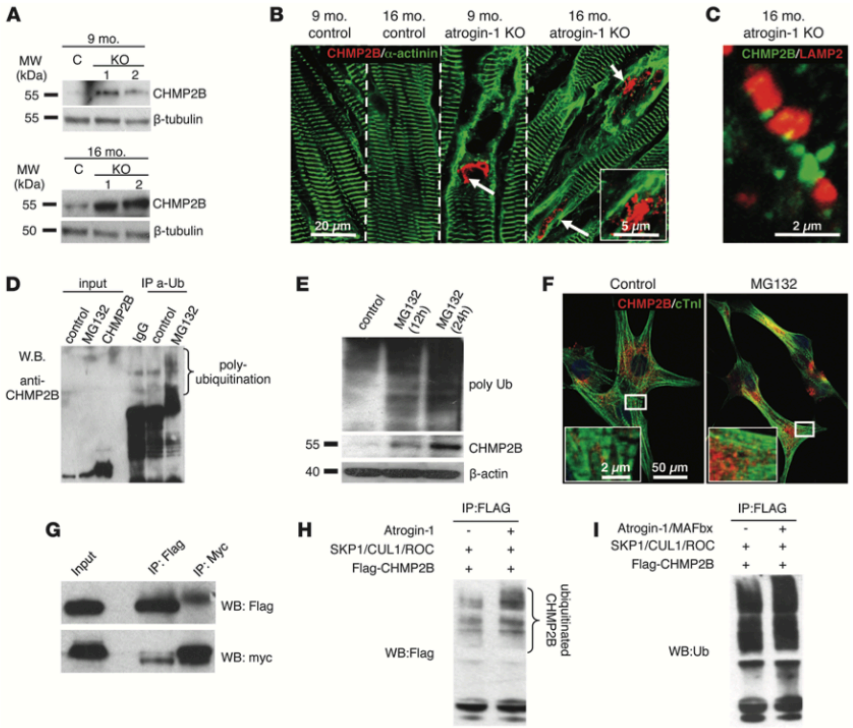

Figure 6

The ESCRT-III protein CHMP2B is a novel target of atrogin-1. (**A**) Western blotting on ventricular extracts from 9- and 16-month-old control and atrogin-1 KO mice. (**B**) Confocal immunofluorescence on ventricular cryosections from 9- and 16-month-old control and atrogin-1 KO mice costained with antibodies against sarcomeric actinin (α-actinin) and CHMP2B. White arrows show CHMP2B accumulation. Scale bar: 20 μm; 5 μm (inset). (**C**) Confocal 3D reconstruction of a ventricular cardiomyocyte costained with antibodies to LAMP2 and CHMP2B. Note no coexpression of LAMP2 and CHMP2B. Scale bar: 2 μm. (**D**) Immunoprecipitation with an anti-CHMP2B antibody on protein extracts from control and MG132-treated cultured cardiomyocytes, showing CHMP2B polyubiquitination upon UPS block. (**E**) Western blotting on protein extracts from control and MG132-treated cultured cardiomyocytes, showing CHMP2B accumulation upon UPS inhibition. (**F**) Confocal immunofluorescence on control and MG132-treated cultured cardiomyocytes costained with antibodies to cardiac troponin I (cTnI) and CHMP2B. Note CHMP2B accumulation in cardiomyocyte areas with sarcomeric disruption. Scale bar: 50 μm; 2 μm (insets). (**G**) Cultured cardiomyocytes were cotransfected with myc-tag atrogin-1 and flag-tag CHMP2B, proteins were isolated and used for coimmunoprecipitation analysis. Note that CHMP2B coimmunoprecipitates with atrogin-1, indicating a direct interaction between CHMP2B and atrogin-1. (**H** and **I**) Immunoprecipitation with an antibody specific for flag-tag (CHMP2B) on extracts from the tibialis anterior of control mice transfected by electroporation with vectors encoding for CHMP2B, SKP1, CUL1, and ROC in the presence or the absence of atrogin-1. The Western blots show increased (**H**) higher molecular weights and (**I**) ubiquitination of CHMP2B in the presence of atrogin-1, as compared with controls.

ESCRT-III complexes, respectively. ESCRT proteins are necessary for autophagosome formation, and they have been shown to have a role in autophagosome/lysosome fusion and/or in sealing the membrane of the autophagosome (37). Interestingly, a mutation in CHMP2B causing its altered turnover has been linked to the block of autophagy and subsequent neurodegeneration (38), and we thus focused on this protein. Western blotting and immunofluorescence demonstrated that CHMP2B was increased in atrogin-1 KO hearts already at 9 months of age and accumulated further at 16 months (Figure 6, A and B). Whereas in control hearts CHMP2B distributed homogenously throughout the cardiomyocyte, in atrogin-1 KO hearts, it was found only in large aggregates in areas depleted of sarcomeric proteins (Figure 6B and Supplemental Figure 5, A and B). Compared with the controls, CHMP2B staining only minimally overlapped with the lysosomal marker LAMP2 in the KO cardiomyocytes (Figure 6C and Supplemental Figure 5C), suggesting that impaired CHMP2B clearance may result in incomplete autophagic flux.

CHMP2B is a target of atrogin-1. We used in vitro experiments to directly test the hypothesis that CHMP2B is degraded by the UPS upon interaction with atrogin-1. WT rat neonatal cardiomyocytes were treated with the proteasome inhibitor MG132, which

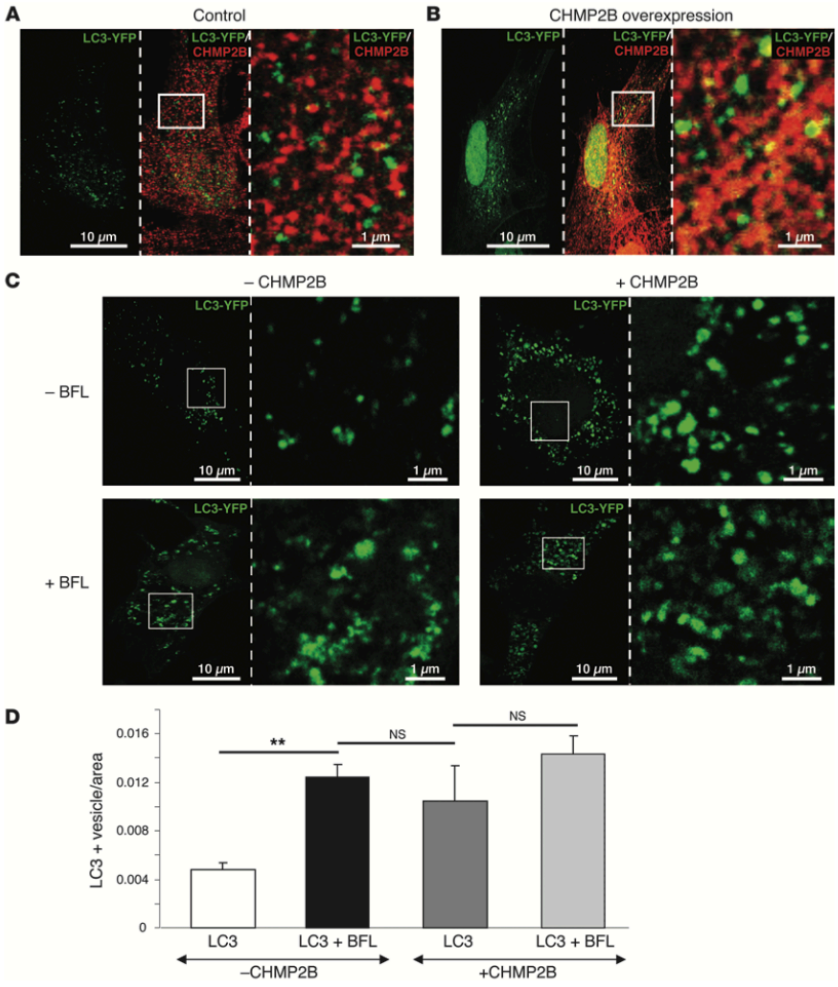

Figure 7
CHMP2B overexpression causes an impairment in the autophagy flux per se. (**A** and **B**) Confocal immunofluorescence analysis of neonatal WT cardiomyocytes transfected either with (**A**) LC3-YFP (green signal) or (**B**) LC3-YFP/CHMP2B and stained with an antibody against CHMP2B (red signal). (**C**) Cultured neonatal cardiomyocytes were transfected either with YFP-LC3 (green signal, –CHMPB) or cotransfected with YFP-LC3– and CHMP2B-expressing vectors (+CHMP2B). Autophagosomes were analyzed by confocal microscopy. The same analysis was performed also in the presence of the autophagy inhibitor bafilomycin (+BFL). The right-most images in **A**–**C** show high-magnification views of the white boxes in the left images. Scale bar: 10 μm (left and middle images); 1 μm (right images). (**D**) Quantification of the total number of YFP-LC3 vesicles in cardiomyocytes both at baseline and upon CHMP2B overexpression both in presence and absence of bafilomycin. Error bars indicate SEM (**$P < 0.01$; $n = 50$ cardiomyocytes for each group).

caused CHMP2B polyubiquitination (Figure 6D) and accumulation (Figure 6E) that occurred predominantly in areas depleted of sarcomeric proteins (Figure 6F and Supplemental Figure 6). In addition, flag-tagged CHMP2B coimmunoprecipitated with myc-tagged atrogin-1 in cells cotransfected with atrogin-1 and CHMP2B (Figure 6G). Atrogin-1 is a ubiquitin ligase belonging to the SCF family that binds the substrate and forms a complex with SKP1/CUL1/ROC to transfer ubiquitin from the E2 enzyme to the substrate. Importantly, when atrogin-1 was coexpressed with the SKP1/CUL1/ROC complex in skeletal muscles, it enhanced

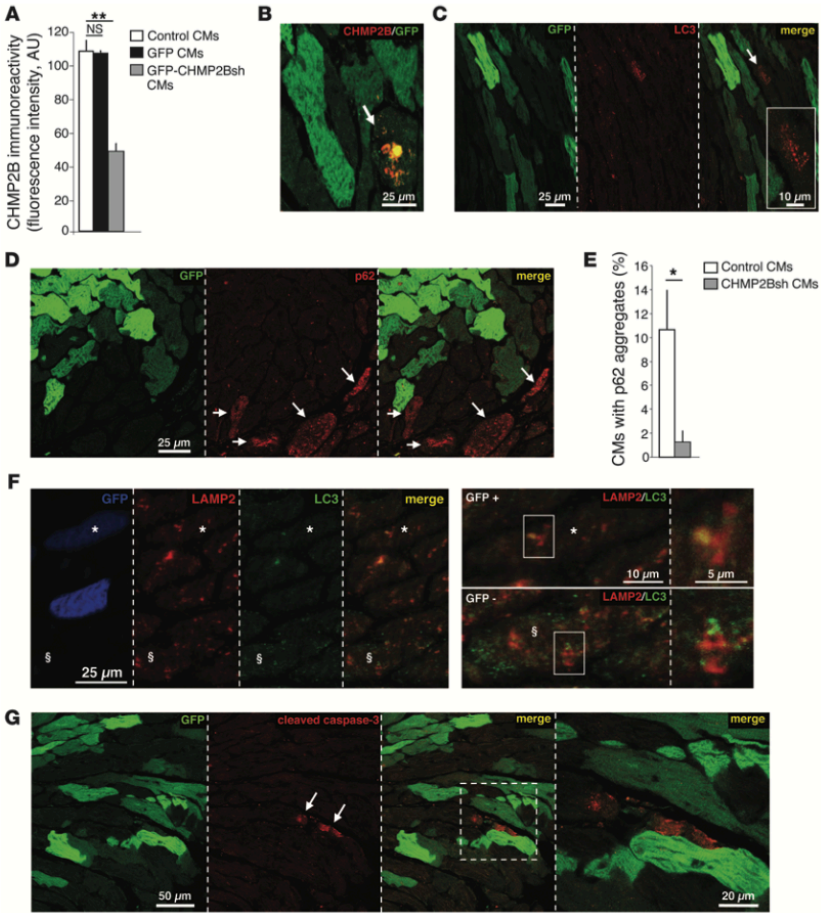

Figure 8

CHMP2B knockdown protects atrogin-1 KO hearts from block of autophagy and cardiomyocyte apoptosis. (**A**) Evaluation of mean CHMP2B fluorescence intensity in cryosections from AAV9-GFP-U6-CHMP2Bsh– and AAV9-GFP–treated atrogin-1 KO mice, costained with antibodies to CHMP2B and GFP. Both control (GFP^-) and silenced GFP^+ cardiomyocytes were analyzed. Error bars represent SEM (**$P < 0.01$; $n = 800$ cardiomyocytes from 4 hearts). CHMP2Bsh cardiomyocytes show a significant decrease in CHMP2B fluorescence, as compared with that of controls. No decrease in CHMP2B fluorescence was observed in cardiomyocytes transduced with control viral vector. (**B**) 3D reconstruction of a cryosection from an AAV9-GFP-U6-CHMP2Bsh–treated atrogin-1 KO mouse costained with antibodies to CHMP2B and GFP, showing no CHMP2B accumulation in GFP^+ cells. The white arrow indicates GFP-negative, nonsilenced cells with CHMP2B aggregates visible. Scale bar: 25 μm. (**C** and **D**) Confocal immunofluorescence on cryosections from AAV9-GFP-U6-CHMP2Bsh–treated atrogin-1 KO mice, costained with antibodies to GFP and (**C**) LC3 or (**D**) p62, showing no accumulation of LC3 and p62 in GFP^+ CHMP2Bsh cardiomyocytes (arrows). Scale bar: 25 μm; 10 μm (inset in **C**). (**E**) Evaluation of percentage of p62-accumulating cardiomyocytes in GFP^- noninfected and GFP^+ CHMP2Bsh cells, showing that CHMP2B silencing prevents p62 accumulation. Error bars represent SEM (*$0.01 < P < 0.05$; $n = 450$ cardiomyocytes from 4 hearts). (**F**) Confocal immunofluorescence on cryosections from AAV9-GFP-U6-CHMP2Bsh–treated atrogin-1 KO mice, costained with antibodies to GFP (blue signal), LC3 (green signal), and LAMP2 (red signal), showing colocalization of LC3 and LAMP2 in GFP^+ CHMP2Bsh cardiomyocytes. Asterisks indicate GFP-positive, CHMP2Bsh cardiomyocytes. Section symbols indicate GFP-negative, nonsilenced cardiomyocytes. Higher-magnification views of boxed images appears to the right. Scale bar: 25 μm (costaining images); 5 μm (right colocalization images); 10 μm (left colocalization images). (**G**) Confocal immunofluorescence on cryosections from AAV9-GFP-U6-CHMP2Bsh–treated atrogin-1 KO mice costained with antibodies to GFP and cleaved caspase-3. Higher-magnification views of boxed images appears to the right. Arrows indicate GFP-negative, nonsilenced cardiomyocytes showing cleaved caspase-3 expression. Scale bar: 50 μm (left 3 images); 20 μm (right-most image).

CHMP2B ubiquitination (Figure 6H). Altogether, these data indicate that atrogin-1 interacts directly with CHMP2B and mediates its targeting to the UPS for degradation.

Since our in vivo results also suggest that accumulation of CHMP2B in atrogin-1 KO hearts may result in autophagy impairment, we used CHMP2B overexpression to test the hypothesis that accumulation of this ESCRT-III protein impairs autophagic flux in normal cardiomyocytes. Cells were transiently transfected with YFP-LC3 to label autophagic vesicles, thus enabling quantification of the cell fraction occupied by autophagosomes with confocal microscopy. Consistent with our hypothesis, CHMP2B overexpression was sufficient to increase the number of YFP-LC3 vesicles (Figure 7, A–C). Importantly, bafilomycin treatment did not increase LC3-positive puncta in CHMP2B-overexpressing cardiomyocytes, further supporting the concept that CHMP2B accumulation negatively regulates the autophagic flux (Figure 7, C and D).

Collectively, our in vitro data corroborate the in vivo findings and demonstrate that CHMP2B is a molecular target of atrogin-1 and support the concept that the failure to degrade CHMP2B results in its accumulation and consequent block of autophagy.

In vivo silencing of CHMP2B in atrogin-1 KO cardiomyocytes removes the block of autophagy and decreases apoptosis. Based on our observations, we hypothesized that CHMP2B downregulation in atrogin-1 KO hearts would reduce its accumulation and minimize its inhibitory effect on autophagy, thus reducing UPR activation and protecting cardiomyocytes from apoptosis. To this purpose, 9-month-old atrogin-1 KO mice were transduced with an adeno-associated viral vector (AAV9) encoding both small hairpin RNA (shRNA) against the *CHMP2B* gene and GFP to label infected cells. Four weeks after infection, about 50% of the cardiomyocytes expressed GFP and had reduced immunoreactivity for anti-CHMP2B antibody (mean CHMP2B fluorescence intensity: GFP-positive cardiomyocytes, 108 ± 8 AU; non-GFP-expressing cardiomyocytes, 44 ± 2 AU), indicating that CHMP2B was significantly knocked down in infected cells (Figure 8A and Supplemental Figure 7A). No decrease in CHMP2B fluorescence was observed in cardiomyocytes from hearts transduced with a control adeno-associated viral vector (AAV9) encoding GFP (mean CHMP2B fluorescence intensity: GFP-positive cardiomyocytes, 108 ± 8 AU; non-GFP-expressing cardiomyocytes: 108 ± 0.3 AU) (Figure 8A and Supplemental Figure 7B). Remarkably, in the shRNA-treated mice, most of the nontransduced cells had intracellular CHMP2B aggregates (Figure 8B, white arrow), which were never observed in GFP-positive cardiomyocytes. Furthermore, LC3 and p62 aggregates, which were frequently detected in cardiomyocytes of 9-month-old atrogin-1 KO mice (Figure 8, C–E), were present in cardiomyocytes that did not express shRNAs against CHMP2B but were never observed in cells that expressed oligos against CHMP2B (Figure 8, C–E), suggesting that knockdown of CHMP2B restored normal autophagy. That CHMP2B knockdown restored the autophagic flux in atrogin-1 KO mice was further supported by the colocalization of autophagosomes and lysosomes in CHMP2B-downregulated cardiomyocytes (Figure 8F). Moreover, while a marked fraction of GFP-negative cardiomyocytes expressed cleaved caspase-3, apoptosis markers were never expressed in cardiomyocytes in which CHMP2B was knocked down (Figure 8G). These results validate the notion that the reduction of CHMP2B protein level protects atrogin-1 KO cardiomyocytes from the block of autophagy and induction of cell death resulting from CHMP2B proteotoxicity.

Discussion

Tight regulation of proteostasis plays a housekeeping cellular function in postmitotic tissues, such as the myocardium and the nervous tissue, that rely critically on mechanisms to control both the quality of newly synthesized proteins and the efficient removal of damaged and unfolded/misfolded proteins. The coordinated work of the UPS and the autophagy/lysosome system (7–9) is necessary, i.e., when UPS targets are too large/too numerous to be degraded by the proteasome, autophagy must intervene. Here, we identify a novel link between UPS and autophagy and show that the muscle-specific ubiquitin ligase atrogin-1 controls turnover of the ESCRT-III family protein CHMP2B, which controls the autophagy system (39). In atrogin-1 KO hearts, the primary failure to regulate CHMP2B turnover causes its intracellular aggregation (Figure 6B and Supplemental Figure 5B), contributing to the secondary impairment of autophagy that, by amplifying unfolded/misfolded proteotoxicity, ensues in cardiomyopathy. These results highlight the importance of regulated proteolysis in the heart and show that the loss of atrogin-1 per se is sufficient to cause cardiac damage, which leads to cardiomyopathy when protein quality control becomes less efficient, as occurring in aging (ref. 25 and Figure 9).

Proteotoxicity cardiomyopathy in the atrogin-1 KO mice. Initially, atrogin-1 was identified as a mediator of skeletal muscle atrophy and being involved in the degradation of calcineurin and the activation of FoxO1 and FoxO3 transcription factors (18, 19, 40, 41); more recently, a role in the proteolysis of the NF-κB inhibitor IkB (20) has been reported. Our systematic morphological, functional, and biochemical analyses of the atrogin-1 KO hearts at different ages, ranging from 6 to 16 months, demonstrated aging-related myocardial remodeling, which was characterized by the coexistence of hypertrophic and atrophic cells (42) in the LV (Figure 1, E and F). When looked at at the ultrastructural level, abnormalities observed included ER proliferation, disappearance of contractile elements, and abnormal mitochondria, all of which are consistent with activated ER stress and impairment of autophagy (Figures 4 and 5). Such reduction of the autophagy flux resulted in the accumulation of p62- and LC3-positive autophagosomes and was further supported by the blunted increase in the lipidated form of LC3 upon lysosome inhibition (Figure 5I). The resulting defect caused the formation of p62-positive aggregates and increased cardiomyocyte apoptosis, which was followed by fibrotic myocardial replacement, eventually causing diastolic dysfunction (Figures 2 and 3).

Defective control of proteostasis has been implicated in cardiomyopathies due to either accumulation of incorrectly folded proteins (e.g., the product of mutant cMyBP-C and CryAB genes) (43, 44) or acquired dysfunction of protein quality control, as occurring in heart failure (45–47). In the former scenario, the myocardium features abundant fibrotic replacement, and these cardiomyopathies have a restrictive pattern, similar to that observed in the atrogin-1 KO mice (Figure 2, A and B).

In other models, the genetic ablation of *Atg5*, a critical gene for autophagosome formation, causes cardiomyopathy and heart failure, supporting the concept that autophagy inhibition is detrimental for cardiac function (48). Conversely, it has been demonstrated recently that enhancement of autophagy ameliorates cardiac function and prevents accumulation of intracellular aggregates in a murine model of proteotoxic cardiomyopathy caused by mutant $CryAB^{R120G}$ (49).

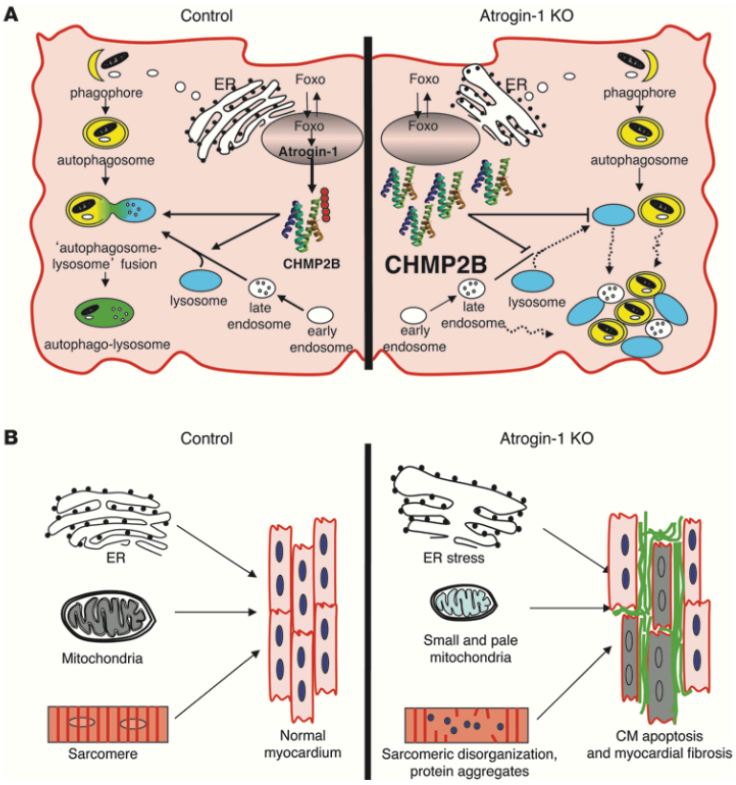

Figure 9
Role of atrogin-1 in the cross-talk between cardiomyocyte UPS and autophagy/lysosome system. (**A**) The muscle-specific ubiquitin ligase atrogin-1 regulates the turnover of CHMP2B, an ESCRT-III protein essential for lysosome biogenesis and autophagosome/lysosome fusion to form the autophagosome/lysosome. Ablation of atrogin-1 reduces CHMP2B turnover, leading to CHMP2B accumulation into cardiomyocyte areas characterized by sarcomeric depletion. (**B**) The impaired turnover of CHMP2B compromises endosome maturation and autophagosome/lysosome fusion, resulting in the block of the autophagic flux (i.e., lysosome and autophagosome accumulation), activation of markers of ER stress, expansion of ER cisternae, and modifications of mitochondria morphology, all of which lead to cardiomyocyte apoptosis, resulting in a diffuse myocardial interstitial fibrosis (Figures 3 and 4).

When we explored autophagy at higher detail in the atrogin-1 KO mice, autophagosomes and lysosomes appeared increased in number and size but segregated (Figure 5, F–H), suggesting a failure in the late steps of autophagy. This feature resembles that of myopathies with lysosomal defect (e.g., Danon disease) (50, 51) and prompted us to search whether atrogin-1 targets included proteins involved in the endosome/lysosome maturation and fusion with autophagosomes. The use of unbiased pulsed labeled proteomics in vivo (SILAC) allowed us to identify, among the proteins with increased turnover in the KO hearts, the ESCRT-III family protein CHMP2B, a previously unrecognized target of atrogin-1.

CHMP2B is a novel target of atrogin-1. The combined molecular, biochemical, proteomic, and in vivo approaches in the KO murine model identified CHMP2B as a novel target of atrogin-1. CHMP2B is a component of the heteromeric ESCRT-III complex essential for endosome trafficking, virus budding, cytokinesis, and the autophagy process (26). CHMP2B is necessary for cell viability, and its ablation impairs autophagy, causing inhibition of autophagosome/lysosome fusion and, therefore, accumulation of autophagosomes. Mutations in CHMP2B have been found in familial neurodegenerative diseases (e.g., frontotemporal dementia and amyotrophic lateral sclerosis), in which, consistent with a modulatory role in autophagy, brain pathology shows intracellular accumulation of p62-positive protein aggregates (22, 39).

Since the turnover of CHMP2B is defective in the atrogin-1 KO hearts, the clearance of the unfolded/misfolded forms of the protein is compromised. The progressive build up of the aggregate-prone CHMP2B would inevitably increase the possibility of aggregation and inclusion formation. Interestingly, when CHMP2B is expressed in WT-cultured cardiomyocytes, intracellular aggregates develop in a time-dependent manner (our unpublished data), suggesting that, above a given concentration threshold, the protein has the tendency to form amyloid-like complexes. In support of this, bioinformatics prediction (Protein Aggregation Prediction Server; http://www.abl.ku.edu/ProA/) (52) shows 3 aggregation-prone domains in CHMP2B, resulting in a high aggregation score. It may be speculated that formation of intracellular CHMP2B aggregates impairs autophagy either by sequestering the functional form of the protein or other regulatory factors (e.g., interacting components of the ESCRT-III or ESCRT-II complexes), with subsequent inhibition of ESCRT complex function that ultimately affects lysosomes maturation and the autophagy system.

During aging, the reduced efficiency of autophagy in the atrogin-1 KO mice adds to the decreased protein quality control, aggravating the proteotoxic load and triggering activation of UPR and ER stress,

which eventually lead to increased cardiomyocyte apoptosis. Among the proteins with impaired turnover in the atrogin-1 KO heart, our proteomics analysis identified other putative targets of the ubiquitin ligase, e.g., ribosomal S6 kinase 2 (RSK2), that might contribute to the pathological events that lead to the cardiomyopathy in addition to CHMP2B. It is thus likely that the atrogin-1 KO cardiomyopathy results from the impairment of multiple signaling pathways converging in ER stress and apoptosis. However, the downregulation of CHMP2B is sufficient to significantly reduce cardiomyocyte death, indicating that its accumulation has a dominant role in the pathogenesis of myocardial remodeling in the absence of atrogin-1.

Proteasome inhibition: friend or foe? Usui et al. demonstrated recently that atrogin-1 KO mice are protected from developing myocardial hypertrophy upon transverse aortic coarctation through sustained IkB-mediated NF-κB inhibition (20), suggesting that proteasome inhibition might be beneficial to prevent hypertrophy in pressure overload (53, 54). Our findings support the concept that sustained inhibition of atrogin-1 is deleterious for cardiac muscle and should be avoided because it affects basic cellular functions, including autophagy regulation and ER function. In addition, our results are of immediate clinical relevance given the increasing use of proteasome inhibitors as antitumor treatment (55). Recent case reports provide alarming signals that treatment with bortezomib, a proteasome inhibitor approved by the FDA for multiple myeloma, might be associated with cardiotoxicity (56–58), and in experimental models, bortezomib treatment caused protein accumulation, ER stress, and ultrastructural abnormalities in both cardiac sarcomeres and mitochondria (59).

Conclusions. In conclusion, these data highlight the importance of regulated proteolysis in the heart and show that the loss of atrogin-1 per se is sufficient to cause cardiac damage, which evolves into cardiomyopathy when protein quality control becomes less efficient, as occurring in aging. Such cardiomyopathy represents a novel model of proteotoxic myocardial remodeling, which will be useful to determine the mechanism of impaired proteostasis and its contribution to cardiomyocyte damage. Further studies will aim to determine whether mutations in the genes connected to the atrogin-1 signaling cascade may be responsible for human familial cardiomyopathies of undetermined genetic cause.

Methods

Mice. Atrogin-1 KO mice were provided by David Glass (Novartis Institutes for Biomedical Research, Cambridge, Massachusetts, USA). Atrogin-1$^{+/-}$ mice were backcrossed with the inbred C57BL/6J strain (Charles River) for 7 generations. Atrogin-1 KO mice were obtained by crossing heterozygous atrogin-1$^{+/-}$ mice and identified by PCR analysis. All experiments were conduced in 6-, 9-, and 16-month-old atrogin-1$^{+/-}$, atrogin-1, and C57BL/6J WT male mice.

Echocardiography and echo-Doppler. Echocardiography was performed both in adult and aged atrogin-1 KO mice and age- and sex-matched littermate controls, using a Vevo 2100 (VisualSonics) system equipped with a 30-MHz transducer. Anesthesia was induced with 3% isoflurane and maintained with 1.5% isoflurane during constant monitoring of temperature, respiration rate, and ECG. Two-dimensional cine loops with frame rates of 200 frames per second of a long-axis view and a short-axis view at proximal, mid, and apical level of the LV were recorded. IVS and LV posterior wall thicknesses, LV internal diameter, and maximal LV length were measured in systole and in diastole from the long-axis B-mode image, according to standard procedures. Ejection fraction (EF) was determined by the following formula, based on the Simple method (Simp): %EF = 100 × systolic LV volume/diastolic LV volume.

To assess changes in LV shape, the sphericity index was calculated at end-diastole and end-systole as the volume of the LV divided by the volume of a sphere with a diameter equal to the LV longest axis (measured in the apical view) using the following formulas (4, 5):

$$\text{End-diastolic sphericity index} = \text{end-diastolic LV volume}/(3/4 \times \pi \times [\text{end-diastolic Simp length}]^3) \quad \text{(Equation 1)}$$

$$\text{End-systolic sphericity index} = \text{end-systolic LV volume}/(3/4 \times \pi \times [\text{end-systolic Simp length}]^3) \quad \text{(Equation 2)}$$

As this ratio increases, the ventricle becomes more spherical. The Doppler frequency images of ascending aorta and mitral flow were acquired from the long-axis B-mode image. The Doppler frequency image of pulmonary artery flow was acquired from a cranial long-axis view. Doppler analysis of mitral valve flow was performed from the long-axis B-mode image, placing the sample volume in the LV below the mitral annulus. Echocardiographic image acquisition and analysis were performed by a single operator, blinded to the mouse genotype.

Telemetry implantation and ECG recording. Telemeters (Data Sciences International) were implanted in 15-month-old WT and atrogin-1 KO male mice. Animals were anesthetized with 1.5% isoflurane (v/v O_2), and implantation was performed according to the manufacturer's procedure. After 10 days to allow complete recovery from surgery, ECG recording was started and carried on for 2 months.

Tissue samples and immunofluorescence analysis. The hearts were harvested from C57BL/6J WT, atrogin-1$^{+/-}$, and atrogin-1 KO mice; fixed in 1% paraformaldehyde (Sigma-Aldrich) at room temperature for 15 minutes; equilibrated in sucrose gradient; frozen in liquid nitrogen; sectioned; and processed for histological and immunofluorescence analyses. Ten-micron myocardial sections were obtained with a cryostat (Leica CM1850, Leica Microsystems GmbH) and incubated with primary antibodies diluted in PBS supplemented with 1% BSA and 0.5% Triton X-100 overnight at 4°C. Antibodies used in this study are listed in Supplemental Table 5. FITC- and TRITC-conjugated secondary antibodies, all from Jackson lab, were used to detect primary antibodies.

TUNEL assay. TUNEL assay was performed in 9- and 16-month-old control and atrogin-1 KO heart cryosections, by using the ApopTag peroxidase in situ apoptosis detection system, following the procedure suggested by the manufacturer (Chemicon). A total of 6 nonconsecutive 10-μm cryosections from the mid-portion of the ventricles for each heart were analyzed. Cryosections were stained with an antibody to dystrophin, and nuclei were counterstained with DAPI. The number of apoptotic nuclei was estimated in 18 randomly selected fields from the RV (n = 6) and the LV (n = 6) walls and the IVS (n = 6) using ImageJ software.

Morphometric quantification of cardiomyocyte cross-sectional area. Cardiomyocyte cross-sectional area was quantified in both adult and aged control and atrogin-1 KO mouse hearts. Five nonconsecutive cryosections from the mid-portion of the ventricles per heart were stained with an antibody against dystrophin and analyzed with fluorescence microscopy. The images of 12 randomly chosen fields, area of 69,000 μm^2 from the RV (n = 6) and the LV (n = 6), were acquired with a fluorescence microscope (Leica DC130, Leica Microscopes), and cardiomyocyte cross-sectional area was evaluated using a custom-developed routine running in Matlab (MathWorks).

Electron microscopy analysis. We used conventional fixation-embedding procedures based on glutaraldehyde-osmium fixation and Epon embedding (33).

Western blotting. For details, see the Supplemental Methods.

Real-time quantitative PCR. For details, see the Supplemental Methods and Supplemental Table 6.

Immunoprecipitation. While cells were lysed as described for Western blot, tissues were ground in Nitrogen and then added to lysis buffer (50 mM Tris-HCl pH 7.5, 1 mM EGTA, 10% glycerol, 0.1% Triton, 50 mM $MgCl_2$) and further homogenized with a Polytron (Kinematica). Lysates were then centrifuged for 5 minutes at 5,000 *g*, supernatant was collected, and protein concentration was quantified. 500 μg of and 1 mg of total proteins, respectively from cells and muscles, were used for every immunoprecipitation. After a preclearing with A/G+ beads (Santa Cruz), lysates were cleaned from beads and incubated overnight with the selected antibody. The following day, A/G+ beads were added to lysate to bind the antibody-protein complex and left 2 hours in agitation at 4°C. Then, precipitated proteins were washed with ice-cold PBS and loaded in a denaturating gel.

Mass spectrometry–based proteomics. For details, see the Supplemental Methods.

Bafilomycin mouse treatment. Bafilomycin (Sigma-Aldrich) was dissolved in DMSO and intraperitoneally injected in adult (9-month-old) control and atrogin-1 KO mice at a dosage of 2 mg/kg. Mice were maintained in absence of food. Four hours after injection, mice were sacrificed and hearts were removed and processed for molecular and biochemical analyses. A group of control mice injected with the same amount of the vehicle was also tested.

In vitro UPS blockage. Cardiomyocytes cultured for 4 days were treated with 20 μM MG132 for either 12 or 24 hours. At the end of MG132 treatment, cells were either fixed for immunofluorescence analyses or used for protein isolation, as described in the Supplemental Methods.

In vivo CHMP2B silencing. Fifty μl of either 1×10^{13} per ml AAV9-GFP-U6-CHMP32Bsh or 1×10^{13} per ml AAV9-GFP (both from VECTOR BIOLABS) were injected via tail vein in 10-month-old atrogin-1 KO mice. Mice were sacrificed 3 and 4 weeks upon infection, and hearts were harvested and processed for immunofluorescence and molecular analyses.

Statistics. All data are expressed as mean ± SEM. Comparison between the experimental groups was performed by using 2-tailed Student's *t* test. $P < 0.05$ was considered statistically significant.

Study approval. All experimental procedures were performed according to the European Commission guidelines and have been approved by the local ethical committee and the relevant Italian authority (Ministero della Salute, Ufficio VI), in compliance of Italian Animal Welfare Law (law no. 116/1992 and subsequent modifications) and complying with the Directive 2010/63/EU of the European Parliament.

Acknowledgments

This work was supported by the Foundation Leducq, Telethon-Italy (TCP04009); the European Community Seventh Framework Program of FP7 (MYOAGE, contract 223576); the European Research Council (MyoPHAGY, contract 282310); the Italian Ministry of Education to M. Sandri; University of Padova (Progetto Ateneo 2010, contract CPDA0977); the European Community Seventh Framework Program FP7/2007-2013 under grant agreement HEALTH-F2-2009-241526, EUTrigTreat, and Telethon-Italy (GGP11224) to M. Mongillo; and University of Padova (Progetto Giovani Studiosi 2010, contract: GRIC101133) to T. Zaglia. We thank David J. Glass for providing atrogin-1 KO mice; Stefano Schiaffino for critical reading; Domenico Corrado for interpretation of ECG data; Giulia Borile, Emilio Bigon, Eleonora Piasentini, and Silvia Gaiani for technical assistance.

Received for publication January 22, 2014, and accepted in revised form March 20, 2014.

Address correspondence to: Marco Sandri or Marco Mongillo, Venetian Institute of Molecular Medicine, via Orus 2, 35129 Padova, Italy. Phone: 390497923258; Fax: 390497923250; E-mail: marco.sandri@unipd.it (M. Sandri). Phone: 390497923229; Fax: 390497923250, E-mail: marco.mongillo@unipd.it (M. Mongillo).

Andrea Carpi's present address is: Department of Biomedical Sciences, University of Padova, Padova, Italy.

1. Weeks KL, McMullen JR. The athlete's heart vs. the failing heart: can signaling explain the two distinct outcomes? *Physiology (Bethesda)*. 2011; 26(2):97–105.
2. Abel ED, Doenst T. Mitochondrial adaptations to physiological vs. pathological cardiac hypertrophy. *Cardiovasc Res*. 2011;90(2):234–242.
3. Baskin KK, Taegtmeyer H. Taking pressure off the heart: the ins and outs of atrophic remodelling. *Cardiovasc Res*. 2011;90(2):243–250.
4. Schlossarek S, Carrier L. The ubiquitin-proteasome system in cardiomyopathies. *Curr Opin Cardiol*. 2011;26(3):190–195.
5. Willis MS, Townley-Tilson WH, Kang EY, Homeister JW, Patterson C. Sent to destroy: the ubiquitin proteasome system regulates cell signaling and protein quality control in cardiovascular development and disease. *Circ Res*. 2010;106(3):463–478.
6. Willis MS, Patterson C. Into the heart: the emerging role of the ubiquitin-proteasome system. *J Mol Cell Cardiol*. 2006;41(4):567–579.
7. Zheng Q, Li J, Wang X. Interplay between the ubiquitin-proteasome system and autophagy in proteinopathies. *Int J Physiol Pathophysiol Pharmacol*. 2009;1(2):127–142.
8. Korolchuk VI, Menzies FM, Rubinsztein DC. Mechanisms of cross-talk between the ubiquitin-proteasome and autophagy-lysosome systems. *FEBS Lett*. 2010;584(7):1393–1398.
9. Korolchuk VI, Menzies FM, Rubinsztein DC. A novel link between autophagy and the ubiquitin-proteasome system. *Autophagy*. 2009; 5(6):862–863.
10. Wang X, Robbins J. Heart failure and protein quality control. *Circ Res*. 2006;99(12):1315–1328.
11. Gomes AV, Zong C, Ping P. Protein degradation by the 26S proteasome system in the normal and stressed myocardium. *Antioxid Redox Signal*. 2006;8(9–10):1677–1691.
12. Bodine SC, et al. Identification of ubiquitin ligases required for skeletal muscle atrophy. *Science*. 2001;294(5547):1704–1708.
13. Gomes MD, Lecker SH, Jagoe RT, Navon A, Goldberg AL. Atrogin-1, a muscle-specific F-box protein highly expressed during muscle atrophy. *Proc Natl Acad Sci U S A*. 2001;98(25):14440–14445.
14. Sandri M, et al. Foxo transcription factors induce the atrophy-related ubiquitin ligase atrogin-1 and cause skeletal muscle atrophy. *Cell*. 2004;117(3):399–412.
15. Stitt TN, et al. The IGF-1/PI3K/Akt pathway prevents expression of muscle atrophy-induced ubiquitin ligases by inhibiting FOXO transcription factors. *Mol Cell*. 2004;14(3):395–403.
16. Zaglia T, et al. Cardiac sympathetic neurons provide trophic signal to the heart via beta2-adrenoceptor-dependent regulation of proteolysis. *Cardiovasc Res*. 2013;97(2):240–250.
17. Skurk C, et al. The FOXO3a transcription factor regulates cardiac myocyte size downstream of AKT signaling. *J Biol Chem*. 2005;280(21):20814–20823.
18. Li HH, et al. Atrogin-1/muscle atrophy F-box inhibits calcineurin-dependent cardiac hypertrophy by participating in an SCF ubiquitin ligase complex. *J Clin Invest*. 2004;114(8):1058–1071.
19. Li HH, et al. Atrogin-1 inhibits Akt-dependent cardiac hypertrophy in mice via ubiquitin-dependent coactivation of Forkhead proteins. *J Clin Invest*. 2007;117(11):3211–3223.
20. Usui S, et al. Endogenous muscle atrophy F-box mediates pressure overload-induced cardiac hypertrophy through regulation of nuclear factor-κB. *Circ Res*. 2011;109(2):161–171.
21. Portbury AL, Willis MS, Patterson C. Tearin' up my heart: proteolysis in the cardiac sarcomere. *J Biol Chem*. 2011;286(12):9929–9934.
22. Filimonenko M, et al. Functional multivesicular bodies are required for autophagic clearance of protein aggregates associated with neurodegenerative disease. *J Cell Biol*. 2007;179(3):485–500.
23. Lee JA, Beigneux A, Ahmad ST, Young SG, Gao FB. ESCRT-III dysfunction causes autophagosome accumulation and neurodegeneration. *Curr Biol*. 2007;17(18):1561–1567.
24. Rusten TE, et al. ESCRTs and Fab1 regulate distinct steps of autophagy. *Curr Biol*. 2007;17(20):1817–1825.
25. Powell SR. The ubiquitin-proteasome system in cardiac physiology and pathology. *Am J Physiol Heart Circ Physiol*. 2006;291(1):H1–H19.
26. Raiborg C, Stenmark H. The ESCRT machinery in endosomal sorting of ubiquitylated membrane proteins. *Nature*. 2009;458(7237):445–452.
27. Higami Y, Shimokawa I. Apoptosis in the aging process. *Cell Tissue Res*. 2000;301(1):125–132.
28. Frey N, Katus HA, Olson EN, Hill JA. Hypertrophy of the heart: a new therapeutic target? *Circulation*. 2004;109(13):1580–1589.
29. Kehat I, Molkentin JD. Molecular pathways underlying cardiac remodeling during pathophysiological

stimulation. *Circulation*. 2010;122(25):2727–2735.
30. Kushwaha SS, Fallon JT, Fuster V. Restrictive cardiomyopathy. *N Engl J Med*. 1997;336(4):267–276.
31. Grumati P, et al. Autophagy is defective in collagen VI muscular dystrophies, and its reactivation rescues myofiber degeneration. *Nat Med*. 2010; 16(11):1313–1320.
32. Yu Z, et al. Macroautophagy is regulated by the UPR-mediator CHOP and accentuates the phenotype of SBMA mice. *PLoS Genet*. 2011; 7(10):e1002321.
33. Masiero E, et al. Autophagy is required to maintain muscle mass. *Cell Metab*. 2009;10(6):507–515.
34. Cecarini V, et al. Crosstalk between the ubiquitin-proteasome system and autophagy in a human cellular model of Alzheimer's disease. *Biochim Biophys Acta*. 2012;1822(11):1741–1751.
35. Klionsky DJ, et al. Guidelines for the use and interpretation of assays for monitoring autophagy. *Autophagy*. 2012;8(4):445–544.
36. Larsen KB, Lamark T, Overvatn A, Harneshaug I, Johansen T, Bjorkoy G. A reporter cell system to monitor autophagy based on p62/SQSTM1. *Autophagy*. 2010;6(6):784–793.
37. Metcalf D, Isaacs AM. The role of ESCRT proteins in fusion events involving lysosomes, endosomes and autophagosomes. *Biochem Soc Trans*. 2010;38(6):1469–1473.
38. Lee JA, Liu L, Gao FB. Autophagy defects contribute to neurodegeneration induced by dysfunctional ESCRT-III. *Autophagy*. 2009;5(7):1070–1072.
39. Lee JA, Gao FB. Roles of ESCRT in autophagy-associated neurodegeneration. *Autophagy*. 2008; 4(2):230–232.
40. Nakayama H, Wilkin BJ, Bodi I, Molkentin JD. Calcineurin-dependent cardiomyopathy is activated by TRPC in the adult mouse heart. *FASEB J*. 2006;20(10):1660–1670.
41. Heineke J, et al. Calcineurin protects the heart in a murine model of dilated cardiomyopathy. *J Mol Cell Cardiol*. 2010;48(6):1080–1087.
42. Maron BJ, Ferrans VJ, Roberts WC. Ultrastructural features of degenerated cardiac muscle cells in patients with cardiac hypertrophy. *Am J Pathol*. 1975;79(3):387–434.
43. Pattison JS, Osinska H, Robbins J. Atg7 induces basal autophagy and rescues autophagic deficiency in CryABR120G cardiomyocytes. *Circ Res*. 2011;109(2):151–160.
44. Schlossarek S, Mearini G, Carrier L. Cardiac myosin-binding protein C in hypertrophic cardiomyopathy: mechanisms and therapeutic opportunities. *J Mol Cell Cardiol*. 2011;50(4):613–620.
45. Tresse E, et al. VCP/p97 is essential for maturation of ubiquitin-containing autophagosomes and this function is impaired by mutations that cause IBMPFD. *Autophagy*. 2010;6(2):217–227.
46. Predmore JM, et al. Ubiquitin proteasome dysfunction in human hypertrophic and dilated cardiomyopathies. *Circulation*. 2010;121(8):997–1004.
47. Caleshu C, et al. Furthering the link between the sarcomere and primary cardiomyopathies: restrictive cardiomyopathy associated with multiple mutations in genes previously associated with hypertrophic or dilated cardiomyopathy. *Am J Med Genet A*. 2011;155A(9):2229–2235.
48. Taneike M, et al. Inhibition of autophagy in the heart induces age-related cardiomyopathy. *Autophagy*. 2010;6(5):600–606.
49. Bhuiyan MS, et al. Enhanced autophagy ameliorates cardiac proteinopathy. *J Clin Invest*. 2013; 123(12):5284–5297.
50. Malicdan MC, Noguchi S, Nonaka I, Saftig P, Nishino I. Lysosomal myopathies: an excessive build-up in autophagosomes is too much to handle. *Neuromuscul Disord*. 2008;18(7):521–529.
51. Sugimoto S. A novel vacuolar myopathy with dilated cardiomyopathy. *Autophagy*. 2007;3(6):638–639.
52. Fang Y, Gao S, Tai D, Middaugh CR, Fang J. Identification of properties important to protein aggregation using feature selection. *BMC Bioinformatics*. 2013;14:314.
53. Depre C, et al. Activation of the cardiac proteasome during pressure overload promotes ventricular hypertrophy. *Circulation*. 2006;114(17):1821–1828.
54. Stansfield WE, Moss NC, Willis MS, Tang R, Selzman CH. Proteasome inhibition attenuates infarct size and preserves cardiac function in a murine model of myocardial ischemia-reperfusion injury. *Ann Thorac Surg*. 2007;84(1):120–125.
55. Micel LN, Tentler JJ, Smith PG, Eckhardt GS. Role of ubiquitin ligases and the proteasome in oncogenesis: novel targets for anticancer therapies. *J Clin Oncol*. 2013;31(9):1231–1238.
56. Enrico O, et al. Unexpected cardiotoxicity in haematological bortezomib treated patients. *Br J Haematol*. 2007;138(3):396–397.
57. Hacihanefioglu A, Tarkun P, Gonullu E. Acute severe cardiac failure in a myeloma patient due to proteasome inhibitor bortezomib. *Int J Hematol*. 2008;88(2):219–222.
58. Voortman J, Giaccone G. Severe reversible cardiac failure after bortezomib treatment combined with chemotherapy in a non-small cell lung cancer patient: a case report. *BMC Cancer*. 2006;6:129.
59. Nowis D, et al. Cardiotoxicity of the anticancer therapeutic agent bortezomib. *Am J Pathol*. 2010;176(6):2658–2668.

Cardiovascular Research (2013) **97**, 240–250
doi:10.1093/cvr/cvs320

Cardiac sympathetic neurons provide trophic signal to the heart via β2-adrenoceptor-dependent regulation of proteolysis

Tania Zaglia[1,2], Giulia Milan[2], Mauro Franzoso[1,2], Enrico Bertaggia[2], Nicola Pianca[2], Eleonora Piasentini[2], Vanessa A. Voltarelli[3], David Chiavegato[2], Patricia C. Brum[3], David J. Glass[4], Stefano Schiaffino[2,5], Marco Sandri[1,2,5], and Marco Mongillo[1,2,5]*

[1]Department of Biomedical Sciences, University of Padova, Viale G. Colombo 3, Padova 35121, Italy; [2]Venetian Institute of Molecular Medicine (VIMM), University of Padova, Via Orus 2, Padova 35129, Italy; [3]Affiliation-School of Physical Education and Sport, University of São Paulo, 65 Butantã, São Paulo 05508-900, Brazil; [4]Muscle Diseases, Novartis Institutes for Biomedical Research, 100 Technology Square, Cambridge, MA 02139, USA; and [5]CNR Institute of Neuroscience, Viale G. Colombo 3, Padova 35121, Italy

Received 4 July 2012; revised 30 September 2012; accepted 15 October 2012; online publish-ahead-of-print 22 October 2012

Time for primary review: 33 days

Aims Increased cardiac sympathetic neuron (SN) activity has been associated with pathologies such as heart failure and hypertrophy, suggesting that cardiac innervation regulates cardiomyocyte trophism. Whether continuous input from the SNs is required for the maintenance of the cardiomyocyte size has not been determined thus far.

Methods and results To address the role of cardiac innervation in cardiomyocyte size regulation, we monitored the effect of pharmacological sympathetic denervation in mice on cardiac structure, function, and signalling from 24 h to 30 days in the absence of other pathological stimuli. SN ablation caused an immediate reduction in the cardiomyocyte size with minimal consequences on the resting contractile function. Atrophic remodelling was mediated by the ubiquitin–proteasome system through FOXO-dependent early induction of the muscle-specific E3 ubiquitin ligases Atrogin-1/MAFbx and MuRF1, which was followed by activation of the autophagy–lysosome system. MuRF1 was found to be determinant in denervation atrophy as remodelling did not develop in denervated MuRF1 knock-out (KO) hearts. These effects were caused by decreased basal stimulation of cardiomyocyte β2-adrenoceptor (AR), as atrophy was prevented by treatment of denervated mice with the β2-AR agonist clenbuterol. Consistent with these data, we also observed that β2-AR KO mice showed cardiac atrophy at rest.

Conclusion Cardiac SNs are strong regulators of the cardiomyocyte size via β2-AR-dependent repression of proteolysis, demonstrating that the neuro-cardiac axis operates constitutively for the determination of the physiological cardiomyocyte size. These results are of great clinical relevance given the role of β-AR in cardiovascular diseases and their modulation in therapy.

Keywords β-adreoceptors • Ubiquitin–proteasome system • Atrophy • Sympathetic nervous system • Cardiac remodelling

1. Introduction

The heart adapts its mass in response to various stimuli including mechanical, metabolic, and neuro/hormonal signals, all of which cause changes in the relative rates of protein synthesis and degradation.[1] Protein degradation occurs either via autophagy–lysosome system, mainly involved in organelle removal, or through the ubiquitin–proteasome system (UPS).[2] The UPS relies on the activity of three enzymes: E1, a ubiquitin-activating enzyme; E2, mediating ubiquitin conjugation; and E3, a ubiquitin ligase enzyme.[2,3] Atrogin-1/MAFbx and MuRF1 are muscle-specific ubiquitin ligases[4,5] whose activity contributes to cell size regulation both in skeletal and cardiac muscles. Consistent with their role in mediating proteolysis, over-expression of cardiac atrogin-1/MAFbx or MuRF1 has been shown to prevent surgically or pharmacologically induced cardiomyocyte hypertrophy,[6–8] while genetic ablation of MuRF1 increases the propensity to develop cardiac hypertrophy upon pressure overload.[9] Conversely, it has been demonstrated that MuRF1 is up-regulated

* Corresponding author. Tel: +39 0497923229; fax: +39 0497923250, Email: marco.mongillo@unipd.it

during regression of cardiac hypertrophy as well as in nutrient deprivation- and dexamethasone-induced atrophy.[10,11]

Cardiac atrophy following food deprivation or mechanical unloading is characterized both by increased proteolysis and decreased protein synthesis.[10,12] In skeletal muscle, similar changes in the relative rates of protein synthesis and degradation[13,14] leading to atrophy have been shown to depend on the loss of neuro/hormonal signals upon denervation, which resulted in increased MuRF1-mediated degradation of myosin heavy chain [15] and myosin-binding proteins.[16]

The heart is densely innervated by sympathetic neurons (SNs) that, by releasing norepinephrine (NE) and activating β-adrenergic receptors (β-ARs), operate physiologically as a short-term enhancer of the heart rate, conduction velocity, and cardiac contractility to match blood flow requirements of peripheral organs.[17] β-Adrenergic stimulation has also longer-lasting effects on cellular metabolism, survival and on the modulation of cardiomyocyte growth. Both mice lacking the pre-synaptic α2-ARs, that are characterized by a higher basal sympathetic outflow,[18,19] and NGF-overexpressing mice, which show sympathetic hyper-innervation, develop cardiac hypertrophy.[20] Systemic administration of formoterol and salmeterol, two β2-adrenoceptor (AR) agonists, elicits cardiac muscle hypertrophy,[21] and β-AR activation prevents left ventricular (LV) atrophy experimentally induced by cardiac haemodynamic unloading.[22,23] Conversely, mice with total β-AR deficiency,[24] as well as rabbits chronically treated with β-AR blockers[25] have reduced the cardiac mass. Interestingly, a link between β2-AR-dependent signalling and expression of atrogin-1/MAFbx and MuRF1 has recently been proposed.[26]

Taken together, these data suggest that cardiac SN activity may constitutively tune the physiological cardiac mass, by modulating the cellular mechanisms of protein synthesis and degradation, but this hypothesis has not been investigated directly thus far.

2. Methods

2.1 Mice

The following animal models were used in this study: CD1, C57BL/6J, and FVB WT mice (Charles River, Milan, Italy), MuRF1 knock-out (KO) and β2-AR KO mice, P1 Sprague-Dawley neonatal rats. All experimental procedures were performed according to the European Commission guidelines and have been approved by the local ethical committee and the relevant Italian authority (Ministero della Salute, Ufficio VI), in compliance of Italian Animal Welfare Law (Law n 116/1992 and subsequent modifications), and complying with the Directive 2010/63/EU of the European Parliament.

2.2 Pharmacological sympathectomy

Pharmacological sympathectomy was obtained with 6-hydroxy-dopamine (6-OH-DOPA) (100 mg/kg, ip) (Tocris Bioscience, R&D Systems, Inc., Minneapolis, MN, USA).[39] The drug was administered at days $t = 0$, $t = 2$, and $t = 7$. Animals were sacrificed 2, 4, 8, and 30 days after the first 6-OH-DOPA injection using excess anaesthesia. Control mice were treated with the vehicle (0.9% NaCl and 0.1% ascorbic acid).

2.3 Echocardiography

Echocardiography was performed both in control and 30-day-denervated mice under anaesthesia during constant monitoring of temperature, respiratory rate, and ECG, using a Vevo 2100™ (VisualSonics, Toronto, Canada) system equipped with a 30 MHz transducer. For more details, see Supplementary material online.

2.4 Tissue samples and immunofluorescence analysis

For histological and immunofluorescence analyses, hearts were harvested from mice and either frozen directly in liquid nitrogen or fixed in 1% paraformaldehyde (Sigma). More details and the primary antibodies used in this are described in the Supplementary material online Section and *Table S1*, respectively.

2.5 RT–qPCR analysis

Total RNA was prepared using the SV Total RNA Isolation System according to the manufacturer's protocol; for details, see Supplementary material online. Primers are listed in Supplementary material online, *Table S2*.

2.6 Western blotting

Total ventricular extracts from both the right and the left ventricles were obtained as previously described[41] and protein concentration was determined by the BCA assay (Pierce). SDS–PAGE was performed on 3–8 and 4–12% gradient gels (Invitrogen) loading from 10 to 60 μg protein/lane. Extracts transferred onto PVDF (Invitrogen) were processed with the primary antibodies described in Supplementary material online, *Table S1* either 1 h at room temperature or over night at 4°C. The blots were then incubated with secondary antibodies conjugated to horseradish peroxidase and the reactivity was revealed by enhanced chemiluminescence (Pierce).

2.7 Cardiomyocyte culture

Details of the procedure are described in the Supplementary material online.

2.8 Statistical analysis

All data are expressed as the mean ± SEM. Comparison between the experimental groups was made by using the non-paired Student's *t*-test and ANOVA tests followed by Bonferroni correction, with $P < 0.05$ being considered statistically significant.

3. Results

3.1 Pharmacological ablation of the cardiac sympathetic nervous system causes reduction in cardiomyocyte size

Cardiac sympathetic nerve terminals, as identified by immunoreactivity to tyrosine hydroxylase, DOPA β-hydroxylase, and synapsin I, are interspersed among the cardiomyocytes in all regions of the adult mouse heart, with a higher density in the right ventricle (RV) and the subepicardium of both the LV and the RV (Supplementary material online, *Figure S1*). To obtain cardiac sympathetic denervation, we used 6-OH-DOPA, which induces peripheral autonomic neuron degeneration without affecting central adrenergic neurons,[27] with only minimal consequences on resting blood pressure (BP) and cardiac haemodynamics.[28,29] Such treatment ablated ~90% of cardiac sympathetic nerve terminals already 24 h after the first 6-OH-DOPA injection, and caused complete and persistent denervation after 8 and 30 days (*Figure 1A* and *C*). In accord with the removal of cardiac sympathetic efferents, the chronotropic response to parasympathetic antagonism elicited by atropine administration was significantly reduced in denervated mice, when compared with vehicle-treated controls (*Figure 1B*).

Denervated hearts were characterized by a significant reduction in size, as demonstrated by the decrease in the heart weight/body weight

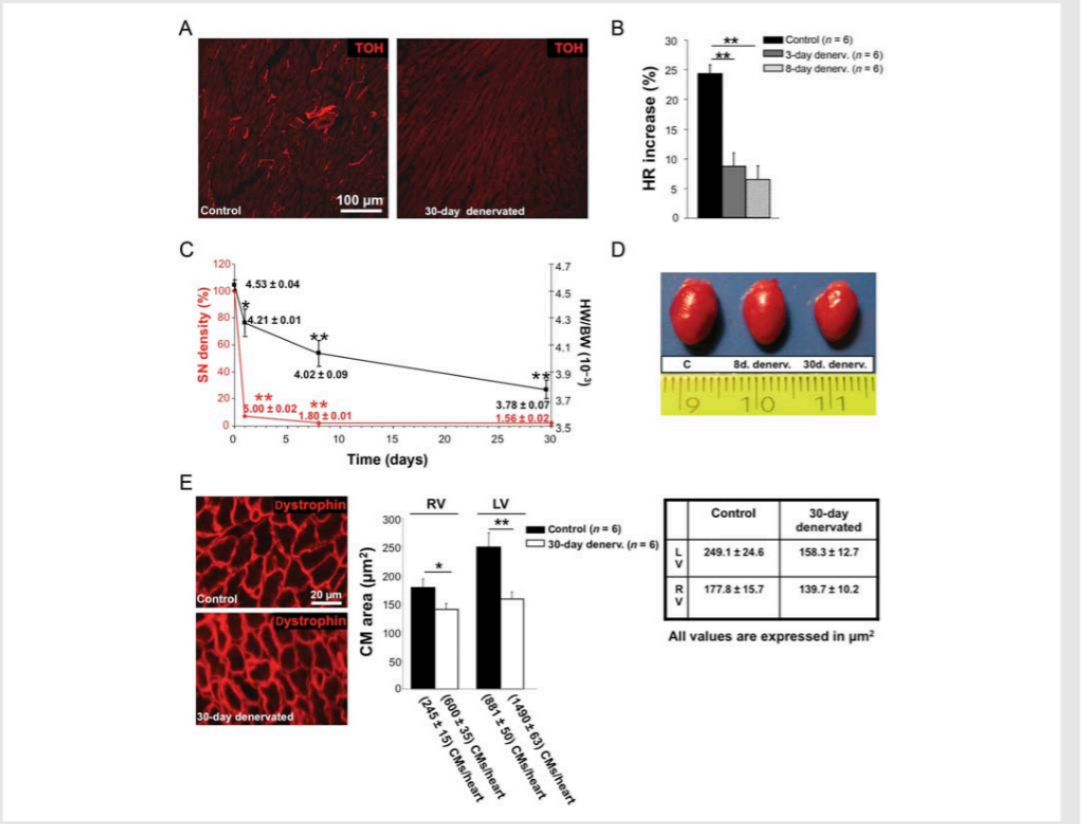

Figure 1 Cardiac sympathetic nervous system ablation induces heart atrophy. (*A*) Confocal immunofluorescence analysis of ventricular cryosection from control and 30-day denervated hearts stained with an antibody against tyrosine hydroxylase (TOH, red signal). Bar: 100 µm. (*B*) Evaluation of heart rate (HR) changes upon atropine injection in control, 3- and 8-day denervated mice (**$P < 0.01$; $n = 6$ mice for each group). (*C*) Evaluation of sympathetic neuron (SN) density and heart weight/body weight (HW/BW) in vehicle-treated control and 1-, 8-, and 30-day-denervated mice. Error bars indicate SEM (**$P < 0.01$; $n = 16$ mice for each group). (*D*) Hearts from adult vehicle-treated control, 8- and 30-day-denervated mice. (*E*) Immunofluorescence analysis of cryosections from vehicle-treated and 30-day-denervated mice stained with an antibody to dystrophin (left panel) and morphometric evaluation of the cardiomyocyte cross-sectional area (right panels). Error bars indicate SEM (** $P < 0.01$; $n = 6$ mice for each group). The number of CMs (mean ± SD) evaluated for each heart is shown on the graph.

ratio (HW/BW), that started rapidly 24 h after treatment, and progressed with time, reaching a 15% decrease at Day 30 (*Figure 1C* and *D*). This was confirmed by a significant reduction in the cross-sectional area of ventricular cardiomyocytes, which was already evident 8 days (data not shown) upon denervation and maximal at Day 30 (*Figure 1E*). The denervated myocardium had normal histology (*Figure 2A*), with no signs of infiltration, cardiomyocyte necrosis, or interstitial fibrosis (*Figure 2B*), that retained normal sarcomeric organization (*Figure 2C*). The assessment of cardiac function by echocardiography suggested that atrophic remodelling in the denervated hearts was not dependent on reduced haemodynamic stress, even when the degree of atrophic remodelling was maximal in this model (e.g. 30 days), as the hearts of 6-OH-DOPA-treated mice had unchanged contractility [fractional shortening (FS) denervated: 31.17 ± 1.37% vs. control: 29.64 ± 1.50%] and only a moderate decrease of the ejection fraction (EF), when compared with vehicle-treated controls (EF, denervated: 67.53 ± 2.97% vs. control: 76.33 ± 2.36%) (Supplementary material online, *Figure S2*). Furthermore, the assessment of myocardial strain using speckle tracking imaging demonstrated that both circumferential and radial strain were unchanged in the denervated mice (circumferential strain: denervated: −15.89 ± 2.58 vs. controls: −14.43 ± 1.92; radial strain: denervated −27.9 ± 5 vs. controls: −27.8 ± 8.1). In line with the functional measurements, we did not detect changes in the expression level of foetal genes associated to cardiac hypertrophy and unloading atrophy (alpha-skeletal actin and atrial natriuretic factor),[30] with the exception of β-MHC, which was increased in 30-day-denervated hearts, when compared with controls (*Figure 2D–F*). Nutrient deprivation is a well-accepted activator of atrophic remodelling in both cardiac and skeletal muscles.[31] In the

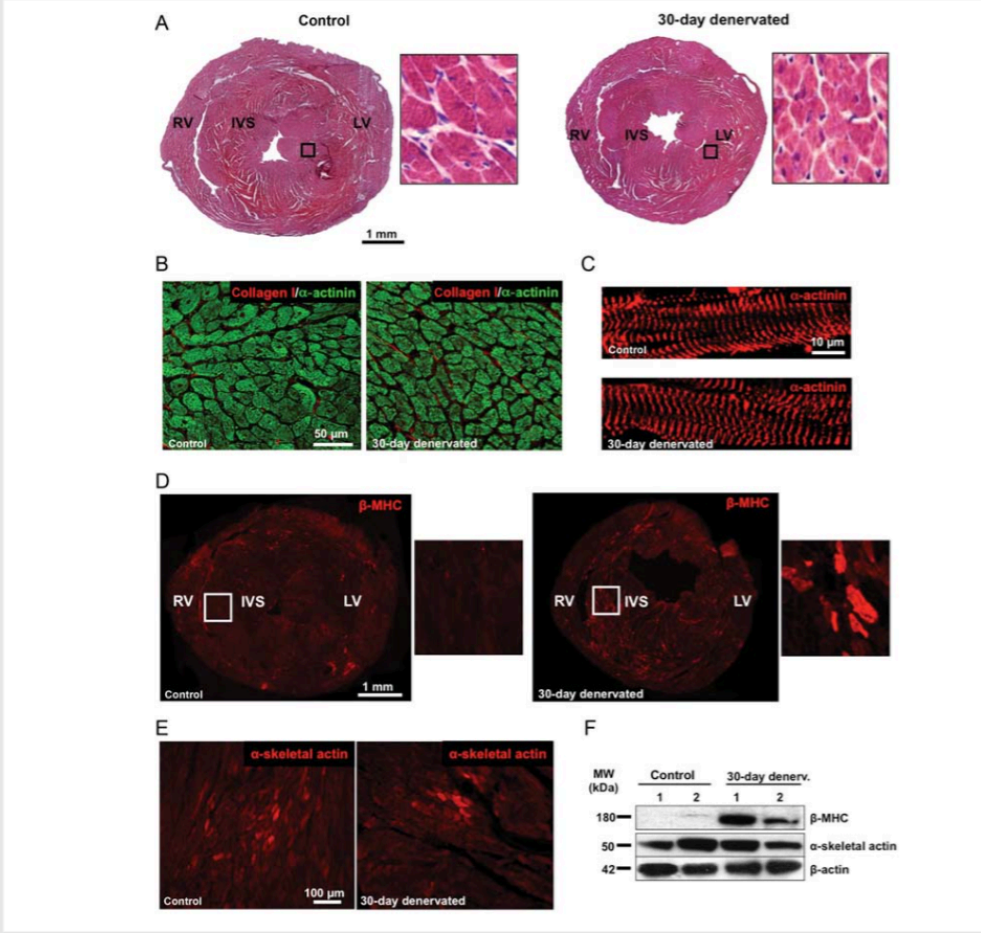

Figure 2 Denervated hearts do not show histological alterations. (*A*) Haematoxilin–eosin of heart cryosections from vehicle-treated and 30-day-denervated mice. Bar: 1 mm. RV, right ventricle; IVS, interventricular septum; LV, left ventricle. (*B*) Confocal immunofluorescence analysis of ventricular cryosections from vehicle-treated control and 30-day-denervated mice co-stained with antibodies to sarcomeric actinin (green signal) and collagen I (red signal), showing no signs of myocardial interstitial fibrosis upon 6-OH-DOPA treatment. Bar: 50 μm. (*C*) Immunofluorescence analysis of ventricular cryosections from vehicle-treated control and 30-day-denervated mice stained with an antibody specific for sarcomeric actinin, showing no sarcomeric disorganization in denervated hearts. Bar: 10 μm. (*D* and *E*) Immunofluorescence analysis of ventricular cryosections from vehicle-treated and 30-day-denervated mice stained with antibodies specific for β-myosin heavy chain (β-MHC) (*D*) and skeletal actin (*E*). Bars: (*D*) 1 mm; (*E*) 100 μm. (*F*) Western blot analysis on total ventricular extracts from control and 30-day-denervated hearts. MW, molecular weight.

first 3 days of 6-OH-DOPA treatment, the mice underwent a modest and transient BW reduction (~10% at Day 3), which is completely recovered from the eighth day after treatment onwards (Supplementary material online, *Figure S3A*). To determine whether metabolic changes could be responsible for denervation atrophy, mice underwent caloric restriction (4 g of normal chow food/day)[32,33] for 3 (group II) or 7 days (group I), followed by free food access causing a 10–15% reduction in BW. Consistent with previous reports, we observed a significant reduction in cardiac weight (HW/BW, 8-day diet: 0.0041 ± 0.0002 vs. control: 0.0045 ± 0.0002) during the diet. However, at difference with the denervated mice, the heart size returned identical to controls after normal diet was re-established (HW/BW, 30-day diet: 0.0046 ± 0.0003 vs. C: 0.0045 ± 0.0002) (Supplementary material online, *Figure S3B–D*).

Taken together, these results suggest that atrophic remodelling upon cardiac denervation does not depend on haemodynamic unloading or metabolic deprivation, but suggests that sympathetic innervation attends to an independent mechanism that provides constitutive trophic signal to cardiomyocytes, and therefore regulating their physiologic size.

3.2 Atrophic remodelling in denervated hearts is mediated by FOXO (*Forkhead box protein O*)-dependent up-regulation of the ubiquitin ligases atrogin-1/MAFbx and MuRF1

Based on the evidence that the cardiomyocyte size is regulated by the relative rates of protein synthesis and degradation, we sought to determine whether the removal of sympathetic input to the heart influenced the regulation of proteostasis. We, therefore, assessed the expression level of the main genes controlling the UPS, namely the ubiquitin ligases MuRF-1 and atrogin-1/MAFbx, and the autophagy-related genes LC3, Beclin, p62, Bnip3, and cathepsin L. Atrogin1/MAFbx and MuRF1 were induced at the transcript level 24 h after 6-OH-DOPA treatment and progressively decreased 8 and 30 days upon heart denervation (*Figure 3A*). Based on the evidence that in skeletal muscle activation of the autophagy programme follows UPS activation,[34] we sought to determine whether autophagy was activated in denervated hearts. No significant changes in the autophagy-related genes were detected at Days 8 and 30 (*Figure 3B*). However, in 30-day-denervated hearts, there was a significant increase in the protein level of the low molecular weight LC3II band (*Figure 3C*), a marker of autophagosome activation, and decreased protein levels of p62, the best-known mammalian autophagy-specific substrate, both molecular events associated to activation of the autophagy–lysosome system. In addition, Beclin1 and Bnip3 appeared significantly down-regulated in both 8- and 30-day-denervated hearts (*Figure 3C*), which also supports activation of autophagy. These data indicate that denervation increased UPS-dependent proteolysis, which was subsequently accompanied by activation of the autophagy–lysosome system. As the transcriptional regulation of atrogin-1/MAFbx and MuRF1 is modulated by the FOXO family of transcription factors and inhibitor of nuclear factor kappa-B kinase subunit β (IkKβ)/nuclear factor kappa-light-chain-enhancer of activated B cells (NF-kB) pathways,[35,36] we assessed whether these pathways were activated following denervation. In denervated hearts, there was a progressive decrease in the phosphorylation level of FOXO1 which started already 24 h after denervation and persisted for the time of the analysis (*Figure 4A*). Moreover, the protein level of the phosphorylated isoform of IkKβ was decreased 24 h after 6-OH-DOPA treatment, but returned to levels comparable with controls at Days 8 and 30 (*Figure 4B*). These results suggest that ablation of sympathetic efferents to the heart leads to up-regulation of the ubiquitin ligases atrogin-1/MAFbx and MuRF-1 through a FOXO-dependent pathway. We next investigated signalling dependent on the serine–threonine kinase Akt, which is a known regulator of FOXO transcription factors, as well as being central to the modulation of protein synthesis. Western blot analyses demonstrated a decrease in phospho-Akt in denervated hearts which started already 24 h after denervation (*Figure 4C*) and persisted at 8 and 30 days (*Figure 4D*). In addition, denervated hearts showed a significant reduction in the phosphorylated isoform of the ribosomal protein S6, as well as the p-S6/S6 ratio, when compared with vehicle-treated controls (*Figure 4C* and *D*). These data suggest that upon ablation of cardiac SNs, a decrease in the activated form of Akt leads to rapid up-regulation of the muscle-specific ubiquitin ligases Atrogin-1/MAFbx and MuRF-1, through activation of FOXO transcription factors, initiating cardiac atrophic remodelling.

3.3 MURF1 knock-out mice are protected from denervation-induced cardiac atrophy

The ubiquitin ligase MuRF1 has previously been shown to control degradation of sarcomeric proteins.[9] To address the role of MuRF1 in denervation-induced cardiac atrophy, we denervated MuRF1 KO mice (MuRF1−/−, in the C57BL6 background), which have been previously demonstrated to have normal cardiac structure and function.[9] MuRF1−/− mice examined 30 days after 6-OH-DOPA treatment were compared with MuRF1 littermate controls (MuRF1+/+) as well as to vehicle-treated MuRF1−/−. Denervation, which in MuRF1+/+ controls induced cardiac atrophy to a degree comparable with that of CD1 mice (HW/BW, denervated: 0.0041 ± 0.0001 vs. vehicle-treated controls: 0.0048 ± 0.0004) (*Figure 5A–C*) did not cause atrophic remodelling in MuRF1−/− hearts, as demonstrated by unchanged HW/BW and cardiomyocyte cross-sectional area (HW/BW, denervated: 0.0053 ± 0.0002 vs. vehicle-treated controls: 0.0052 ± 0.0002) (*Figure 5A–C*). These results indicate that genetic ablation of MuRF1 protects the heart from denervation atrophy, supporting the conclusion that MuRF1 is a central regulator in such remodelling process.

3.4 Noradrenaline modulates MuRF1 expression through β2-AR signalling both *in vivo* and in cultured cardiomyocytes

At least two different neurotransmitters released by cardiac SNs, namely noradrenaline (NE) and Neuropeptide Y (NPY), have been shown to have a role in regulating cardiomyocyte trophism *in vitro*.[37,38] To identify the sympathetic neurotransmitter involved in the regulation of MuRF1 expression, we evaluated changes in the expression level of this ubiquitin ligase in neonatal cardiomyocytes treated with beta-adrenergic stimuli. We assessed MuRF1 levels in cells treated with a non-selective adrenergic agonist, NE, and upon treatment with the beta2 selective agonist clenbuterol (CL), or with NPY. Serum starvation caused a significant increase in cardiomyocyte MuRF1 expression, which was prevented both by NE and CL treatment, whereas NPY treatment did not have effects (*Figure 6A*). Based on these results and the effects of CL in skeletal muscle,[39] we hypothesized that stimulation of β2-AR would prevent cardiac atrophic remodelling following denervation. Denervated mice were administered CL, delivered at constant concentration by subcutaneous osmotic minipumps, and such treatment prevented both the decrease in HW/BW (denervated: 0.00380 ± 0.00007, denervated + CL: 0.00420 ± 0.00012, CL: 0.0046 ± 0.00012 vs. control: 0.00450 ± 0.00004) and the reduction in the cardiomyocyte cross-sectional area (*Figure 6B* and *C*). These results support that β2-AR signalling has a role in the determination of the physiological myocardial mass. To further validate the notion that β2-AR signalling has a major role in the determination of the physiological myocardial mass, we examined the heart size in β2-AR KO mice. As expected, β2-AR KO mice had decreased HW/BW and cardiomyocyte cross-sectional area, at baseline when compared with littermate controls (HW/BW, β2-AR KO: 0.0030 ± 0.0001 vs. control: 0.0038 ± 0.0001; CM cross-sectional area, β2-AR KO: 252.20 ± 25.01 μm^2 vs. control: 306.94 ± 26.29 μm^2) (*Figure 6D*). Akin to denervated hearts, β2-AR KO mice did not show impairment of cardiac contractility (FS: β2-AR KO: 45 ± 1% vs. control: 48 ± 2%), or significant changes in tail-cuff BP (β2-AR KO: 109 ± 6 mmHg vs. control: 109 ± 1 mmHg) and heart

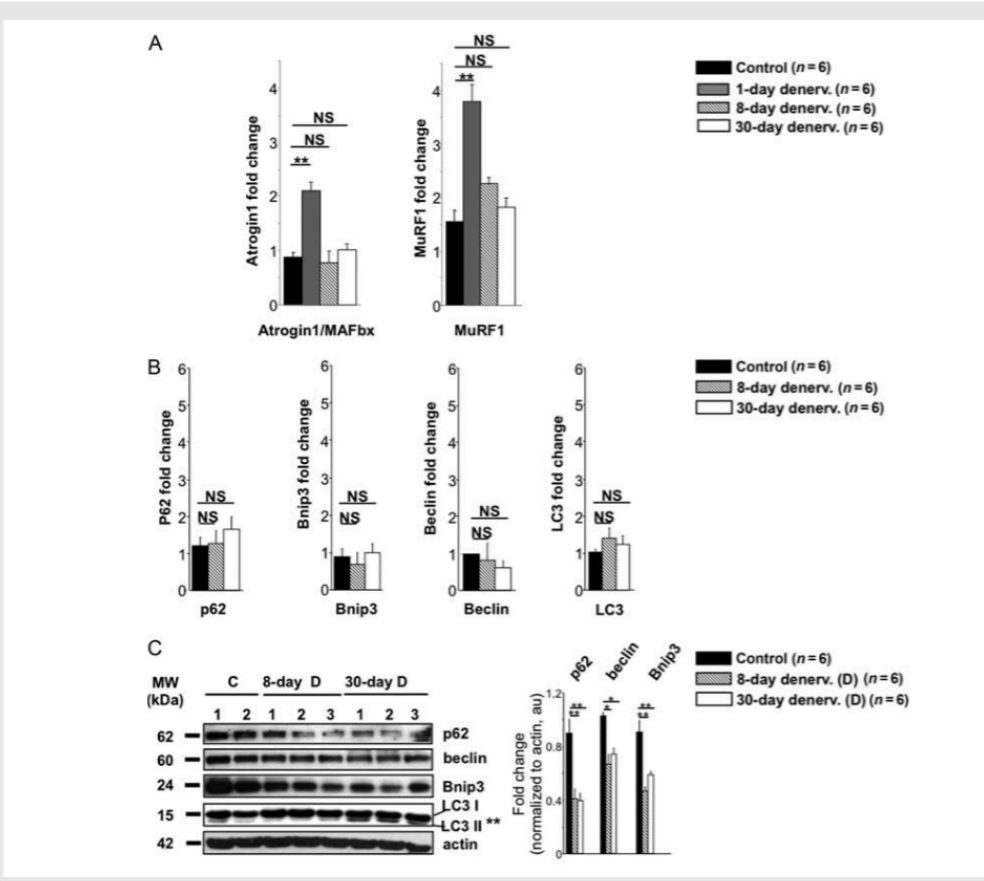

Figure 3 Denervation-induced cardiac atrophy is mediated by activation of the ubiquitine proteasome and the autophagy–lysosome systems. (*A*) Atrogin-1/MAFbx and MURF1 gene expression detected by RT–qPCR in total ventricular extracts from vehicle-treated control, 1-, 8-, and 30-day-denervated mice. Error bars indicate SEM (**P <0.01; NS, no significant; $n = 6$ mice for each group). (*B*) Autophagy-related gene expression was detected by RT–qPCR in total ventricular extracts from vehicle-treated, 8- and 30-day-denervated mice. Error bars indicate SEM (**$P < 0.01$; NS, not significant; $n = 6$ mice for each group). (*C*) Western blot analysis on total ventricular extracts from vehicle-treated control, 8- and 30-day-denervated hearts. MW, molecular weight. The densitometric analysis is reported. Error bars indicate SEM (*$0.01 < P < 0.05$, **$P < 0.01$; NS, not significant; $n = 6$ mice for each group).

rate (HR: β2-AR KO: 523 ± 30 b.p.m. vs. control: 502 ± 4 b.p.m.) (*Figure 6E–G*). Altogether, these results suggest that constitutive β2-AR signalling regulates the cardiac mass by controlling UPS activity through repression of MuRF1 expression.

4. Discussion

The heart has the ability to adjust its performance to the perfusional demand of peripheral tissues, through both acute control of contractility and reversible changes in the cardiac mass.[17,40] Although it is well-accepted that the autonomic nervous system tunes contractile function on a beat-to-beat basis,[41] it is not clear whether the regulation of the physiological cardiomyocyte size relies on continuous trophic input from the cardiac neurons.

Mechanical, metabolic, and neuro/hormonal signals have all been implicated in the modulation of cardiomyocyte growth in exercise- or disease-induced cardiac hypertrophy.[42] Conversely, termination of these signals upon relief of the pro-hypertrophic stimulus (e.g. mechanical unloading or removal of aortic banding) has been shown to induce 'reverse' remodelling.[43,44] Such plasticity in the cardiomyocyte size requires mechanisms that control the relative rates of protein synthesis and degradation, the latter depending mainly on proteasome activity and autophagy.[45,46] Here, we show that ablation of sympathetic efferents to the heart offsets the proteolytic machinery by up-regulating the muscle-specific ubiquitin ligases MuRF1 and atrogin-1/MAFbx, with subsequent activation of the autophagy–lysosome system, and reduces Akt-S6K signalling, suggesting reduced protein synthesis. The combined effect of such processes is the

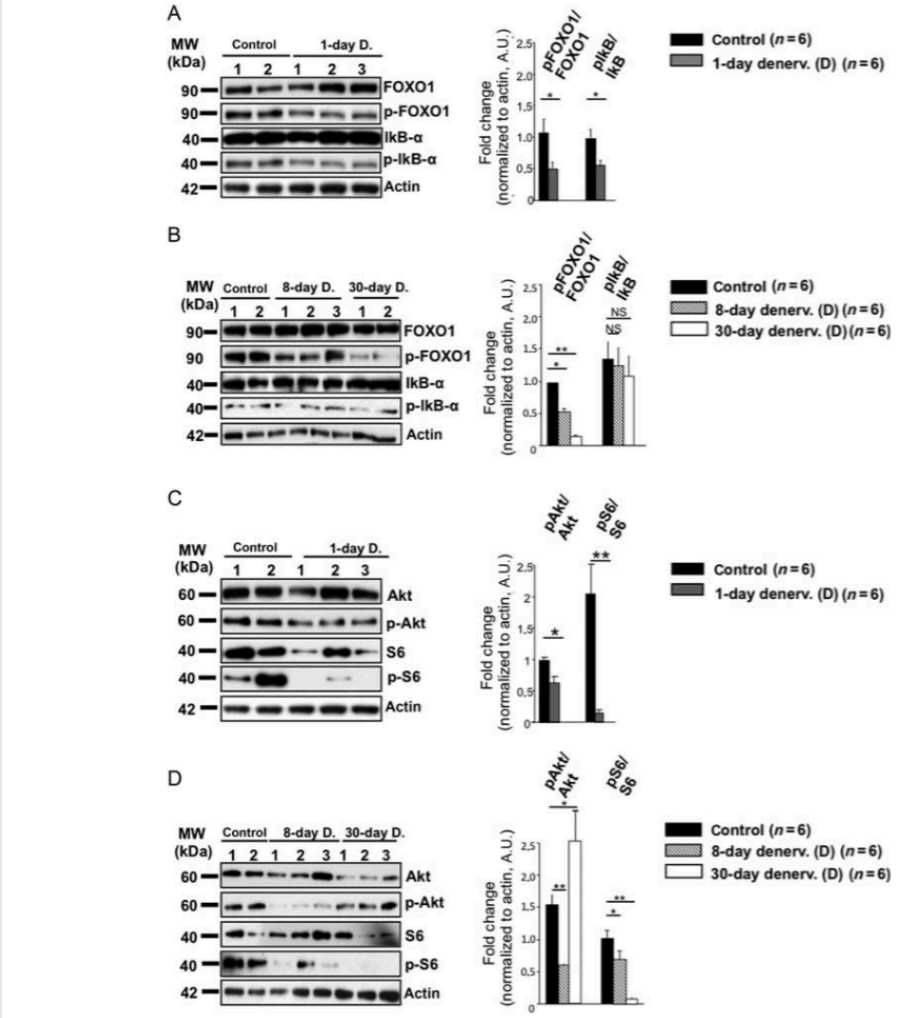

Figure 4 UPS activation in denervated hearts is mediated by FOXO-dependent pathway. (*A–D*) Western blot analysis of total ventricular extracts from vehicle-treated, 1-, 8-, and 30-day-denervated hearts. MW, molecular weight. The densitometric analysis is reported. Error bars indicate SEM (*$0.01 < P < 0.05$, **$P < 0.01$; NS, no significant; $n = 6$ mice for each group).

induction of atrophic remodelling in cardiomyocytes, which become smaller than in normally innervated hearts, in the context of a structurally and functionally normal myocardium. Induction of the atrogenes depends on the reduction of constitutive adrenergic input to the β2-AR, with subsequent decrease in PI3K/Akt signalling that allows activation of the FOXO family of transcription factors and of their target genes MuRF1 and atrogin1/MAFbx. Therefore, our data indicate that the physiological cardiomyocyte size relies on constitutive activation of β2-AR signalling by neuronally released NE that negatively regulates the proteolytic machinery. Consistently, chronic administration of the β2-AR agonist CL prevented atrophic remodelling in denervated hearts, and mice lacking β2-ARs had smaller hearts in the absence of significant impairment in cardiac function. Furthermore, denervation atrophy did not develop in MuRF1 KO mice, indicating that among the main cardiac ubiquitin ligases, MuRF1 is dominant in determining the cardiomyocyte mass, a view consistent with the observation that MuRF1 targets include constituents of the sarcomere, which is responsible for nearly half of cardiac cell volume.[4] These results are in line with a recent report showing that acute β2-AR stimulation down-regulates MuRF1 and atrogin-1/MAFbx

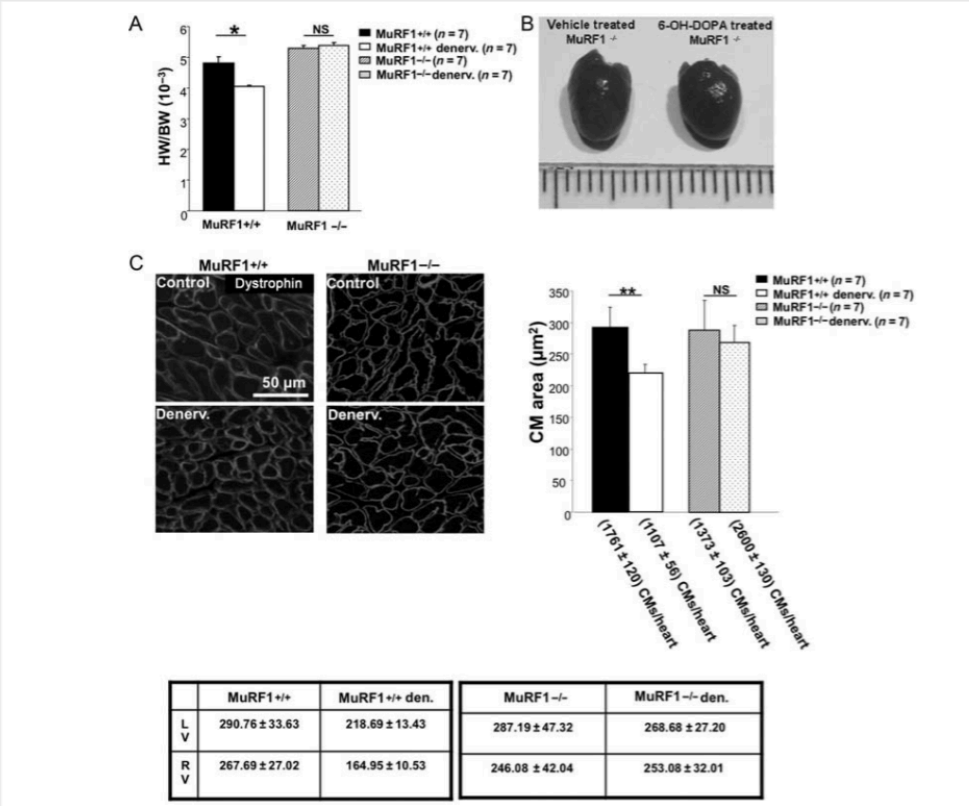

	MuRF1+/+	MuRF1+/+ den.	MuRF1−/−	MuRF1−/− den.
LV	290.76 ± 33.63	218.69 ± 13.43	287.19 ± 47.32	268.68 ± 27.20
RV	267.69 ± 27.02	164.95 ± 10.53	246.08 ± 42.04	253.08 ± 32.01

Figure 5 MuRF1 knock-out (MurF1−/−) mice do not develop denervation-induced cardiac atrophy. (*A*) Evaluation of the heart weight/body weight (HW/BW) ratio in vehicle-treated control and 30-day-denervated MuRF1+/+ mice and vehicle-treated and 30-day-denervated MuRF1−/− mice. Error bars indicate SEM (*0.01 < P < 0.05; n = 7 mice for each group). (*B*) Hearts from vehicle-treated and denervated MuRF1−/− mice. (*C*) Immunofluorescence analysis of ventricular cryosections from vehicle-treated and 30-day-denervated MuRF1+/+ mice and vehicle-treated and 30-day-denervated MuRF1−/− mice stained with an antibody against dystrophin (left panel). Bar: 50 μm. Morphometric evaluation of the cardiomyocyte cross-sectional area is shown in the right panel. RV, right ventricle; LV, left ventricle. Error bars indicate SEM (*0.01 < P < 0.05, **P < 0.01; n = 6 mice for each group). The number of LV CMs (mean ± SD) evaluated for each heart is reported at the bottom of the graph.

genes,[26] and with those described in skeletal muscle, which undergoes atrophy upon sympathetic denervation, a process mediated by MuRF1 induction and antagonized by β2-AR stimulation.[39]

Although the mechanisms leading to cardiac hypertrophy have extensively been studied, using a variety of pharmacological, surgical, and genetic approaches, the mediators of cardiac atrophy are much less clarified. Atrophic remodelling of the heart has mainly been investigated in response to changes in metabolic and mechanical signals, for instance in models of caloric restriction and haemodynamic unloading [heterotopic heart transplantation (hht)], respectively.[32,47] These conditions mediate cardiac atrophy through up-regulation of ubiquitin ligases. In the case of caloric restriction atrophy, the AMPK pathway activates atrogenes responding to changes in the metabolic intake. In unloading atrophy, the ubiquitin ligases are activated by extreme haemodynamic unloading, with a nearly complete loss of contractility[48] and a degree of atrophic remodelling incompatible with cardiac function. The results of this study add to the picture the autonomic neuro-endocrine axis of cardiac size regulation, whereby the trophic effect of β2-AR-dependent signalling finely tunes cardiomyocyte protein balance within a more limited range. In fact, denervated hearts developed a much smaller atrophic remodelling even in long-term observation (HW/BW decrease, denervated: 15% vs. hht: 45%), in the absence of significant changes in cardiac function.

Further investigation will be needed to determine whether in the normal heart persistent activation of β2-AR signalling is obtained by an increase in the resting NE levels in the myocardium, or by repeated transient bursts of NE discharge. In the second model, receptor stimulation is obtained with repeated sympathetic discharge during locomotor activity, postural changes, or environmental stimulation.

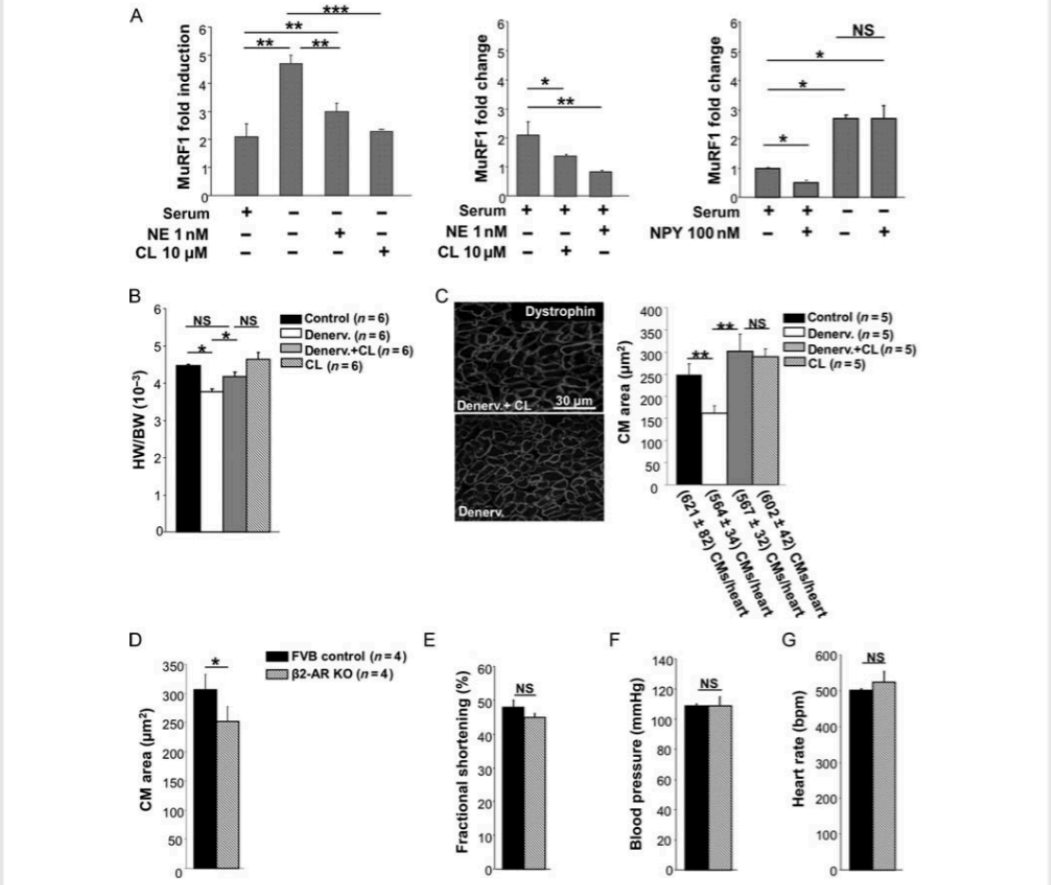

Figure 6 β2-adrenoceptor (β2-AR) stimulation modulates cardiomyocyte trophism. (*A*) RT–qPCR analysis in extracts from rat neonatal cultured cardiomyocytes. Error bars indicate SEM (***$P < 0.001$; **$P < 0.01$; NS, no significant; $n = 6$, for each group). NE, norepinephrine; CL, clenbuterol; NPY, Neuropeptide Y. (*B*) Evaluation of heart weight/body weight (HW/BW) in vehicle-treated control, denervated, denervated + CL- and CL-treated mice. Error bars indicate SEM (*$P < 0.05$; $n = 6$, for each group). (*C*) Immunofluorescence analysis of ventricular cryosections from 30-day-denervated and 30-day-denervated + CL-treated mice stained with an antibody against dystrophin (left panel). Bar: 30 μm. Morphometric evaluation of the cardiomyocyte cross-sectional area of vehicle-treated control, denervated, denervated + CL- and CL-treated mice (right panel). Error bars indicate SEM (*$0.01 < P < 0.05$; NS, not significant; $n = 5$ mice for each group). The number of LV CMs (mean ± SD) evaluated for each heart is reported. (*D*) Morphometric evaluation of the cardiomyocyte cross-sectional area β2-adrenoceptor (β2-AR) KO mice and relative littermate controls. Error bars indicate SEM (*$P < 0.05$; number of animals = 4, for each group). (e.g.) Evaluation of fractional shortening (*E*), blood pressure (*F*), and heart rate (*G*) in vehicle-treated control and β2-AR KO mice. Error bars indicate SEM (*$P < 0.05$; NS, not significant; number of animals = 6 for each group).

Consistent with this model, we observed circadian variation in MuRF1 gene transcription with the lowest level detected during the dark period[29,49] (and Dyar, in preparation), when bursts of sympathetic activity are more frequent.[50]

Interestingly, β2-ARs are capable of independently control different signalling pathways through both Gs or β-arrestin-dependent pathways.[51] The reduction in Akt and ERK (Supplementary material online, *Figure S4*) pathways occurring in the denervated hearts in the absence of impaired contractile function suggests the intriguing hypothesis that the continuously active mechanism of transcriptional regulation of β2-AR on the atrogenes might be mediated by β-arrestin 2.[52–55]

5. Conclusions

Our results demonstrate that the sympathetic nervous system constitutively regulates the physiological cardiomyocyte size, through β2-AR-dependent modulation of protein degradation by the UPS.

This mechanism underlines the importance of regulated proteolysis in cardiac cell physiology, and expands our current knowledge on cardiac cell and tissue homoeostasis. Furthermore, the identification of a previously unrecognized function of the cardiac sympathetic innervation is of great clinical relevance given that prolonged activation of β-ARs is associated to hypertrophy and failure, and β-AR modulation is central in the treatment of these conditions.

Supplementary material

Supplementary material is available at *Cardiovascular Research* online.

Acknowledgements

We are grateful to Dr Ken Dyar and Prof. Tullio Pozzan for helpful discussion, Dr Paola Pesce and D.C. for echocardiography analyses, Prof. Antoon Moorman for anti-βMHC antibody, Lino Bigon, Giulia Carotta, Valentina Mazzariol, and Dr. Anne Picard for technical assistance.

Conflict of interest: none declared.

Funding

This work was supported by: University of Padova (Progetto di Ricerca di Ateneo 2010 to M.M. CPDA0977 and Progetto Giovani Studiosi 2010 to T.Z. GRIC101133), the Telethon Foundation, Grant n. GGP11224 to M.M.; Fondation Leducq and the Italian Ministry of Education (MiUR) to MS; Grants-Fundação de Amparo à Pesquisa do Estado de São Paulo (FAPESP, 2008/56483-1 and 2010/50048-1) to P.C.B.

References

1. Baskin KK, Taegtmeyer H. AMP-activated protein kinase regulates E3 ligases in rodent heart. *Circ Res* 2011;**109**:1153–1161.
2. Willis MS, Townley-Tilson WHD, Kang EY, Homeister JW, Patterson C. Sent to destroy: the ubiquitin proteasome system regulates cell signaling and protein quality control in cardiovascular development and disease. *Circ Res* 2010;**106**: 463–478.
3. Wang X, Robbins J. Heart failure and protein quality control. *Circ Res* 2006;**99**: 1315–1328.
4. Bodine SC, Latres E, Baumhueter S, Lai VK, Nunez L, Clarke BA *et al.* Identification of ubiquitin ligases required for skeletal muscle atrophy. *Science* 2001;**294**:1704–1708.
5. Gomes MD, Lecker SH, Jagoe RT, Navon A, Goldberg AL. Atrogin-1, a muscle-specific F-box protein highly expressed during muscle atrophy. *Proc Natl Acad Sci USA* 2001;**98**:14440–14445.
6. Li H-H, Kedar V, Zhang C, McDonough H, Arya R, Wang D-Z *et al.* Atrogin-1/muscle atrophy F-box inhibits calcineurin-dependent cardiac hypertrophy by participating in an SCF ubiquitin ligase complex. *J Clin Invest* 2004;**114**:1058–1071.
7. Li H-H, Willis MS, Lockyer P, Miller N, McDonough H, Glass DJ *et al.* Atrogin-1 inhibits Akt-dependent cardiac hypertrophy in mice via ubiquitin-dependent coactivation of Forkhead proteins. *J Clin Invest* 2007;**117**:3211–3223.
8. Arya R, Kedar V, Hwang JR, McDonough H, Li H-H, Taylor J *et al.* Muscle ring finger protein-1 inhibits PKC{epsilon} activation and prevents cardiomyocyte hypertrophy. *J Cell Biol* 2004;**167**:1147–1159.
9. Willis MS, Ike C, Li L, Wang D-Z, Glass DJ, Patterson C. Muscle ring finger 1, but not muscle ring finger 2, regulates cardiac hypertrophy *in vivo*. *Circ Res* 2007;**100**:456–459.
10. Preedy VR, Smith DM, Kearney NF, Sugden PH. Rates of protein turnover *in vivo* and *in vitro* in ventricular muscle of hearts from fed and starved rats. *Biochem J* 1984;**222**: 395–400.
11. Samarel AM, Parmacek MS, Magid NM, Decker RS, Lesch M. Protein synthesis and degradation during starvation-induced cardiac atrophy in rabbits. *Circ Res* 1987;**60**: 933–941.
12. Klein I, Hong C, Schreiber SS. Cardiac atrophy in the heterotopically transplanted rat heart: *in vitro* protein synthesis. *J Mol Cell Cardiol* 1990;**22**:461–468.
13. Sacheck JM, Hyatt J-PK, Raffaello A, Jagoe RT, Roy RR, Edgerton VR *et al.* Rapid disuse and denervation atrophy involve transcriptional changes similar to those of muscle wasting during systemic diseases. *FASEB J* 2007;**21**:140–155.
14. Wing SS, Haas AL, Goldberg AL. Increase in ubiquitin-protein conjugates concomitant with the increase in proteolysis in rat skeletal muscle during starvation and atrophy denervation. *Biochem J* 1995;**307**:639–645.
15. Clarke BA, Drujan D, Willis MS, Murphy LO, Corpina RA, Burova E *et al.* The E3 Ligase MuRF1 degrades myosin heavy chain protein in dexamethasone-treated skeletal muscle. *Cell Metab* 2007;**6**:376–385.
16. Cohen S, Brault JJ, Gygi SP, Glass DJ, Valenzuela DM, Gartner C *et al.* During muscle atrophy, thick, but not thin, filament components are degraded by MuRF1-dependent ubiquitylation. *J Cell Biol* 2009;**185**:1083–1095.
17. Sampson KJ, Kass RS. Molecular mechanisms of adrenergic stimulation in the heart. *Heart Rhythm* 2010;**7**:1151–1153.
18. Altman JD, Trendelenburg AU, MacMillan L, Bernstein D, Limbird L, Starke K *et al.* Abnormal regulation of the sympathetic nervous system in alpha2A-adrenergic receptor knockout mice. *Mol Pharmacol* 1999;**56**:154–161.
19. Hein L, Altman JD, Kobilka BK. Two functionally distinct alpha2-adrenergic receptors regulate sympathetic neurotransmission. *Nature* 1999;**402**:181–184.
20. Kiriazis H, Du XJ, Feng X, Hotchkin E, Marshall T, Finch S *et al.* Preserved left ventricular structure and function in mice with cardiac sympathetic hyperinnervation. *Am J Physiol Heart Circ Physiol* 2005;**289**:H1359–H1365.
21. Ryall JG, Sillence MN, Lynch GS. Systemic administration of beta2-adrenoceptor agonists, formoterol and salmeterol, elicit skeletal muscle hypertrophy in rats at micromolar doses. *Br J Pharmacol* 2006;**147**:587–595.
22. Tevaearai HT, Eckhart AD, Walton GB, Keys JR, Wilson K, Koch WJ. Myocardial gene transfer and overexpression of beta2-adrenergic receptors potentiates the functional recovery of unloaded failing hearts. *Circulation* 2002;**106**:124–129.
23. Birks EJ, Tansley PD, Hardy J, George RS, Bowles CT, Burke M *et al.* Left ventricular assist device and drug therapy for the reversal of heart failure. *N Engl J Med* 2006;**355**: 1873–1884.
24. Lee S, Grafweg S, Schneider T, Jimenez M, Giacobino JP, Ghanem A *et al.* Total beta-adrenoceptor deficiency results in cardiac hypotrophy and negative inotropy. *Physiol Res* 2010;**59**:679–689.
25. Nayler WG, Slade A, Vaughan Williams EM, Yepez CE. Effect of prolonged beta-adrenoceptor blockade on heart weight and ultrastructure in young rabbits. *Br J Pharmacol* 1980;**68**:363–371.
26. Zhang W, Yano N, Deng M, Mao Q, Shaw SK, Tseng Y-T. β-Adrenergic receptor-PI3K signaling crosstalk in mouse heart: elucidation of immediate downstream signaling cascades. *PLoS One* 2011;**6**:e26581.
27. Finch L, Haeusler G, Thoenen H. A comparison of the effects of chemical sympathectomy by 6-hydroxydopamine in newborn and adult rats. *Br J Pharmacol* 1973;**47**: 249–260.
28. Daffonchio A, Franzelli C, Di Rienzo M, Castiglioni P, Ramirez AJ, Parati G *et al.* Effect of sympathectomy on blood pressure variability in the conscious rat. *J Hypertens Suppl* 1991;**9**:S70–S71.
29. Makino M, Hayashi H, Takezawa H, Hirai M, Saito H, Ebihara S. Circadian rhythms of cardiovascular functions are modulated by the baroreflex and the autonomic nervous system in the rat. *Circulation* 1997;**96**:1667–1674.
30. Depre C, Davies PJ, Taegtmeyer H. Transcriptional adaptation of the heart to mechanical unloading. *Am J Cardiol* 1999;**83**:58H–63H.
31. Jagoe RT, Goldberg AL. What do we really know about the ubiquitin-proteasome pathway in muscle atrophy? *Curr Opin Clin Nutr Metab Care* 2001;**4**:183–190.
32. Gruber C, Nink N, Nikam S, Magdowski G, Kripp G, Voswinckel R *et al.* Myocardial remodelling in left ventricular atrophy induced by caloric restriction. *J Anat* 2012;**220**: 179–185.
33. Kruger M, Moser M, Ussar S, Thievessen I, Luber CA, Forner F *et al.* SILAC mouse for quantitative proteomics uncovers kindlin-3 as an essential factor for red blood cell function. *Cell* 2008;**134**:353–364.
34. Sandri M. Autophagy in health and disease. 3. Involvement of autophagy in muscle atrophy. *Am J Physiol Cell Physiol* 2010;**298**:C1291–C1297.
35. Skurk C, Izumiya Y, Maatz H, Razeghi P, Shiojima I, Sandri M *et al.* The FOXO3a transcription factor regulates cardiac myocyte size downstream of AKT signaling. *J Biol Chem* 2005;**280**:20814–20823.
36. Cai D, Frantz JD, Tawa NE, Melendez PA, Oh B-C, Lidov HGW *et al.* IKKbeta/NF-kappaB activation causes severe muscle wasting in mice. *Cell* 2004;**119**:285–298.
37. Nicholl SM, Bell D, Spiers Jp, McDermott BJ. Neuropeptide Y Y(1) receptor regulates protein turnover and constitutive gene expression in hypertrophying cardiomyocytes. *Eur J Pharmacol* 2002;**441**:23–34.
38. Deng XF, Rokosh DG, Simpson PC. Autonomous and growth factor-induced hypertrophy in cultured neonatal mouse cardiac myocytes. Comparison with rat. *Circ Res* 2000;**87**:781–788.
39. Goncalves DA, Silveira WA, Lira EC, Graca FA, Paula-Gomes S, Zanon NM *et al.* Clenbuterol suppresses proteasomal and lysosomal proteolysis and atrophy-related genes in denervated rat soleus muscles independently of Akt. *Am J Physiol Endocrinol Metab* 2012;**302**:E123–E133.
40. Triposkiadis F, Karayannis G, Giamouzis G, Skoularigis J, Louridas G, Butler J. The sympathetic nervous system in heart failure physiology, pathophysiology, and clinical implications. *J Am Coll Cardiol* 2009;**54**:1747–1762.
41. Wang W, Zhu W, Wang S, Yang D, Crow MT, Xiao RP *et al.* Sustained beta1-adrenergic stimulation modulates cardiac contractility by Ca2+/calmodulin kinase signaling pathway. *Circ Res* 2004;**95**:798–806.
42. Schluter KD, Millar BC, McDermott BJ, Piper HM. Regulation of protein synthesis and degradation in adult ventricular cardiomyocytes. *Am J Physiol* 1995;**269**:C1347–C1355.

43. Levin HR, Oz MC, Chen JM, Packer M, Rose EA, Burkhoff D. Reversal of chronic ventricular dilation in patients with end-stage cardiomyopathy by prolonged mechanical unloading. *Circulation* 1995;**91**:2717–2720.
44. Razeghi P, Sharma S, Ying J, Li Y-P, Stepkowski S, Reid MB *et al.* Atrophic remodeling of the heart *in vivo* simultaneously activates pathways of protein synthesis and degradation. *Circulation* 2003;**108**:2536–2541.
45. Kundu M, Thompson CB. Macroautophagy versus mitochondrial autophagy: a question of fate? *Cell Death Differ* 2005;**12**(Suppl 2):1484–1489.
46. Zheng Q, Li J, Wang X. Interplay between the ubiquitin-proteasome system and autophagy in proteinopathies. *Int J Physiol Pathophysiol Pharmacol* 2009;**1**:127–142.
47. Sharma S, Ying J, Razeghi P, Stepkowski S, Taegtmeyer H. Atrophic remodeling of the transplanted rat heart. *Cardiology* 2006;**105**:128–136.
48. Razeghi P, Volpini KC, Wang M-E, Youker KA, Stepkowski S, Taegtmeyer H. Mechanical unloading of the heart activates the calpain system. *J Mol Cell Cardiol* 2007;**42**:449–452.
49. Oosting J, Struijker-Boudier HA, Janssen BJ. Autonomic control of ultradian and circadian rhythms of blood pressure, heart rate, and baroreflex sensitivity in spontaneously hypertensive rats. *J Hypertens* 1997;**15**:401–410.
50. Wang N, Yang G, Jia Z, Zhang H, Aoyagi T, Soodvilai S *et al.* Vascular PPARgamma controls circadian variation in blood pressure and heart rate through Bmal1. *Cell Metab* 2008;**8**:482–491.
51. Nobles KN, Xiao K, Ahn S, Shukla AK, Lam CM, Rajagopal S *et al.* Distinct phosphorylation sites on the beta(2)-adrenergic receptor establish a barcode that encodes differential functions of beta-arrestin. *Sci Signal* 2011;**4**:ra51.
52. Shenoy SK, Drake MT, Nelson CD, Houtz DA, Xiao K, Madabushi S *et al.* beta-arrestin-dependent, G protein-independent ERK1/2 activation by the beta2 adrenergic receptor. *J Biol Chem* 2006;**281**:1261–1273.
53. Drake MT, Shenoy SK, Lefkowitz RJ. Trafficking of G protein-coupled receptors. *Circ Res* 2006;**99**:570–582.
54. Zhu WZ, Zheng M, Koch WJ, Lefkowitz RJ, Kobilka BK, Xiao RP. Dual modulation of cell survival and cell death by beta(2)-adrenergic signaling in adult mouse cardiac myocytes. *Proc Natl Acad Sci USA* 2001;**98**:1607–1612.
55. Chesley A, Lundberg MS, Asai T, Xiao RP, Ohtani S, Lakatta EG *et al.* The beta(2)-adrenergic receptor delivers an antiapoptotic signal to cardiac myocytes through G(i)-dependent coupling to phosphatidylinositol 3′-kinase. *Circ Res* 2000;**87**:1172–1179.

Acknowledgments